Alma Mater Studiorum – Università di Bologna

DOTTORATO DI RICERCA IN

AUTOMOTIVE PER UNA MOBILITA' INTELLIGENTE

Ciclo 34

Settore Concorsuale: 09/A3 - PROGETTAZIONE INDUSTRIALE, COSTRUZIONI MECCANICHE E METALLURGIA

Settore Scientifico Disciplinare: ING-IND/14 - PROGETTAZIONE MECCANICA E COSTRUZIONE DI MACCHINE

JOINTS AND INNOVATIVE COMPONENTS FOR AUTOMOTIVE APPLICATIONS

Presentata da: Luca Paiardini

Coordinatore Dottorato

Prof. Nicolò Cavina

Supervisore

Prof. Giorgio Olmi

Co-supervisore

Prof. Dario Croccolo

Esame finale anno 2022

A mio papà Giuseppe

ABSTRACT

The research activities described in this thesis were focused on two main topics: the study of shaft-hub joint performance, with particular regard to interference-fitted and adhesively bonded connection, and the fatigue characterization of additively processed metal alloys. The research on interference-fitted shaft-hub joints dealt with some studies in the field of fretting fatigue. Rotating bending fatigue tests were performed on different materials by not conventional specimens to determine the fatigue properties of interference-fitted joints and to investigate the fretting fatigue phenomenon, which led to novel and original results. In adhesively bonded and interference-fitted shaft-hub connections (called hybrid joints) the synergic effect of anaerobic adhesive and interference has the capability of improving the joint strength. However, the adhesive contribution depends on several factors. Therefore, its behavior was investigated for different coupling pressure, coupling procedure, operating temperature and joint design. The study on additively manufactured metal alloy deals with rotating banding fatigue tests. AlSi10Mg and Maraging Stainless Steel CX were involved in the campaign for their wide applicability in Automotive. Build direction, heat and surface treatments were considered as input parameters. Fatigue results were interpreted by statistical method and microscopy analyses in order to determine the effectiveness and the beneficial or detrimental effects of the considered factors. Fracture mode and microstructure were investigated by fractographic and micrographic analyses.

INDEX

INTRODUCTION 5

CHAPTER 1. FRETTING FATIGUE IN SHAFT-HUB INTERFERNCE JOINTS 7

1.1 Introduction 7

1.2 Rotating bending fatigue tests: ISO 12107 calculation method 11

1.3 Materials and methods 16

1.3.1 Equipment 16

1.3.2 Samples 19

1.3.3 Experimental plan 19

1.3.4 Experimental procedure 20

1.4 Results and discussion 23

1.4.1 Fatigue tests 23

1.4.2 Surface analyses 25

1.4.3 Fretting fatigue fracture initiating 29

1.5 Conclusions 36

1.6 References 37

CHAPTER 2. SHAFT-HUB HYBRID CONNECTIONS: ANAEROBIC ADHESIVE TO OPTIMIZE AND IMPROVE JOINT PERFORMANCE 39

2.1 Main parameters affecting the adhesively bonded joint strength 41

2.1.1 Bonding clearance and interference 42

2.1.2 Roughness 43

2.1.3 Grooves and hoop channels 44

2.1.4 Assembly process 45

2.1.5 Curing condition 46

2.1.6 Operating temperature 47

2.2 Calculation method for shaft hub hybrid joints 48

2.3 Materials and methods 51

2.3.1 Specimens 51

2.3.2 Equipment 52

2.3.3 Experimental procedure 55

2.4 Dry coupling to determine the first release friction coefficient 58

2.5 Influence of the assembly process and of the interference level on the Loctite 648 adhesive strength 66

2.6 Loctite 648 shear strength at high temperature 72

2.7 The effect of the shaft geometry on the joint strength 78

2.8 Checks for completeness of the experiment 85

2.9 Conclusions 87

2.10 References 88

CHAPTER 3. FATIGUE RESPONSE OF ADDITIVELY PROCESSED METAL ALLOYS: ALSI10MG AND MARAGING STAINLESS STEEL CX 90

3.1 Introduction 90

3.2 Materials and equipment 95

3.2.1 Specimens 95

3.2.2 Equipment 97

3.3 The AlSi10Mg aluminum alloy 100

3.3.1 The experimental plan 100

3.3.2 Preliminary checks 102

3.3.3 Static tensile tests 103

3.3.4 Fatigue tests 105

3.3.5 Density measurement for porosity evaluation 116

3.3.6 Fractographic analyses 117

3.3.7 Micrographic analyses 123

3.3.8 Conclusions 130

3.4 The Stainless Steel CX 132

3.4.1 The experimental plan 132

3.4.2 Preliminary checks 134

3.4.3 Fatigue tests 135

3.4.4 Porosity evaluation 140

3.4.5 Fractographic analyses 142

3.4.6 Micrographic analyses 145

3.4.7 Conclusions 147

3.5 References 149

Appendix: AlSi10Mg fatigue curves 153

INTRODUCTION

The research project reported in the next chapters concerns the study of some topics in the field of mechanical joint design and innovative components to be used in automotive applications.

Improvements in safety, reliability, ecology, lightness, comfort and performance are increasingly required by the automotive market. The optimization process involves both individual components and joining techniques.

In the field of torque and power transmissions, a widely used technique to connect a shaft and a hub is interference fitting. Interference-fitted joints work as frictional couplings: their load capability mostly depends on the coupling pressure. The latter generates stress inside the parts that combine to those generated by the external load to be transmitted. Furthermore, at the ends of the connection, stress concentration appears. Although the coupling pressure ensures joint integrity, microscopic relative displacements can occur between the parts, which are likely to lead to fretting corrosion development. When parts operate under fatigue loads, this occurrence is commonly regarded as fretting fatigue. Several failures are attributed to this phenomenon, which in the past has also caused serious accidents. Calculation methods, which are applied for joint design, do not take fretting fatigue into account. In the first chapter of the present thesis, an experimental study on fretting fatigue in interference-fitted shaft-hub joints is reported. The aim was to study with more detail fretting phenomenon and to provide original quantitative data that can be used in numerical predictive models.

Adding anaerobic adhesive to an interference-fitted connection is a useful method to improve joint strength and to reduce fretting damage. When the presence of adhesive is combined with the coupling interference, the connection is called hybrid joint. The strength of a hybrid joints is closely related to the adhesive shear strength, which is affected by several factors, such as the coupling pressure, the assembly process, the operating temperature and the joint design. Therefore, in the second chapter of the thesis, the performance of a hybrid shaft-hub joint, to be used in a mechanical powertrain, is analyzed. The study provides experimental data regarding both conventional interference fitted and hybrid connections, even up to high interference levels. The above-mentioned factors are considered as input parameters and the adhesive shear strength is assessed.

Component optimization may arise from not only structural optimization, but also technological process improvement. Additive manufacturing processes make it possible

to fabricate parts with complex geometry (as a monolithic component) and to obtain lightweight and resistant components, as required for many automotive applications. However, the additively manufactured part strength is affected by several process parameters as well as post-process treatments. The recent industrial development of additive manufacturing technologies and the increasing availability of alloys to be used in these processes are requiring further investigations on the mechanical properties and how process and post process parameters can improve the components strength with specific regard to fatigue. However, results in the literature, sometimes, are often missing and are, therefore, not enough to ensure an efficient design. For these reasons, in the third chapter of the thesis, the mechanical response, with particular regard to fatigue properties, of two additively processed metal alloys is experimentally investigated and furtherly analyzed. Several original fatigue data are provided. The effects of the main process parameters, like the build orientation, the heat treatment and the surface treatment, on the fatigue strength are extensively investigated by experimental campaign and subsequent result statistical processing.

CHAPTER 1

FRETTING FATIGUE IN SHAFT-HUB INTERFERNCE JOINTS

1.1 Introduction

The study that will be reported in the following Sections accounts for interference-fitted shaft-hub joints. Although the contact pressure in these connections warrants joint integrity, micrometric relative displacements, which are likely to lead to fretting corrosion, may occur between the shaft and the hub.

Fretting corrosion occurs, when two metallic or non-metallic surfaces, in contact with each other, operate under a repeated and relative movement, even of very small amplitude.

Fretting corrosion can promote the nucleation of cracks, which under fatigue loads can then grow quickly, triggering premature failure. In fact, the combination of these detrimental normal tensile and shear stresses and the interface displacements lead to oxidation, wear and crack initiation. This complicated damage may result in the decrease of original fatigue strength of materials and components [1.1 - 1.2].

The problem of fretting corrosion was investigated from the first half of the 20th century. Nevertheless, a considerable number of failures that can be related to fretting damaging were observed even in the last years. A typical example of fretting damage is found in railway axle members [1.3 - 1.5] and this phenomenon was the primary cause of some serious accidents. Fretting damage is also a common issue even in turbine shafts [1.6 - 1.10] and metallic cables [1.11 - 1.13].

In shaft-hub joints, fretting corrosion appears next to the ends of the press-fit coupling. In the same region, stress concentrations caused by the component geometry furtherly reduce the fatigue life of the shaft [1.14 - 1.15]. When parts are subject to fretting corrosion as well to fatigue loads, this phenomenon is commonly regarded as fretting fatigue. Fretting corrosion can promote the nucleation of cracks, which under fatigue loads can grow quickly leading to premature failure.

The fretting damage mechanism is very complex. When a bending moment is applied to a press-fitted shaft, the alternating elongation and contraction of the axle fibers lead to a slight relative slip that can be observed between the shaft and the hub near the end of the press-fit. If parts are rotated under bending moment, the entire shaft contour near the end

of the press-fit is exposed to cyclic relative slip. Wear particles are produced, but, due to the small relative movements, these are accumulated between the two surfaces [1.16]. As an affect of the small amplitude of the sliding, the produced debris are often retained within the contact area, thus accelerating the wear process. In this stage of fretting, debris build up and metal-to-metal contact reduces: frictional forces and slip motion become stable. As cyclic loads continue to be applied, the contact area is gradually worn out as the result of wear particle abrasive action: the relative slip grows up again due to the clamping pressure decreasing.

Fretting wear causes a reduction of fatigue strength, as the mechanical abrasion leads to the generation of pits, which act as stress raisers. In fact, cavities caused by fretting could be initiation sites of fatigue cracks.

Chemical corrosion also appears in worn areas: especially in steel specimens, it is quite frequent to find effects in the form of rust. However, corrosion also has a secondary effect on fatigue strength decay. Testing under fatigue loads steel specimens in both air and oil environment, a slightly higher fatigue limit was observed for samples in oil rather than for those in air. [1.17 - 1.18]. Therefore, the surface roughening caused by fretting was pointed out as the main factor of fatigue strength lowering.

The secondary effect of chemical corrosion was also investigated by tests at different load frequencies. In fact, load frequency can also affect temperature components, thus promoting chemical corrosion deterioration. However, results in [1.16] highlight no particular variations in the fretting fatigue behavior for tests carried out at different load frequencies behavior, thus indicating the major cause of failure is due to mechanical phenomena.

Fatigue fretting fractures are different from conventional fatigue fractures because of some features. In fretting fatigue fractures, secondary cracks are located close to the main fracture. Furthermore, shear stresses are induced due to the relative slip between the mating parts. Due to the presence of shear stresses, fractures are not radially oriented, but they exhibit a slope angle between 0° and 45° with respect to a radial direction (Figure 1).

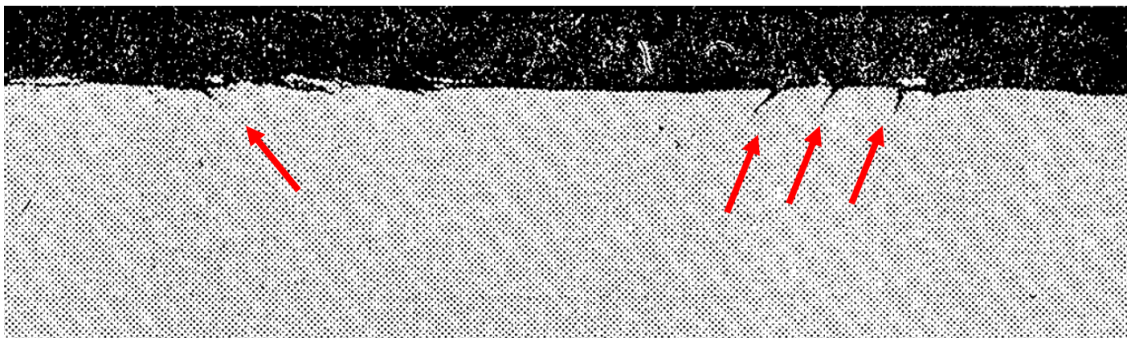

Figure 1: Cross section of a cracked sample. Example of fretting fatigue cracks [1.17]

Although the fretting phenomenon has been known for a long time, some issues regarding the experimental procedure are currently unsolved. No standardized sample exists for determining the fatigue behavior of interference-fitted shaft-hub joints. The experimental studies often involve large specimens [1.19]. Moreover, the used experimental methods were often time consuming due to low working frequency. The assessing of fretting fatigue properties would be easier, if a scaled model could be used to replicate the effect of interference pressure and cyclic loads combined to relative displacements. For this reason, in [1.20] a small specimen, which can be used for rotating bending fatigue tests, was introduced. However, it showed some issue related to the observation of the fretting damage, preventing a complete study of the phenomenon.

Another important shortage in the field of fretting phenomenon concerns the limited availability of numerical predictive models.

In this thesis, an innovative specimen, which makes it possible to speed up the tests, to reduce overall sample dimensions and to analyze the corroded fretting area, was utilized for the first time, in order to overcome the aforementioned issues. The fretting fatigue behavior of the Aluminum 7075 and the C40 Steel was analyzed by rotating bending tests on interference-fitted samples. The aims of this study are:

- to use this test equipment for the first time, highlighting its strengths and criticalities and the capability of making the damaged area easily accessible for microscopy analyses
- to determine the fatigue performance of the aforementioned materials in interference-fitted shaft-hub joints under different contact pressure, in order to provide quantitative data for the future development of FEA models.

The results of fatigue tests were processed in agreement with Standard ISO 12107, calculating the fatigue curves with their confidence bands and the fatigue limits.

The damaged surfaces were observed by a stereoscopic microscope. Furthermore, non-destructive tests were carried out to locate fractures in fatigued but not failed shafts: the fracture area was observed by longitudinally cutting the shafts, thus assessing the fracture initiation and propagation.

In the following Sections, the fatigue test calculation method is initially detailed. Afterwards, the developed equipment for the fretting fatigue tests was analyzed. Subsequently, fatigue results are reported and the initiation of fretting cracks is investigated.

1.2 Rotating bending fatigue tests: ISO 12107 calculation method.

The progressive damage that occurs in materials stressed with cyclic loads, even much lower than the ultimate tensile strength or than the yield strength, is called fatigue failure. Rotating bending tests are very useful to study the fatigue phenomenon. By testing a set of specimens at various stress levels it is possible to determine a relationship of the fatigue life as a function of the stress. Results are usually expressed as an S-N curve. These are generally either log-log plots with the life cycles (N) on the abscissa and fatigue strength (S) on the ordinate. As ISO 12107 explains: *"Fatigue test results usually display significant scatter even when the tests are carefully conducted to minimize experimental error. A component of this variation is due to inequalities, related to chemical composition or heat treatment, among the specimens, but another component is related to the fatigue process, an example being the initiation and growth of small cracks under test environments"*. Therefore, by testing similar specimens under the same loads, different life cycles will be obtained. A method for the analysis of fatigue properties at different stress levels using a relationship that can approximate the material response is provided in Standard ISO 12107 and it is described in the following pages.

The Standard provides for the use of two interpolation methods, the first one linear (Eq. 1.1) and the second one quadratic (Eq. 1.2), and suggests a method for choosing the better one.

$$\boldsymbol{log_{10}(N) = b_0 + b_1 \cdot log_{10}(S)} \qquad \textit{Eq. 1.1}$$

$$\boldsymbol{log_{10}(N) = b_0 + b_1 \cdot log_{10}(S) + b_2 \cdot log_{10}^2(S)} \qquad \textit{Eq. 1.2}$$

S is the stress and N is the number of cycles. b_0, b_1 and b_2 are linear regression coefficients. They can be calculate using the "regr.lin" function already implemented in Excel.

To evaluate which model is best to use, residual terms (R_{SSE}), function of the difference between the experimental point and the interpolation curve, have to be evaluated.

$$\boldsymbol{R_{SSE} = \sum_{i=1}^{n} \left(log_{10}(N_{i\_exp}) - log_{10}(N_{i\_calc}) \right)^2} \qquad \textit{Eq. 1.3}$$

Where "n" is the number of experimental points, $Log_{10}(N_{i\_exp})$ is the logarithm of the experimental observed life for a considered stress level "i" and $Log_{10}(N_{i\_calc})$ is the logarithm of the calculated fatigue life for the same considered stress. If the linear model

is used to calculate N_{calc}, the corresponding residual term is called R_{SSE1}, whereas if the quadratic model is applied, the residual term is called R_{SSE2}.

The quadratic model significantly improves the fit if:

$$F_{\alpha} < F^{*} = \frac{R_{SSE1} - R_{SSE2}}{R_{SSE1}} \qquad \textit{Eq. 1.4}$$

Where Fα is the value obtained from the F distribution table considering a number of parameters in the candidate model equal to 1, the quadratic model degrees of freedom and the choice of the confidence level α.

Once the model should be used for data representation where determined, confidence bands can be calculated. Confidence bands delimit a space of the S-N graph in which there are certain probabilities of failure/survival.

Assuming to use the linear model, confidence bands are two lines parallel to the interpolation line. The interpolation line refers to a 50% a failure probability, whereas the confidence bands refer to higher and lower failure probability. In this thesis all the confidence bands were chosen with a 10% probability of failure/survival. For a fixed cycle number, this means that 90% of samples survive at stress levels lower than that delimitated by the lower curve and at least 90% of samples survive at stress levels lower than that delimitated by the upper curve. An example of experimental fatigue data, the interpolation curve and its confidence bands is shown in Figure 2.

Confidence bands (CB) can be calculated as:

$$log_{10}(N_{CB}) = b_0 + b_1 \cdot log_{10}(S) \pm \sigma_y \cdot k_{(p,1-\alpha,\nu)} \qquad \textit{Eq. 1.5}$$

Standard deviation σ_y is given by Eq. 1.5 and $K_{(p,1-\alpha,\nu)}$ is a factor yielded by the Standard (see Table 1) as a function of the failure/survival probability P, the confidence level 1-α and the degree of freedom ν. Degree of freedom are equal to the difference between the number of experimental points "n" and the number of parameter "p". The latter is worth 2 for linear model or 3 for the quadratic.

$$\sigma_y = \sqrt{\frac{\sum_{i=1}^{n}(log_{10}(N_{i\_exp}) - log_{10}(N_{i\_calc}))^2}{n-p}} \qquad \textit{Eq. 1.6}$$

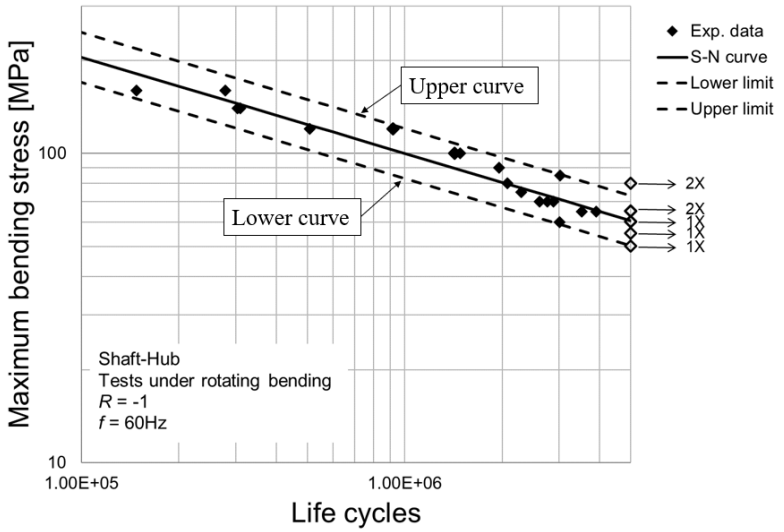

Figure 2: Example of fatigue curve with confidence bands

Table 1: coefficient $K_{(p,1-\alpha,v)}$ for the one-sided tolerance limit for a normal distribution, from ISO 12107

Number of degrees of freedom	Probability, P (%)							
	10		5		1		0,1	
	Confidence level, $100 - \alpha$ (%)							
v	90	95	90	95	90	95	90	95
2	4,258	6,158	5,310	7,655	7,340	10,55	9,651	13,86
3	3,187	4,163	3,957	5,145	5,437	7,042	7,128	9,215
4	2,742	3,407	3,400	4,202	4,666	5,741	6,112	7,501
5	2,494	3,006	3,091	3,707	4,242	5,062	5,556	6,612
6	2,333	2,755	2,894	3,399	3,972	4,641	5,201	6,061
7	2,219	2,582	2,755	3,188	3,783	4,353	4,955	5,686
8	2,133	2,454	2,649	3,031	3,641	4,143	4,772	5,414
9	2,065	2,355	2,568	2,911	3,532	3,981	4,629	5,203
10	2,012	2,275	2,503	2,815	3,444	3,852	4,515	5,036
11	1,966	2,210	2,448	2,736	3,370	3,747	4,420	4,900
12	1,928	2,155	2,403	2,670	3,310	3,659	4,341	4,787
13	1,895	2,108	2,363	2,614	3,257	3,585	4,274	4,690
14	1,866	2,068	2,329	2,566	3,212	3,520	4,215	4,607
15	1,842	2,032	2,299	2,523	3,172	3,463	4,164	4,534
16	1,820	2,001	2,272	2,486	3,136	3,415	4,118	4,471
17	1,800	1,974	2,249	2,453	3,106	3,370	4,078	4,415
18	1,781	1,949	2,228	2,423	3,078	3,331	4,041	4,364
19	1,765	1,926	2,208	2,396	3,052	3,295	4,009	4,319
20	1,750	1,905	2,190	2,371	3,028	3,262	3,979	4,276
21	1,736	1,887	2,174	2,350	3,007	3,233	3,952	4,238
22	1,724	1,869	2,159	2,329	2,987	3,206	3,927	4,204
23	1,712	1,853	2,145	2,309	2,969	3,181	3,904	4,171
24	1,702	1,838	2,132	2,292	2,952	3,158	3,882	4,143
25	1,657	1,778	2,080	2,220	2,884	3,064	3,794	4,022

To estimate the fatigue strength, i.e., the stress level below which fatigue failure does not occur, the staircase method can be used.

The method consists in fatigue tests, which differ one from each other for a step load “d”. If the i-th specimen is tested at a load S_i and it does not fail, the next specimen (i + 1) is

tested at a load equal to the previous one increased by "d" ($S_{i+1} = S_i + d$). On the contrary, if the i-th specimen fails, the next one will be tested at a decremented load ($S_{i+1} = S_i - d$). Fifteen samples have to be used for the analysis. The results of each fatigue test were recorded in a table marking the failures by a "x" and not-failure by a "o". An example with 5 MPa stress step is reported in Table 2.

Table 2: Staircase example for fatigue limit evaluation

	Specimen ID														
Stress level [MPa]	1	2	3	4	5	6	7	8	9	10	11	12	13	14	15
85		**X**													
80	**O**		**X**												
75				**X**											
70					**X**						**X**		**X**		
65						**X**				**O**		**O**		**X**	
60							**X**		**O**						**O**
55								**O**							

For the calculation of the fatigue limit, the Standard suggests to considerate the least frequent event among those that occurred (between failure or not-failure). For example, following the results in Table 2, the least frequent event is not-failure, that occurs six times, whereas failure occurs nine times.

Subsequently, four terms have to be computed:

$$\mathbf{A} = \sum_{i=1}^{l} \boldsymbol{i \cdot f_i} \qquad \textit{Eq. 1.7}$$

$$\mathbf{B} = \sum_{i=1}^{l} \boldsymbol{i^2 \cdot f_i} \qquad \textit{Eq. 1.8}$$

$$\mathbf{C} = \sum_{i=1}^{l} \boldsymbol{f_i} \qquad \textit{Eq. 1.9}$$

$$\mathbf{D} = \frac{\boldsymbol{BC - A^2}}{\boldsymbol{C^2}} \qquad \textit{Eq. 1.10}$$

In the last formulas, "i" ranges from "0" to "l", where the latter is the number subtracted one of the different stress levels observed in Table 2, for the considered behavior (failure or not failure). In this example, considering not failure, the level "0" is 55 MPa.

The "f_i " term refers to the number of recorded un-failure event at the i-th stress level (if failure is the least frequent event, f_i refers to fails). Values of "i" and "f_i" related to the example in Table 2 are reported in Table 3.

Table 3: Example of staircase coefficient determination, based on data in table 2

Case O (not failure)				
Stress [MPa]	i	fi	i*fi	i^2*fi
85	6	0	0	0
80	5	1	5	25
75	4	0	0	0
70	3	0	0	0
65	2	2	4	8
60	1	2	2	2
55	0	1	0	0

Then, the mean value of the fatigue limit (μ_y) can be calculated as in Eq. 1.11

$$\mu_y = \boldsymbol{S_0} + \boldsymbol{d} \cdot \left(\frac{\boldsymbol{A}}{\boldsymbol{C}} \pm \frac{\mathbf{1}}{\mathbf{2}}\right) \qquad \textit{Eq. 1.11}$$

If un-failure was set as least frequent event, sign "+" have to be used in Eq. 1.11, on the contrary, sign "-" have to be used.

The standard deviation σ_y related to the fatigue limits is:

$$\boldsymbol{\sigma_y} = \mathbf{1.62}\,\boldsymbol{d} \cdot (\boldsymbol{D} + \mathbf{0.029}) \qquad \textit{Eq. 1.12}$$

Where d is the stress step that in this example it is equal to 5 MPa.

1.3 Materials and methods

1.3.1 Equipment

The study of fretting on interference fitted shaft-hub joints often involves large specimens. Due to inertial phenomena, large geometries do not usually allow for tests at high frequencies. Moreover, to test connections very often only alternate bending test are reported in the literature and few results on rotating bending tests are available (Figure 3). Another important issue, concerns the possibility of observing fretting corroded surfaces. In fact, in interference fitted couplings, the high geometric interference can cause damage to the surfaces during the coupling and the decoupling phases, making it difficult to fully observe the phenomenon.

In 2013, a specimen for rotating bending fatigue tests was introduced by Croccolo et. Al. [1.21] (Figure 4). Although this specimen exhibited compact dimensions, it could not overcome the issue of the surfaces damage during the coupling and the decoupling phases. Therefore, in this study a new equipment for fretting fatigue investigation in interference fitted shaft-hub joints was utilized for the first time.

The sample has compact dimensions and it makes it possible to run rotating bending fatigue tests (11 mm of coupling diameter between the shaft and the hub and 16 mm of coupling diameter between the sample and the Moore machine). It consists of four parts, as showed in Figure 5. The main characteristic is that initially there is clearance between the shaft and the hub. This allows to couple and decouple the parts without surface damaging. The coupling surfaces between the hub and the carrier are slightly conical.

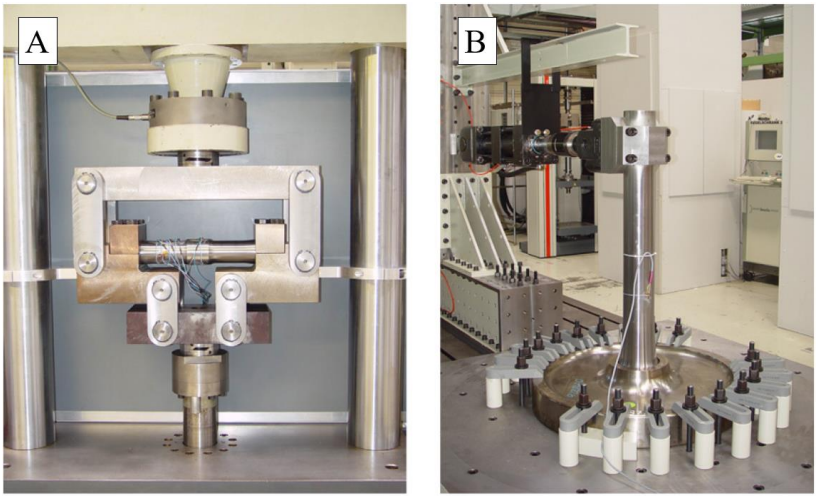

Figure 3: Example of alternate bending fatigue test on specimens with a diameter of 50 mm in (A) and 140 mm in (B) [1.16]

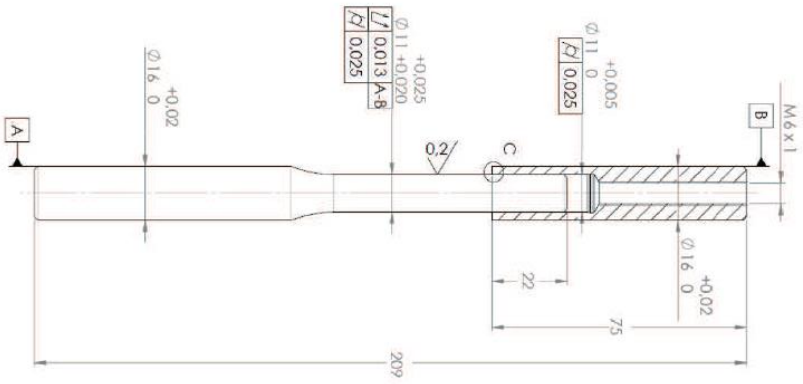

Figure 4: Shaft-hub specimen for rotating bending fatigue tests [1.21]

First, the shaft is inserting into the hub. By gradually inserting the hub into the carrier through the nut, the hub is compressed until the clearance drops down to zero. A further nut tightening gradually generates a coupling pressure between the shaft and the hub, like in an interference coupling. At the end of the test, after nut removal, it is possible to extract the hub from the carrier. The pressure between the shaft and the hub drops down to zero and it is possible to manually disassemble the parts to observe the shaft surface, without damaging it. The initial clearance between the shaft and the hub is recovered by gradually inserting the hub into the carrier. The pressure at the interface between the hub and the carrier (p_1) increases linearly with the hub axial displacement (s) (Figure 6). When the hub radial deformation becomes equal to the initial clearance, pressure between the shaft and the hub (p_2) begins to build up. The pressure (p_1) between the hub and the carrier grows with greater slope. Pressure p_2 is directly proportional to the inserting force given by the nut, which, in turn, is directly proportional to the applied tightening torque.

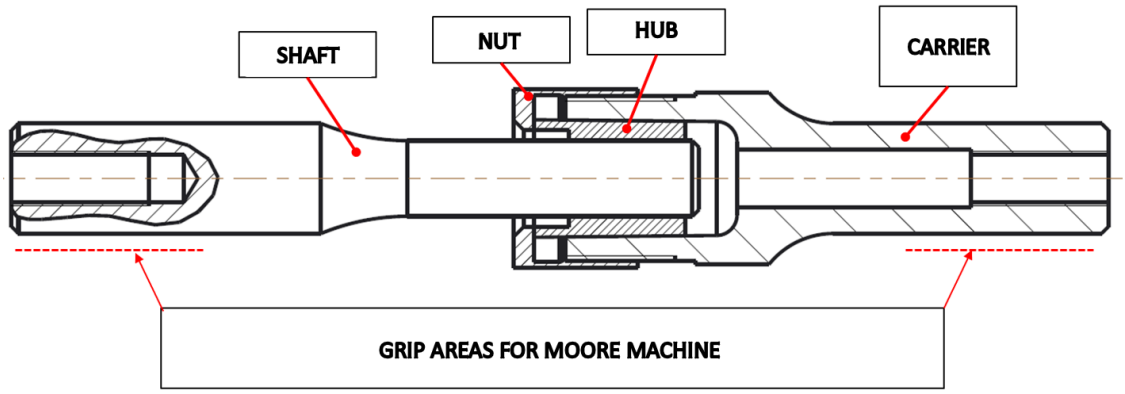

Figure 5: Details of the new specimen for fretting fatigue tests in interference fitted shaft-hub joints.

Therefore, the shaft-hub coupling pressure (p_2) is not experimentally measured, but is calculated based on the applied tightening torque. Consequently, once the desired

coupling pressure and the initial clearance between the shaft and the hub were known, the tightening torque to be applied to the nut was calculated through a calculation sheet. To minimize calculation errors, it is essential to precisely know the friction coefficients of all the surfaces. For this purpose, the threads of both the carrier and the nut, the contact area between the nut and the hub and the conical surface of the carrier were lubricated by a ceramic lubricating grease (Interflon HT 1200). This lubricating grease was utilized in various experiments in the past [1.22 - 1.23] and it warrants constant friction coefficients even after numerous re-tightening/re-couplings. In fact, in order to reduce the costs of the experiment, only the shaft and the hub were replaced after a fatigue test, whereas the nut and the carrier could be re-utilized for several tests. To ensure durability, nut and carrier were made in hardened 39NiCrMo3.

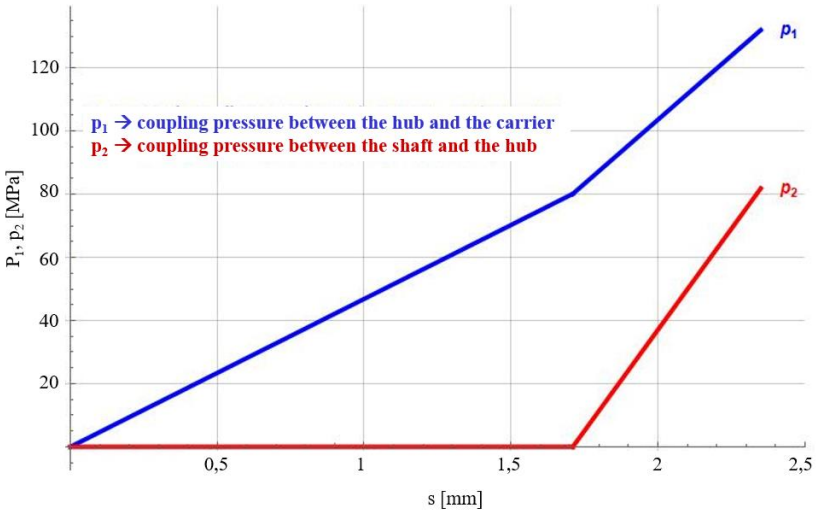

Figure 6: Coupling pressure between the carrier and the hub (p1) and between the shaft and the hub (p2) as a function of the axial displacement (s)

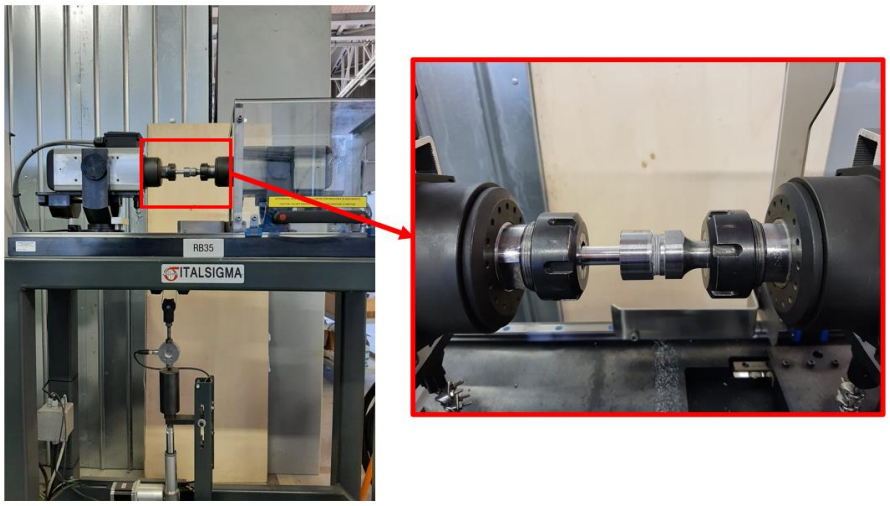

Figure 7: Assembles specimen mounted on the Moore machine

The assembled specimens were tested under a four-point rotating bending machine (RB 35, by Italsigma, Forlì, Italy) (Figure 7). This Moore machine can apply a bending moment up to 35 Nm. Considering a sample gage diameter of 11 mm, it allows to achieve a maximum stress of 270 MPa.

1.3.2 Samples

Some geometry details of the designed shafts and hubs are sketched in Figure 8. As it can be observed in the drawings, the coupling diameters exhibits a very low surface roughness and strict tolerances. As highlighted above, to generate the coupling pressure, the hub external diameter is slightly conical (about 0.6°). The manufacturing process of the samples required an additional check to make sure that the strict tolerance and the fine surface roughness had accomplished. Therefore, both dimensional and roughness checks were performed. All the gage diameters were measured in a controlled environment by a laser scan with 0.1 µm sensibility. The surface roughness was also checked running 6 measurements for each sample in all the coupling surfaces.

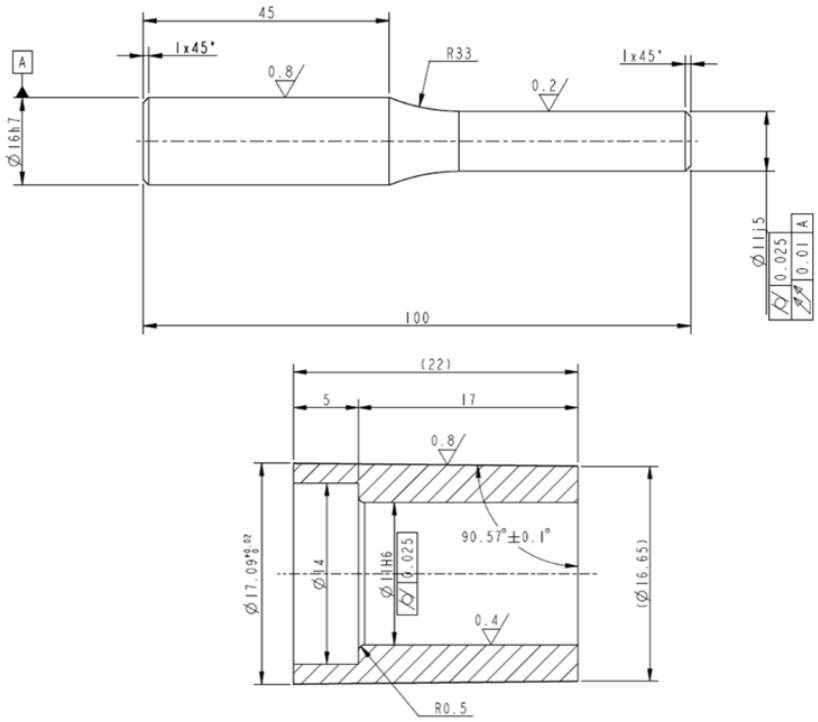

Figure 8: Shaft and hub geometries

1.3.3 Experimental plan

Two materials were considered in this study. A first investigation involved both shaft and hub made of normalized C40 steel. This material was chosen to compare the results of the new

designed specimen with those in [1.21]: in fact, in that research the same alloy had been analyzed, but involving samples with a different geometry as shown in Figure 4. Despite both the fatigue curve and the fatigue limits were assessed in [1.21], due to testing machine capacity limitations, only the fatigue limit was investigated in this study. A total of thirty specimens were manufactured and then coupled under 80 MPa pressure. A first group of fifteen samples was utilized to determine the fatigue limit. Fatigue interrupted tests were carried out with the other samples with the aim of observing the fretting corrosion before the failure and to investigate how fretting fatigue cracks initiate and propagate.

The second material to be considered was aluminum 7075 in the T6 heat treatment condition. This material is widely used for fabricating mechanical parts. Furthermore, its lower fatigue strength, if compared with those of a steel, makes it possible to investigate both the fatigue curve and the fatigue limit without overloading the testing machine. Sixty specimens were manufactured and then divided into two groups. In order to investigate the effect of different coupling pressure on the fretting damage, a first group of thirty samples was coupled under 40 MPa, whereas the others thirty were coupled under 80 MPa.

All the tests were performed at 60 Hz. The runout was set at $2 \cdot 10^6$ cycles for C40 specimens (as in [1.21]) and at $5 \cdot 10^6$ cycles for the aluminum ones, as suggest in Standards for steel (Eurocode 3) and aluminum alloy (Eurocode 9).

Table 4: Fretting fatigue experimental plan

	Coupling pressure	Test Frequency	Run-out [cycles]	Fatigue curve	Fatigue limit	Interrupted fatigue tests
C40 Normalized Steel	80 MPa	60 Hz	$2 \cdot 10^6$	-	V	V
Aluminum 7075 T6	40 MPa	60 Hz	$5 \cdot 10^6$	V	V	V
Aluminum 7075 T6	80 MPa	60 Hz	$5 \cdot 10^6$	V	V	V

1.3.4 Experimental procedure

Before the tests, specimens were accurately checked. All the samples were marked with a three-character code: the first character is a letter (s = shaft, h = hub), whereas the other two are a progressive number. Dimension and roughness measurements were taken respectively by a 3D laser scan and a portable roughness tester. As it was reported in the section 1.3.1 about the specimen configuration, an initial clearance between the shaft and the hub is necessary to avoid surface damaging during the coupling and the decoupling phases. Nevertheless, a limited clearance is required by the equipment: in fact, in case of

high clearance, to reach the desired coupling pressure high radial deformation, which can lead to hub yielding, have to be apply. Therefore, after dimensional checks, shafts and hubs were sorted to minimize the coupling clearance.

When coupling clearance is limited (about 0.01 mm), accurate cleaning is required to perform coupling by hands and without damaging the surfaces. For this purpose, surfaces were properly degreased and then coupled. As a first step, the shaft was insert in to the hub. After that, the ceramic grease (Interflon HT 1200) was utilized to lubricate the threads of the carrier, the nut and the external hub diameter (Figure 9). Subsequently, the assembled sample was tightened by an electronic torque wrench until the coupling pressure was reached.

To check proper assembly, the specimens were mounted on the Moore machine and before starting the fatigue tests the eccentricity was checked (Figure 10). Then, the samples were fatigued until failure or at the run-out cycle number. The fracture surfaces of failed samples were observed by a stereoscopic microscope (Zeiss Stemi 305 stereoscope) a by a scanning electron microscope (SEM-FEG Tescan Mira 3). When failure did not occur, specimens were disassembled: if after nut removal the shaft and the hub keep clamped inside the carrier, in order to push out the specimens, a screw could be inserted through the threaded hole on the right side of the carrier (see Figure 5). Traces of fretting corrosion on the cylindrical surface of un-failed shafts were observed by the aforementioned stereoscope. The hubs were also examined. To clearly see the internal surface, they were longitudinally cut.

Fatigue data were processed complying with ISO 12107. Based on the fatigue properties, some sets of specimens were fatigued at different stress level stopping the tests before the estimated failure. Non-destructive testes (NDT) were carried out on the shafts involved in this part of the experiment. Particularly, die penetrants and Eddy currents NDT were performed on both the considered alloy. Only for steel shafts, NDT with magnetic particles were also performed. The outcomes of NDT provided information about the presence and the location of fatigue cracks due to fretting-fatigue that had not led to complete failure yet. Shafts, where some defects were found, were longitudinally cut. The obtained sections were polished and chemically etched in order to analyze fretting fatigue cracks. A detailed description of the procedure is reported in Section 1.4.3.

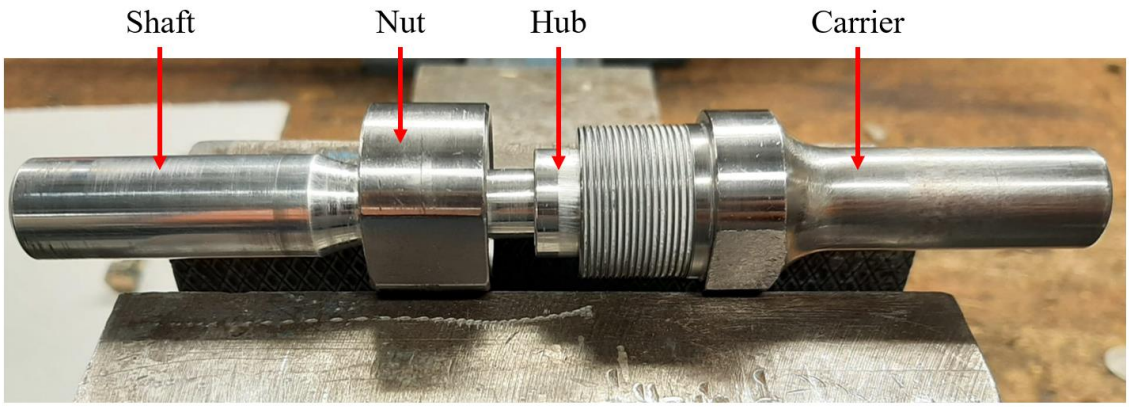

Figure 9: Specimen after application of grease and before final tightening

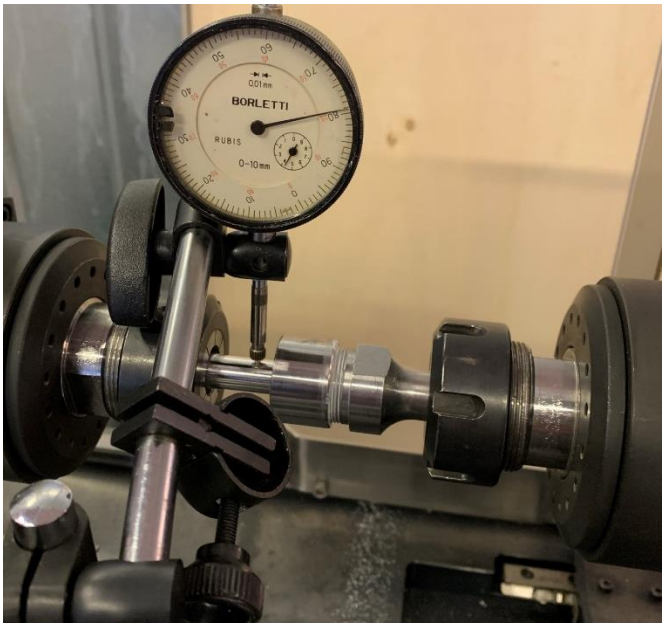

Figure 10: Eccentricity checks before starting fatigue tests

1.4 Results and discussions

1.4.1 Fatigue tests

One of the aims of the testing plan was determining the fatigue performance of the shaft hub specimens. The application of staircase method (as described in Section 1.2) leads to the estimation of an endurance limit. Experimental data are collected in Table 5, Table 6 and Table 7 respectively for steel samples, aluminum specimens coupled under 40 MPa and aluminum samples coupled under 80 MPa. The calculated fatigue strengths with their standard deviations are listed in Table 8.

The fatigue curves for aluminum samples are plotted in Figure 11, according to ISO 12107 with lower and upper bounds (for 10% failure probability and 90% confidence level).

Table 5: Staircase sequence at $2 \cdot 10^6$ cycles for C40 normalized samples coupled under 80 MPa

	Specimens														
Stress [MPa]	S18 H25	S27 H22	S13 H10	S19 H27	S11 H19	S05 H14	S07 H6	S26 H23	S15 H4	S21 H28	S22 H24	S17 H30	S06 H17	S10 H15	S29 H20
260														**X**	
250							**X**				**X**		**O**		**O**
240				**X**		**O**		**X**		**O**		**O**			
230	**X**		**O**		**O**				**O**						
220		**O**													

Table 6: Staircase sequence at $5 \cdot 10^6$ cycles for 7075 T6 samples coupled under 40 MPa

	Specimens														
Stress [MPa]	S20 H44	S02 H22	S05 H18	S13 H12	S14 H11	S19 H49	S32 H32	S27 H17	S28 H43	S16 H28	S45 H41	S22 H46	S53 H13	S58 H24	S33 H36
65															
60				**X**		**X**		**X**		**X**				**X**	
55	**X**		**O**		**O**		**O**		**O**		**X**		**O**		**O**
50		**O**										**O**			
45															

Table 7: Staircase sequence at $5 \cdot 10^6$ cycles for 7075 T6 samples coupled under 80 MPa

	Specimens														
Stress [MPa]	S38 H6	S34 H10	S17 H47	S31 H8	S49 H21	S29 H40	S48 H2	S10 H27	S47 H58	S51 H15	S25 H30	S15 H45	S37 H54	S12 H14	S36 H33
85		**X**													
80	**O**		**X**												
75				**X**											
70					**X**						**X**		**X**		
65						**X**				**O**		**O**		**X**	
60							**X**		**O**						**O**
55								**O**							

Table 8: Fatigue limits for the considered materials and coupling pressure

	Fatigue Limit [MPa]	**St. Dev. [MPa]**
Normalized Steel C40, p = 80 MPa	**240**	**15.3**
Aluminum 7075 T6, p = 40 MPa	**56**	**1.9**
Aluminum 7075 T6, p = 80 MPa	**67**	**20.3**

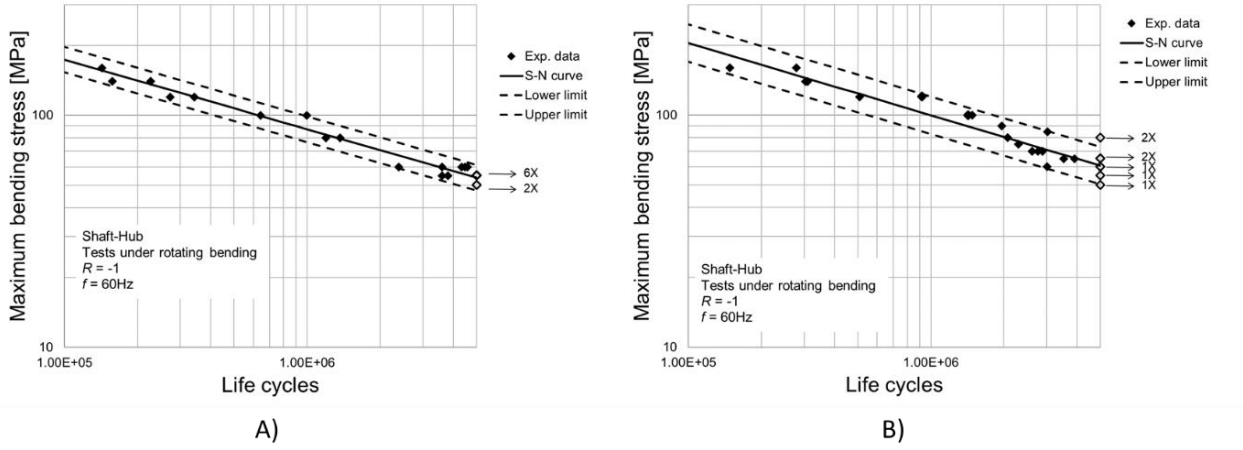

Figure 11: Fatigue curves for 7075 T6 samples. A) Shaft-hub coupled under 40 MPa; B) Shaft-hub coupled under 80 MPa

The calculated fatigue strength for steel samples (50% failure probability at $2 \cdot 10^6$ cycles) was equal to 240 MPa. The obtained value is well aligned with that observed in [1.21] (210 MPa). The small difference can be justified by the different coupling pressure: in fact, in [1.21] a mean coupling pressure of 65 MPa was used, whereas in this study it was set to 80 MPa. For aluminum specimens, a slightly better performance was also observed in coupling under 80 MPa than those under 40 MPa. Considering that higher coupling pressures generally correspond to higher shaft stresses, an opposite behavior to that observed would have been expected. However, as it will be highlighted later in the surface analysis, it appears that low coupling pressures lead to greater sliding between the shaft and hub surfaces, thus increasing the fretting detrimental effect on the fatigue life.

Plain specimens with a cylindrical geometry at the gage and a uniform diameter of 11 mm made of C40 normalized steel were tested under rotating bending in [1.21]. An endurance limit of 364 MPa at $2 \cdot 10^6$ cycles was experimentally observed. It is possible

to compare the latter result with the fatigue strength obtained in this study (240 MPa), thus calculating the fatigue stress concentration factor k_f:

$$k_f = \frac{S_{n\_plain}}{S_{n\_sh}} = \frac{364}{240} = 1.52 \qquad \textit{Eq. 1.13}$$

The fatigue stress concentration factor can also be expressed as:

$$k_f = 1 + q \cdot (k_t - 1) \qquad \textit{Eq. 1.14}$$

Where q is the material notch sensitivity and k_t is stress concentration factor. The notch sensitivity q can vary between 0 and 1. The stress concentration factor k_t can be extrapolated from [1.21]: for a coupling pressure of 80 MPa it is about 1.4. Assuming, in the worst situation, a notch sensitivity equal to 1, the fatigue stress concentration factor k_f should be equal to 1.4. However, the experimentally determined k_f is greater than expected. Therefore, this outcome suggests that an additional phenomenon, such as fretting fatigue, concurs to crack initiation.

Regarding the results of the tests on aluminum specimens, a slightly better performance is observed for the higher coupling pressure. It is then possible to make a comparison between the results of the tests involving steel and aluminum samples. Comparing the observed fatigue limits under 80 MPa pressure with the ultimate tensile strength (820 MPa for normalized C40 steel and 510 MPa for T6 treated aluminum 7075), a ratio of 0.31 was obtained for steel samples, while only 0.13 for aluminum. These results indicate a much worse fretting fatigue behavior of the aluminum compared to steel, with reference to the static mechanical properties.

A second aim of the study was to assess the good functionality of the new specimens. The obtained results in the case of C40 steel shafts and hubs are comparable to those obtained in [1.21], which is a first confirmation the new procedure and the newly designed sample can be used for the study of fretting fatigue.

1.4.2 Surface analyses

After fatigue tests, fracture surfaces were analyzed by a stereoscopic microscope. For both the examined materials, the coupling pressure and alternate fatigue stresses, the same fracture behavior was observed. Multiple crack initiation points were observed on the surface. The overloaded fracture zones have also similar dimensions. An example is illustrated on Figure 12.

Shaft cylindrical surfaces were also checked in both failed and un-failed samples. In Figure 13 a failed steel shaft is shown. A first outcome is that the coupled side of the cylindrical surface does not appear scratched after the coupling and the decoupling with the hub. This result demonstrates the functionality of the new designed specimen to the study of the fretting corrosion in interference-fitted shaft-hub connection.

Near the fracture, it is possible to see the sliding area affected by fretting corrosion. Particularly, two sliding areas can be observed: a first one is characterized by a brownish color due to the formation of oxides in correspondence with the fracture; a second one is characterized by a brighter color a little away from the fracture area, where the sliding had a smaller amplitude.

After fatigue tests, in un-failed specimens the slip area was entirely observed by the stereoscope. In case of steel shafts, a total sliding thickness of 500-600 µm was found. Fractures emerged form the most marked and oxidized wear zone, which extends for about 150-200 µm (Figure 14). The presence of oxides confirms that fretting damage is not only a mechanical phenomenon but it also depends on chemical processes.

In aluminum shafts coupled under 80 MPa pressure a 100-150 µm sliding zone was noticed (Figure 16). Even in this case, no appreciable differences were found varying the alternate fatigue stress. An appreciable increase in sliding width was seen in some shaft coupled under 40 MPa pressure (Figure 15). In the latter case, the greater fretting damage can worsen the fatigue performance. This outcome finds correspondence with fatigue results seen in Figure 11.

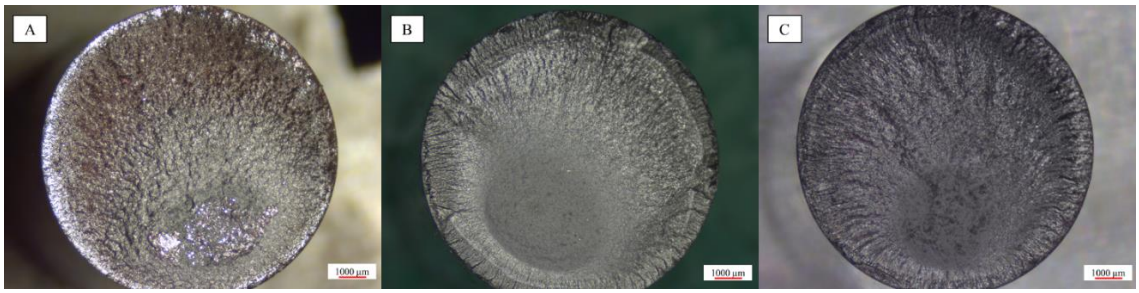

Figure 12: Shaft fracture surfaces: A) steel shaft coupled under 80 MPa pressure, fatigue stress amplitude 270 MPa. B) aluminum shaft coupled under 40 MPa pressure, fatigue stress amplitude 180 MPa. C) aluminum shaft coupled under 80 MPa pressure, fatigue stress amplitude 140 MPa

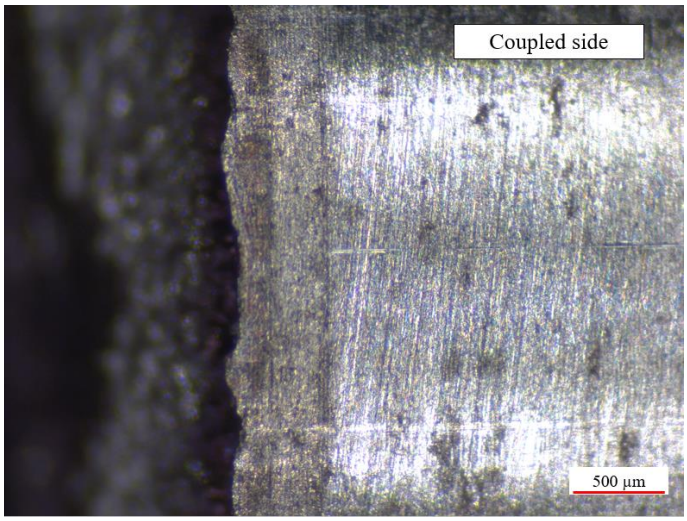

Figure 13: Steel sample cylindrical surface after failure

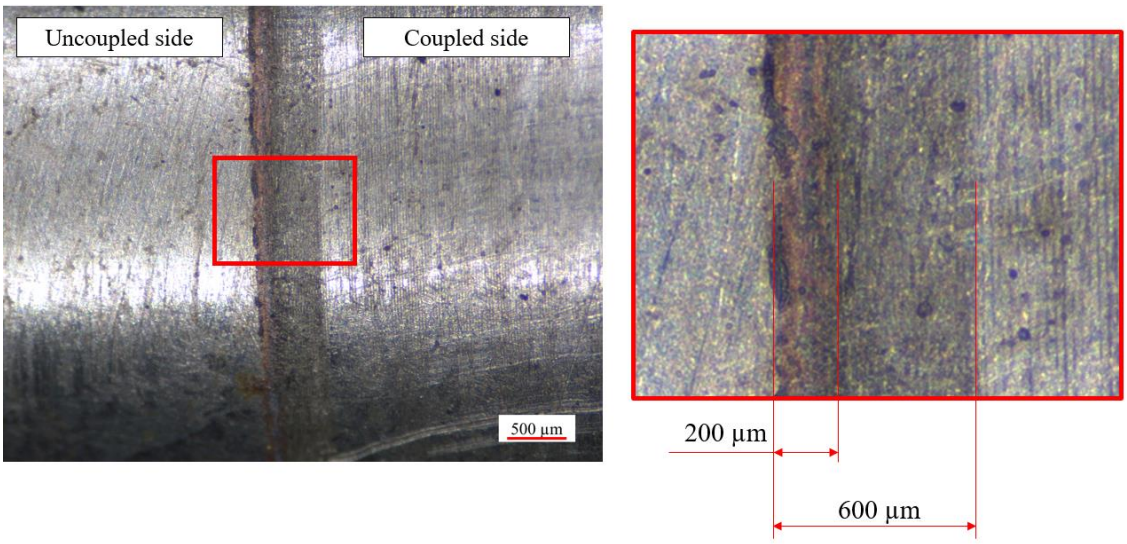

Figure 14: Damaged surfaces of un-failed steel sample

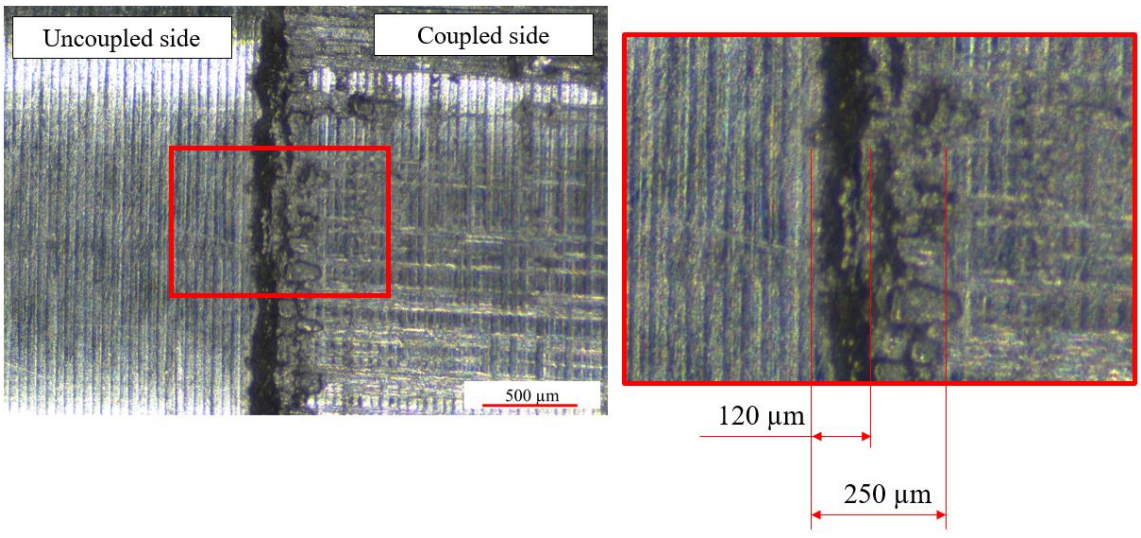

Figure 15: Damaged surfaces of un-failed aluminum sample coupled under 40 MPa pressure

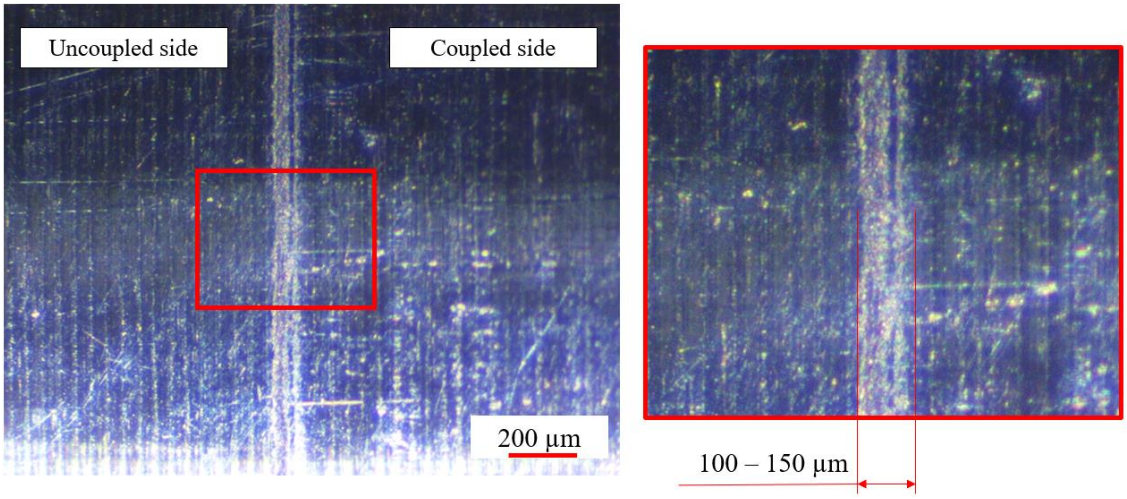

Figure 16: Damaged surfaces of un-failed aluminum sample coupled under 80 MPa pressure

Similar conclusions can be drawn by the stereoscopic images of hub longitudinal section. The area affected by fretting starts from the end of the hub internal radius. Two sliding areas comparable with those in the shafts was observed in steel hubs (Figure 17). Even in aluminum samples, the sliding zone observed in the hubs is similar to that found on the shafts and it exhibits a greater width in case of coupling under 40 MPa pressure (Figure 18).

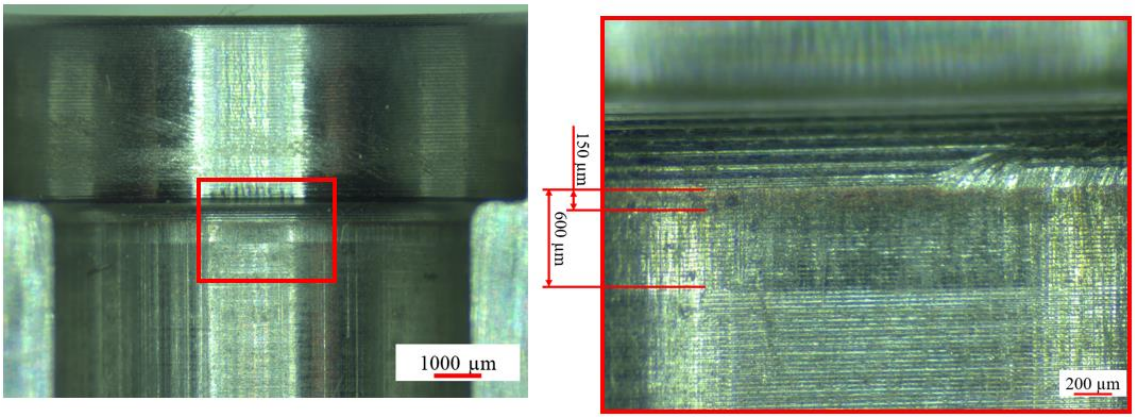

Figure 17: Steel hub longitudinal section

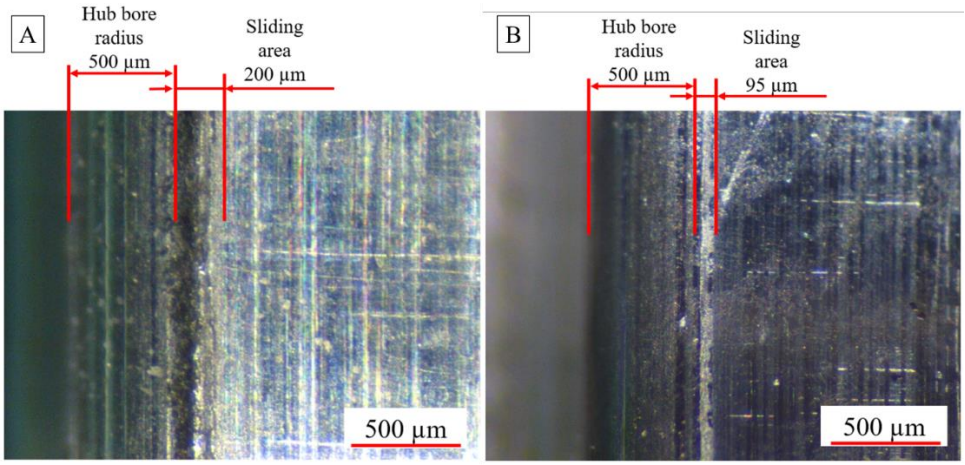

Figure 18: Sliding area in aluminum hubs. (A) Coupled under 40 MPa pressure, (B) coupled under 80 MPa pressure

1.4.3 Fretting fatigue fracture initiating

To investigate the fretting fatigue fracture initiating mechanisms, fatigue interrupted tests were performed. The aim was to experimentally observe the fretting fatigue fractures in order to obtain useful data to be used in numerical models predicting the phenomenon.

The procedure consisted in longitudinally cutting the shafts and then observing the fatigue cracks on a plane being parallel to the specimen axis. For this investigation, shafts that have achieved runout in fatigue tests and shafts from interrupted fatigue tests were used. In the latter case, specimens were subject to an alternate fatigue load higher than the fatigue limit, but the tests were stopped before the expected failure. The section, along which the specimens were cut, was determined by non-destructive tests.

Fretting fatigue cracks initiate from component surfaces. Among the non-destructive test technologies, dye penetrants, Eddy currents and magnetic particles are particularly useful to identify such defects. Among these methodologies, dye penetrants are those that allow the detection of the smallest cracks. However, Eddy current inspection is faster, as it requires less careful specimen preparation. For this reason, it was considered as a second investigation method with the aim of verifying if a method with lower sensitivity was still sufficient to detect fretting fatigue cracks.

Magnetic particle tests were only used in case of steel shafts, as the samples have to be ferromagnetic.

Experience and careful procedure are required in dye penetrant inspection. First, specimens have to be cleaned: an ultrasonic washing machine and a degreasing solvent (Velvet-Solnet) were utilized. After that, a second cleaning with a degreasing solvent spray was performed. Specimens were air dried for an hour. Then, spray fluorescent dye

penetrants were applied (QPL-USAF, which exhibits yellow/green color under ultraviolet light). Two layer of dye penetrant were deposited: the second layer was applied after 15 minutes from the first one. A 30 minutes waiting time were observed to allow the liquid to enter the cracks by capillarity (Figure 19a).

The next step is dye penetrant washing. An emulsifier that forms a foam around the samples and absorbs excess of dye penetrant was sprayed on specimen surfaces. Washing is the most important and delicate phase. The emulsifier must remain on specimen surfaces for 60 seconds: in case of too long time, too dye penetrant could be removed, not allowing to see any cracks. On the other hand, if the emulsifier is early removed, too dye penetrant could remain on the surfaces. In this case some shapes, such as crest roughness, could be wrongly highlighted as cracks. The emulsifying foam was gently washed off by water (Figure 19b).

Subsequently, the specimens were dried by blotting paper and a dye penetrant detector was sprayed. The detector absorbs the dye penetrant trapped inside the cracks. A white detector mixed with a fast-evaporating solvent (Rotrivel U) was utilized (Figure 19c).

To verify the correctness of all the operations, the same procedure is also applied to a gauge plate. The plate is none other than a metal plate, where cracks were deliberately made. The procedure is verified if the gauge plate shows the cracks as reported in its check sheet (Figure 20).

After that, the specimens were observed under ultraviolet light (Figure 21). Areas, where fractures were found, were marked to locate the section, along which to cut the samples.

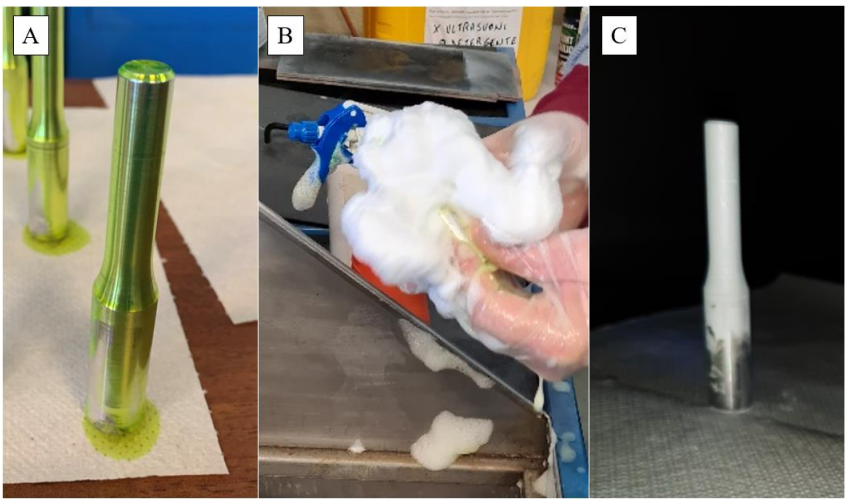

Figure 19: Dye penetrant non-destructive test. (A) Shaft after dye penetrant application, (B) dye penetrant removal by emulsifier, (C) sample after developer application

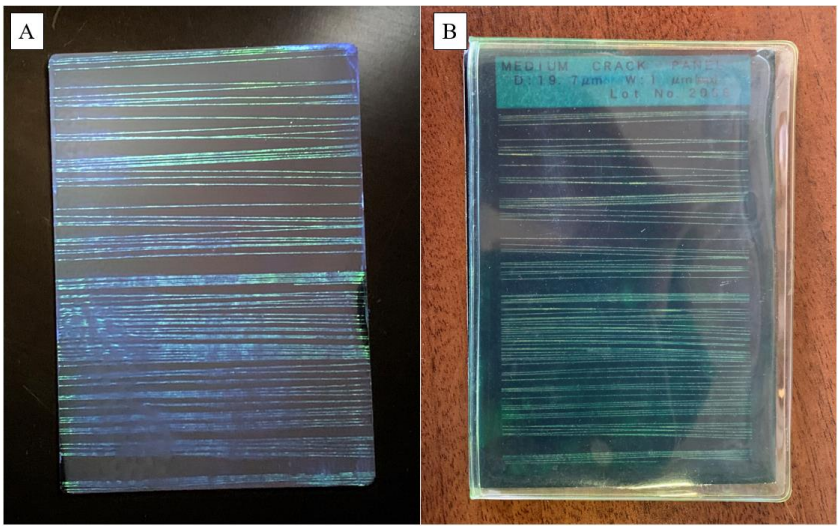

Figure 20: Rating plate (A) used to validate the procedure used with its theoretical feedback (B)

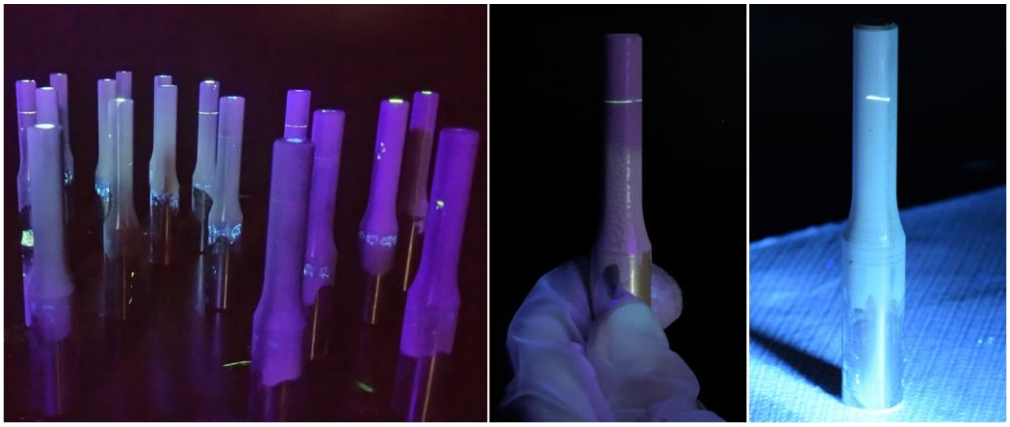

Figure 21: Some examples of dye penetrant NDT results

Before cutting the samples, Eddy current non-destructive tests were performed. For the purpose, a portable tester (Zetec Miz-22) was utilized. This test method is very simple as it does not require specimen careful preparation. However, an accurate calibration is required. Current frequency and phase must be suitably calibrated. Parameter choice depends on the test machine type, the used probe and the sample material.

For the test, a single coil probe was utilized. The power frequency was set at 1200 kHz for steel samples and 200 kHz for aluminum ones. Figure 22 shows some examples of obtained diagrams.

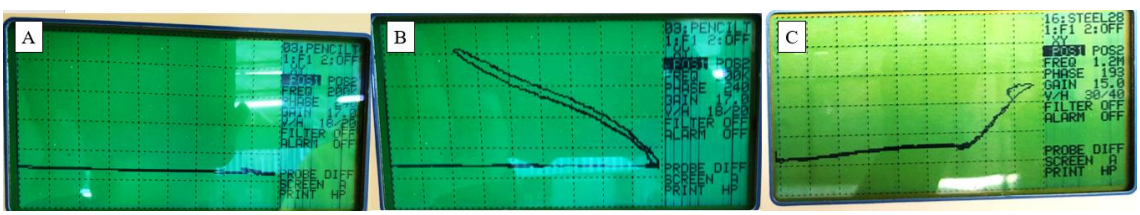

Figure 22: Eddy current diagrams. (A) Response in shaft without defects. Response over fractures in aluminum (B) and steel (C) samples

Magnetic particles test was carried out on steel shafts only. First, specimens were longitudinally magnetized by an electromagnetic yoke; secondly, magnetic particles were applied. Initially, dry magnetic particles consisting of red synthetic oxide (3029M) were used. The particles were sprayed onto the specimen surfaces with low pressure air. However, the sensitivity of the used particles was not sufficient to let them deposit in the cracks (probably due to the large particle size). Therefore, this technique did not allow to observe any defects. Better results were achieved by using wet magnetic particles (black magnetic powder BW2 dispersed in "kerosenoil" oil). The smaller particle size and the use of oil, which improves particle mobility on the specimens, allowed to highlight some fractures. Nevertheless, the sensitivity was barely sufficient. An example is visible in Figure 23: the fracture area is highlighted by a thin dark line.

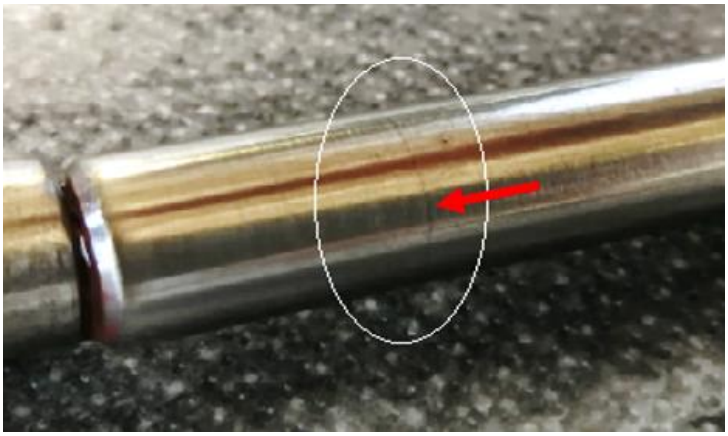

Figure 23: Wet magnetic particle non-destructive test. The fracture is barely highlighted by the thin dark line

After that fracture paths were highlighted by non-destructive tests, samples were longitudinally cut, in order to observe the fracture propagation within the specimens. Cutting was performed by a miter saw equipped with emery discs. After that, to allow better handling, for each sample a longitudinal portion of shaft was incorporated in a resin (Figure 24). The surface of the obtained cylindrical sample was sanded and polished in a lapping machine. For the purpose, sandpaper (grit from P80 to P2500) followed by cloth disks wetted by 0.05 µm alumina powder water mixed were used. After the polishing, steel sample were analyzed by a optical microscope, whereas the aluminum ones were chemical etched and then observed. The chemical etched was performed by Keller reagent applied at room temperature for 30 seconds.

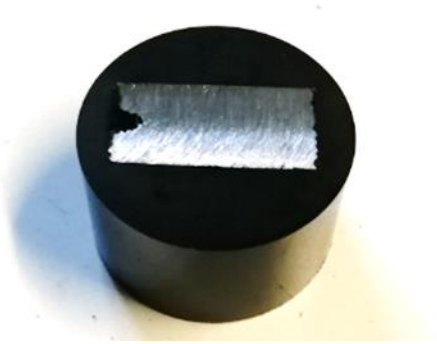

Figure 24: Portion of shaft incorporated in a resin

Some optical microscope images are collected from Figure 25 to Figure 28.

Depending on specimen damage, fractures could be observed on one side or on both sides of the observed section. For both steel and aluminum samples, due to the multiaxial stress state, the fretting cracks do not grow in the radial direction. The crack orientation is slanted by an angle between 0° and 45° due to the shear stress on the sample surface. The crack orientation is higher near the surface than inside the sample. Advancing towards the inside of the specimen, the contribution of shear stresses tends to decrease and the fractures become more radial. Furthermore, alongside the main crack there are minor secondary cracks. These outcomes are aligned with those in the literature [1.1]. In the steel specimen, the surface area, where fretting occurs, appears jagged and damaged. The extension of this area is aligned with that observed by stereoscopic analyses as shown in Figure 14 (about 600 µm). On the other hand, surface damage in not clearly distinguishable in aluminum samples.

The fracture slope angle was measured based on the captured pictures. An average value 21° was obtained in aluminum specimens coupled under 40 MPa pressure, whereas a mean value equal to 18° was found in samples coupled under 80 MPa pressure.

The greater angle observed in specimens coupled under lower pressure strengthens the hypothesis that greater surface shear stresses are present.

A last outcome is that all the cracks are oriented towards the inner side of the joint.

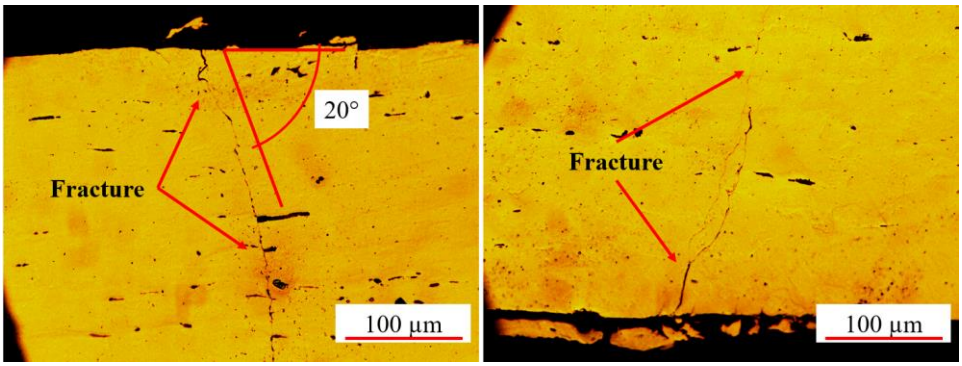

Figure 25: Fretting fatigue cracks in a steel shaft

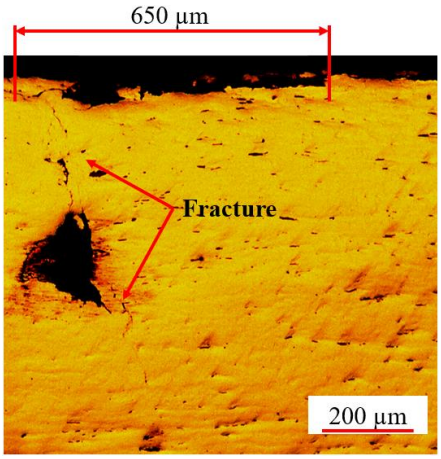

Figure 26: Fretting fatigue crack and extension of eroded surface on a steel shaft

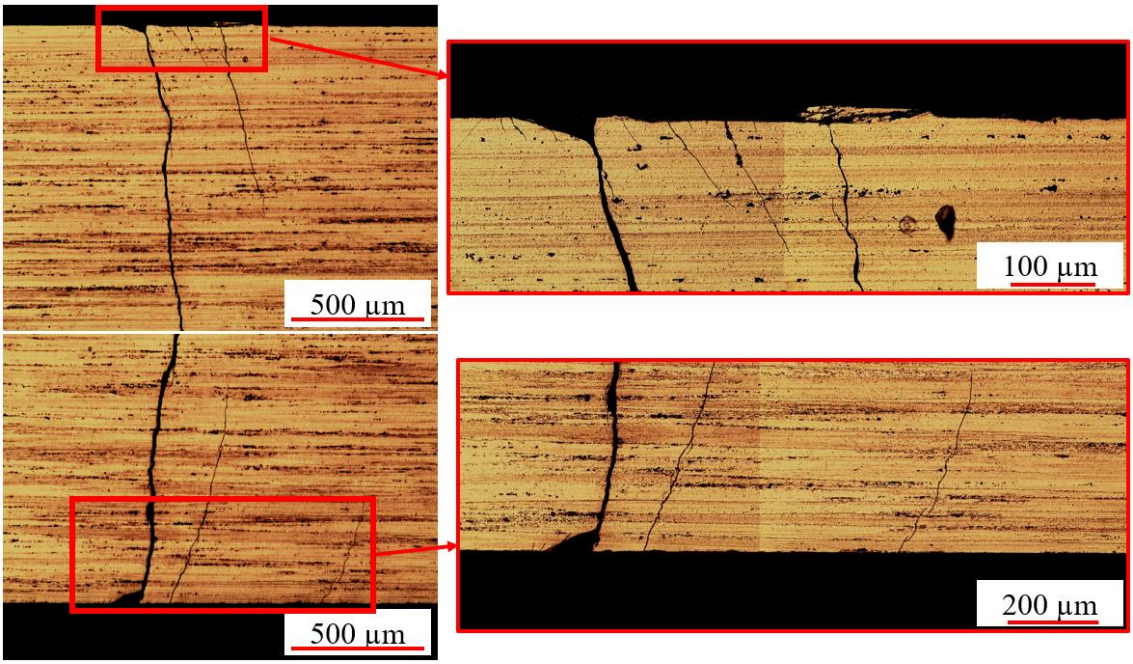

Figure 27: Fretting fatigue cracks in an aluminum sample coupled under 40 MPa pressure

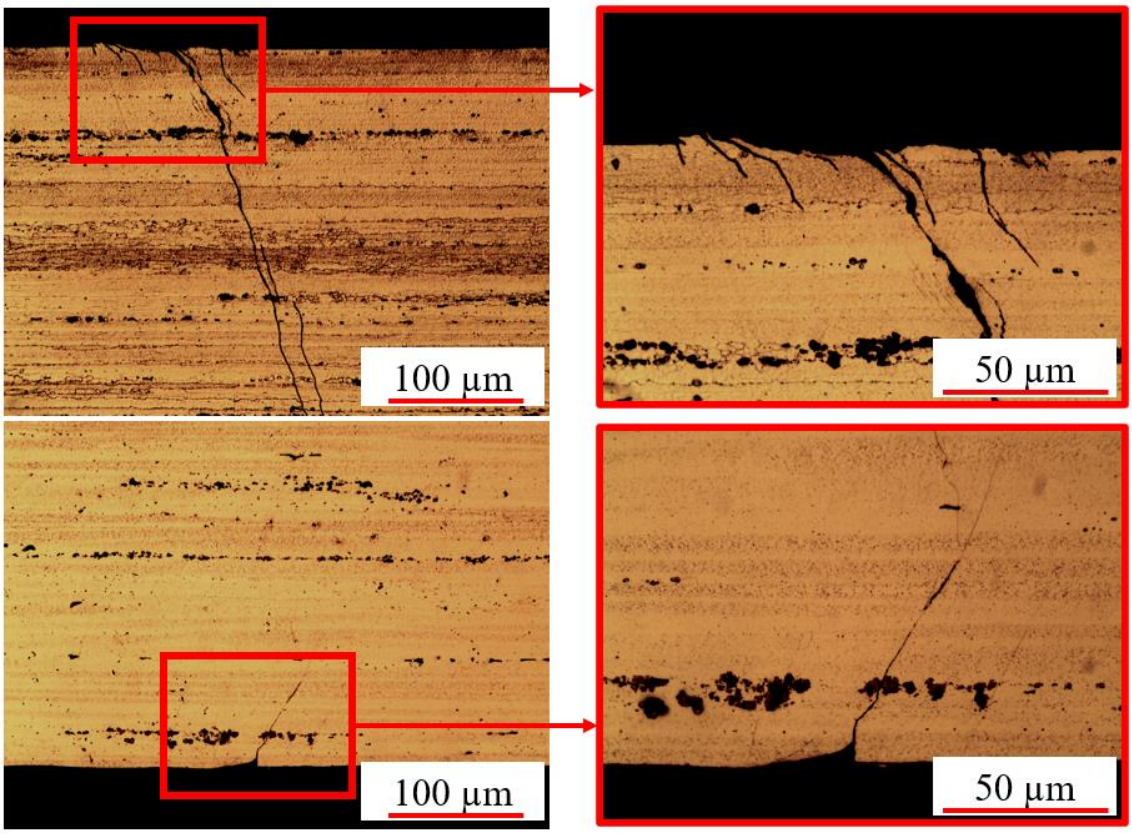

Figure 28: Fretting fatigue cracks in an aluminum sample coupled under 80 MPa pressure

1.5 Conclusions

The fretting fatigue damage, which can occur in interference-fitted shaft-hub joints, was analyzed by means of a new investigation method. The aims of this study were to verify the proper functionality of the used method, to obtain original experimental fatigue data and to observe fretting crack properties.

The investigation method concerns rotating bending fatigue tests on interference-fitted shaft-hub specimens made of C40 normalized steel and of aluminum 7075, the latter joined under different coupling pressures. The newly designed specimen makes it possible to assemble and disassemble the hubs and the shafts without damaging the surfaces. Test results on steel samples are comparable with those in the literature achieved by testing traditional shaft-hub joints. Therefore, the developed not conventional specimen proved to be particularly suitable for fretting fatigue study.

In case of normalized C40 steel specimens, a fatigue strength of 240 MPa at $2 \cdot 10^6$ cycles was obtained. The observed resistance is much lower than that calculated, dividing the fatigue strength for smooth specimens by the fatigue stress concentration factor k_f. This outcome testifies that fretting alters fatigue performance, making it worse.

In aluminum shaft-hub samples, a better fatigue performance was observed in specimens coupled under higher pressure. A fatigue limit of 67 MPa was determined in agreement with ISO 12107 for couplings under 80 MPa pressure, whereas 56 MPa were achieved in couplings under 40 MPa pressure.

Fretting corrosion was observed on shaft and hub surfaces. Oxidations were found near the fracture initiation zone of steel samples. In aluminum coupling, the highest coupling pressure corresponds to the lowest slip amplitude. Therefore, increasing the coupling pressure appears to drop down the relative sliding between shaft and hub, limiting fretting damage.

The fracture propagation inside the shafts was also observed. Fretting fatigue cracks initiates from the surface. Fractures propagate towards the inside of the coupling. Cracks are slanted between 0° and 45° with respect to a radial direction due to the presence of superficial shear stress. The mean slope angle was higher in specimens coupled under 40 MPa than in the other, confirming a more damaging fretting effect at the lower of coupling pressure.

1.6 REFERENCES

[1.1] Jingchen Wang, Yukui Gao. Numerical and experimental investigations on fretting fatigue properties of GH4169 superalloy at the elevated temperature. International Journal of Fatigue 149 (2021) 106274.

[1.2] Sun Y, Bell T. Consideration of fretting fatigue properties of plasma nitrided En19 steel: Second Prize. Surf Eng 2013;15:149–53.

[1.3] Zeng D, Zhang Y, Lu L, Zou L, Zhu S. Fretting wear and fatigue in press-fitted railway axle: a simulation study of the influence of stress relief groove. Int J Fatigue 2019;118:225–36.

[1.4] Zhang YB, Lu LT, Zou L, Zeng DF, Zhang JW. Finite element simulation of the influence of fretting wear on fretting crack initiation in press-fitted shaft under rotating bending. Wear 2018;400–401:177–83.

[1.5] Gürer G, Gür CH. Failure analysis of fretting fatigue initiation and growth on railway axle press-fits. Eng Fail Anal 2018;84:151–66.

[1.6] Golden PJ, Naboulsi S. Hybrid contact stress analysis of a turbine engine blade to disk attachment. Int J Fatigue 2012;42:296–303.

[1.7] Su Y, Han Q-N, Zhang C-C, Shi H-J, Niu L-S, Deng G-J, et al. Effects of secondary orientation and temperature on the fretting fatigue behaviors of Ni-based single crystal superalloys. Tribol Int 2019;130:9–18.

[1.8] Yang Q, Zhou W, Zheng X, Niu Z, Li Z, Zou B, et al. Investigation of shot peening combined with plasma-sprayed CuNiIn coating on the fretting fatigue behavior of Ti-6Al-4V dovetail joint specimens. Surf Coat Technol 2019;358:833–42.

[1.9] Mangardich D, Abrari F, Fawaz Z. A fracture mechanics based approach for the fretting fatigue of aircraft engine fan dovetail attachments. Int J Fatigue 2019;129: 105213.

[1.10] Hu C, Wei D, Wang Y, Jiang X. Introduction of fretting-contact-induced crack closure: numerical simulation of crack initiation and growth path in disk/blade attachment. Chin J Aeronaut 2019;32:1923–32.

[1.11] Guo T, Liu Z, Correia J, de Jesus AMP. Experimental study on fretting-fatigue of bridge cable wires. Int J Fatigue 2020;131:105321.

[1.12] Wang X, Wang D, Zhang D, Ge S, Alexander Araújo J. Effect of torsion angle on tension-torsion multiaxial fretting fatigue behaviors of steel wires. Int J Fatigue 2018;106:159–64.

[1.13] Fortes Da Cruz J, Da Silva Botelho T, Lemaire-Caron I, Durand AM, Messager D. Role of WS 2, WS 2 +CrC and bonded coatings on damage and friction of Inconel 718 flat rough surfaces at high temperature. Tribol Int 2016;100:430–40.

[1.14] Kunio Nishioka, Kenji Hirakawa. Fundamental investigation of fretting fatigue, part II. Bulletin of JSME (1969) 620.178.311.868:539.388.1

[1.15] O.H. Horger. Proc. Int. Conf., Fatigue of Metals, (1956), p.352, Inst. Mech. Engr.

[1.16] Kunio Nishioka, Seiichi Nishimura, Kenji Hirakawa. Fundamental investigation of fretting fatigue, part I. Bulletin of JSME (1969) 620.194:621.88.084

[1.17] Kunio Nishioka, Kenji Hirakawa. Fundamental investigation of fretting fatigue, part III. Bulletin of JSME (1969)

[1.18] Thum, F. Wunderlich. Z. Metal-kde. Jg. 27, Ht. 12 (1935), p. 227

[1.19] M. Luke, I. Varfolomeev, K. Lütkepohl, A. Esderts. Fatigue crack growth in railway axles: Assessment concept and validation tests. Engineering Fracture Mechanics. 2011

[1.20] Croccolo D, De Agostinis M, Fini S, Morri A, Olmi G. Analisys of influence of fretting on the fatigue life of interference fitted joints.

[1.21] Croccolo, D., De Agostinis, M., and Olmi, G. "Fatigue life characterisation of interference fitted joints". Proceedings of the ASME 2013 International Mechanical Engineering Congress and Exposition, Volume 2B: Advanced Manufacturing, pp. 106–116.

[1.22] Croccolo, D., De Agostinis, M., Fini, S., Olmi, G., Robusto, F., Cavalli, O., Vincenzi, N. (2018). Experimental measurement of the shank torque as a function of the stiffness and frictional characteristics of the bolted joint. Paper presented at the American Society of Mechanical Engineers, Pressure Vessels and Piping Division (Publication) PVP, doi:10.1115/PVP2018-84531

[1.23] Croccolo, D., De Agostinis, M., Fini, S., Olmi, G., Robusto, F., Cavalli, O., & Vincenzi, N. (2018). The influence of material, hardness, roughness and surface treatment on the frictional characteristics of the underhead contact in socket-head screws. Paper presented at the American Society of Mechanical Engineers, Pressure Vessels and Piping Division (Publication) PVP, doi:10.1115/PVP2018-84530

CHAPTER 2

SHAFT-HUB HYBRID CONNECTIONS: ANAEROBIC ADHESIVE TO OPTIMIZE AND IMPROVE JOINT PERFORMANCE

A shaft-hub hybrid connection is a mechanical joint that exploits the combined action of the geometrical interference between the coupled parts and the presence of an adhesive to transmit loads.

As reported in the previous chapter, shaft-hub joints are widely used in the field of torque transmission. Anaerobic adhesive can be added to the conventional joints to increase the load to be transmitted and to improve performance, also achieving lightweight properties. For example, for transmitting the same load, a hybrid joint may have lower interference than a conventional one. The stress state in the shaft-hub joints, is consequently reduced, thus dropping down the risk of fatigue failure. Another important point is that, as an effect of the bonding at the interface between the hub ends and the shaft, hybrid joints exhibit a better fretting corrosion resistance.

Among the available adhesive, anaerobic ones are suitable to join metal components. Anaerobic adhesives cure in an oxygen free environment and they exhibit high shear strength.

In the following Sections, the main parameters affecting the mechanical properties of anaerobic adhesives will be described. Subsequently, the calculation method used to design a hybrid shaft hub joint will be explained and then the performed experimental tests will be reported. This research aims at providing quantitative data for design purposes with regard to shaft hub hybrid joints. The attention will be focused on the influence of the interference level, the assembly process, the operating temperature and the shaft geometry on the adhesive shear strength. The study is based on a real application in an angular gearbox. The involved materials were hardened steel for the specimens, typically used in mechanical transmissions, and Loctite 648 for the adhesive.

Some trials were devoted to address some occurrences that may seriously affect the estimation of the adhesive strength. During the assembly phase, the adhesive can be stripped away due to high interference and scratches can be created. For this purpose, tests with press-fitted and shrink-fitted specimens without adhesive were carried out for determining the static friction coefficient in a wide interference range. Preliminary tests

on pin and collar specimens, based on Standard ISO 10123, were also performed to check the adhesive shear strength and to compare it to the reference values provided by the supplier. To assess the adhesive behavior in a heated environment, some tests were carried out at high temperature. Finally, in order to enhance the hybrid joint performance, a solution that may be worked out to increase the amount of adhesive remaining trapped at the joint interface was investigated.

2.1 Main parameters affecting the adhesively bonded joint strength.

An adhesive is defined as a substance with high shear strength, that is able to hold together two surfaces, in a strong and permanent way. Particularly, adhesives with high shear strength (above 7 MPa) and high resistance to environmental factors are defined as structural adhesives. They work based on the adhesion and cohesion properties: the first one depends on the generated intermolecular adhesion force between the adhesive and the adherends, the second is based on the intermolecular force that arises within the adhesive. This distinction is important to differentiate the fracture mode. In fact, two types of failure can occur in an adhesively bonded joint. Adhesive failure occurs when the adhesive detaches from the adherends, while the cohesive fracture happens when the maximum threshold of the cohesive force between the adhesive molecules is exceeded (Figure 29 [2.1]). Therefore, the performance of a bonded joint does not depend only on the adhesive properties, but also on the nature of the adherends and the surfaces conditions. It is also particularly important to ensure:

- Accurate cleaning of the substrates: foreign materials such as dirt, oil, moisture and oxides must be removed from the surface of the substrate, to prevent the adhesive sticking to it rather than to the substrate.
- Correct wetting of the substrate with the adhesive: the adhesive must be liquid so that it can be smoothly applied and cover the entire geometry. It is necessary that the adhesive fills the gaps due to surface roughness. Good wetting provides a greater contact area between adherent and adhesive thus increasing the adhesion strength available.
- Correct cure: before applying loads, the adhesive must be cured. The time required for the solidification depends on adhesive type and curing. The cure takes place in oxygen free environments, so it is difficult to achieve good mechanical properties for high adhesive thickness. For this reason, in pin-and-collar joints, it is important to accurately check the clearance between the shaft and the hub.

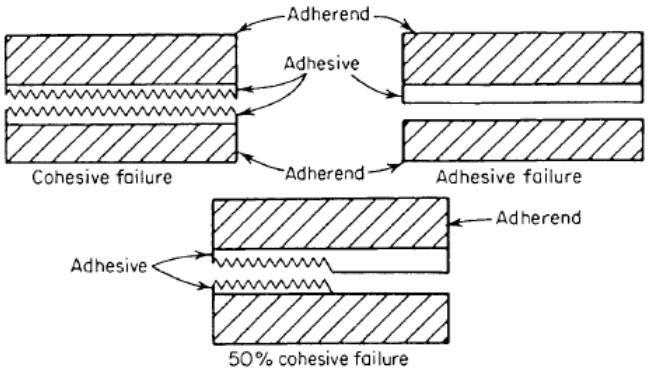

Figure 29: Adhesive and cohesive failure [2.1]

2.1.1 Bonding clearance and interference

When cylindrical components are to be joined, the presence of clearance allows to manually connect the parts. The recommended value for anaerobic adhesives is in the range from 0.05 to 0.15 mm [2.2]. As the coupling clearance between shaft and hub increases, the thickness of the adhesive increases as well, and a significant decrease of both the static and dynamic strengths can be observed. When the bonding clearance increases, even to 0.5 mm, epoxy resin may show better performance than anaerobic adhesives [2.1]. On the other hand, if the adhesive thickness is too thin the penetration of the adhesive on the entire surface to be bonded is no longer feasible, thus reducing the strength of the joint [2.3]. In the research by T. Sekercioglu et Al. [2.3], both static and dynamic responses of Loctite 638 were studied for five different clearance thicknesses and two different interference levels. Cylindrical steel samples were used for the tests, manufactured in S235JR – EN 10025, with a roughness of 1.5 µm. Figure 30 and Figure 31 show the experimental results (dynamic tests refer to a mean stress τ_m = 5.3 MPa and a stress amplitude τ_a = 3.5 MPa): a considerable reduction of the joint strength occurs when the thickness of the adhesive increases.

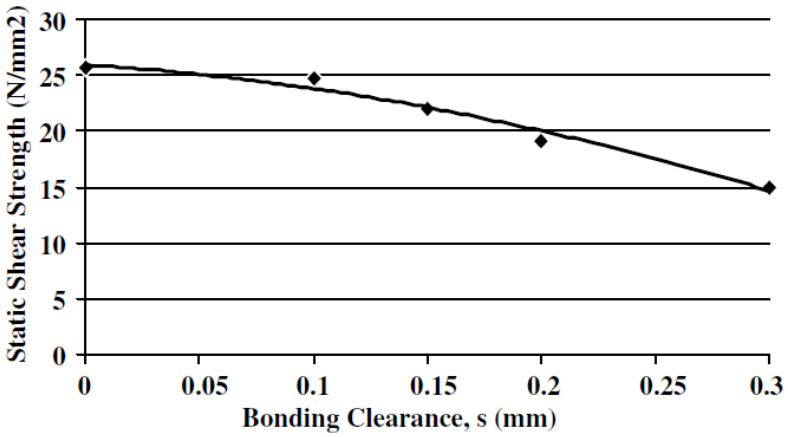

Figure 30: Static shear strength as a function of the bonding clearance [2.3]

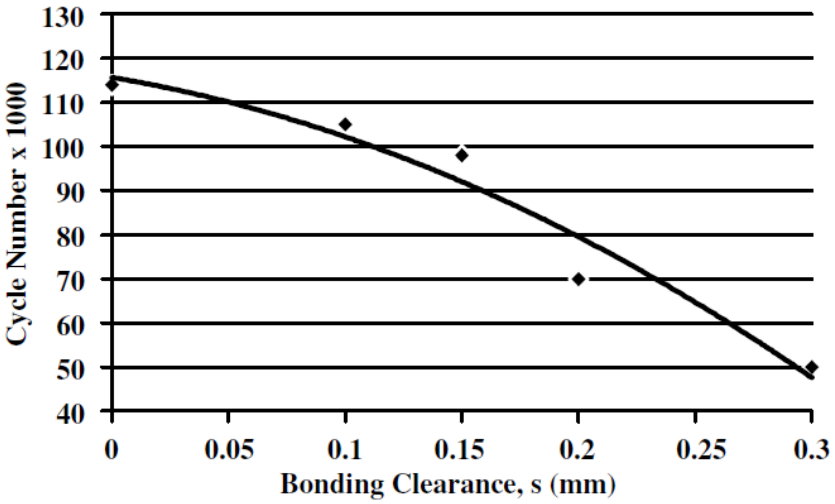

Figure 31: Life cycles as a function of the bonding clearance [2.3]

With specific regard to interference coupling, the aforementioned research [2.3] does not tackle this point. Nevertheless, the beneficial effect of the anaerobic adhesive was highlighted for two different interference fit levels (H7/r6 and H7/u6). Results show a high increment for both static and dynamic strength (at least four times with respect to dry coupling). These results can be explained as follows: in a dry interference coupling it is difficult to warrant full contact between the coupled parts. By applying adhesive, the bonding surface can be increased to about 100%.

2.1.2 Roughness

Roughness affects the adhesive behavior. Abrasion, sanding or machining are able to increase the adhesion force between the adhesive and the adherend. In another study of T. Sekercioglu et Al. [2.4] five surface roughnesses were considered in tests performed with cylindrical shaft hub specimens coupled with the same clearance. The maximum

shear strengths are found for surface roughness values between Ra = 1.5 and 2.0 μm. In the case of smooth surfaces, i.e. for roughness values lower than Ra = 0.45μm, the shear strength decreases significantly due to the inadequate penetration of the adhesive on the surface.

On the other hand, when the roughness increases too much, the joint strength decrease. For high roughness, the adhesive thickness increases and the crests of the roughness act as an obstacle to the spread of the adhesive, causing insufficient wetting.

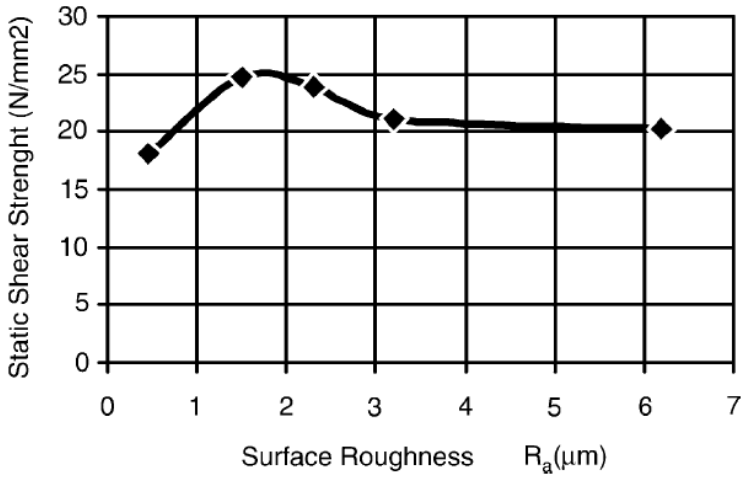

Figure 32: Effect of the specimen roughness on the adhesive strength [2.4].

2.1.3 Grooves and hoop channels

Roughness refers indeed to a measurement of micrometric order. To furtherly increase the hybrid joint performance, it is recommended to work on more macroscopic aspects, such as the creation of grooves or channels on the mating surfaces. In a study by L.F.M da Silva et Al. [2.5] the effects of scratches and their direction with respect to the application of the load were studied for different adhesive types. Scratches can increase mechanical performance thanks to a mechanical interlocking phenomenon (it is like the joint works as a shape coupling). The beneficial effect of the scratches depends on the applied adhesive type. In fact, in the study an improvement in joint strength was seen for an epoxy adhesive with a brittle behavior (Araldite AV138 / HV998, typically used in the aerospace sector), while no benefits were found using a ductile adhesive. Figure 33 shows the obtained results on a single-lap joints for different pattern of the grooves.

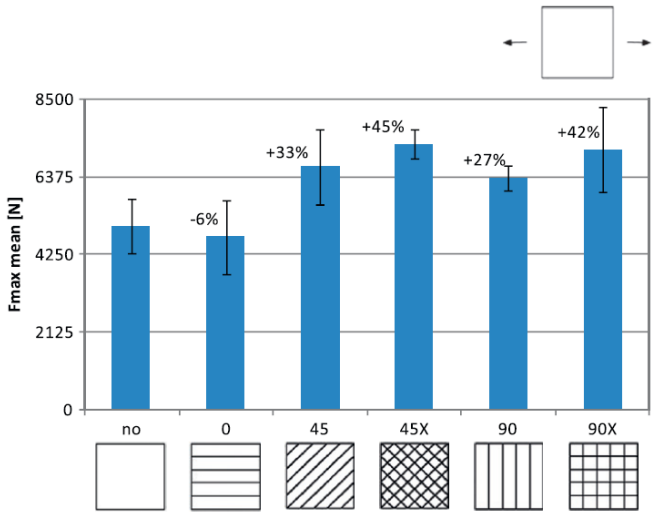

Figure 33:Effect of scratches direction on the strength of a single-lap joint [2.5]

Moreover, in a study by Croccolo et Al [2.6], which involved the anaerobic Loctite 648, an increase in performance of a joint was found, as an effect of machined hoop channels on carbon-epoxy composite which are press fitted into steel housings bushes (Figure 34).

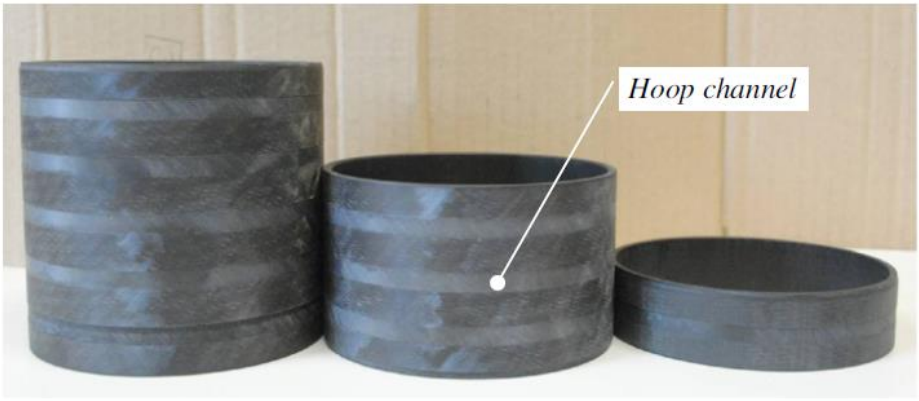

Figure 34: Hoop channels in a carbon-epoxy composite bush [2.6]

2.1.4 Assembly process

With the aim of coupling the parts of an interference joint, three methods are commonly used: the first is the press fitting at room temperature, the second consists in a heating of the hub (shrink fitting) and the third in a shaft cooling by using liquid nitrogen. When the interference level is low, coupling by press fitting ensures good adhesive strength. However, at medium or high interference levels some scratches could be created during the coupling procedure. Furthermore, some adhesive could be stripped away from the adherend surfaces, thus decreasing the wetted area. Heating the hub is a solution that ensures clearance between the shaft and the hub during the assembly phase. In this way the adhesive is not expelled from the joint. Nevertheless, when parts are made of steel,

heating may lead to oxides generation. In fact, in Croccolo et Al. [2.6] some traces of rust were found on the surfaces of hubs made in C40 steel after heating at 180°C. In this research, the axial release force found in pin and collar samples coupled after heating the hubs was lower than that measured in couplings at room temperature. When there is interference between the shaft and the hub, heating the hub has the beneficial effect of avoiding the removal of the adhesive from the surfaces during the coupling. This beneficial effect is greater than the harmful effect caused by the possible formation of oxides. In fact, in the research [2.7], a better performance was found in interference specimens shrink fitted.

Between the three considered coupling procedures, cooling the shaft using liquid nitrogen leads to the worst results. Humidity that forms on the shaft surfaces due to the cooling leads to low quality adhesive polymerization.

2.1.5 *Curing condition*

Before applying loads to a bonded joint, the adhesive must be cured. During the polymerization, residual stresses could be induced in the adhesive, due to the volumetric contraction.

Pressure and temperature are two important parameters that alter the curing phase. When the adhesive is cured under pressure, the joint shows better strength. This can be explained by the fact that, during the polymerization, the adhesive volumetric constriction leads to the presence of radial tensile stresses that prevent sufficient adhesion. Pressure compensates for the effect of the adhesive volumetric shrinkage avoiding the emergence of residual stresses. It was assessed that in strong adhesives an increased pressure during curing improves the bond strength under quasi-static as well as under fatigue loading [2.7].

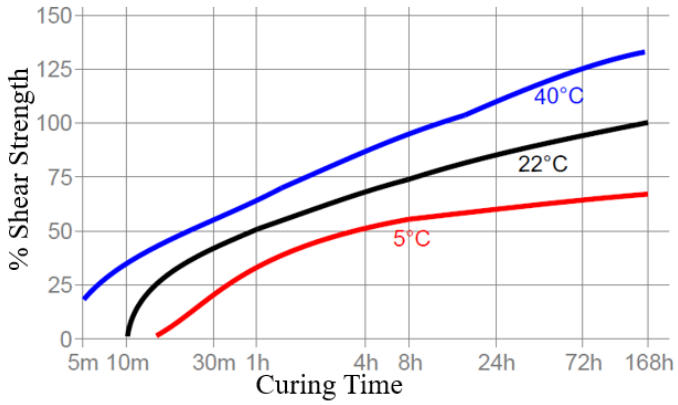

Figure 35: % Shear strength of Loctite 648 applied on steel sample for three different curing temperature [2.8]

Temperature affects both residual stresses and polymerization times. In fact, if two materials of different nature are to be joined, the difference in the coefficient of thermal expansion of the parts is likely to cause residual stresses to emerge inside the adhesive. However, increasing the joint temperature of a few degrees allows for faster chemical reactions. In Figure 35 the achievable shear strength, as a percentage of that available after a cure of a week at 22°C, is shown for three different curing temperature. As it is possible to see, after a cure at 40°C for 10 hours, it is possible to achieve the same shear strength than a cure al 22°C for 7 days.

2.1.6 Operating temperature

The strength degradation as an effect of temperature is very important for adhesives. An adhesively bonded joint designed for use at ambient temperature can exhibit strong but brittle behavior at lower temperature or low strength and ductility at higher temperature. An example of strength degradation due to high operating temperature is shown in Figure 36 [2.9]. As it can be noticed, 40% of shear strength was lost as an effect of temperature increase from 20 to 80°C. The behavior at low temperatures strongly depends on the adhesive nature. The strength could initially increase for not too low temperature, but if temperature decreases too much, some adhesives may show a brittle behavior (Figure 37)[2.10]. About the Loctite 648 anaerobic adhesive, only temperature data reported in its datasheet are available in the literature (Figure 38).

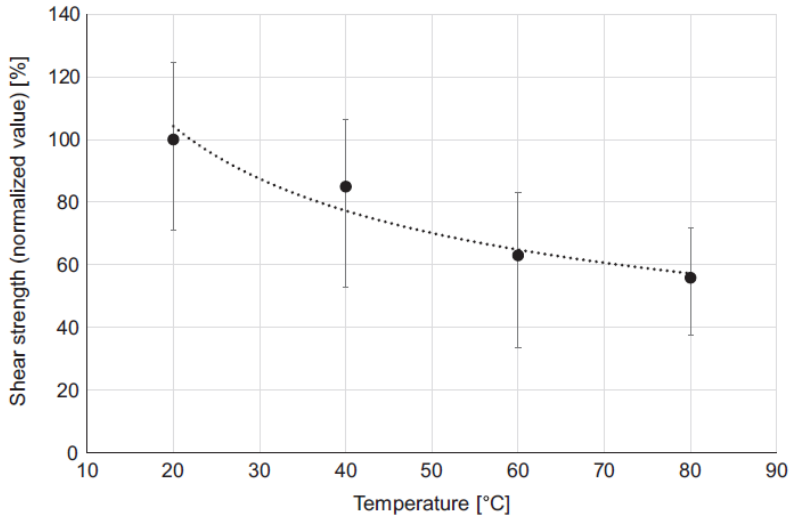

Figure 36: Shear strength normalized with respect to the response at room temperature for the epoxy adhesive Loctite 9466 [2.9]

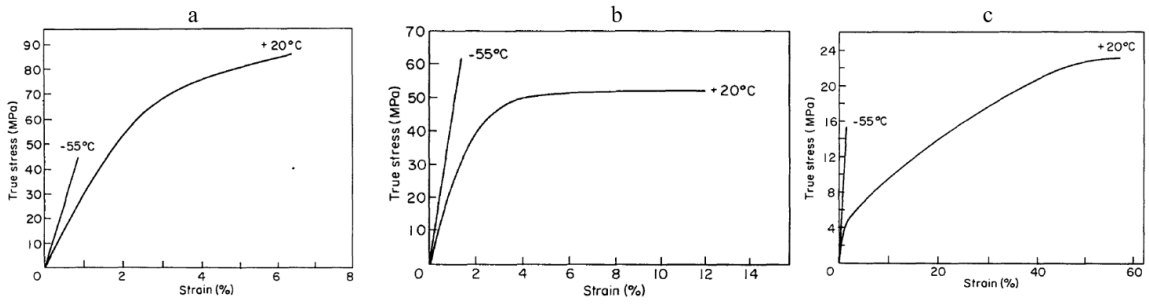

Figure 37: Strength at +20°C and -55°C for: a) Unmodified epoxy resin, b) Araldite 2005, c) Oxirane-acrylic [2.10]

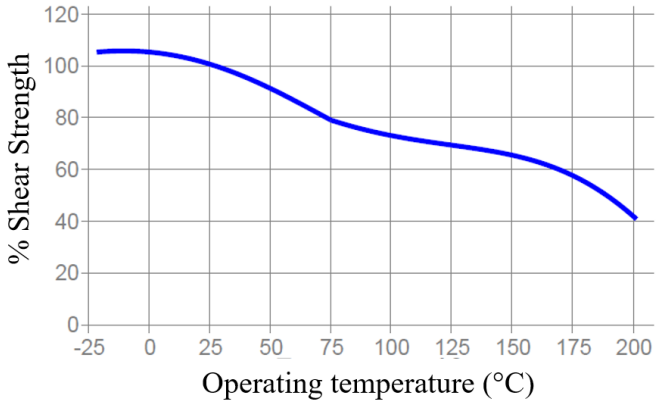

Figure 38: Loctite 648 shear strength as a function of the operating temperature [2.8]

2.2 Calculation method for shaft hub hybrid joints.

The calculation method used in this research for the study of shaft-hub hybrid joints consists in the superimposition of two effects: the first one is the contribution due to the coupling interference, whereas the second one is the effect of the adhesive strength. It must be pointed out that this simple approach keeps its validity for strong anaerobic adhesives, like the utilized LOCTITE 648, for which the strength is not detrimentally affected by the amount of the interface pressure [2.11 - 2.12]. The total strength of the joints was experimentally determined by axial release tests performed on cylindrical sample by a hydraulic press (ref. chapter 2.3). The total axial release force of a cylindrical hybrid joint (F_{tot}) can be written as:

$$\boldsymbol{F_{tot} = F_{ad} + F_{int}} \qquad \textit{Eq. 2.1}$$

Where F_{ad} is the adhesive force and F_{int} is the interference force. The adhesive contribution, can be calculated multiplying the adhesive shear strength τ_{ad} by the bonded area A.

$$\boldsymbol{F_{ad} = \tau_{ad} \cdot A} \qquad \textit{Eq. 2.2}$$

The interference contribution F_{int} was calculated by Eq. 2.3.

$$\boldsymbol{F_{int} = \mu_{ll} \cdot p_c \cdot A} \qquad \textit{Eq. 2.3}$$

Where μ_{ll} is the first release friction coefficient, p_c the coupling pressure and A the coupling area.

The value of the coupling pressure p_c was determined as a function of the specific interference ξ by the Lame's theory. Eq. 2.4 applies for this purpose, accounting for shafts and hubs with the same elastic modulus.

$$\boldsymbol{p_c = 0.5 \cdot \xi \cdot E \cdot (1 - Q_h^2)} \qquad \textit{Eq. 2.4}$$

Where E is the normal elastic module and Q_h is the aspect ratio defined as the ratio between the internal and the external diameters of the hub. The specific interference ξ is given by the ratio between the real diametral interference Z_d and the nominal coupling diameter d_c.

$$\boldsymbol{\xi = \frac{Z_d}{d_c}} \qquad \textit{Eq. 2.5}$$

The value of the real interference Z_d depends on the joining technique: for shrink-fitted couplings is given by Eq. 2.6, whereas, for press-fitted joints is yielded by Eq. 2.7.

$$\boldsymbol{Z_d = U_d} \qquad \textit{Eq. 2.6}$$

$$Z_d = U_d - 3 \cdot (R_{a_h} + R_{a_s}) \qquad \textit{Eq. 2.7}$$

Where R_{ah} is the hub roughness and R_{as} the shaft roughness. U_d represents the nominal interference, that is yielded by the difference between the measured diameters of shaft d_s and hub d_h respectively.

$$U_d = d_s - d_h \qquad \textit{Eq. 2.8}$$

Eq. 2.7 accounts for the flattening of the roughness crests, in agreement with Standard DIN 7190 (Interference fit – Calculation and design rules; 2001) and with [2.13].
The final outputs of the study reported in the following chapters will be the adhesive shear strength τ_{ad} and the joint release force F_{tot}. The last term is a direct measure that comes from the test machine, whereas the adhesive shear strength was calculated as follow.
Based on the measurements regarding roughness of the specimens and the diameter dimensions, it is then possible to calculate the specific interference ξ for each couple of samples (Eq. 2.5), considering Eq. 2.6 for the real interference Z_d when specimens were shrink fitted or Eq. 2.7 when press-fitted. After that, the coupling pressure can be computed thanks to Eq. 2.4. If the first release friction coefficient μ_{II} is known, it is possible to estimate the interference term F_{int} by Eq. 2.3. From the Eq. 2.1 it is possible to isolate the adhesive force F_{ad}:

$$F_{ad} = F_{tot} - F_{int} \qquad \textit{Eq. 2.9}$$

Finally, the adhesive shear strength is obtained by inverting Eq. 2.2:

$$\tau_{ad} = F_{ad}/A \qquad \textit{Eq. 2.10}$$

An important note should be made regarding the first release friction coefficient μ_{II}. As will be discussed in detail in the following chapters, the friction coefficient does not remain constant as the interference level varies. Some experimental tests were carried out to assess its value and to understand how it varies if the interference level changes.
The first release friction coefficient was calculated by Eq. 2.11:

$$\mu_{II} = \frac{F_\mu}{p_c \cdot A} \qquad \textit{Eq. 2.11}$$

Where F_μ is the axial release force measured in push-out tests performed in dry coupled samples (without adhesive).

2.3 Materials and methods

The main characteristics of the specimens used for the tests will initially describe in this paragraph. Then the procedure used for dimensional checks and roughness measurement will be explained. Finally, the tools used for the execution of the couplings and the push-out tests will be described.

2.3.1 Specimens

The specimens were designed and produced, considering a real application concerning an angular gearbox, and based on the Standard ISO 10123. The angular gearbox has 17 mm shafts with conical wheels coupled by keys. Although the Standard recommends a coupling diameter of 20 mm, in the present study specimens were designed with a coupling diameter of 17 mm, in order to have a full agreement with the aforementioned real application. Despite the Standard deals with pin-and-collar joints, whereas interference was needed in the present study, ISO 10123 was considered to design the specimens and the test tools. The shaft length was greater than that recommended by the Standard (60 mm against 40 mm), to facilitate the handling of the components during the assembly phases.

The shafts were obtained, grinding commercial steel bars made of 42CrMo4 steel alloy. The hub material was 16CrNi4Pb hardened steel. Two geometries were used for the shafts: the first one, with smooth cylindrical shape and 13 mm engagement length, was used for determine the adhesive strength at room temperature and at high temperature in tests carried out at different coupling pressure and with different coupling procedure. It may be argued that the small diameter dimension with respect to that recommended in Standard has a limited impact on the length over diameter aspect ratio. In particular, it is just incremented from 0.65 to 0.76: regarding this point, it is worth mentioning the study in [2.9] has highlighted that the influence of the engagement ratio on the joint strength keeps negligible over a much wider interval.

The second geometry, exhibiting two hoop channels in the coupling area, was used in the last part of the study, to assess the capability of this solution of overcoming the issue related to adhesive inefficiency under high inference. Sample geometries are shown in Figure 39. The hoop channels were designed with one millimeter width. The depth was chosen, so that the clearance with the hub was near to that recommended by the aforementioned Standard for pin-and-collar samples. Two channels were cut for each

specimen. Due to its presence, the coupling length available for interference was reduced to 11 mm, instead of 13 mm for the smooth geometry.

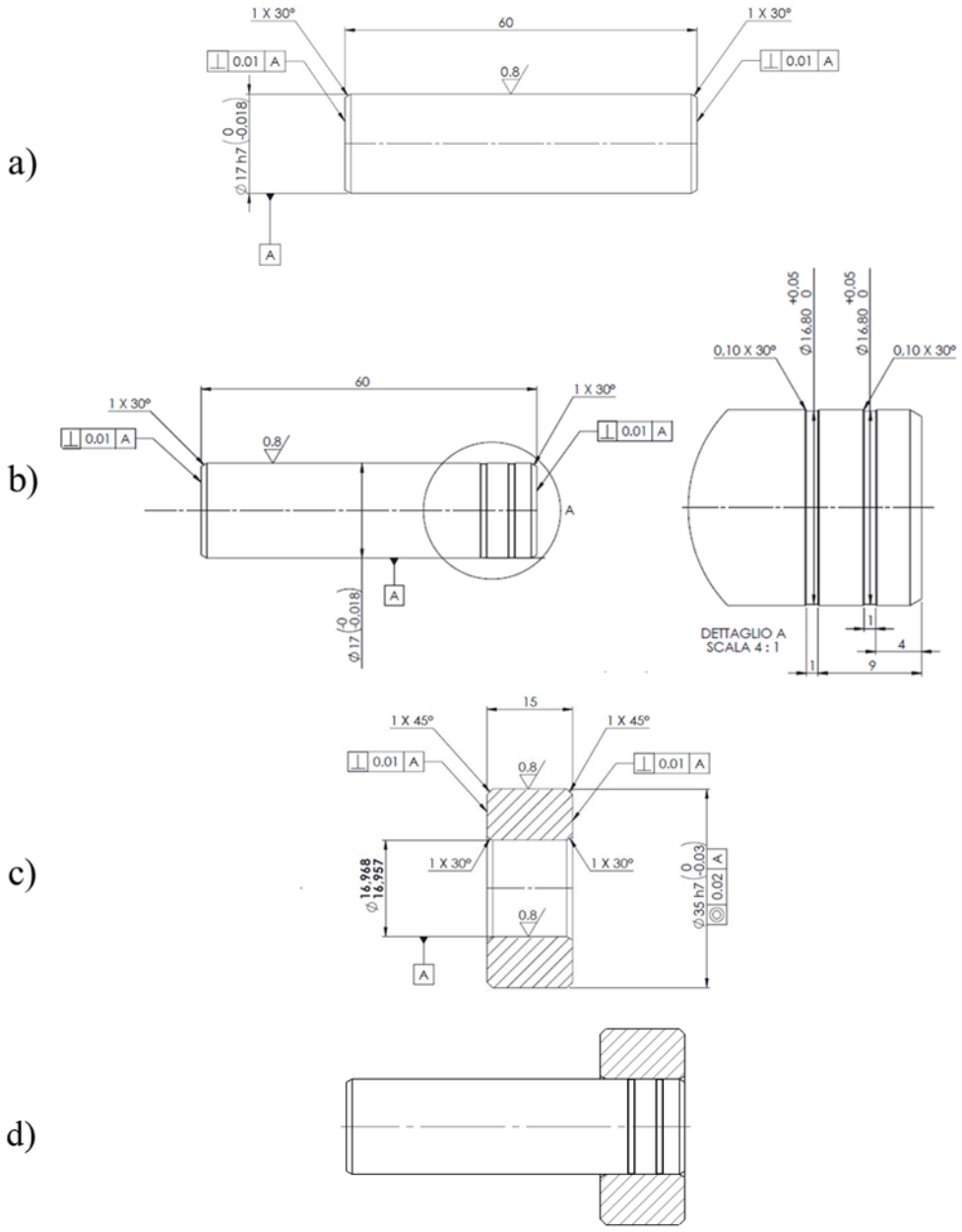

Figure 39: a) Smooth shaft geometry; b) shaft with hoop channels and its detail; c) hub geometry; d) shaft-hub relative position after the coupling (all dimensions are in mm).

2.3.2 Equipment

The main characteristics, which were likely to affect the joint performance, were carefully determined (Figure 40). Using a roughness tester, the roughness Ra of all the hubs was measured along the axial direction at three equiangled points of the coupling diameter. As for the shafts, they were obtained from six different bars with very close roughness.

Therefore, three measurements were performed on random specimens and the average roughness value was used to calculate the real interference (Zd).

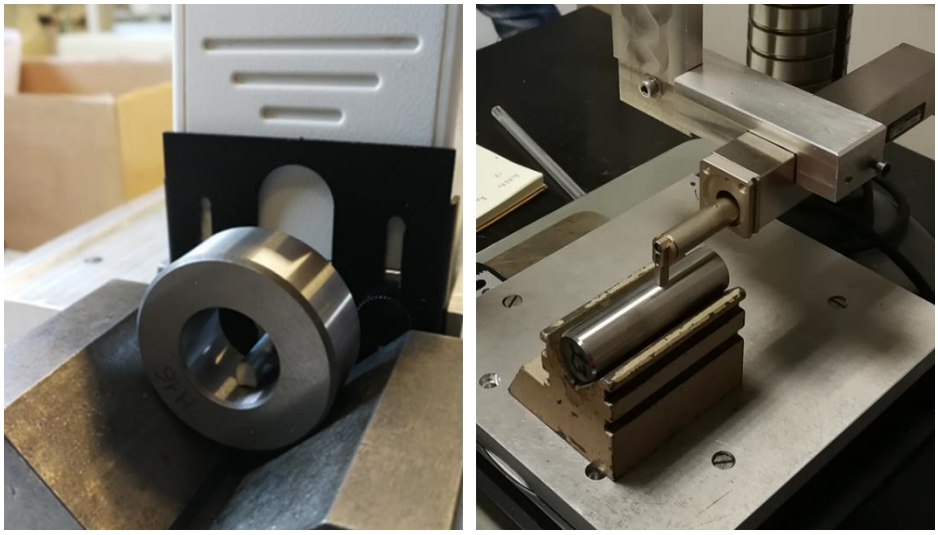

Figure 40: Measurements of hubs internal roughness on the left and of the shafts on the right.

Diameter measurements were performed in a metrology room at the temperature of 20 °C. An electronic micrometer was used for the shafts with a certified accuracy of +/- 1 µm. For the hubs, a Cartesian machine was used with a probe whose certified precision is +/- 1 µm, as shown in Figure 41. To minimize the measurement error a particular measurement strategy was used. This consisted in determining the position of four 90° angled points placed on a circumference at the middle height of the hub hole. The software is able to disregard one of the four points, thus retrieving the ideal circumference passing through the other three. The same procedure is then repeated, disregarding each of the other three points, thus determining a total of four circumferences. The average diameter is yielded by the average of the diameters of the four circumferences; moreover, the difference between the larger and the smaller diameters is returned by the software, as an index of circularity error. An oval hole could alter the pressure distribution influencing the experimental force value. All the other geometrical specifications of the hub were successfully checked using an electronic caliper.

After measuring them, the samples were sorted out, to obtain the final population of 170 shaft-hub specimens to be assembled and then decoupled. All the samples were split into four levels of interference (as will be described later, four interference levels were chosen to investigate the adhesive behavior, ranging from $\xi = 4 \bullet 10^{-4}$ to $\xi = 2.2 \bullet 10^{-3}$). The shafts and the hubs were sorted out by size, from the largest to the smallest, and categorized into four groups, using an electronic datasheet. To obtain the highest level of interference,

shafts from the group with the largest diameters were combined with the hubs from the group with smaller sizes. On the contrary, to get the lowest interference level, the smallest shafts were joined to the largest hubs. The same logic was followed to achieve the combination of the remaining shafts and hubs classified in the remaining groups, thus obtaining the two intermediate levels of interference. More specimens than theoretically needed were manufactured.

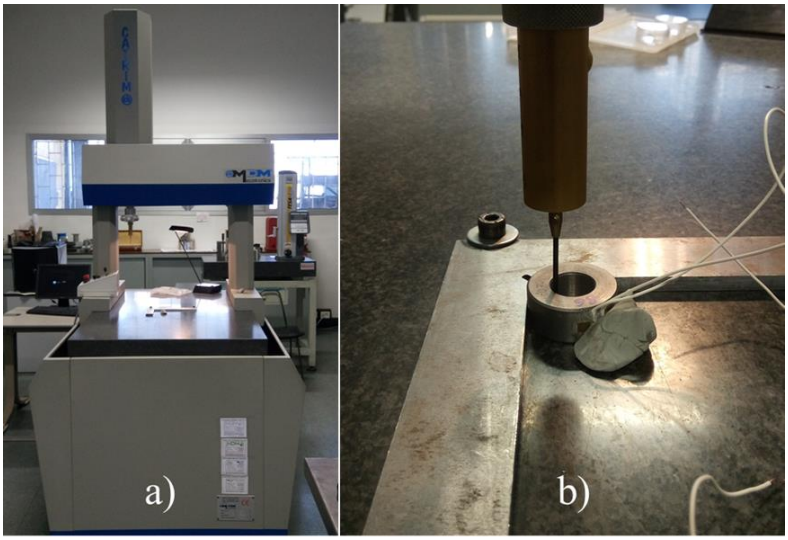

Figure 41:(a) Cartesian measurement machine used for hubs; (b) a detail of machine probe

The experimental tests were carried out by the equipment shown in Figure 42. For the assembly phases only, a PTFE centering tool was used, as recommended in ISO 10123 Standard.

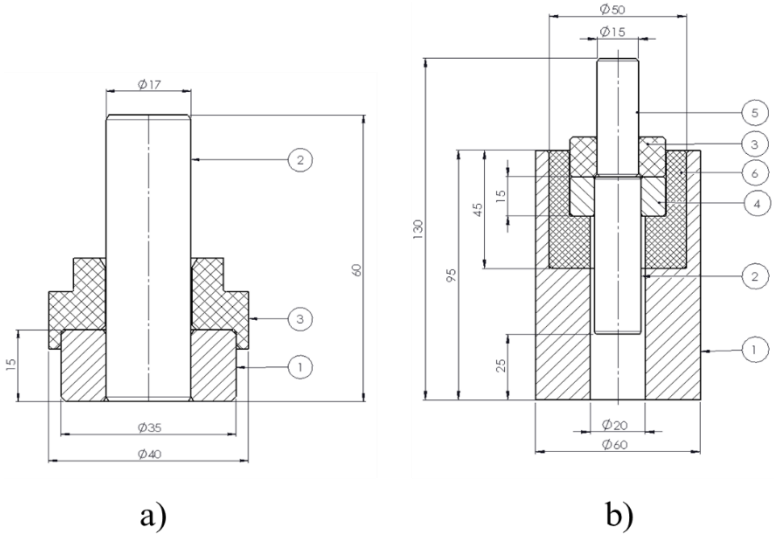

Figure 42: Fixtures used for (a) coupling phases: 1 hub, 2 shaft, 3 centering tool. (b) decoupling tests: 1 cylindrical support, 2 shaft, 3 centering tool, 4 hub, 5 pin, 6 heat insulating support. All dimensions in millimeters

The equipment used for the disassembly consists of a cylindrical steel cup containing a PVC pad.

This pad, which has the additional purpose of thermal insulation, was implemented for tests in heated conditions. The standing press used for the pushing out trials is a servo hydraulic machine with a load cell of 100 kN (a photo with some tags is shown in Figure 43).

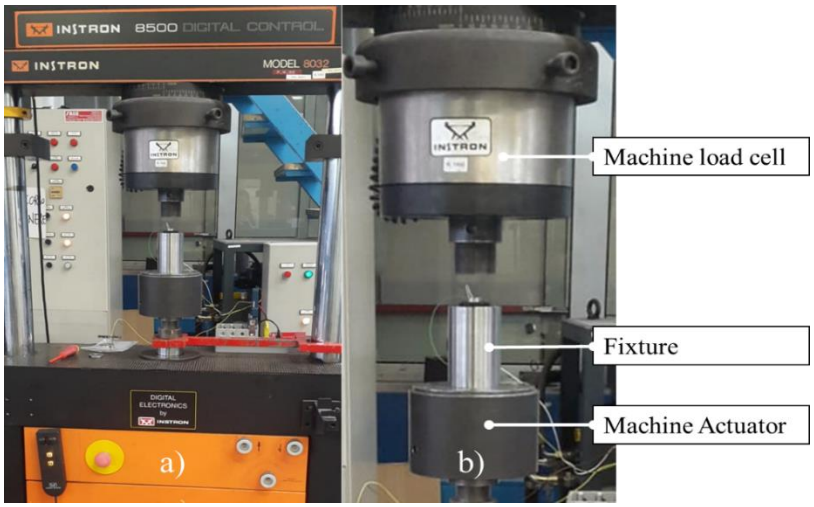

Figure 43: (a) Instron servo hydraulic machine and (b) a detail of its machine load cell, the machine actuator and the fixture.

2.3.3 Experimental procedure

Considering the difficulty of making couplings with similar interference levels, more specimens than necessary were produced. Before the dimensional and roughness assessment, all the specimens were carefully cleaned. It was preferred not to run degreasing, to avoid the formation of oxides. After that, all the samples were split into four levels of specific interference: level 1 from $\xi = 4 \cdot 10^{-4}$ to $\xi = 6 \cdot 10^{-4}$, level 2 from $\xi = 9 \cdot 10^{-4}$ to $\xi = 1.1 \cdot 10^{-3}$, level 3 from $\xi = 1.6 \cdot 10^{-3}$ to $\xi = 1.8 \cdot 10^{-3}$, level 4 from $\xi = 2.0 \cdot 10^{-3}$ to $\xi = 2.2 \cdot 10^{-3}$. Before the coupling all the samples were degreased by Loctite 7063 (Manufacturer: Henkel, Dusseldorf, Germany) and then dried for 30 minutes. A heated plate was used to heat the hubs to be shrink fitted. Hubs were heated for 30 minutes at 250°C (Figure 44). When planned, the adhesive was applied to the shaft and by a little brush (Figure 45). Samples were coupled by hand when shrink fitted or by a manual hydraulic press when press fitted. After completing the coupling with the desired hub, samples were cured for 72 hours, in a room at the temperature of 25 °C. In addition, the specimens mounted without adhesive were decoupled after 72 hours [2.14]. Decoupling

tests were performed at room temperature and at 100°C. The angular gear box, which is the real application the tests are based on, during its operation is likely to heat up. For this reason, push-out tests at high temperature were also considered. A heating chamber with forced convection was used to heat the coupled specimens up to 110°C (Figure 46). The heating temperature was deliberately set 10°C higher than the established one for testing, provided the specimens were expected to cool slightly during the test. The samples were extracted from the heating chamber one at a time and immediately tested, to prevent temperature drop: regarding this point the PTFE insulation of the grips (part n°6 in Figure 42b) helped to preserve heat. The shafts temperature was also checked by a thermocouple acting on the surface, which ensured temperature was always kept between 100°C and 105°C during every push-out trial. The decoupling tests were carried out under the displacement-controlled mode. The speed rate during the test varied over two levels: it was set initially to 0.025 mm/s, in agreement with ISO 10123, and then increased up to 1 mm/s after the breakage of the joint, in order to speed up the tests. The sampling rate was set at 30 Hz.

Figure 44: Heated plate used to heat shrink fitted hubs.

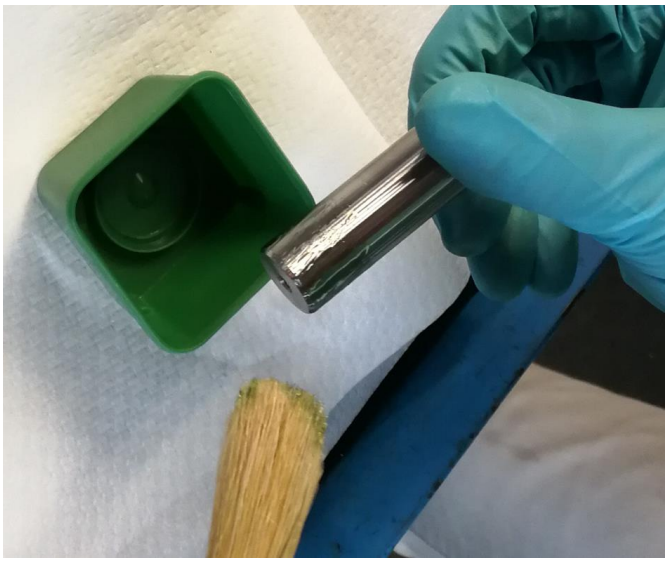

Figure 45: Adhesive applied to cleaned shafts with a little brush

Figure 46: Oven used to heat samples for high temperature tests

2.4 Dry coupling to determine the first release friction coefficient

The results available in the literature about the strength of hybrid joints were obtained for specimens with a not particularly high interference level. In fact, studies usually regarded a specific interference of $\xi = 8 \cdot 10^{-4}$ as a maximum threshold. In commonly used interference coupling, the specific interference can range up to larger values. For this reason, in this study an interference level up to $\xi = 2.2 \cdot 10^{-3}$ was considered. When samples are press fitted, high interference levels can lead to the generation of scratches and shavings (Figure 47) on the mating surfaces during the assembly process. The scratches generated during the coupling can lead to a higher joint resistance to the decoupling. In addition, micro welds could be created between the shaft and hub materials.

Let's take for example a dry coupling case with the following input: shaft diameter d_s = 16.983 mm, shaft roughness $R_{a,s}$ = 0.261 µm, hub diameter d_h = 16.972 mm, shaft roughness $R_{a,h}$ = 0.523 µm. By performing press fitting, the real interference Z_d yielded by Eq. 2.7 is 9 µm, whereas the specific interference ξ (by Eq. 2.5) is $5 \cdot 10^{-4}$. The coupling pressure amount at 40 MPa (Eq. 2.4 with a Young Modulus of 207 GPa). The coupling area A is 694 mm^2, (coupling length L_c = 13 mm and nominal diameter coupling d_c = 17 mm, see Figure 39). By supposing a static friction coefficient of 0.25 [2.14], the expected release force F_{teor}, from Eq 2.3 should be:

$$\boldsymbol{F_{teor} = \mu_{ll} \cdot p_c \cdot A = 0.25 \cdot 40 \cdot 694 = 6,940\ N} \qquad \textit{Eq. 2.12}$$

However, during the test that involved the aforementioned samples the measured axial release force F_μ was 15,430 N, more than two times the expected one. Since the area A and the coupling pressure p_c are fixed, if the release force is greater than its expected value, it means that the first release friction coefficient is higher than the expected.

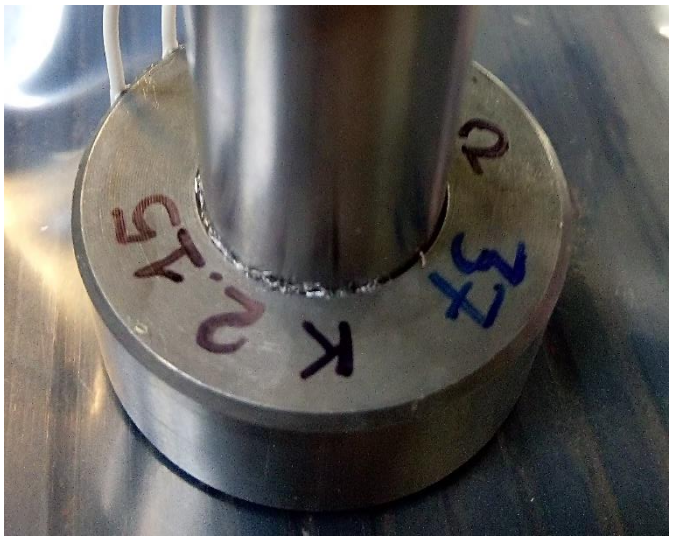

Figure 47: Presence of shavings after a press fitted coupling

For the occurrence described above, tests without adhesive were devoted to the determination of the performance of the joint in dry conditions (F_μ) and to the estimation of the friction coefficient μ_{II}. Both shrink fit and press fit methods were considered. The aforementioned four interference levels were considered. Five replicas for each level were tested. The axial release force was measured directly by the hydraulic press acquisition system, and Eq. 2.11 yielded the first release friction coefficient was calculated. To assess a possible lubricating effect of the adhesive during assembly, which could be beneficial at reducing the number of scratches and thus varying the friction coefficient, a further coupling strategy with uncured adhesive was planned (only for press fitting). In order to prevent the adhesive cure, the specimens involved in this joining technique, were coupled and then immediately decoupled one by one. The waiting time between the two phases was kept very short and was approximately 15-20 s. Thus, the joint was decoupled much earlier with respect to the expected beginning of polymerization. The complete experimental plan is shown in Table 9.

Table 9: Experimental design involving the two factors, i.e. the joining technique and the specific interference

Factor n. 1	**Joining Technique**			
Levels	**PN** (Press fitted, without adhesive)	**SN** (Shrink fitted, without adhesive)	**PA_NC** (Press fitted, with uncured adhesive)	
Factor n. 2	**Specific Interference ξ**			
Levels	$4 \cdot 10^{-4}$ to $6 \cdot 10^{-4}$	$9 \cdot 10^{-4}$ to $1.1 \cdot 10^{-3}$	$1.6 \cdot 10^{-3}$ to $1.8 \cdot 10^{-3}$	$2 \cdot 10^{-3}$ to $2.2 \cdot 10^{-3}$

The results of the push-out tests are provided below (Table 10 to Table 12). Each table refers to a joining technique, considering those listed in Table 9.

Figure 48 shows the results in terms of average axial release force, grouped based on the specific interferences. The results referenced as PN are referred to the press-fitted couplings without adhesive, whereas those marked with SN were retrieved from shrink-fitted joints without adhesive. Finally, PA_NC indicates the results for press-fitting with not cured adhesive. The release force F_μ, only due to friction, increases for higher interference levels, as an effect of the greater contact pressure p_c. As it can be noticed from Figure 48, the highest force values occur for shrink-fitted joints. This outcome can be related to the occurrence that the roughness ridges are not flattened during hot

mounting. Conversely, in cold couplings, during the assembly phase, the roughness is smoothed, thus decreasing the real coupling interference.

Table 10: Experimental results: press-fit without adhesive (PN)

Shaft ID	d_s *[mm]*	*Hub ID*	d_h *[mm]*	*Hub Roughness [μm]*	U_d *[mm]*	Z_d *[mm]*	*ξ[-]*	*Decoupling Force* F_μ *[N]*
S1-43	16.996	H-110	16.959	0.698	0.037	0.034	0.0020	34,660
S1-45	16.996	H-148	16.959	0.327	0.037	0.035	0.0021	41,600
S1-47	16.996	H-159	16.959	0.336	0.037	0.035	0.0021	39,350
S1-52	16.996	H-166	16.959	0.507	0.037	0.035	0.0020	38,250
S1-67	16.996	H-169	16.959	0.397	0.037	0.035	0.0021	32,960
S1-58	16.993	H-129	16.963	0.677	0.030	0.027	0.0016	35,240
S1-66	16.993	H-151	16.963	0.522	0.030	0.028	0.0016	30,560
S1-70	16.993	H-187	16.963	0.475	0.030	0.028	0.0016	38,330
S1-71	16.993	H-209	16.963	0.404	0.030	0.028	0.0016	29,350
S1-75	16.993	H-212	16.963	0.304	0.030	0.028	0.0017	28,910
S1-131	16.985	H-218	16.967	0.401	0.018	0.016	0.0009	20,550
S1-132	16.985	H-06	16.966	0.654	0.019	0.016	0.0010	20,390
S1-81	16.984	H-56	16.966	0.449	0.018	0.016	0.0009	18,490
S1-88	16.984	H-127	16.966	0.378	0.018	0.016	0.0009	21,730
S1-91	16.984	H-204	16.966	0.557	0.018	0.016	0.0009	22,600
S1-139	16.983	H-207	16.973	0.374	0.010	0.008	0.0005	17,450
S1-140	16.983	H-229	16.973	0.313	0.010	0.008	0.0005	9,740
S1-141	16.983	H-57	16.972	0.599	0.011	0.008	0.0005	9,240
S1-150	16.983	H-66	16.972	0.741	0.011	0.008	0.0005	17,450
S1-152	16.983	H-71	16.972	0.523	0.011	0.009	0.0005	15,430

Table 11: Experimental results: shrink-fit without adhesive (SN)

Shaft ID	*d_s [mm]*	*Hub ID*	*d_h [mm]*	*Hub Roughness [µm]*	*U_d [mm]*	*Z_d [mm]*	*ξ[-]*	*Decoupling Force F_μ[N]*
S1-21	16.997	H-37	16.961	0.781	0.036	0.036	0.0021	53,310
S1-22	16.997	H-88	16.961	0.679	0.036	0.036	0.0021	40,250
S1-24	16.997	H-108	16.961	0.486	0.036	0.036	0.0021	48,790
S1-30	16.997	H-167	16.961	0.436	0.036	0.036	0.0021	51,030
S1-40	16.997	H-178	16.961	0.477	0.036	0.036	0.0021	48,345
S1-51	16.995	H-60	16.965	0.476	0.030	0.030	0.0018	38,470
S1-55	16.995	H-85	16.965	0.404	0.030	0.030	0.0018	33,640
S1-57	16.995	H-102	16.965	0.322	0.030	0.030	0.0018	22,000
S1-62	16.995	H-155	16.965	0.440	0.030	0.030	0.0018	43,930
S1-69	16.995	H-184	16.965	0.464	0.030	0.030	0.0018	42,920
S1-84	16.986	H-35	16.969	0.492	0.017	0.017	0.0010	27,380
S1-99	16.986	H-63	16.969	0.626	0.017	0.017	0.0010	28,390
S1-106	16.986	H-75	16.969	0.584	0.017	0.017	0.0010	26,310
S1-112	16.986	H-81	16.969	0.382	0.017	0.017	0.0010	24,350
S1-115	16.986	H-15	16.968	0.580	0.018	0.018	0.0011	27,060
S1-142	16.984	H-237	16.978	0.291	0.006	0.006	0.0004	13,870
S1-144	16.984	H-05	16.977	0.542	0.007	0.007	0.0004	18,320
S1-146	16.984	H-49	16.977	0.660	0.007	0.007	0.0004	17,840
S1-148	16.984	H-213	16.977	0.354	0.007	0.007	0.0004	20,120
S1-153	16.984	H-238	16.977	0.571	0.007	0.007	0.0004	20,650

Table 12: Experimental results: press-fit with not cured adhesive (PA_NC)

Shaft ID	ds [mm]	Hub ID	dh [mm]	Hub Roughness [μm]	U_d [mm]	Z_d [mm]	ξ[-]	Decoupling Force F_μ[N]
S1-79	16.996	H-180	16.959	0.584	0.037	0.034	0.0020	31,290
S1-80	16.996	H-208	16.959	0.339	0.037	0.035	0.0021	34,280
S1-17	16.995	H-219	16.959	0.343	0.036	0.034	0.0020	25,260
S1-23	16.995	H-185	16.958	0.357	0.037	0.035	0.0021	39,080
S1-25	16.995	H-189	16.958	0.783	0.037	0.034	0.0020	33,180
S1-78	16.993	H-224	16.963	0.371	0.030	0.028	0.0017	28,060
S1-07	16.992	H-190	16.962	0.779	0.030	0.027	0.0016	32,010
S1-53	16.992	H-210	16.962	0.316	0.030	0.028	0.0017	32,280
S1-64	16.992	H-226	16.962	0.282	0.030	0.028	0.0017	34,130
S1-72	16.992	H-230	16.962	0.500	0.030	0.028	0.0016	30,810
S1-95	16.984	H-217	16.966	0.375	0.018	0.016	0.0009	20,350
S1-98	16.984	H-233	16.966	0.485	0.018	0.016	0.0009	23,650
S1-101	16.984	H-234	16.966	0.481	0.018	0.016	0.0009	25,040
S1-104	16.984	H-236	16.966	0.467	0.018	0.016	0.0009	20,920
S1-107	16.984	H-54	16.966	0.631	0.018	0.015	0.0009	19,640
S1-159	16.983	H-205	16.972	0.492	0.011	0.009	0.0005	12,990
S1-111	16.982	H-12	16.971	0.401	0.011	0.009	0.0005	19,510
S1-87	16.980	H-77	16.970	0.581	0.010	0.007	0.0004	16,990
S1-122	16.980	H-206	16.970	0.398	0.010	0.008	0.0005	18,140
S1-124	16.980	H-228	16.970	0.504	0.010	0.008	0.0005	16,130

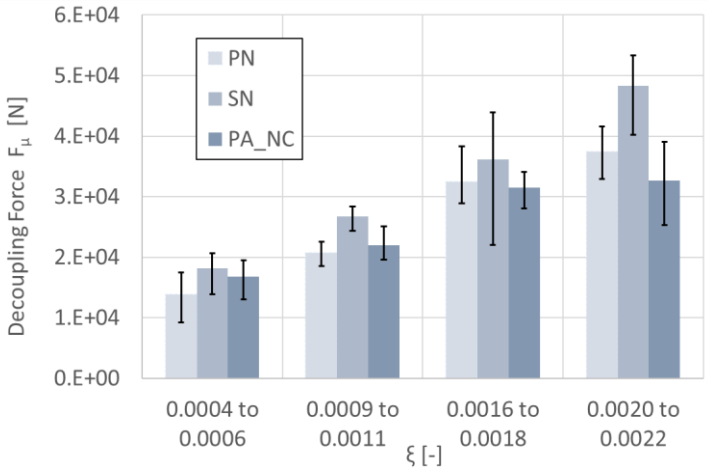

Figure 48: Axial release force for test: Press Fit without adhesive (PN), shrink fit without adhesive (SN), press fit with not cured adhesive (PA_NC)

Figure 49 shows the surfaces of three shafts and their hubs after decoupling. The specimens in this image had been previously coupled with the maximum interference level (ξ = 2.2·10-3). The shaft (a) exhibits some evident scratches; moreover, in the respective hub (b) signs of seizing are present. Small seizing marks can also be observed in the hot-mounted hub (d). The related shaft (c) exhibits some slight grooves and the smoothening of the roughness as an effect of the decoupling. The shaft depicted in Figure 49(e) was press-fitted with uncured adhesive. The cylindrical surface appears to be less damaged, if compared to the same surface following press-fitting in dry conditions (a).

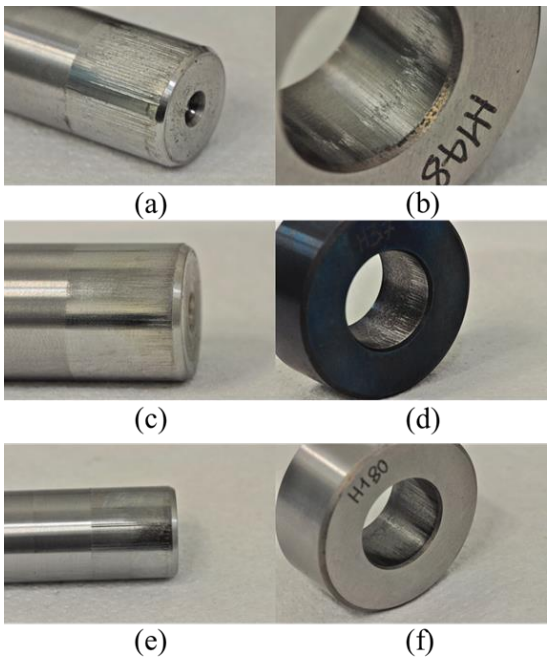

Figure 49:Example of shaft and hub coupled with: (a)-(b) press-fitting technique and no adhesive, (c)-(d) shrink-fitting technique and no adhesive, (e)-(f) press-fitting technique and not cured adhesive

This could suggest that the adhesive acts as a lubricant during assembly. In order to assess this point, the results were processed by two-way ANOVA and F-test, comparing the release forces F_μ for press-fitting in dry conditions (PN) and with uncured adhesive (PA_NC). The outcome of this analysis (p-value is 0.69) indicates these differences are not significant. Therefore, the reduced surface damage does not reflect in a different strength of the joint.

The coupling pressure was obtained by Eq. 2.4. Then, using that result together with the related decoupling force in the test (F_μ), it was finally possible to work out the friction coefficient by Eq. 2.11. The obtained values are shown in Figure 50, where they are grouped, based on their specific interference level. The error bands refer to the minimum and maximum values obtained at each level. It is remarkable the friction coefficient does not keep constant as it could be expected, but decreases for increasing interference. At high levels of interference, it seems to get steady.

For every level the highest average value was found in the shrink-fit case (SN). For low interference levels the press-fitted couplings without adhesive (PN) exhibited a lower coefficient than the couplings with unpolymerized adhesive (PA_NC). At high levels, the relationship tends to reverse, but the average values keep very similar, and the error bands are overlapped. As mentioned above, the analysis of variance indicates that the differences between press-fitted couplings without adhesive (PN) and press-fitting with uncured adhesive (PA_NC) are not significant. For this reason, press-fitting with not cured adhesive (PA_NC) will no longer be considered.

It could be argued that the retrieved values, in particular those at low interference, are remarkably high with respect to those being usually considered, when designing shaft-hub couplings (for instance, those mentioned in [2.14]). A possible hypothesis is that values up to 0.90 are due to galling as an effect of micro-weldings occurring at the interface between the shaft and the hub upon coupling. These micro-weldings are presumably due to surface asperities on the shaft or, more probably, on the hub that penetrate on the counter face. Consequently, upon decoupling, the release force must be high enough to remove these micro-weldings. After decoupling, the surface exhibits long scratches and shavings generated by asperity sliding on the opposed surface. A literature survey indicates that the study [2.15] has dealt with the effect of the average number of undulations of pin/bush round profiles on the bearing capability of shaft-hub shrink-fitted couplings. The results indicate that this factor significantly affects the loading capacity that increases for increasing number of undulations. Therefore, this outcome confirms

that surface irregularities, altering the theoretically circular profile, highly affect the local pressure and the entity of the friction coefficient that can be strongly incremented. In addition, the numerical study for the optimal dimensioning of interference-fitted shaft/hubs in [2.16] also accounts for a friction coefficient that may vary on a wide range up to 1.

The mean value of the decoupling force and of the first separation friction coefficient are provided in Table 13 with regard to the four interference levels and to the two joining strategies (PN, SN). In the following chapters, these friction values will then be used to work out the adhesive contribution.

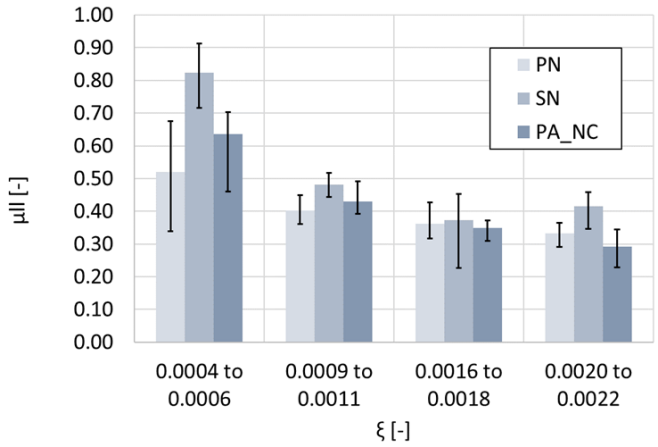

Figure 50:First separation friction coefficient determined by testing: press-fitting without adhesive (PN), shrink-fitting without adhesive (SN), press-fitting with not cured adhesive (PA_NC)

Table 13: Mean coupling force and mean first separation friction coefficient for press-fitting without adhesive (PN) and for shrink-fitting without adhesive (SN)

	Press-fitting without adhesive (PN)		*Shrink-fitting without adhesive (SN)*	
Specific interference ξ [-]	*Decoupling Force F_μ [N]*	*First separation friction coefficient μ_{II} [-]*	*Decoupling Force F_μ [N]*	*First separation friction coefficient μ_{II} [-]*
$4 \cdot 10^{-4}$ to $6 \cdot 10^{-4}$	13,862	0.52	18,160	0.82
$9 \cdot 10^{-4}$ to $1.1 \cdot 10^{-3}$	20,752	0.40	26,698	0.48
$1.6 \cdot 10^{-3}$ to $1.8 \cdot 10^{-3}$	32,478	0.36	36,192	0.37
$2.0 \cdot 10^{-3}$to $2.2 \cdot 10^{-3}$	37,364	0.33	48,345	0.42

2.5 Influence of the assembly process and of the interference level on the Loctite 648 adhesive strength.

In this chapter the influence of the assembly process and of the interference level are considered. The experimental plan is show in Table 14.

Table 14: Two factors experimental plan involving Loctite 648

Factor n. 1	**Joining Technique**			
Levels	**PA** (Press fitted, with adhesive)		**SA** (Shrink fitted, with adhesive)	
Factor n. 2	**Specific Interference ξ**			
Levels	$4 \cdot 10^{-4}$ to $6 \cdot 10^{-4}$	$9 \cdot 10^{-4}$ to $1.1 \cdot 10^{-3}$	$1.6 \cdot 10^{-3}$ to $1.8 \cdot 10^{-3}$	$2 \cdot 10^{-3}$ to $2.2 \cdot 10^{-3}$

The same interference levels of the previous chapter were analyzed. The joining technique varied over two levels: press fitted with adhesive (PA) and shrink-fitted with adhesive (SA). As reported in 2.3.3, the Loctite 648 was applied on shafts and then they were coupled with hubs by a hydraulic press at room temperature in case of press fit, or manually after hub heating for shrink fit. Specimens were cured at 25° for 72 hours. Five replicas for each level were tested. In Table 15 and Table 16 all the test details are reported.

The decoupling forces obtained for the press-fitting with adhesive (PA) and the shrink-fitting with adhesive (SA) specimens are plotted in Figure 51. The highest values were obtained for samples coupled with shrink fit, in agreement with previous results in the literature. The trend of the decoupling force at high interference level is particularly interesting. It can be observed that the contribution of the adhesive decreases, as the release force of the hybrid joint has a peak and then drops down slightly. This can be noticed in Figure 52 that shows the axial release force for the shrink-fitted joint with (SA) and without adhesive (SN). The measured decoupling forces are similar at the highest interference level, regardless of the presence of the anaerobic adhesive, thus indicating that its contribution becomes negligible.

Table 15: Experimental results: press-fit with adhesive (PA)

Shaft ID	*d_s [mm]*	*Hub ID*	*d_h [mm]*	*Hub Roughness [μm]*	*U_d [mm]*	*Z_d [mm]*	*ξ[-]*	*Decoupling Force F_{tot} [N]*
S1-20	16.996	H-92	16.959	0.404	0.037	0.035	0.0021	34,880
S1-29	16.996	H-96	16.959	0.725	0.037	0.034	0.0020	31,150
S1-35	16.996	H-98	16.959	0.353	0.037	0.035	0.0021	36,200
S1-36	16.996	H-101	16.959	0.527	0.037	0.035	0.0020	31,600
S1-42	16.996	H-106	16.959	0.365	0.037	0.035	0.0021	37,220
S1-32	16.993	H-83	16.963	0.456	0.030	0.028	0.0016	25,700
S1-39	16.993	H-87	16.963	0.467	0.030	0.028	0.0016	33,820
S1-49	16.993	H-97	16.963	0.381	0.030	0.028	0.0017	33,250
S1-50	16.993	H-116	16.963	0.708	0.030	0.027	0.0016	29,630
S1-56	16.993	H-121	16.963	0.602	0.030	0.027	0.0016	32,820
S1-92	16.985	H-24	16.967	0.483	0.018	0.016	0.0009	20,650
S1-103	16.985	H-26	16.967	0.448	0.018	0.016	0.0009	22,610
S1-109	16.985	H-30	16.967	0.398	0.018	0.016	0.0009	24,580
S1-123	16.985	H-62	16.967	0.473	0.018	0.016	0.0009	23,830
S1-126	16.985	H-172	16.967	0.495	0.018	0.016	0.0009	24,870
S1-129	16.983	H-13	16.973	0.502	0.010	0.008	0.0005	20,130
S1-134	16.983	H-14	16.973	0.536	0.010	0.008	0.0004	16,970
S1-135	16.983	H-25	16.973	0.393	0.010	0.008	0.0005	19,540
S1-136	16.983	H-36	16.973	0.552	0.010	0.008	0.0004	19,830
S1-138	16.983	H-45	16.973	0.433	0.010	0.008	0.0005	22,550

Table 16: Experimental results: shrink-fit with adhesive (SA)

Shaft ID	*d_s [mm]*	*Hub ID*	*d_h [mm]*	*Hub Roughness [µm]*	*U_d [mm]*	*Z_d [mm]*	*ξ[-]*	*Decoupling Force F_{tot} [N]*
S1-41	16.997	H-196	16.961	0.418	0.036	0.036	0.0021	38,040
S1-46	16.997	H-216	16.961	0.387	0.036	0.036	0.0021	60,140
S1-54	16.997	H-84	16.960	0.457	0.037	0.037	0.0022	41,230
S1-60	16.997	H-117	16.960	0.432	0.037	0.037	0.0022	53,070
S1-65	16.997	H-160	16.960	0.424	0.037	0.037	0.0022	45,290
S1-13	16.994	H-82	16.964	0.369	0.030	0.030	0.0018	62,450
S1-18	16.994	H-111	16.964	0.460	0.030	0.030	0.0018	57,030
S1-31	16.994	H-123	16.964	0.580	0.030	0.030	0.0018	41,830
S1-59	16.994	H-137	16.964	0.418	0.030	0.030	0.0018	59,150
S1-61	16.994	H-147	16.964	0.397	0.030	0.030	0.0018	61,060
S1-116	16.986	H-16	16.968	0.441	0.018	0.018	0.0011	54,670
S1-117	16.986	H-27	16.968	0.590	0.018	0.018	0.0011	50,040
S1-118	16.986	H-31	16.968	0.461	0.018	0.018	0.0011	53,610
S1-119	16.986	H-38	16.968	0.560	0.018	0.018	0.0011	43,990
S1-137	16.986	H-39	16.968	0.447	0.018	0.018	0.0011	58,690
S1-155	16.984	H-41	16.976	0.528	0.008	0.008	0.0005	47,260
S1-156	16.984	H-232	16.976	0.425	0.008	0.008	0.0005	46,620
S1-160	16.984	H-20	16.975	0.541	0.009	0.009	0.0005	29,190
S1-86	16.983	H-28	16.975	0.525	0.008	0.008	0.0005	47,100
S1-94	16.983	H-70	16.975	0.511	0.008	0.008	0.0005	51,243

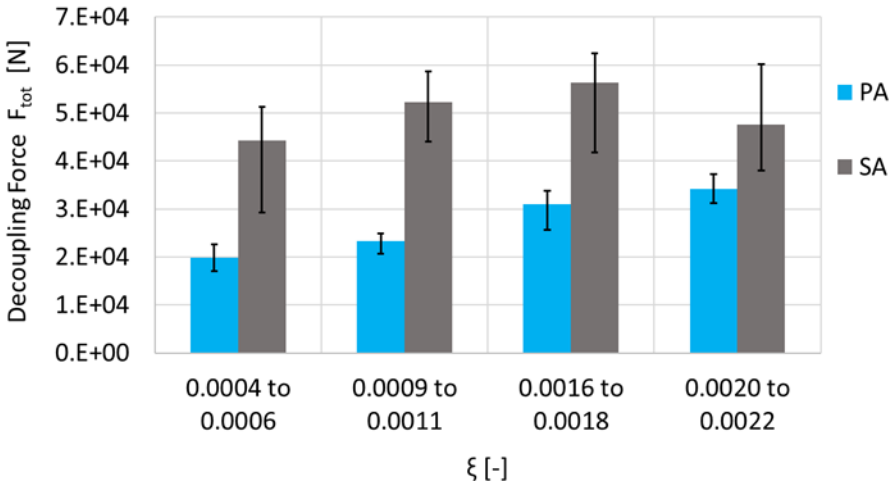

Figure 51: Axial release force in hybrid joints: press-fitting with adhesive (PA) and shrink-fitting with adhesive (SA)

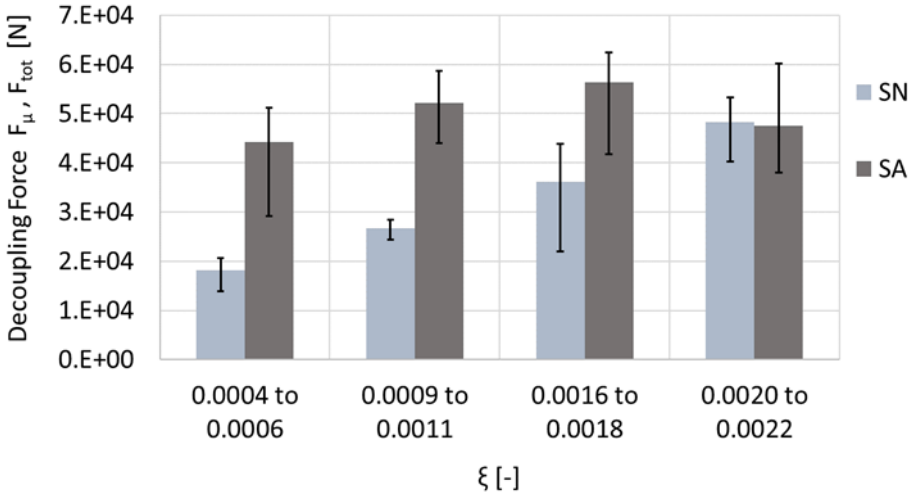

Figure 52: Axial release force for shrink-fitting without adhesive (SN) and shrink-fitting with adhesive (SA)

Figure 53 shows a comparison between the decoupling force for the press-fitted specimens with (PA) and without adhesive (PN). The contribution of the adhesive is significant only for low levels of interference, in particular for the first two ones: at high levels the pushing-out forces turn to be approximately the same (in terms of mean value and variation interval), regardless of the presence of the adhesive. The shafts and the hubs used in this experiment have a low roughness value (0.28 µm for the shafts and from 0.3 to 0.8 for the hubs). A low roughness reduces the wettability of the surfaces, leading to premature adhesive failure. However, failures have mostly been cohesive. The resulting shear strength is shown in the bar graph in Figure 54. According to the computational procedure above, the shear strength was calculated by Eq. 2.10 and Eq. 2.09. F_{tot} was the measured force during the test, and F_{int} the interference contribution calculated using the friction coefficient experimentally estimated in the chapter 2.4. For each interference

level, the corresponding friction coefficient in Table 13 was used. It can be pointed out the contribution of the adhesive is evident in shrink-fitted specimen (SA): the average shear strength is greater than 30 MPa for the first two levels of interference and just below for the third.

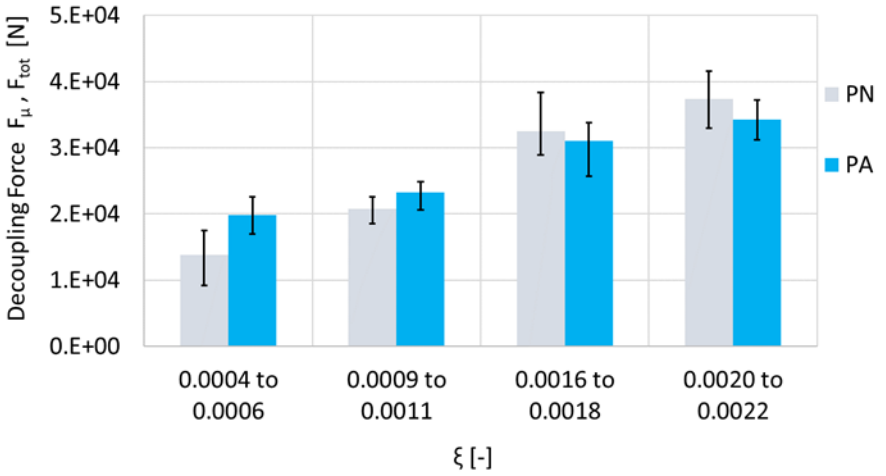

Figure 53: Axial release force for press-fitting without adhesive (PN) and press-fitting with adhesive (PA)

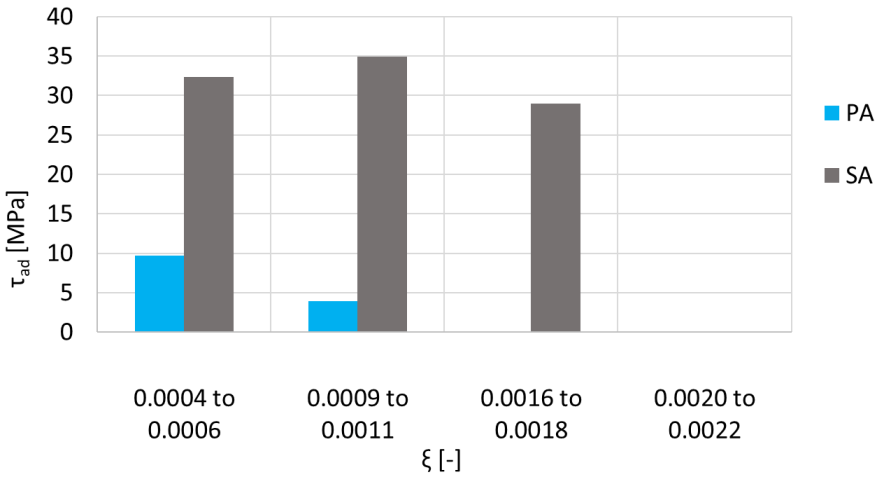

Figure 54: Adhesive shear strength in press-fitted (PA) and shrink-fitted (SA) couplings

The retrieved outcomes were also analyzed in the light of the observation of the samples after decoupling, with particular reference to the shafts. The mating surfaces were observed to check the adhesive presence and its failure mode. It can be remarked that a significant part of the adhesive is stripped away during the assembly in case of high interference. As exposed above, to carry out shrink-fitting, the hubs are pre-heated up to 250°C, in order to create a clearance at the interface with the shafts. However, the higher the interference level, the lower the clearance that can be generated. Despite the presence

of clearance, when it is very low, a large part of the adhesive is teared off, as it is clearly visible in Figure 55(d). On the other hand, at lower interference levels (Figure 55 (a, b, c)) the adhesive is not removed upon fitting: it provides a contribution against decoupling and the failure mode is cohesive.

It could be argued that, due to the remarkably high estimated friction coefficient, the amount of force attributed to interference could have been overestimated. As a consequence, for the same total decoupling force, its portion due to the adhesive should have been, on the other hand, underestimated. On the contrary, the retrieved values for the adhesive shear strength are absolutely consistent or even higher than those in the datasheet of the tested adhesive and those retrieved in the preliminary campaign on pin-and-collars. This outcome can be easily observed, considering the strength results for the shrink-fitted samples (SA), for which the highest values of friction were determined (Figure 50). The retrieved remarkably high values of adhesive shear strength, following shrink fitting, can be regarded as a further proof for the adhesive properties being left unchanged by heating.

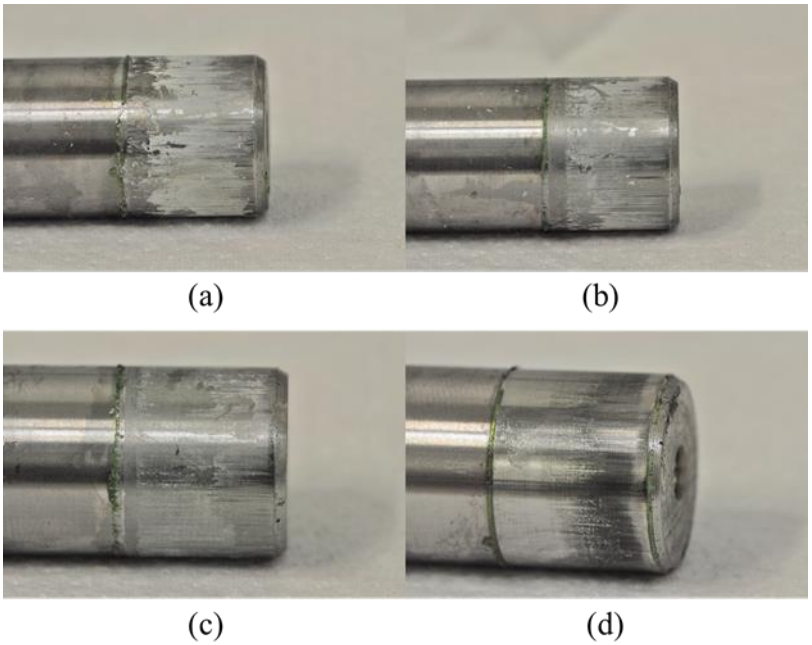

Figure 55: : Shrink-fitted adhesively bonded shafts after the axial release test, coupled: (a) ξ = 0.0005; (b) ξ = 0.0010; (c) ξ = 0.0017; (d) ξ = 0.0022.

2.6 Loctite 648 shear strength at high temperature.

Among the parameters listed in the chapter 2.1, the degradation as an effect of temperature is very important. For anaerobic adhesives, such as LOCTITE 648, the shear strength may be sharply decreased, as temperature is increased from 25°C to 100°C [2.8]. Specific studies dealing with the response under high temperature and involving practical applications in hybrid joints are missing in the literature. The angular gearbox, which motivated this study, can operate up to 100°C. Therefore, with the aim of simulating the actual working conditions, push-out tests were performed. To compare the results to those at room temperature, the same interference level above and both the assembly process press fit and shrink fit were considered Table 17. Experimental data and results are listed in Table 18 for press fitted samples and Table 19 for shrink fitted one.

Table 17: Two factor experimental plan involving axial release tests at high temperature

Factor n. 1	**Joining Technique**			
Levels	**PA** (Press fitted, with adhesive)		**SA** (Shrink fitted, with adhesive)	
Factor n. 2	**Specific Interference ξ**			
Levels	$4 \bullet 10^{-4}$ to $6 \bullet 10^{-4}$	$9 \bullet 10^{-4}$ to $1.1 \bullet 10^{-3}$	$1.6 \bullet 10^{-3}$ to $1.8 \bullet 10^{-3}$	$2 \bullet 10^{-3}$ to $2.2 \bullet 10^{-3}$

The retrieved decoupling forces F_{tot} for the press-fitted samples are collected in the bar graph in Figure 56. The "PA_100°C" set refers to high temperature push-out tests: for comparison purpose they were plotted together the "PA" bars, which deal with the decoupling tests at room temperature, and the "PN" set that refers to joints without adhesive decoupled at room temperature. With respect to the room temperature condition, the mean force is reduced by 26% at 100°C. The release force under high temperature is comparable to that in dry condition at lower interference, which is supportive for poor adhesive effect in this condition. However, a quite surprising outcome is that it becomes even lower at the other levels corresponding to greater interference.

Table 18: Experimental results: push-out tests at 100°C for press-fitted specimens

Shaft ID	*d_s [mm]*	*Hub ID*	*d_h [mm]*	*Hub Roughness [µm]*	*U_d [mm]*	*Z_d [mm]*	*ξ[-]*	*Decoupling Force F_μ[N]*
S1-01	16.996	H-161	16.960	0.310	0.036	0.034	0.0020	30,560
S1-03	16.996	H-165	16.960	0.929	0.036	0.032	0.0019	27,760
S1-04	16.996	H-177	16.960	0.555	0.036	0.034	0.0020	25,190
S1-15	16.996	H-188	16.960	0.444	0.036	0.034	0.0020	24,900
S1-19	16.996	H-199	16.960	0.423	0.036	0.034	0.0020	29,000
S1-68	16.994	H-170	16.964	0.629	0.030	0.027	0.0016	28,040
S1-76	16.994	H-200	16.964	0.464	0.030	0.028	0.0016	23,890
S1-77	16.994	H-214	16.964	0.336	0.030	0.028	0.0017	21,000
S1-02	16.993	H-33	16.963	0.562	0.030	0.028	0.0016	22,440
S1-26	16.993	H-43	16.963	0.643	0.030	0.027	0.0016	24,540
S1-149	16.986	H-40	16.968	0.448	0.018	0.016	0.0009	16,680
S1-157	16.986	H-64	16.968	0.420	0.018	0.016	0.0009	13,130
S1-161	16.986	H-80	16.968	0.417	0.018	0.016	0.0009	19,560
S1-85	16.985	H-01	16.967	0.505	0.018	0.016	0.0009	14,740
S1-90	16.985	H-19	16.967	0.478	0.018	0.016	0.0009	15,270
S1-96	16.983	H-78	16.975	0.563	0.008	0.006	0.0003	12,140
S1-97	16.983	H-18	16.974	0.427	0.009	0.007	0.0004	13,950
S1-100	16.983	H-21	16.974	0.505	0.009	0.007	0.0004	15,230
S1-110	16.983	H-47	16.974	0.515	0.009	0.007	0.0004	14,720
S1-128	16.983	H-72	16.974	0.532	0.009	0.007	0.0004	13,520

Table 19: Experimental results: push-out tests at 100°C for shrink-fitted specimens

Shaft ID	*d_s [mm]*	*Hub ID*	*d_h [mm]*	*Hub Roughness [μm]*	*U_d [mm]*	*Z_d [mm]*	*ξ[-]*	*Decoupling Force F_μ [N]*
S1-09	16.998	H-79	16.962	0.682	0.036	0.036	0.0021	46,430
S1-16	16.998	H-99	16.962	0.518	0.036	0.036	0.0021	31,680
S1-27	16.998	H-100	16.962	0.656	0.036	0.036	0.0021	36,040
S1-28	16.998	H-103	16.962	0.505	0.036	0.036	0.0021	35,090
S1-34	16.998	H-109	16.962	0.443	0.036	0.036	0.0021	30,070
S1-33	16.995	H-08	16.965	0.341	0.030	0.030	0.0018	30,590
S1-37	16.995	H-10	16.965	0.476	0.030	0.030	0.0018	30,440
S1-38	16.995	H-44	16.965	0.434	0.030	0.030	0.0018	28,040
S1-44	16.995	H-48	16.965	0.639	0.030	0.030	0.0018	47,120
S1-48	16.995	H-52	16.965	0.746	0.030	0.030	0.0018	42,680
S1-82	16.987	H-23	16.970	0.335	0.017	0.017	0.0010	43,470
S1-89	16.987	H-29	16.970	0.421	0.017	0.017	0.0010	32,060
S1-93	16.987	H-09	16.969	0.262	0.018	0.018	0.0011	33,870
S1-105	16.987	H-11	16.969	0.522	0.018	0.018	0.0011	42,040
S1-113	16.987	H-34	16.969	0.481	0.018	0.018	0.0011	45,080
S1-108	16.984	H-55	16.979	0.501	0.005	0.005	0.0003	35,710
S1-114	16.984	H-61	16.979	0.413	0.005	0.005	0.0003	32,650
S1-120	16.984	H-65	16.979	0.731	0.005	0.005	0.0003	31,170
S1-121	16.984	H-69	16.978	0.697	0.006	0.006	0.0004	29,440
S1-125	16.984	H-215	16.978	0.544	0.006	0.006	0.0004	34,780

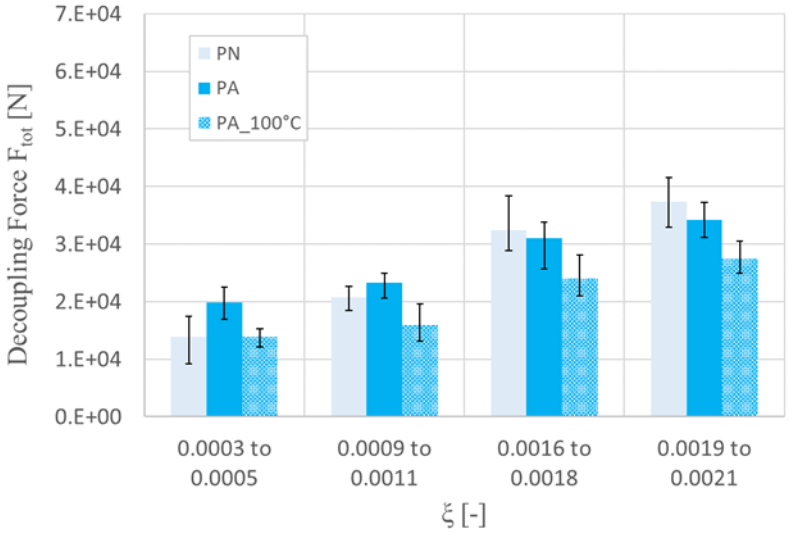

Figure 56: Decoupling force for press-fitted specimens. PN: dry coupled and decoupled at room temperature; PA: coupled with adhesive and decoupled at room temperature; PA_100°C coupled with adhesive and decoupled at 100°C.

It must be argued the temperature of the performed test is very close to the glass transition temperature, which is the threshold, beyond which the adhesive turns to have a rubber-like behavior [2.17]. Another interesting point is that temperature not only affects the adhesive performance, but also the interference-related contribution. This remark stems from the release force (with adhesive) under high temperature being lower than the release force in dry conditions at room temperature. This outcome is presumably due to friction coefficient decrease. This phenomenon has been investigated in the scientific literature, mainly in studies dealing with tribology and wear. As reported in [2.18 - 2.19], the friction coefficient drops down monotonically, as temperature increases, in particular in the range from 20 to 150°C. Therefore, the combined effect of the adhesive degradation and the reduction of the friction coefficient justifies, from the qualitative point of view, the occurrence detailed above.

To compute the adhesive shear strength, the effect of temperature on the friction coefficient was accounted, reducing by 24% the values of μ_{II} obtained in Figure 50 at room temperature. This reduction was applied, according to the aforementioned references [2.18 - 2.19] that deal with similar materials and with friction over the same temperature range (20 to 100 °C). The outcomes in terms of adhesive shear strengths are shown in Figure 57. Due to the temperature increment, the shear strength strongly decreases: its contribution is appreciable only in the first interference level.

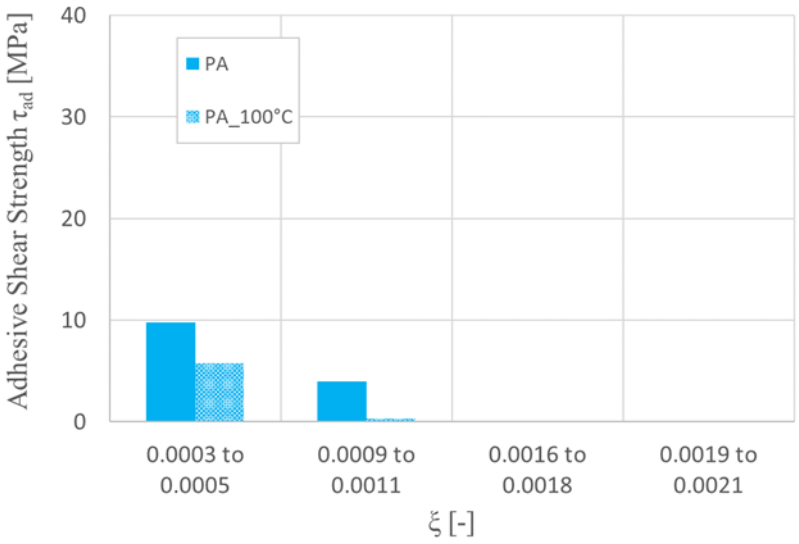

Figure 57: Adhesive shear strength (average values) for press-fitted samples tested at room temperature (PA) and at 100°C (PA_100°C)

The same comparisons for shrink-fitted samples are plotted in Figure 58. When comparing decoupling results at room temperature (SA series) to that at 100°C (SA_100 series), a mean reduction by 28% affecting the decoupling force was observed. Unlike for press-fitted couplings, the adhesive contribution on the joint performance keeps significant even for higher interference levels under shrink-fitting. However, the adhesive contribution vanishes at the highest interference level, as the amount of adhesive that remains trapped in the joint drops down due to the too small available clearance despite hub heating. The release force is higher for shrink-fitted couplings than for press-fitted ones, regardless of the presence of the adhesive. As mentioned in the previous chapter, the reason is that, under shrink-fitting, the crests of the roughness do not flatten during assembly. The adhesive shear strength for shrink fitted specimens is shown in Figure 59. Due to the temperature increment, the adhesive strength decreases of 28% up to $\xi = 0.0011$. This drop is quite reasonable, as in the same order of that reported in the datasheet regarding the plain properties of the adhesive. Under higher interference levels, the percentage drop increases sharply. However, the data regarding shear strength at increased interference are not reliable: as highlighted above, they indicate most adhesive is teared off upon coupling due to the high contact pressure. At the highest interference level, the adhesive contribution drops down to zero.

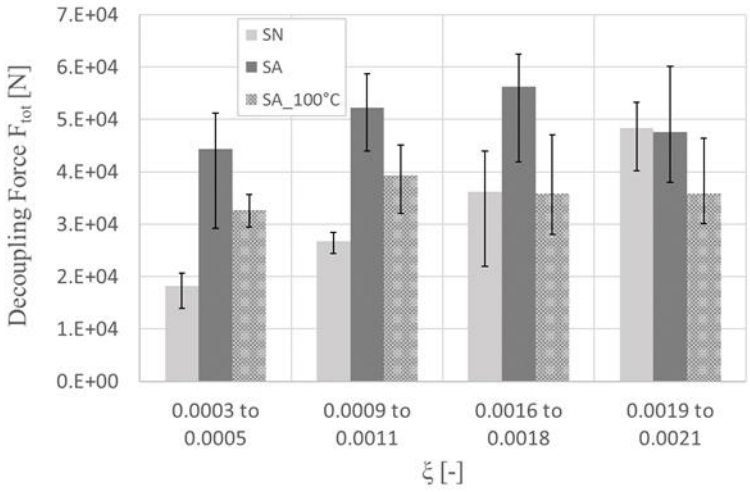

Figure 58: Decoupling force for shrink-fitted specimens. SN: dry coupled and decoupled at room temperature; SA: coupled with adhesive and decoupled at room temperature; SA_100°C: coupled with adhesive and decoupled at 100°C.

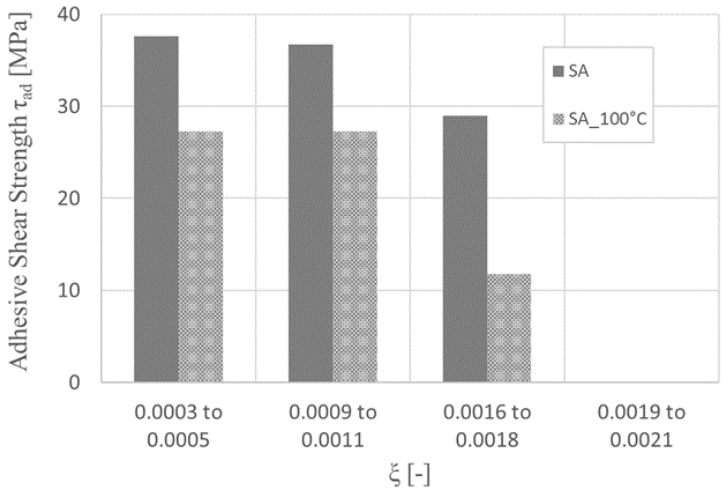

Figure 59: Adhesive shear strength (average values) for shrink-fitted samples tested at room temperature (SA) and at 100°C (SA_100°C)

2.7 The effect of the shaft geometry on the joint strength.

As reported in 2.1.3, in order to enhance the hybrid joint performance, some solutions can be considered. Two main approaches are discussed in the literature: a first one could be to increase the roughness of the coupled surfaces, for example by a sanding treatment [2.4; - 2.20 – 2.21]. Otherwise, hoop channels may be machined on the shaft, so that they can act as adhesive pockets. In this study, this second approach was considered. The reason is that the shaft used for the angular gearbox derives from a tempered steel bars worked out on a lathe. Cutting some hoop channels is an operation that does not involve a high increase in costs and time on the overall manufacturing cycle. Whereas performing superficial treatment as sandblasting adds an extra step to the production cycle. Machining hoop channels on the shaft makes it possible to create a portion of clearance needed for entrapping the adhesive. The hoop channels work as an adhesively bonded slip-fit joint, whereas the remaining portion of the joint acts as a conventional interference-fitted one. The samples geometry is the same reported in Figure 39b and Figure 39d. The coupling strategy was also investigated, accounting for both press-fitted and shrink-fitted joints. About the input data, it is highlight that the coupling length in which the interference acts its effects is reduced of the hoop channel width (11 mm instead of 13 mm), whereas the area wetted by the adhesive is unchanged. A difference with respect to previous experiments is that the analysis was focused on the highest interference levels, which are the most detrimentally affected by the occurrence of adhesive stripping. Therefore, three interference levels were considered instead of four: the two highest levels were kept barely unchanged with respect to those of the previous campaign. The third one can be regarded as intermediate between the two previously considered lowest levels. The overall plan, including, for comparison purposes, the results for smooth shafts with and without the adhesive, is provided in Table 20.

The decoupling tests were carried out at room temperature. The experimental data and the measured decoupling forces are listed in Table 21 and Table 22.

Table 20: Experimental plan regarding hoop channel effect

		Press Fitted			Shrink Fitted		
		Dry	Adhesive smooth	Adhesive Hoop c.	Dry	Adhesive smooth	Adhesive Hoop c.
Interference level	Low $6 \cdot 10^{-4} \leq \xi \leq 9 \cdot 10^{-4}$						
	Medium $1.5 \cdot 10^{-3} \leq \xi \leq 1.6 \cdot 10^{-3}$						
	High $2 \cdot 10^{-3} \leq \xi \leq 2.2 \cdot 10^{-3}$						

Table 21: Experimental results: push-out tests at room temperature. Press-fitted shafts with hoop channels

Shaft ID	*d_s [mm]*	*Hub ID*	*d_h [mm]*	*Hub Roughness [µm]*	*U_d [mm]*	*Z_d [mm]*	*ξ[-]*	*Decoupling Force F_μ[N]*
S3-28	16.993	H-153	16.957	0.497	0.036	0.034	0.0020	39,050
S3-29	16.993	H-175	16.957	0.491	0.036	0.034	0.0020	43,690
S3-33	16.993	H-176	16.957	0.513	0.036	0.034	0.0020	44,530
S3-40	16.993	H-202	16.957	0.515	0.036	0.034	0.0020	43,970
S3-45	16.993	H-222	16.957	0.384	0.036	0.034	0.0020	39,290
S3-20	16.987	H-113	16.958	0.345	0.029	0.027	0.0016	36,880
S3-21	16.987	H-114	16.958	0.389	0.029	0.027	0.0016	40,540
S3-22	16.987	H-122	16.958	0.517	0.029	0.027	0.0016	41,390
S3-01	16.986	H-124	16.958	0.359	0.028	0.026	0.0015	38,360
S3-03	16.986	H-152	16.958	0.332	0.028	0.026	0.0015	39,150
S3-16	16.983	H-07	16.971	0.465	0.012	0.010	0.0006	23,820
S3-23	16.983	H-67	16.971	0.478	0.012	0.010	0.0006	20,650
S3-43	16.997	H-227	16.981	0.458	0.016	0.014	0.0008	29,460
S3-44	16.997	H-194	16.982	0.474	0.015	0.013	0.0008	27,920
S3-53	16.999	H-225	16.986	0.332	0.013	0.011	0.0007	22,280

Table 22: Experimental results: push-out tests at room temperature. Shrink-fitted shafts with hoop channels

Shaft ID	*d_s [mm]*	*Hub ID*	*d_h [mm]*	*Hub Roughness [μm]*	*U_d [mm]*	*Z_d [mm]*	*ξ[-]*	*Decoupling Force F_μ [N]*
S3-27	16.994	H-164	16.956	0.587	0.038	0.038	0.0022	41,000
S3-36	16.994	H-182	16.956	0.612	0.038	0.038	0.0022	40,380
S3-46	16.994	H-02	16.957	0.402	0.037	0.037	0.0022	50,320
S3-51	16.994	H-107	16.957	0.630	0.037	0.037	0.0022	41,710
S3-54	16.994	H-112	16.957	0.709	0.037	0.037	0.0022	35,640
S3-06	16.987	H-04	16.962	0.367	0.025	0.025	0.0015	45,440
S3-09	16.987	H-139	16.962	0.467	0.025	0.025	0.0015	48,550
S3-11	16.987	H-156	16.962	0.605	0.025	0.025	0.0015	46,210
S3-17	16.987	H-115	16.962	0.641	0.025	0.025	0.0015	45,270
S3-18	16.987	H-119	16.962	0.414	0.025	0.025	0.0015	44,180
S3-10	16.985	H-17	16.971	0.605	0.014	0.014	0.0008	38,450
S3-12	16.985	H-68	16.969	0.370	0.016	0.016	0.0009	42,210
S3-14	16.985	H-42	16.970	0.497	0.015	0.015	0.0009	42,280
S3-19	16.985	H-50	16.970	0.541	0.015	0.015	0.0009	44,570
S3-26	16.985	H-51	16.970	0.498	0.015	0.015	0.0009	44,030

Regarding press-fitted and adhesively bonded samples, the decoupling forces obtained for specimens with hoop channels (PA_HC set) are compared to those for samples with smooth geometry (PA set) in Figure 60. The results for smooth specimens without adhesive (dry) are appended as well (PN set).

The improved geometry leads to much higher decoupling forces. The results were also processed by the tool of analysis of variance that confirmed for medium and high interference levels the improvement yielded by the hoop channel geometry is highly significant with respect to the coupling with adhesive and smooth geometry. Conversely, at lower interference level, the resistance increment provided by the hoop channels does not reach the significance threshold. In this case, a smooth geometry is still efficient at trapping a sufficient amount of adhesive. These outcomes may be qualitatively explained, observing that cutting hoop channels implies a decrease of the contact area (engagement length for friction) between the shaft and the hub, thus decreasing the interference contribution to the overall performance of the joint. However, this improved geometry compensates with a double positive effect. First, the hoop channels act as a supply reservoir for the adhesive: the hub, during its coupling with the shaft, drags the exceeding adhesive and spreads it slightly on the shaft, thus covering its entire coupling length. Secondly, the adhesive filling the hoop channels provides an additional contribution,

being proportional to the adhesive shear strength and to the area of the grooves, like for a slip-fit joint.

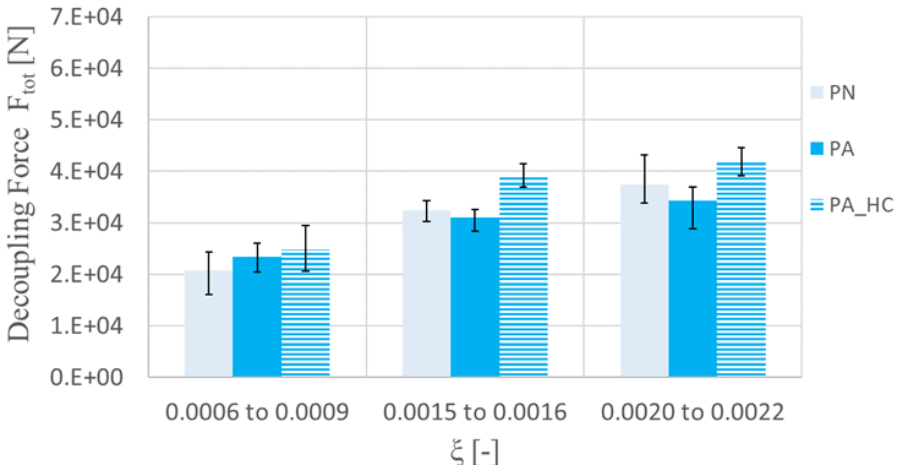

Figure 60: Decoupling force for press-fitted specimens. PN: dry coupled with smooth geometry; PA: coupled with adhesive with smooth geometry; PA_HC: coupled with adhesive with hoop channels.

The images in Figure 61 show two press-fitted and adhesively bonded smooth shafts at medium (Figure 61 (a)) and high (Figure 61 (b)) interference. These are compared to press-fitted and adhesively bonded shafts with hoop channels for the same interference levels (Figure 61 (c) and Figure 61 (d)). It can be remarked the coupling surfaces in case of hoop channels appear to be less scratched. In addition, areas with polymerized adhesive are slightly visible even far away from the hoop channels. Conversely, the surface of smooth shafts is badly damaged and no traces of adhesive can be observed.

The shear strength has been determined, according to the aforementioned model, based on the principle of the superposition of the effects.

Note that in case of hoop channels, the adhesive contribution and the interference contribution operate on two different areas: the first one is proportional to the coupling surface as in smooth shaft geometry (A), whereas the second one is proportional to the coupling surface for hoop-channeled geometry (A_h). Eq. 2.3 must be rewritten as:

$$\boldsymbol{F_{int} = \mu_{ll} \cdot p_c \cdot A_h}$$

Eq. 2.13

This processing has led to the results collected in Figure 62, where the beneficial contribution by the hoop channels is clearly visible. On one hand, for smooth shafts, the adhesive shear strength tends to zero at the two top levels of the specific interference range for this campaign, indicating the adhesive is completely teared off upon coupling, whereas a small amount is retained at the low level. On the other hand, when hoop

channels are present, the shear strength reaches values between 15 and 20 MPa, even at the highest interference level. The retrieved values are a bit lower than the typical strength (which should be at least 25 MPa) for the investigated adhesive (according to its datasheet) but confirm that, thanks to the hoop channels, the adhesive can work properly and provide a relevant contribution to the joint response. However, their collocation under the typical range may indicate that a small amount of adhesive is still stripped away during coupling.

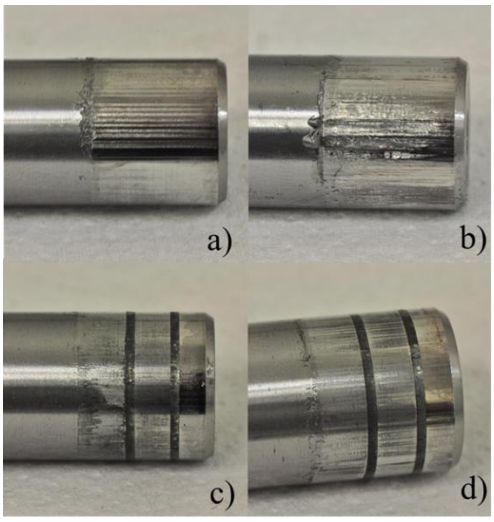

Figure 61: Press-fitted shafts. a) PA set, medium interference. b) PA set, high interference. c) PA_HC set, medium interference. d) PA_HC set, high interference.

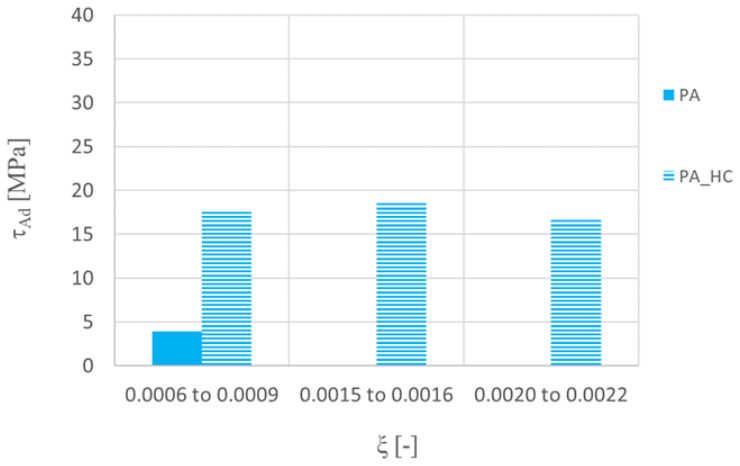

Figure 62: Adhesive shear strength (average values) for press-fitted specimens: smooth geometry (PA) vs. hoop channels (PA_HC)

The advantages introduced by the hoop channel geometry are not found in the case of shrink-fit couplings (Figure 63). The results indicate the joint resistance is even decreased by the new geometry. The same statistical tools described above (two-way ANOVA and F-test) indicate the decoupling force drop is not significant for the highest interference level, whereas it turns to be relevant for the medium and low ones. This occurrence may

be explained, considering that a higher interference contribution is normally present under shrink-fitting, as roughness crests are not flattened. Moreover, upon coupling, a much higher amount of adhesive is retained as an effect of hub expansion. Consequently, when hoop channels are present, the aforementioned effect concerning the decrease of the nominal mating area for friction prevails on the other beneficial ones. It is worth mentioning the decoupling force is always lower than that retrieved for smooth shafts. From the quantitative point of view, it can be observed that the force decrease is aligned with the percentage drop (15%) of the available length for interference, following hoop channel machining.

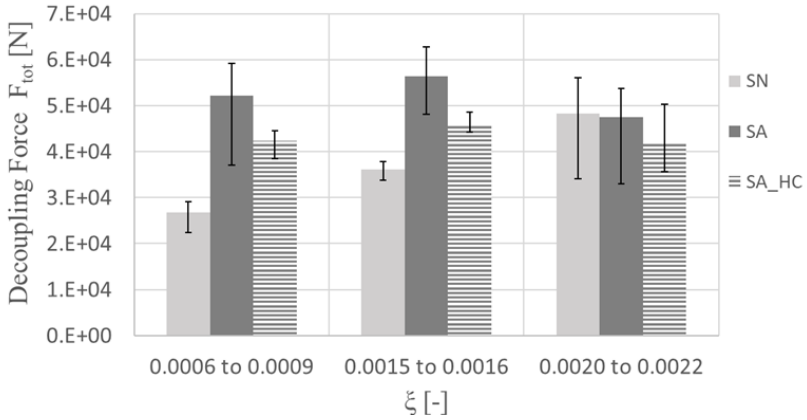

Figure 63: Decoupling force for shrink-fitted specimens. SN: dry coupled with smooth geometry; SA: coupled with adhesive with smooth geometry; SA_HC: coupled with adhesive with hoop channels

The same analysis has been run, to work out the adhesive shear strength for shrink-fitted couplings. The results displayed in Figure 64 indicate the adhesive works properly at low and medium specific interference levels: in this case, the retrieved strengths are independent of geometry (smooth vs channeled geometry) and well aligned with the typical properties of the adhesive. Smooth geometry is in this case sufficient to retain the adhesive, thanks to hub heating, and, therefore, hoop channels do not add any beneficial contribution. This is a further proof it is the reduction of the interference-related term to be responsible for overall joint resistance worsening.

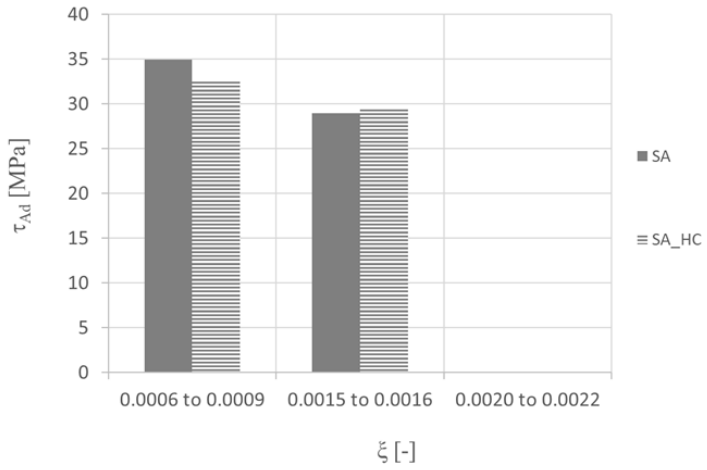

Figure 64: Adhesive shear strength (average values) for shrink-fitted specimens: smooth geometry (SA) vs. hoop channels (SA_HC)

2.8 Checks for completeness of the experiment.

To complete the study, the results of a further investigations are reported. The investigated coupling regards a real coupling between a shaft and a bevel gear on an angular gearbox. To ensure high wear resistance, the bevel gear is made of 16CrNi4Pb hardened steel. To couple by shrink fitting, the gear has to be heated up to 250°C by the heated plate that is shown in Figure 44 . In the assembly chain, about thirty shafts were heated at the same time. It is possible that between the first gear that is placed on the plate and the last one that is picked up, an elapsed time of 30 minutes could be estimated. Keeping the gear at 250°C for a long time is like applying a soft stress relief to the material, thus decreasing the hardness of the gear and worsening its wear resistance. Following this concern, to verify that the mechanical properties were maintained unchanged after this thermal cycle, Vickers hardness tests were performed on six bevel gears before and after a heat at 250°C for 30 minutes. An example of Vickers marks is shown in Figure 65. As it possible to observe, the diagonal dimensions are about the same before or after the heating. In Table 23 all the hardness measure are listed. The average value after the heating is slightly smaller than before the treatment, but it is aligned with what the specifications of the bevel gearbox.

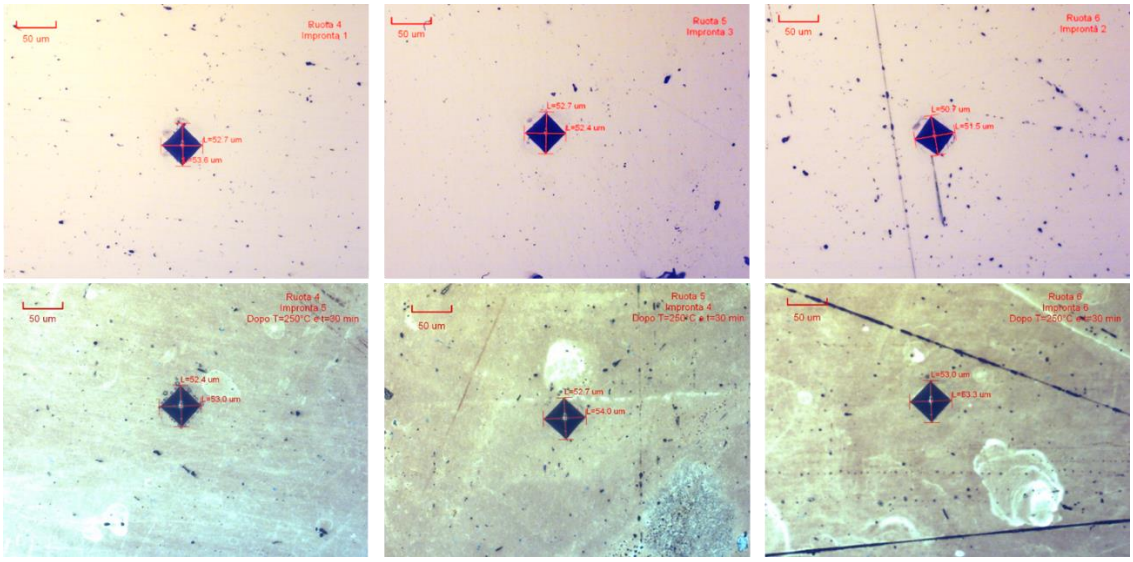

Figure 65: Vickers hardness test on three bevel gears. Top row before the heating, bottom row after heating

Table 23: Vickers hardness measurements

		Gear 1	Gear 2	Gear 3	Gear 4	Gear 5	Gear 6
T=20°	Mark 1	732	736	678	657	652	678
	Mark 2	713	709	706	677	715	710
	Mark 3	710	727	716	664	672	704
	Average $HV_{1/15}$	718	724	700	666	680	697
	Average HRC	61.0	61.0	60.1	58.6	59.2	60.0
	Total Average	**60.0**					
T=250° t=30 min	Mark 4	662	673	672	660	652	710
	Mark 5	668	686	672	668	672	668
	Mark 6	672	677	648	668	679	657
	Average $HV_{1/15}$	667	679	664	665	668	678
	Average HRC	58.6	59.2	58.5	58.6	58.7	59.1
	Total Average	**58.8**					

To conclude, a further analysis was run, to evaluate the radial displacement of the gear due to the coupling interference. The assembly precision between gears is very important to ensure a high transmission efficiency and to contain the operation noise of the angular gear box. A FEM analysis was performed by applying the maximum theoretical coupling pressure. The maximum coupling pressure can be achieved if the shaft has a diameter corresponding to its maximum tolerance dimension and the internal diameter hub is equal to the minimum value. The radial displacement calculated at the smallest outside diameter was approximatively 0.01 mm, as in Figure 66, which is not enough to alter the correct operation of the angular gearbox.

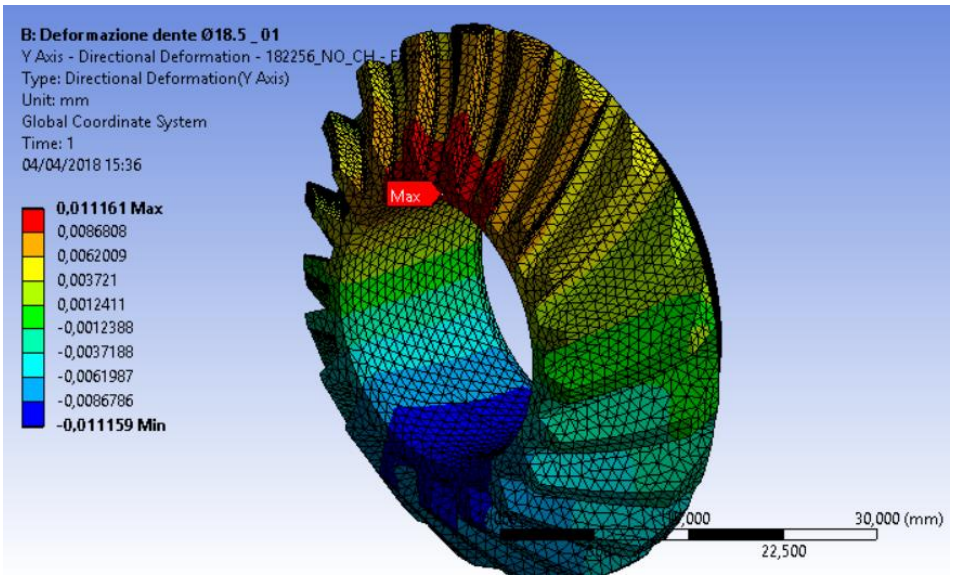

Figure 66: Bevel gear directional displacement under the maximum coupling pressure

2.9 Conclusions

This chapter provides some design-oriented data for shaft-hub hybrid joints.

The friction coefficient and its trend with respect to specific interference was assessed for both press-fit and shrink-fit coupling process. Results indicate that the first separation friction coefficient is strongly affected by the level of specific interference. In particular, the higher interference, the lower friction for the three studied assembly strategies without the adhesive: dry press-fitting, dry shrink-fitting and press-fitting with not cured adhesive. The presence of the adhesive (Loctite 648) during assembly undoubtedly leads to less damage on the mating surfaces, but does not significantly affect the value of the friction coefficient.

The greatest contribution of the adhesive was retrieved with shrink-fitted couplings, where the induced clearance during the assembly was able to avoid adhesive stripping. As the specific interference increases, and consequently the available clearance upon coupling (following hub swelling) decreases, the contribution of the adhesive drops down to zero. In press fitted couplings the trend is the same, but the contribution of the adhesive becomes negligible for lower interference level than in shrink fitted coupling.

Tests at high temperature (100°C) lead to a release force reduction by 26% in press-fitted samples and by 28% in shrink-fitted ones. It was observed that high temperature is critical in hybrid joints, as it detrimentally affects not only the adhesive strength, but also the friction coefficient, which decreases as temperature increases. The combined effect leads to an axial release force that is even lower than that achievable without adhesive at room temperature.

A possible shaft design with two hoop channels in the bonding area was evaluated with the aim of improving the joint strength. The results indicate that, for press-fitted joints, even at high interference, hoop channels act as adhesive reservoir and facilitate adhesive dragging over the entire coupling length. This beneficial effect is highly significant and prevails on the reduction of the available mating area for interference fitting. Conversely, for shrink-fitted joints, for which the occurrence of adhesive stripping is more reduced, cutting hoop channels does not enhance the adhesive performance. In addition, it entails a lower engagement length for interference, which implies a significant reduction of the interference-related contribution with respect to smooth geometry.

2.10 References

[2.1] Petrie E. M, Handbook of adhesives and sealants, McGraw-Hill Handbooks, Second Edition (2015).

[2.2] Romanos G. Strength evaluation of axisymmetric bonded joints using anaerobic adhesives. Int. J Mater Prod Technol 1999;14:430–43.

[2.3] Sekercioglu T, Gulsoz A, Rende H. The effects of bonding clearance and interference fit on the strength of adhesively bonded cylindrical components. Materials and Design 2005;26:377–381.

[2.4] Sekercioglu T, Gulsoz A, Rende H, Meran C. The effects of surface roughness on the strength of adhesively bonded cylindrical components. Journal of Materials Processing Technology 2003;142:82–86.

[2.5] da Silva LFM, Ferreira N.M.A.J, Richter-Trummer V, Marques E.A.S. Effect of grooves on the strength of adhesively bonded joints. International Journal of Adhesion & Adhesives 2010;30:735-743.

[2.6] Dario Croccolo, Massimiliano De Agostinis, Nicolò Vincenzi. Design of hybrid steel-composite interference fitted and adhesively bonded connections. International Journal of Adhesion & Adhesives 37 (2012) 19–25

[2.7] Mengel R, Haberle J, Schlimmer M. Mechanical properties of hub/shaft joints adhesively bonded and cured under hydrostatic pressure. International Journal of Adhesion & Adhesives 2007;27:568–573.

[2.8] Loctite 648 datasheet

[2.9] Croccolo, D., De Agostinis, M., Fini, S., & Olmi, G. (2016). Influence of the engagement ratio on the shear strength of an epoxy adhesive by push-out tests on pin-and-collar joints: Part II: Campaign at different temperature levels. International Journal of Adhesion and Adhesives, 67, 76-85. doi:10.1016/j.ijadhadh.2015.12.029.

[2.10] Adams RD, Coppendale J, Mallick V, Al-Hamdan H. The effect of temperature on the strength of adhesive joints .Int J Adhes Adhes1992;12:185–90.

[2.11] Dragoni, E.; Mauri, P. Intrinsic static strength of friction interfaces augmented with anaerobic adhesives. Int. J. Adhes. Adhes. 2000, 20, 315–321.

[2.12] Dragoni, E.; Mauri, P. Cumulative static strength of tightened joints bonded with anaerobic adhesives. Proceedings of the Institution of Mechanical Engineers, Part L: Journal of Materials Design and Applications. 2002, 216 (9).

[2.13] Yang, GM.; Coquille, JC.; Fontaine, JF.; Lambertin, M. Influence of roughness on characteristics of tight interference fit of a shaft and a hub. Int J Solids Struct 2001,38, 7691–701

[2.14] Niemann, G.; Winter, H.; Hohn, B. Maschinenelemente: band 1: Konstruktion und Berechnung von Verbindungen, Lagern, Wellen. Germany: Springer-Verlag, Berlin, 2005

[2.15] Sogalad, I.; Udupa, N. G. S. Load bearing ability of interference-fitted assemblies: a roundness profile analysis. P. I. Mech. Eng. C-J. Mec. 2009, 223 (7), 1623–1632

[2.16] Castagnetti, D.; Dragoni, E. Optimal aspect ratio of interference fits for maximum load transfer capacity. J. Strain Anal. Eng. 2005, 40 (2), 177–184.

[2.17] Carbas, R. J. C., Marques, E. A. S., Da Silva, L. F. M., & Lopes, A. M. (2014). Effect of cure temperature on the glass transition temperature and mechanical properties of epoxy adhesives. Journal of Adhesion, 90(1), 104-119. doi:10.1080/00218464.2013.779559.

[2.18] Pearson, S. R., Shipway, P. H., Abere, J. O., & Hewitt, R. A. A. (2013). The effect of temperature on wear and friction of a high strength steel in fretting. Wear, 303(1-2), 622-631. doi:10.1016/j.wear.2013.03.048.

[2.19] Kayaba, T., & Iwabuchi, A. (1981). The fretting wear of 0.45% C steel and austenitic stainless steel from 20 to 650 °C in air. Wear, 74(2), 229-245. doi:10.1016/0043-1648(81)90165-4.

[2.20] Rudawska, A., Danczak, I., Müller, M., & Valasek, P. (2016). The effect of sandblasting on surface properties for adhesion. International Journal of Adhesion and Adhesives, 70, 176-190. doi:10.1016/j.ijadhadh.2016.06.010.

[2.21] Harris, A. F., & Beevers, A. (1999). Effects of grit-blasting on surface properties for adhesion. International Journal of Adhesion and Adhesives, 19(6), 445-452. doi:10.1016/S0143-7496(98)00061-X.

CHAPTER 3

FATIGUE RESPONSE OF ADDITIVELY PROCESSED METAL ALLOYS: ALSI10MG AND MARAGING STAINLESS STEEL CX

3.1 Introduction

The fatigue properties of two additively manufactured metal alloys, the aluminum AlSi10Mg and the stainless steel CX, which can be used for automotive applications, are analyzed in this chapter. Modern additive manufacturing (AM) processes make it possible to fabricate metal parts with very complex geometries, which are often difficult to obtain (as a monolithic component) by machining or through traditional subtractive processes. Furthermore, it is possible to optimize the components design for lightness purpose, obtaining parts with high strength/weight or stiffness/weight ratios. To manufacture prototypes or definitive components in not numerous batches, additive processes are often faster than conventional ones (and sometimes even cheaper). In fact, components can be directly built from a 3D model, thus reducing the time from conception to market. For the production of metal parts, the most commonly used additive manufacturing processes are based on the powder bed fusion technology (PBF). The model of the parts to be made is divided into many layers. A dispenser deposits a layer of powder on a building plate and an energy source (a laser or an electron beam) selectively fuses the corresponding cross section of the considered layer. Afterwards, the building plate moves by an amount corresponding to the height of the molten layer. Then, a further powder layer is spread again over the baseplate and the aforementioned steps are repeated until part completion. This particular production process may cause the presence of some defects inside the parts, such as porosity or voids.

Furthermore, the thermal cycle the components undergo is very complicated and is affected by many factors. Both the overall number of layers being needed to manufacture a part and the time for scanning a layer are highly dependent on part orientation on the baseplate [3.1 - 3.2]. For example, when fabricating a cylindrical sample lying on the baseplate, a reduced number of layers is needed, but laser scanning of each section takes a longer time than that for a vertically oriented specimen.

Even the number of components simultaneously manufactured on a base plate is likely to affect the final microstructure. For example, if ten identical parts, instead of one, are manufactured at the same time, the time between two subsequent depositions of powder

layers considerably increase. Consequently, the thermal cycle to which the ten parts are subjected is also modified with respect to the case of just one component being fabricated: therefore, the obtained microstructures could be different, also affecting the mechanical properties.

Another important issue concerns surface finishing and the presence of thermal residual stresses. Part made by PBF exhibit a very high surface roughness (even more than 20 μm). It is well known that a poor surface finishing and the presence of residual stresses detrimentally affect fatigue life [3.3 – 3.4 – 3.5 – 3.6].

A solution to the aforementioned problems is to carry out thermal and surface treatments that can improve the microstructure, relax tensile residual stress and enhance surface roughness.

The recent industrial expansion of AM technologies and the continuous development of alloys to be used in these processes are requiring further investigations on the mechanical properties and how process and post process parameters can improve the components strength. However, results in the literature, sometimes, are not enough to ensure an efficient design.

From the available alloys for AM processes, the aluminum AlSi10Mg and stainless steel CX are of particular interest in industrial field. In fact, they can be used to manufacture frame parts, such as motorbike swingarm, pistons or other engine components. The AlSi10Mg aluminum alloy is widely used to manufacture light weight parts with good mechanical performance. Its cast properties make it suitable for additive process and to fabricate thin components. The static properties of the AlSi10Mg, declared from the powder supplier (EOS GmbH [3.7]) are shown in Figure 67. Values were obtained for machined samples, in the as manufactured state (no heat treatment) for both vertically and horizontally oriented specimens. The differences, particularly in term of yield strength and elongation, are relevant. In fact, additively manufactured parts are often very sensitive to the build orientation, mostly if no heat treatment is performed after the process. In this case, the observed microstructure in not homogeneous, but it appears to be affected by the heating transfer. Figure 68 refers to the AlSi10Mg microstructure: for comparison purpose with the original experimental results to be presented in the following Section, these micrographies are taken from the EOS datasheet [3.7]. It is possible to see a non-uniform microstructure of the alloy (Figure 68a), which reflect in non-uniform mechanical properties: after T6 heat treatment the microstructure radically changes and no preferential direction can be observed (Figure 68b).

The build orientation is only one of the several parameters that can affect the mechanical properties.

Powder bed fusion process are characterized by several process parameters, which can alter the mechanical response of the manufactured parts. Laser power, energy density, hatch spacing, scan speed, scanning strategy, number of contour line and remelting are among the most mentioned factors and it is possible to find many results in the literature [3.3; 3.8 - 3.13]. However, since they are not taken into consideration in the present thesis, they will not be deepened further.

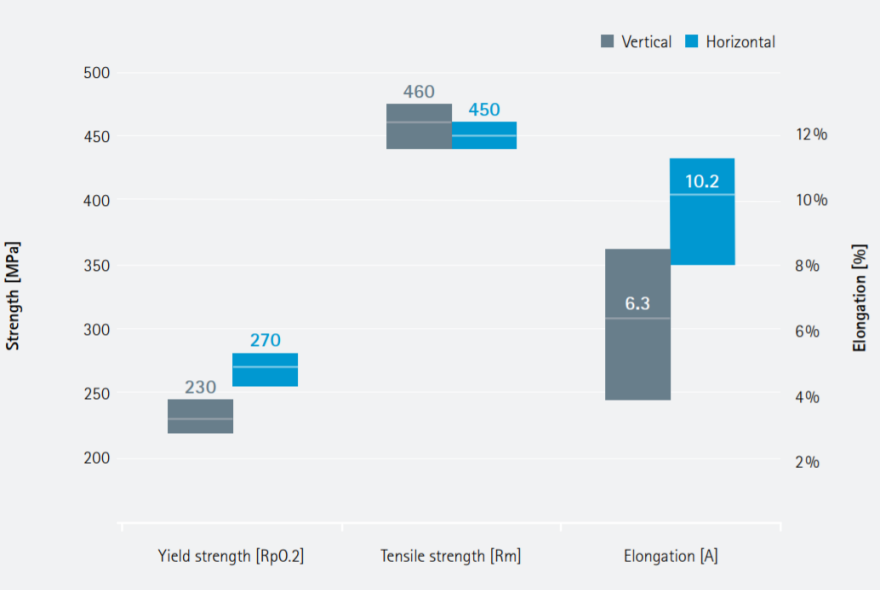

Figure 67: Static properties of AlSi10Mg, from EOS datasheet [3.7]

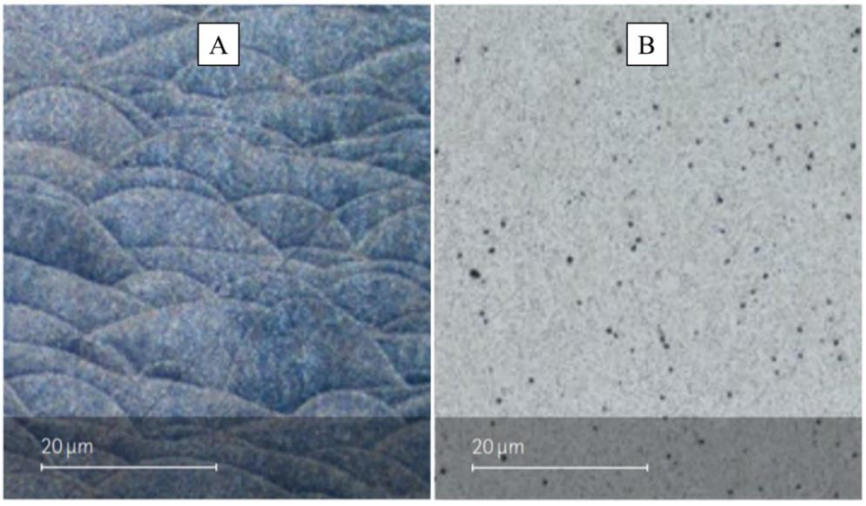

Figure 68: Microstructure of AlSi10Mg: a) not heat-treated state, b) after T6 heat treatment [3.7]

A frequently recommended heat treatment for Al-Si-Mg alloys is the T6 heat treatment consisting of solution annealing, quenching and subsequent natural or artificial aging. The solution annealing is conducted to dissolve soluble phases containing Mg or other trace

elements, homogenize the composition and spheroidize the Si phase. Quenching keeps the solution phase at a high temperature. After aging, a uniform distribution of precipitates is obtained. Solution anneal temperature varies between 515 °C and 530 °C. Temperature must be kept constant for 30 minutes. Then, rapid quenching in water has to be applied [3.14]. Aging can be undertaken at room temperature (natural aging), or between 150°C and 210°C (artificial aging). EOS suggests an artificial aging at 165°C for 6 hours [3.7]. Insights into this treatment can be found in [3.15 - 3.16].

Another typical heat treatment for aluminum alloys is the stress relief (SR), which consists in a heating at about 250°C for two hours and a cooling in an open furnace to room temperature. In general, the variation affecting the microstructure and the mechanical properties along the build orientation, which can be observed in as built samples, is reduced by applying stress relief [3.17].

Hot isostatic pressing (HIP) is a thermo-mechanical process that allows internal porosity reduction. For this reason, it is of particularly effective on PBF parts. However, in case of aluminum components, the thermal cycle induced during the process detrimentally modifies the microstructure. Due to the induced microstructural changes, a significant decrease for the yield and tensile strengths [3.18] is observed after HIP treatment for AlSi10Mg parts.

Despite the high number of papers and the high industrial interest, a lack of data, with particular regard to fatigue properties, also in relation with the combined effect of build orientation and heat treatment, was observed in the scientific literature. Therefore, the AlSi10Mg alloy was considered in this research with the aim of assessing the fatigue strength and how the main process (build orientation) and post process (heat and surface treatment) parameters can alter the fatigue response.

The stainless steel CX can be regarded as a recently introduced Maraging stainless steel featuring a low carbon content and a high amount of chromium. These characteristics lead to interesting properties such as remarkable corrosion resistance, high hardness and high ultimate tensile strength. It is a valid candidate for injection molding tools even in harsh environments [3.19 - 3.20] and also for shipbuilding, constructions in oil and gas field, offshore technologies, nuclear power plants [3.21]. The graphic bars in Figure 69 highlight the excellent static properties [3.22]. The figure refers to the heat treatment condition and, as can be expected in this condition, the differences between the two considered build orientation are minimal.

Only a heat treatment is found in the literature and it consist of two phases: the first one is a solution annealing at 850-900°C for 30-45 minutes followed by a rapid air cooling, with a cooling rate between 20 and 60 °C/min, to room temperature (below 32°C). The second one is an ageing for 2 hours at 525°C, which makes it possible to achieve the maximum hardness and strength (higher temperature are allowed, but lead to lower hardness and strength).

The few papers dealing with Stainless steel CX in the scientific literature are focused on microstructural properties, hardness and micro-hardness features and only static response [3.23]. Studies on other additively manufactured parts highlights that the stacking process may lead to a lower fatigue strength with respect to corresponding wrought materials [3.5 - 3.6]. For conventional wrought materials, the fatigue limit for infinite life may be coarsely estimated as the half of their UTS, but this ratio is significantly dropped down, when considering an additively processed material. For this reason, a lot of research is needed in this field. The stainless steel CX was then considered in this research in order to investigate the relationship between the additive process and the achievable fatigue response also following heat or surface treatments.

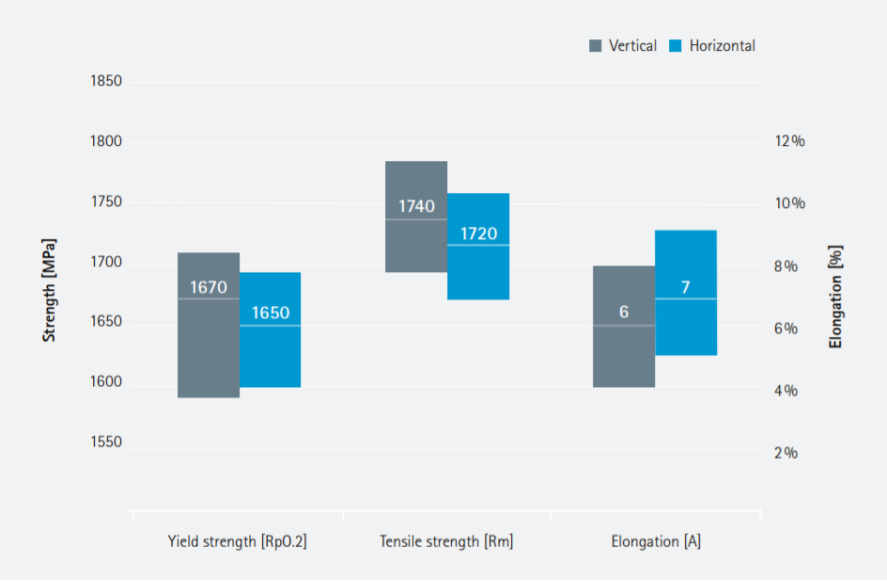

Figure 69: Static properties of stainless steel CX after heat treatment, from EOS datasheet [3.22]

In the following paragraphs, the experimental procedure and the used equipment to assess the fatigue properties of the AlSi10Mg and of the stainless steel CX will be described. Subsequently, the experimental plans and the results will be discussed for each alloy in different paragraphs.

3.2 Materials and equipment.

In this Section the geometry of the samples, the chemical composition and the used equipment are reported. It is pointed out that sample geometry is the same for the two studied materials. The used equipment is also the same, therefore it is going to be described once.

3.2.1 Specimens

Both the aluminum and stainless-steel specimens were designed with a smooth cylindrical geometry according with the ISO 1143 for rotating bending fatigue testing, as indicated in Figure 70. To reduce the experiment costs, the minimum diameter recommended by the Standard was chosen. Samples in the as built state (not machined) often exhibit a higher run-out tolerance than that reported in the ISO 1143 (0.015 mm), especially when they are slanted oriented with respect to the base plate. This is due to the fact slanted specimens need supports. After removing them, the samples are likely to bend due to process induced tensile residual stresses (Figure 71). Furthermore, the area, where the supports have been removed, appears jagged and not perfectly cylindrical. Eccentricity causes vibration during fatigue tests, especially at low rotational speeds, due to resonance phenomena, and load fluctuation, which may alter the nominal test stress.

A machining process could remove the defects and restore cylindrical shape. However, to determine the improvement due to the machining process, it is necessary to assess the performance in the as built state. To overcome this issue, as built specimens with slanted orientation were built without supports in the gage. Furthermore, the gripping areas were made with a larger diameter and then machined up to the final diameter dimension of 10 mm. These arrangements have led to lower misalignments affecting the samples (Figure 72).

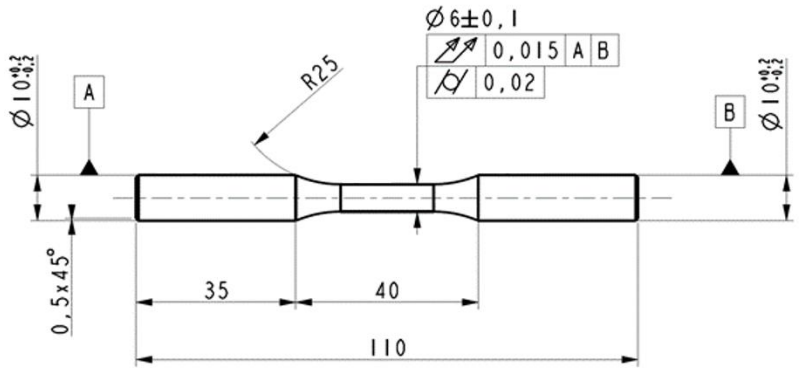

Figure 70: Sample geometry specification, inspired by ISO 1143

Figure 71: Bending in slanted specimens after supports removal.

Figure 72: AlSi10Mg slanted oriented samples, after head machining

The powder was supplied by EOS GmbH. The nominal chemical compositions are listed in Table 24 for the aluminum and Table 25 for the stainless steel. All the specimens were manufactured by EOSINT M290 device.

Table 24: AlSi10Mg chemical composition (wt.-%) [3.7]

Al [%]	Si [%]	Fe [%]	Cu [%]	Mn [%]	Mg [%]	Ni [%]	Zn [%]	Pb[%]	Sn[%]	Ti[%]
11-13	9-11	0.55	0.05	0.45	0.25-0.45	0.05	0.1	0.05	0.05	0.15

Table 25: Stainless Steel CX chemical composition (wt.-%) [3.22]

Cr [%]	Ni [%]	Mo [%]	Al [%]	Mn [%]	Si [%]	C [%]	Fe [%]
11-13	8.4-10	1.1-1.7	1.2-2	≤0.4	≤0.4	≤0.05	Bal.

3.2.2 Equipment

Checks and analyses were performed by the same equipment for both the alloys. The sequence of operations that were carried out can be summarized as follows:

- Diameter measurements
- Roughness measurements
- Eccentricity measurements (only for fatigue tests)
- Static tensile (only for aluminum samples) or fatigue tests
- Density measurements
- Fractographic analyses
- Micrographic and SEM analyses

The diameter measurements were performed by an electronic micrometer (resolution of 0.001mm).

Six diameter measurements were taken at the gage and four at each head. Roughness measurement were carried out both at gage and at the heads with eight replications, by a portable surface roughness tester with the resolution of 0.001 μm (RT25, SM Metrology System, Torino, Italy). Sample misalignment at gage was checked only in case of fatigue tests by a centesimal comparator after the mounting on the Moore machine Figure 73.

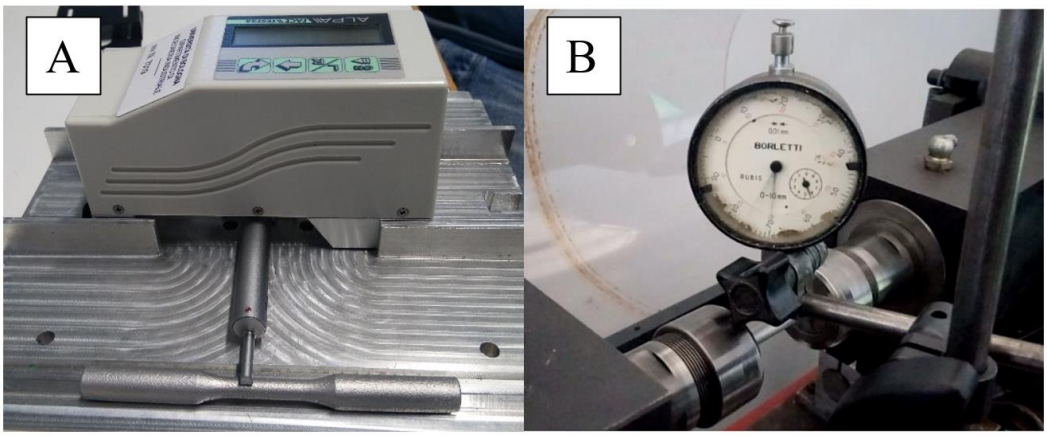

Figure 73: Roughness (a) and eccentricity (b) measurements

Static tensile tests were performed only on aluminum samples. For this purpose, an oleo-dynamic press equipped with a 100 kN load cell was used. The heads of the specimens were threaded to be gripped in the machine. For the elongation measurements, HBM DD1 Extensometer (with initial length l_0 = 25 mm) was used (Figure 74). As for stainless steel samples, data concerning static mechanical properties were provided by foreign partners.

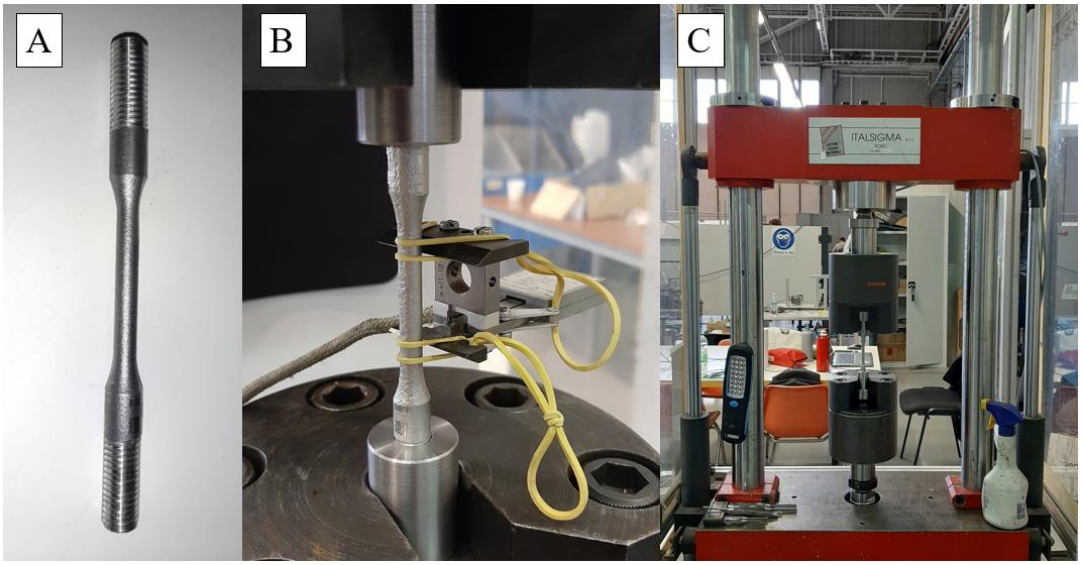

Figure 74: Tensile test on aluminum samples: a) a detail of the threaded head, b) a sample assembled in the machine with the extensometer, c) the press

Fatigue tests were performed by a four-point rotating bending machine controlled by a computer, which makes it possible to have a constant bending moment at the gage and a stress ratio R=-1. The frequencies load was set at 60 Hz for the aluminum sample and 80 Hz for the stainless-steel ones. The aluminum samples were fatigued until failure or up to 10^6 cycles with the purpose of determining the sloping part of the S-N curves. Stainless-steel CX specimens were fatigued until failure or up to 10^7 cycles that was set as runout. After the tests, the porosity was evaluated by density measurements. The immersion method was used for the purpose. The procedure consists of two weight measurements: the first one is the sample weight ($m_{sample\_in\_air}$), whereas the second is the weight taken with sample completely immersed on distilled water ($m_{sample\_in\_liquid}$). Subtracting these two terms and multiplying the result by the gravity acceleration (g) we obtain the Archimedes force (S_{Archim}).

$$\boldsymbol{S_{Archim} = (m_{sample\_in\_air} - m_{sample\_in\_liquid}) \cdot g} \qquad \textit{Eq. 3.01}$$

Dividing the Archimedes force by the gravity acceleration and by the liquid density (ρ), which is calculated by the machine as a function of the temperature, the specimen volume (V_{sample}) is obtained.

$$\boldsymbol{V_{sample} = \frac{S_{Archim}}{\rho \cdot g}} \qquad \textit{Eq. 3.02}$$

The specimen density (ρ_{sample}) is finally calculated by dividing the specimen volume for its weight

$$\rho_{sample} = \frac{V_{sample}}{m_{sample\_in\_air}}$$ *Eq. 3.03*

Fractographic analyses were carried out to assess the fracture mode. Zeiss Stemi 305 stereoscopic microscope was used for the scope. To determine the fracture behavior, the microstructure and the chemical composition, micrographics and high magnification images were captured by an optical microscope (Nikon Optiphot 100) and a Tescan Mira 3 SEM-FEG. Before micrographic analyses, samples had to be cut, incorporated in a resin, polished and finally chemically attached. This procedure differs for the two studied alloy. Therefore, it will be described later with further details.

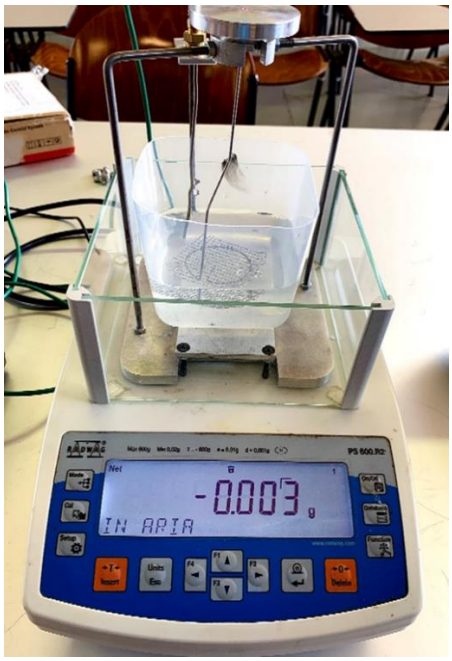

Figure 75: Density measurement machine through the immersion method

3.3 The AlSi10Mg aluminum alloy

3.3.1 The experimental plan

In order to study the mechanical performance of the AlSi10Mg, an extensive experimental plan was designed. To verify the performance of the used powder, static tensile tests were initially performed involving specimens manufactured along three different build orientation (0°, 45° and 90°). Five samples per build orientation were manufactured. Specimens were shot-peened and no heat treatment were applied to have a good matching with results in the supplier data sheet [3.7].

The experimental fatigue test plan accounts for three factors: the build orientation, the heat treatment and the surface treatment. Each factor varies over three levels, as reported in Table 26. The build orientation can probably be considered among the most important parameters. When designing a component, the orientation for its manufacturing is a crucial choice to be made. As reported in previous paragraphs, it can strongly affect the mechanical properties. For this reason, it was considered in the experimental plan. The three levels vary between 0° (horizontally built sample), 45° and 90° (vertically built sample). About the heat treatment, the studied levels are untreated, T6 age hardening and stress relief. The T6 heat treatment is suitable for removing the differences in the microstructure due to the built orientation and for improving the strength. Age hardening was carried out, heating the samples at the temperature of 520°C for one hour. Afterwards, water quenching was run; finally, after keeping the samples at 160°C for six hours, a further water quenching was performed. The stress relief was also considered to determine the effectiveness of this treatment on the residual stress reduction. It was carried out, heating the specimens at 300°C for two hours, and then cooling them in fresh air. Performing treatments indeed entails additional costs in the production process. To quantify the benefit produced by these treatments and to evaluate their usefulness, the untreated level was considered and taken as a reference. Similar reasons are on the base of the choice of the three surface treatments. Following machining and lapping, the surface roughness improves, thus removing most of the superficial and sub-superficial defects that often promote crack initiation and propagation. Theoretically, these treatments increase the fatigue strength. However, they also involve additional costs on the production cycle. Furthermore, very complex geometries could be difficult to machined. Thus, a typical surface treatment, i.e., micro shot-peening followed by fine blasting, was considered. The only micro shot-peening level was set as reference to

quantify the improvements due to the other treatment. Shot-peening was performed by using ceramic beads Z300. The factors were combined in the framework of 3^3 experimental design, accounting for 27 sample families (combinations). When both heat and surface treatment are applied, the surface treatment is performed first.

A total amount of ten specimens per type (270 samples) was tested on a four-point rotating bending machine at the frequency of 60 Hz and under the stress ratio R=-1. The samples were fatigued until failure or up to 10^6 cycles, to be regarded as runout. Ten specimens are not enough to study both the fatigue curve and the fatigue limit. Therefore, only the fatigue curve in the finite life domain was determined, thus working out the fatigue strength at 1 million cycles by interpolation. A five-character alphanumeric code was used to differentiate each specimen (e.g., ADG01). The coding references are reported in Figure 76.

Table 26: AlSi10Mg fatigue experimental plan.

		Levels		
Factors	Build orientation	0°	45°	90°
	Heat treatment	No H.T.	T6	Stress Relief
	Surface treatment	Micro shot-peening.	Micro shot-peening + fine blasting	Allowance + machining + lapping

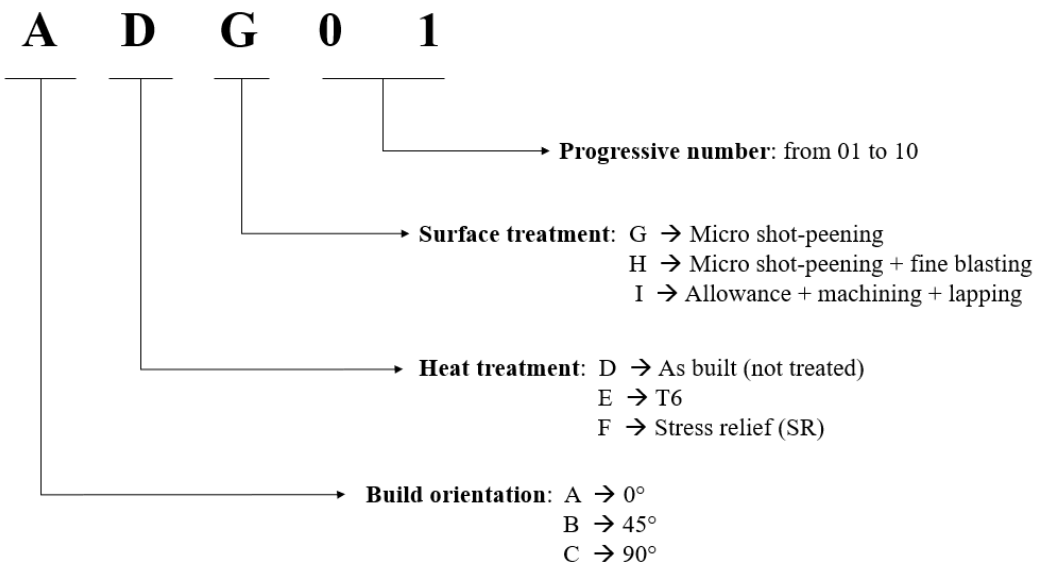

Figure 76: Coding system for AlSi10Mg fatigue samples.

3.3.2 Preliminary checks

Diameter and roughness measurements were performed to check the compliance with design specifications. When a sample diameter very different from the data was found, the real dimensions was used to precisely evaluate the tensile strength or to calculate the correct load to apply during the fatigue test, thus reducing the experiment error.

For the specimens used in the static tensile tests, the mean measured values for the gage diameter and for the gage roughness are reported in Table 27. "AT" group refers to the horizontally oriented samples, "BT" to the slanted oriented specimens and "CT" to the vertically manufactured ones. Six diameter measurements and eight roughness measurements were carried out for each sample. About the gage diameters, values that differ by a few hundredths of a mm from the designed value were found. Since the specimens were not machined, it was difficult to obtain very accurate dimensions. However, the measured diameters were very close to the recommended ones. Therefore, they were considered acceptable. As for roughness, related values were measured and were found to be consistent with the performed process and with the post-process treatments. The roughness exhibits higher value and standard deviation in horizontally sample than in vertically ones. A worse roughness for horizontal specimens is due to a poor finishing that occurs in the lower faces (those facing the base plate). For this set, a mean value of 10.9 µm was calculated, but values up to 22 µm were measured. Nevertheless, for horizontally samples the surface finish was greater than those in the powder supplier datasheet [3.7], whereas for vertically set (CT) comparable values were obtained.

Table 27: Gage diameters (in mm) and gage roughness (in µm). Mean value and standard deviation for samples families used for static tensile tests.

	Gage Diamenter			Gage Roughness	
	Mean Value	St. Dev.		Mean Value	St. Dev.
A T	6.041	0.074	A T	10.929	5.186
B T	6.048	0.044	B T	8.387	1.378
C T	5.978	0.018	C T	7.651	0.936

The same procedure above was used to check the gage diameter and roughness for samples used in fatigue tests. Results are listed in Table 28 and Table 29. It is interesting to observe the standard deviation in case of micro shot peened and sand blasted (xxH) samples is almost always lower than in case for only shot peened ones (xxG), which indicates slightly better dimensional accuracy. Machining improves surface finishing

(xxI); however, a slightly high roughness of that expected, which is likely to affect fatigue properties, was found in ADI, BDI ad CDI families: after a polishing treatment, such as that foreseen for the "xxI" series, the expected roughness should be less than 0.8 µm. No significant differences were observed between shot-peened and fine blasted samples.

Table 28: Gage diameters. Mean value and standard deviation for samples families used in fatigue tests (all dimensions in mm)

	Mean Value	St. Dev.		Mean Value	St. Dev.		Mean Value	St. Dev.
A D G	6.040	0.078	B D G	6.000	0.037	C D G	5.994	0.027
A D H	5.818	0.061	B D H	6.040	0.060	C D H	5.977	0.016
A D I	6.037	0.052	B D I	6.009	0.007	C D I	6.011	0.004
A E G	5.877	0.146	B E G	6.008	0.038	C E G	5.983	0.027
A E H	5.915	0.111	B E H	6.000	0.036	C E H	5.991	0.022
A E I	6.016	0.006	B E I	5.989	0.006	C E I	6.016	0.005
A F G	6.038	0.096	B F G	6.076	0.074	C F G	5.994	0.025
A F H	6.044	0.075	B F H	6.054	0.056	C F H	5.988	0.021
A F I	6.008	0.004	B F I	5.988	0.009	C F I	6.008	0.006

Table 29: Gage roughness. Mean value and standard deviation for samples families used in fatigue tests (all dimensions in µm)

	Mean Value	St. Dev.		Mean Value	St. Dev.		Mean Value	St. Dev.
A D G	5.668	1.945	B D G	4.964	1.530	C D G	5.569	1.361
A D H	3.772	1.266	B D H	5.152	1.708	C D H	6.113	1.495
A D I	1.217	0.272	B D I	2.722	0.522	C D I	1.357	0.126
A E G	6.877	1.821	B E G	7.354	2.547	C E G	5.901	0.936
A E H	8.314	3.287	B E H	6.868	1.665	C E H	6.423	1.786
A E I	0.609	0.077	B E I	0.368	0.060	C E I	0.567	0.061
A F G	5.103	2.275	B F G	8.167	2.935	C F G	7.344	1.330
A F H	7.326	3.231	B F H	9.242	3.520	C F H	7.158	1.356
A F I	0.758	0.027	B F I	0.977	0.154	C F I	1.049	0.071

3.3.3 Static tensile tests

Static tensile tests were carried out to check the static performance of the produced specimens was consistent with the properties declared by the powder manufacturer. The same treatments in the supplier data sheet were considered to compare the results (shot peened surfaces, but no heat treatment) [3.7]. Specimens were manufactured in three different build orientation: 0°, 45° and 90°. Five replicas for each build orientation were considered.

Test were carried out for a stress rate ranging from 7 to 14 MPa/s, in agreement with ISO 6892, which recommends a value between 2 and 20 MPa/s for metallic materials with a Young's modulus lower than 150 GPa. An example of σ-ε curve is shown in Figure 77. Experimental results are reported in the graph bars in Figure 78.

The obtained yield strength (Rp02) and Young's modulus (E) are aligned with those declared in the EOS datasheet. Differences between the build orientations affecting the yield strengths and elastic modulus are not significant (an analysis of variance with subsequent Fisher Test were carried out on the results).

Unexpected results were found with regard to the ultimate tensile strengths (UTS). Lower values, even up to 20%, were measured. Furthermore, the ultimate tensile strength is significantly influenced by the build orientation. Unlike what would to be expected, a higher UTS was found in vertical oriented samples rather than for the horizontally built ones. Probably, defects induced by support detachment, with particular reference to horizontally oriented samples, may have led to ultimate strengths that keep lower than those declared by the supplier.

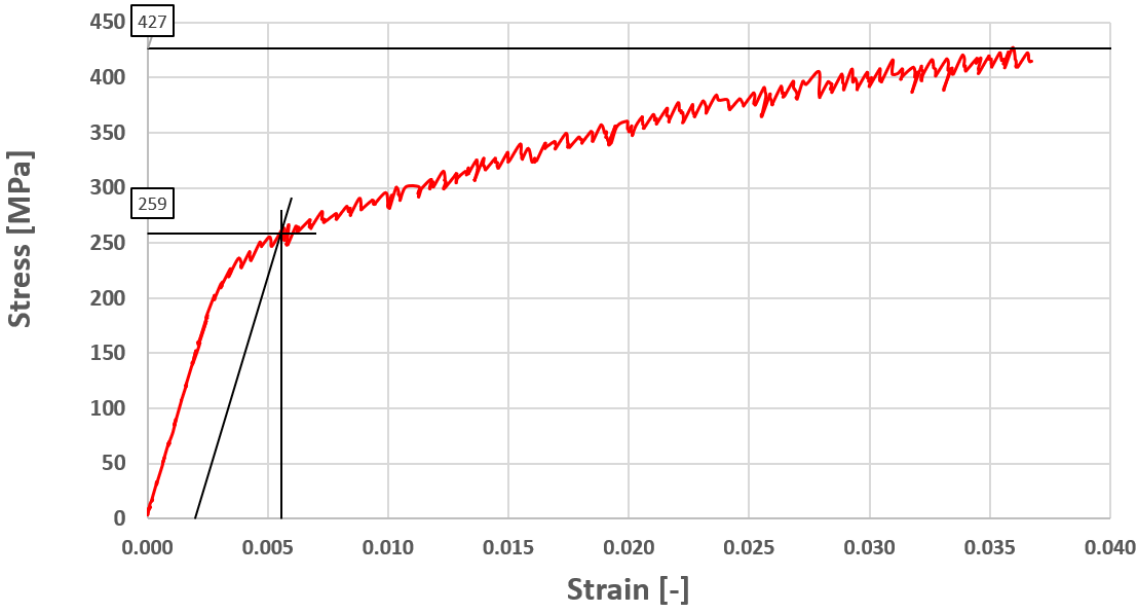

Figure 77: σ-ε graph for a vertically built sample

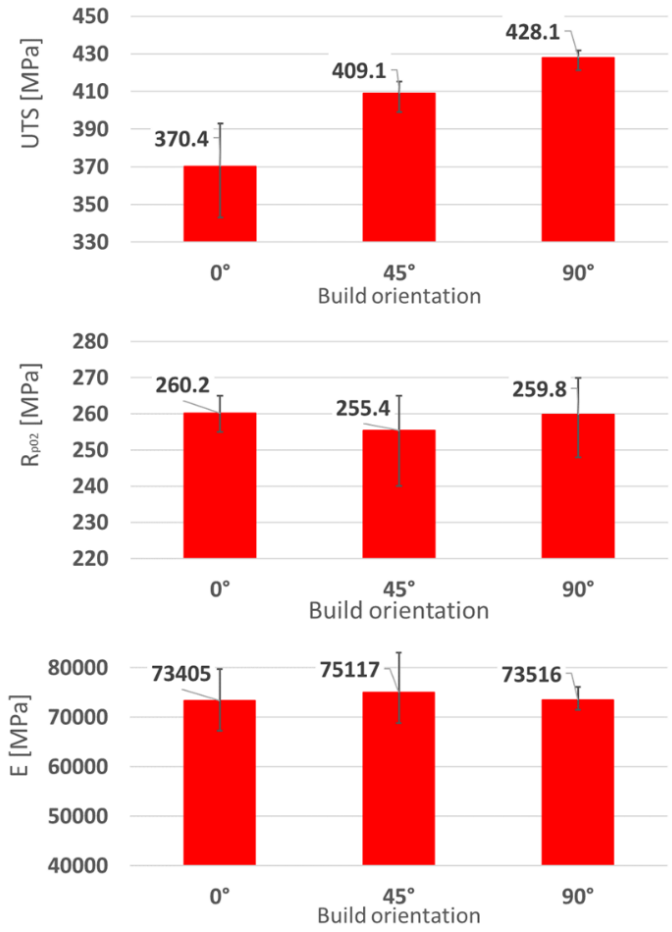

Figure 78: Experimental results of static tensile tests

Experimental

		UTS [MPa]	
		mean	st.dev
BUILD ORIENTATION	0°	370.4	19.9
	45°	409.1	6.1
	90°	428.1	4.4
		Rp_{02} [MPa]	
		mean	st.dev
BUILD ORIENTATION	0°	260.2	4.3
	45°	255.4	9.7
	90°	259.8	9.3
		E [MPa]	
		mean	st.dev
BUILD ORIENTATION	0°	73405	5369
	45°	75117	5299
	90°	73516	1846

EOS datasheet

Mechanical properties of the parts

	As built
Tensile strength [6]	
- in horizontal direction (XY)	460 ± 20 MPa 66.7 ± 2.9 ksi
- in vertical direction (Z)	460 ± 20 MPa 66.7 ± 2.9 ksi
Yield strength (Rp 0.2 %) [6]	
- in horizontal direction (XY)	270 ± 10 MPa 39.2 ± 1.5 ksi
- in vertical direction (Z)	240 ± 10 MPa 34.8 ± 1.5 ksi
Modulus of elasticity	
- in horizontal direction (XY)	75 ± 10 GPa 10.9 ± 0.7 Msi
- in vertical direction (Z)	70 ± 10 GPa 10.2 ± 0.7 Msi

Figure 79: Experimental static properties compared with those given by the powder datasheet

3.3.4 Fatigue tests

The result of the fatigue tests were processed in agreement with ISO 12107 (as in Chapter 1.2). The linear model was found to be adequate to describe the fatigue behavior for all the 27 sample families. Fatigue curves were calculated for a 10% failure probability and a 90% confidence level. An example was reported in Figure 80. Due to the high number of tests the fatigue curves for each sample family, calculated according to the Standard, are detailed in Appendix Section.

The fatigue strengths at 10^6 cycles, then regarded as fatigue limits, are plotted in Figure 81 in form of bar graph along with the related error bars. These limits were obtained considering the values of the S-N curves at 10^6 cycles. The same procedure was utilized in order to estimate the error: for this purpose, the confidence bands at 10^6 cycles were extended to the infinite life domain, thus estimating the likelihood ranges to be applied to the estimated fatigue limits. Black bars refer to no treated samples, the red ones to the T6 heat treated families and the light blue to the stress relieved. The hatched type refers to the surface treatment: continuous for shot-peened specimens, dotted for shot-peened and fine blasted, dashed for machined and polished.

The bar graph shows that the best performance was achieved by the T6 heat treated specimens for slanted and vertical build orientation (series BEG, BEH, CEG, CEH). Poor performance was achieved in horizontally oriented specimens, especially in those with T6 heat treatment and shot-peened or shot-peened and sand blasted surface (series AEG, AEH). Stress relief treatment does not seem to yield considerable benefits: for vertically built specimens (series CFG, CFH, CFI), the performance is even worse than as built samples.

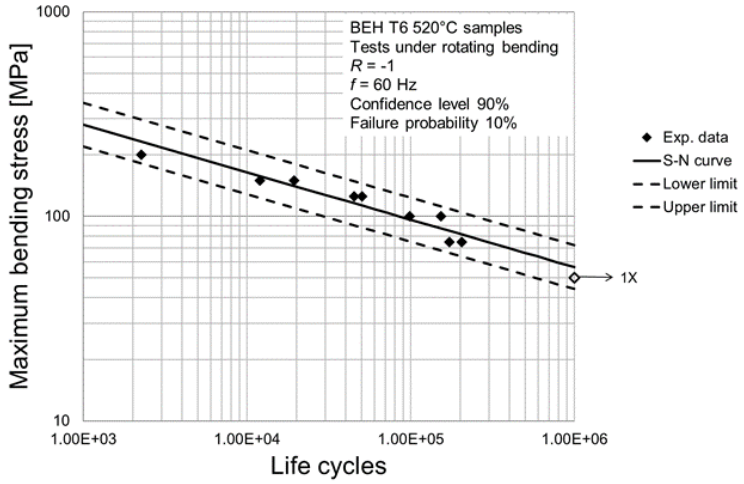

Figure 80: Fatigue curve for BEH set

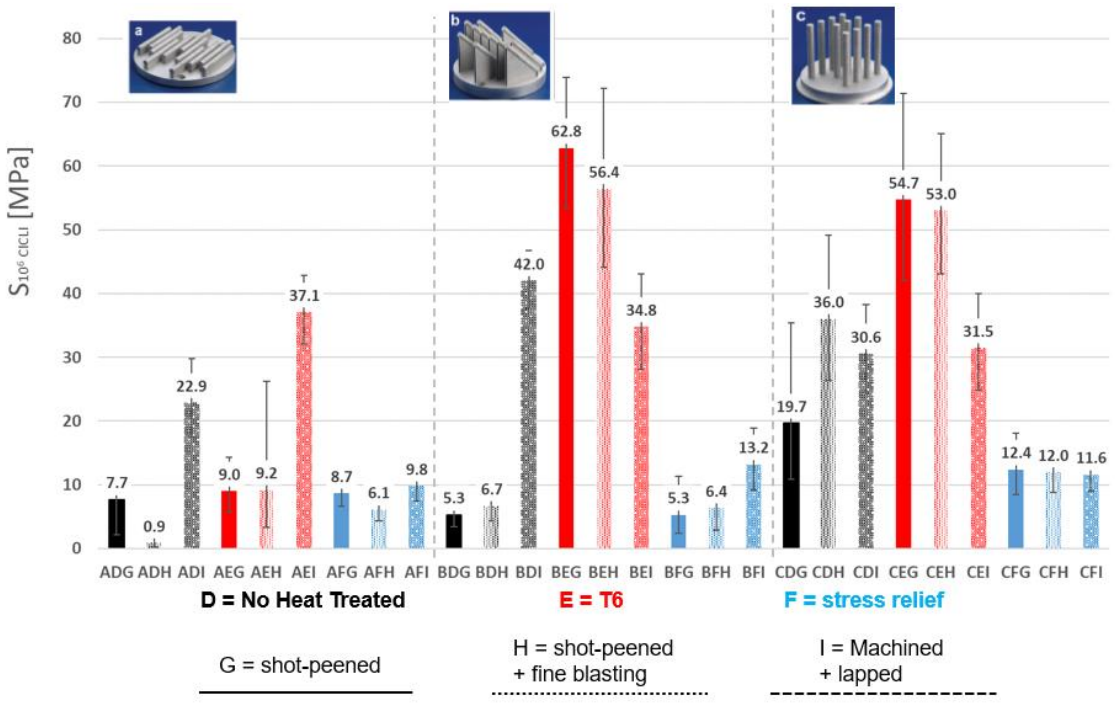

Figure 81: Fatigue limits at 10^6 cycles for each sample family

Due to the high number of results, to efficiently and accurately determine which are factors that most affect the fatigue strength, further analyses were performed. An ANOVA-based extended statistical method was adopted to properly compare the S-N curves. This method was successfully adopted for two-factor experiments in [3.5; 3.24 - 3.26], and was here replicated for the three-factor designed experiment, in order to assess whether the differences among the curves are significant, when compared to the retrieved scatter affecting the curves. The curve trends were compared, averaging their differences over the lifespan ranging from 10^3 to 10^6 cycles, which corresponds to the observed lifespan.

3 WAY-ANOVA EXTENDED METHOD

The analysis starts with the computation of the gran mean curve $\overline{S}$, to be computed as reported in Eq. 3.04.

$$\overline{S} = \frac{\sum_{i=A}^{C}\sum_{j=D}^{F}\sum_{k=G}^{I} S_{ijk}}{n_{tot}} \qquad \textit{Eq. 3.04}$$

Where S_{ijk} indicates the 10-base logarithm of the stress corresponding to a generic fatigue life, whereas the subscript corresponds to the previously described sample families. Note that the usual symbol for summations was used, but with reference to the alphabet letters: "i" can vary between A, B and C; "j" can vary between D, E and F; "k" varies between

G, H and I (see Figure 82). n_{tot} represents the number of the possible combination between the factors, in this case 27. The summation is the sum of all the fatigue curves of the 27 families. The second step of the analysis consists in the computation of the row mean ($S_{i..}$), the column mean ($S_{.j.}$) and the profundity mean ($S_{..k}$), where the symbol "i.." in "$S_{i..}$" refers to the i-th row, all the columns and all the depths. Similar meanings have $S_{.j.}$ and $S_{..k}$. The n_p term symbolizes the number of families considered for the evaluation of the mean terms. In this experiment it is the same for all the three considered factors and it is equal to 9.

$$\boldsymbol{S_{i..} = \frac{\sum_{y=D}^{F}\sum_{z=G}^{I} S_{iyz}}{n_p}} \qquad \textit{Eq. 3.05}$$

$$\boldsymbol{S_{.j.} = \frac{\sum_{x=A}^{C}\sum_{z=G}^{I} S_{xjz}}{n_p}} \qquad \textit{Eq. 3.06}$$

$$\boldsymbol{S_{..k} = \frac{\sum_{x=A}^{A}\sum_{j=D}^{F} S_{xyk}}{n_p}} \qquad \textit{Eq. 3.07}$$

For example, $S_{A..}$ represents the mean fatigue curve of horizontally built samples, $S_{.E.}$ represents the mean fatigue curve of T6 heat treated specimens, $S_{..I}$ represents the mean fatigue curve of machined samples, and so on.

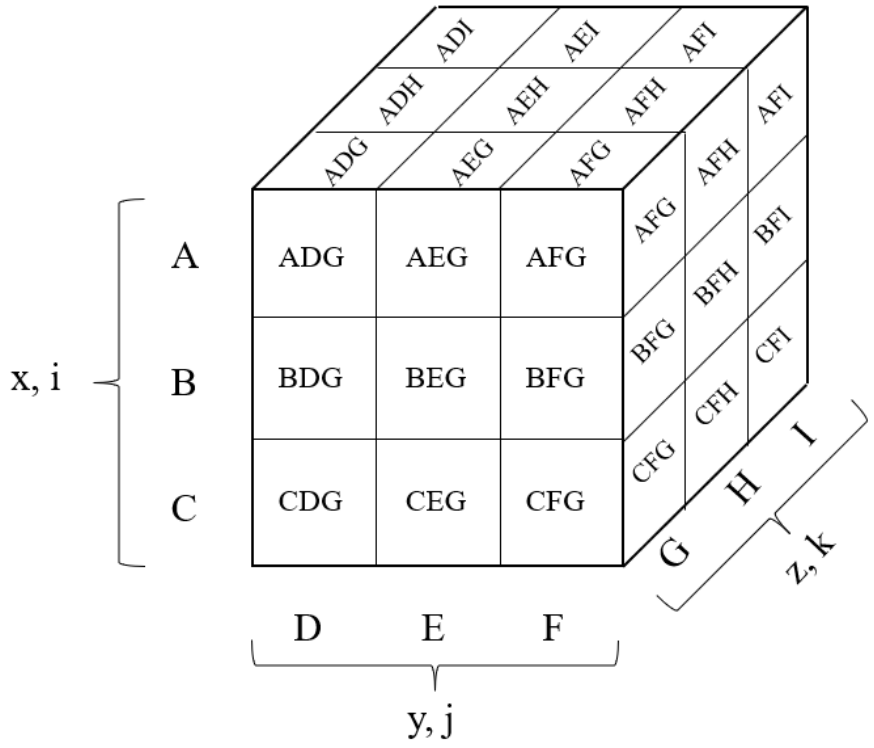

Figure 82: Representation of the 3^3 experimental plan

To evaluate the effect of a singular factor, it is necessary to calculate the following three terms: *SSBR*, *SSBC* and *SSBP*. The *SSBR* term (Sum of Square Between Rows) takes the effect of the "Row" factor into account. Consequently, based on the experimental design in Figure 82, this term deals with the effect of build orientation comparing the fatigue trends for the three considered levels (Eq. 3.08). The *SSBC* term (Sum of Square Between Columns), is related to the effect of the "Column" factor, i.e. heat treatment. The fatigue response in the as built, T6 heat treated and stress relieved is then compared (Eq. 3.09). The *SSBP* term (Sum of Square Between Profundities), deals with the effect of the "Profundity" factor, i.e. surface treatments. Like in conventional ANOVA, sums of the squares of the differences between Row, Column and Profundity Means and the Grand Mean are computed as:

$$\boldsymbol{SSBR = n_p \cdot \sum_{i=A}^{C} (S_{i..} - \bar{S})^2} \qquad \textit{Eq. 3.08}$$

$$\boldsymbol{SSBC = n_p \cdot \sum_{j=D}^{F} (S_{.j.} - \bar{S})^2} \qquad \textit{Eq. 3.09}$$

$$\boldsymbol{SSBP = n_p \cdot \sum_{k=G}^{I} (S_{..k} - \bar{S})^2} \qquad \textit{Eq.3.10}$$

The last series of term we need to compute are related to the interaction between the three factors (*SSI*, Sum of Square Interaction).

$$\boldsymbol{SSI = \sum_{i=A}^{C} \sum_{j=D}^{F} \sum_{k=G}^{I} (S_{ijk} - S_{ij.} - S_{i.k} - S_{.jk} + S_{i..} + S_{.j.} + S_{..k} - \bar{S})^2} \qquad \textit{Eq. 3.11}$$

Where:

$$\boldsymbol{S_{ij.} = \frac{\sum_{k=G}^{I} S_{ijk}}{n_1}} \qquad \textit{Eq. 3.12}$$

$$\boldsymbol{S_{i.k} = \frac{\sum_{J=D}^{F} S_{ijk}}{n_1}} \qquad \textit{Eq. 3.13}$$

$$\boldsymbol{S_{.jk} = \frac{\sum_{i=A}^{C} S_{ijk}}{n_1}} \qquad \textit{Eq. 3.14}$$

The number of families considered for the mean computation n_1 is 3.

The interactions between pairs of factors are also taken into account through the terms:

$$\boldsymbol{SSI(RC) = n_1 \cdot \sum_{i=A}^{C} \sum_{j=D}^{F} (S_{ij.} - S_{i..} - S_{.j.} + \bar{S})^2} \qquad \textit{Eq. 3.15}$$

$$\boldsymbol{SSI(CP) = n_1 \cdot \sum_{j=D}^{F} \sum_{k=G}^{I} (S_{.jk} - S_{.j.} - S_{..k} + \bar{S})^2} \qquad \textit{Eq. 3.16}$$

$$SSI(RP) = n_1 \cdot \sum_{i=A}^{C} \sum_{k=G}^{I} (S_{i.k} - S_{i..} - S_{..k} + \bar{S})^2 \qquad \textit{Eq. 3.17}$$

The aforementioned terms were computed over the entire lifespan with a sufficiently refined step, using an Excel sheet. Afterwards, they were turned into scalars, taking the respective integral means over the entire life range, in order to have global reliable indicators of the average impacts of factors and interaction over the investigated life domain.

The last term we need to compute in the ANOVA analysis is the error-related term *SSE*. It can be regarded as the sum of the squares of the residuals between the experimental data distributions and the retrieved S-N curves. This term may be estimated, based on Eq.3.18, where S_{exp} represents the logarithm of the stress level corresponding to an observed life and S_{calc} indicates the same stress level in the logarithm scale, based on the interpolated S-N curve for the same life extent. In this formula, the subscripts "i", "j" and "k" retain the same meanings as above, indicating the rows, the column and the profundity of the experimental design in Figure 82, whereas "l" identifies the l-th experimental point and n_{ijk} is the number of available points for the family i, j, k.

$$SSE = \sum_{i=A}^{C} \sum_{j=D}^{F} \sum_{k=G}^{I} \sum_{l=1}^{n_{i,j,k}} (S_{exp_{i,j,k,l}} - S_{calc_{i,j,k,l}})^2 \qquad \textit{Eq. 3.18}$$

A final step was needed to make comparable the determined yields one another, and to process them in a conventional two-factor ANOVA: the aforementioned terms were scaled, rationalizing them by the related degree of freedom. The outcome of the statistical assessment is reported in Table 30. Results highlight the significant effect of all the factors (with a 95% confidence level). Furthermore, all the interaction terms are significant.

*Table 30: ANOVA results of the 3^3 experimental plan: **SSBR** refers to the **build orientation**, **SSBC** refers to the **heat treatment**, **SSBP** refers to the **surface treatment**.*

	SSQ	DoF	MSQ	Fcalc.	p-value	Significant?
SSBR	0.3757	2	0.1878	19.85	1.42E-08	YES
SSBC	0.8447	2	0.4223	44.64	1.09E-16	YES
SSBP	0.3275	2	0.1637	17.31	1.21E-07	YES
SSI(RC)	0.1433	4	0.0358	3.78	5.47E-03	YES
SSI(RP)	0.2589	4	0.0647	6.84	3.57E-05	YES
SSI(CP)	0.1556	4	0.0389	4.11	3.20E-03	YES
SSI	0.1975	8	0.0247	2.61	9.84E-03	YES
Error	1.8451	195	0.0095			
Total	4.1483	221				

Despite the complex procedure carried out, the results of the 3-way ANOVA analysis does not allow to derive detailed conclusions. If one of the three factors had been found to be not significant, it would have been feasible to exclude it from the analysis, and to focus on the other two factors. Consequently, analyses on smaller groups of tests were performed. A first analysis was carried out, for fixed build orientation and evaluating the effect of the heat treatment and of the surface treatment. The detailed results are shown below, starting from horizontally built samples.

Effect of the heat treatment and of the surface treatment for horizontally built samples (Series Axx).

The experimental points and the S-N curves for the horizontally built samples are sketched in Figure 83. The same ANOVA analysis described above was performed in this case, with the simplification that only two factors (each varying in three levels) were considered. In this case the row factor is the heat treatment, whereas the column factor is the surface condition. The results of the ANOVA test are shown in Table 31. Both the heat and surface treatments significantly affect the fatigue life. The red curves in Figure 83 refers to the heat-treated samples: they exhibit a slightly better performance, despite the curves intersect each other quite a lot. This outcome is also confirmed by the positive results of the interaction term SSI in the ANOVA test (Table 31).

A particular issue occurred for horizontally built samples, which compromised the results of some fatigue tests. In fact, the fatigue curves of the T6 heat treated specimens appear much less performing than the analogous ones of the samples of the B and C series. Before the tests, two types of geometric errors in the ADG, ADH, AEG and AEH series were found. The first is a circularity error: specimens exhibited an oval section with a measurements difference between two orthogonal diametrical up to 0.4mm. The second error concerned the rotation eccentricity: the Table 32 shows the average values and maximum values found in the above-mentioned series.

Horizontally built samples require supports at the gage diameter. After supports removing, residual stress can be released and specimens could distort. Furthermore, if the removing operation is carried out without attention, more material than necessary could be removed, damaging the surface. The result is a gage diameter being smaller than expected and with an oval cross section.

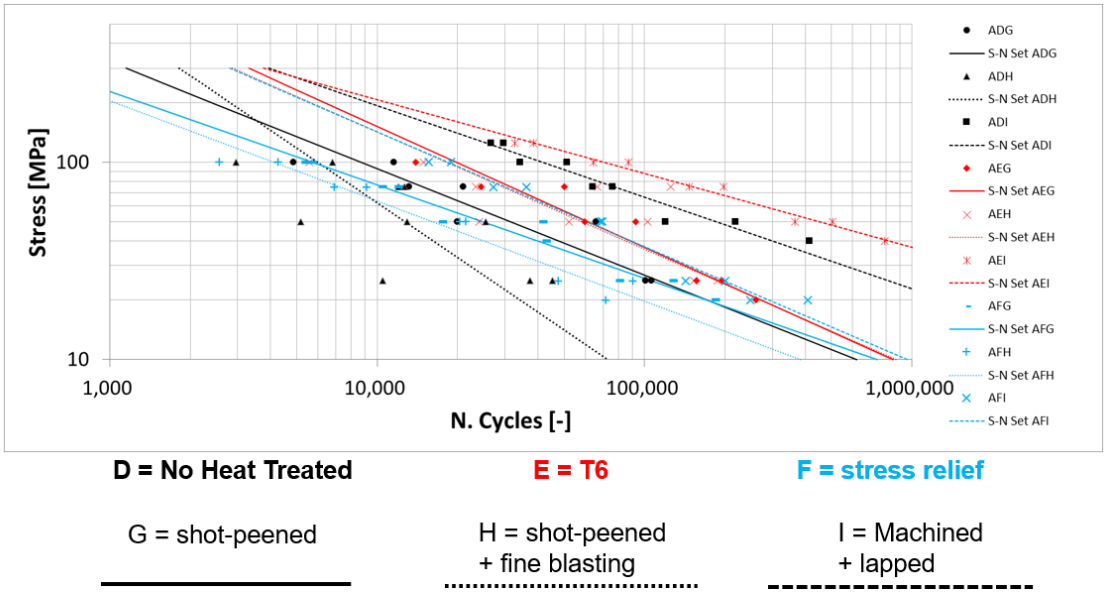

Figure 83: Experimental points and calculated S-N curves for horizontally built samples (0°)

*Table 31: ANOVA results for the horizontally built samples (0°, Axx family): **SSBR** refers to the **heat treatment**, **SSBC** refers to the **surface treatment***

	SSQ	DoF	MSQ	Fcalc.	p-value	Significant?
SSBR	0.1857	2	0.0928	7.21	1.51E-03	YES
SSBC	0.4552	2	0.2276	17.68	8.03E-07	YES
SSI	0.1909	4	0.0477	3.71	8.99E-03	YES
Error	0.8110	63	0.0129			
Total	1.6427	71				

Table 32: Eccentricity errors in horizontally built samples

Series	Mean Eccentricity [mm]	Maximum measured value [mm]
ADG	2,13	2,65
ADH	4,42	5,10
AEG	1,91	2,90
AEH	2,34	3,75

Effect of the heat treatment and of the surface treatment for slanted built samples (Series Bxx).

As above for the horizontally built samples, the experimental points and the S-N curves for the slanted built ones are shown in Figure 84 and the relative results of the ANOVA analysis in Table 33. The colors referred to the curves and the row (SSBR) and the column (SSBC) factors are consistent with those in the previous Section. Both the heat and surface treatments significantly affect the fatigue life. Furthermore, they interact each other. The

smaller p-value for the row factor, if compared to that of the column factor, highlights a greater statistical effect of the heat treatment with respect to that of the surface treatment. Red curves (T6 heat treated samples) exhibit a better fatigue performance, whereas the black (as built) and the light blue ones (stress relieved) overlap each other. The machining process (xxI series), leads to the better fatigue performance at high cycles for the as built and the stress relieved specimens, whereas in T6 heat treated samples the behavior changes and the worst performance is obtained. This outcome is confirmed by the positive results of the interaction term SSI in the ANOVA analysis.

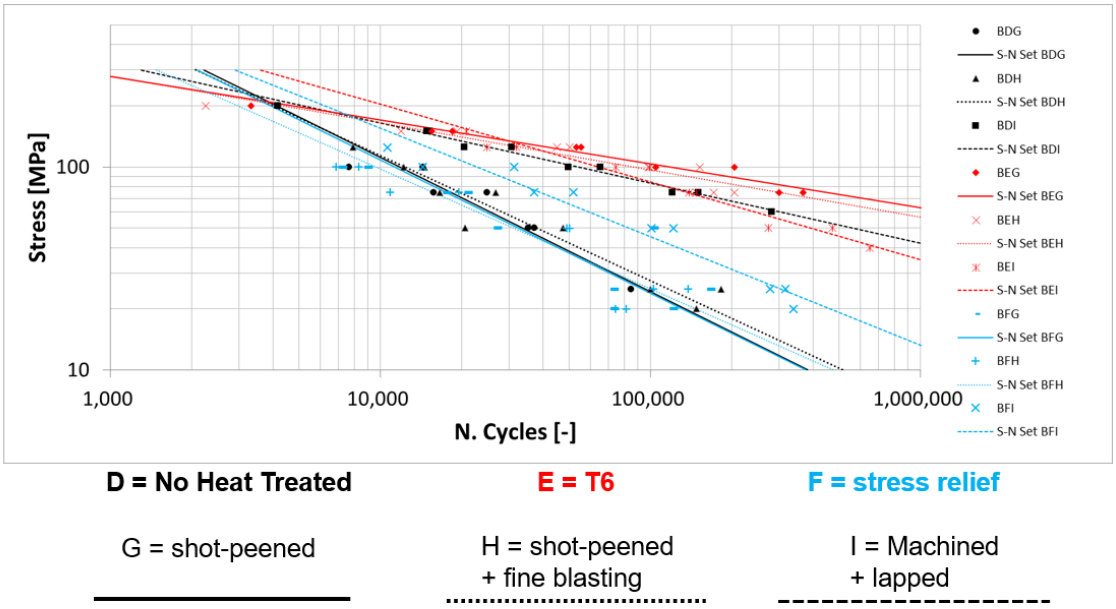

Figure 84: Experimental points and calculated S-N curves for slanted built samples (45°)

*Table 33: ANOVA results for the slanted built samples (45°, Bxx family): **SSBR** refers to the **heat treatment**, **SSBC** refers to the **surface treatment***

	SSQ	DoF	MSQ	Fcalc.	p-value	Significant?
SSBR	0.4872	2	0.2436	33.39	8.70E-11	YES
SSBC	0.1214	2	0.0607	8.32	5.93E-04	YES
SSI	0.1450	4	0.0362	4.97	1.44E-03	YES
Error	0.4888	67	0.0073			
Total	1.2424	75				

Effect of the heat treatment and of the surface treatment for vertically built samples (Series Cxx).

Finally, the experimental results, the S-N curves and the ANOVA outcomes for the vertically built samples are reported in Figure 85 and in To deepen the beneficial or detrimental effects of the factors, two further analyses were carried out.

To exclude the geometrical errors found in the horizontally built samples, machined samples only were considered in a first analysis to assess the effects of the build orientation and of the heat treatment. A second analysis was then carried out for the samples that had been heat treated by T6, which seems to lead to the best fatigue performance among those considered, with the aim of highlighting the effects of the build orientation and the surface finish.

Table 34. The T6 heat treatment again appears as the best one (red curves), followed by the as built (black curves) and the stress relieved (light blue curves) families. For the same heat treatment, the curves intersect quite a lot each other, thus indicating the surface treatment is not significant in case of vertically built samples. The ANOVA analysis confirms this outcome, highlighting a significant effect only for the heat treatment.

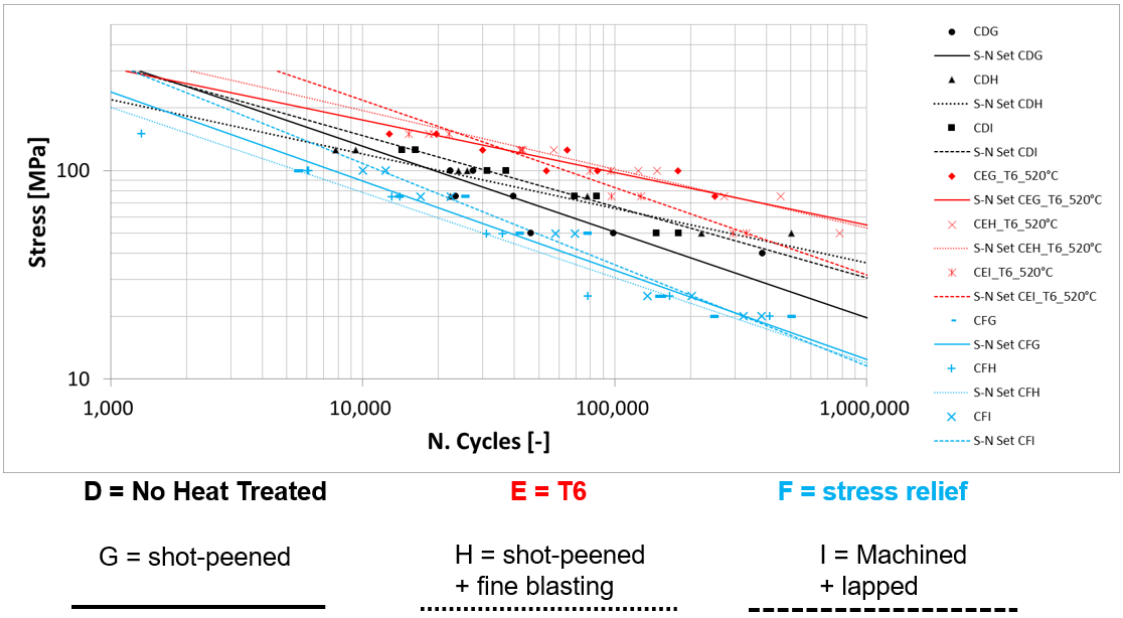

Figure 85: Experimental points and calculated S-N curves for vertically built samples (90°)

To deepen the beneficial or detrimental effects of the factors, two further analyses were carried out.

To exclude the geometrical errors found in the horizontally built samples, machined samples only were considered in a first analysis to assess the effects of the build orientation and of the heat treatment. A second analysis was then carried out for the samples that had been heat treated by T6, which seems to lead to the best fatigue performance among those considered, with the aim of highlighting the effects of the build orientation and the surface finish.

*Table 34: ANOVA results for the vertically built samples (90°, Cxx family): **SSBR** refers to the **heat treatment**, **SSBC** refers to the **surface treatment***

	SSQ	DoF	MSQ	Fcalc.	p-value	Significant?
SSBR	0.3183	2	0.1592	43.85	1.17E-12	YES
SSBC	0.0064	2	0.0032	0.89	4.17E-01	NO
SSI	0.0192	4	0.0048	1.32	2.72E-01	NO
Error	0.2287	63	0.0036			
Total	0.5726	71				

Figure 86 shows the S-N curves for the machined samples. Colors refer to the heat treatment (black for as built, red for T6 heat treatment, light blue for stress relief), whereas the line type deals with the build orientation (horizontally continuous, dashed lines for slanted samples, dotted line for vertically built).

Table 35 is the related ANOVA table. The heat treatment significantly affects the fatigue curves (positive SSBR term). Particularly, a negative contribution of the stress relief is highlighted from Figure 86 (light blue lines are the lowest of all). The T6 heat treatment seems to ensure better fatigue properties, but the differences between the as built families are not very relevant.

The build orientation appears not to significantly affect the fatigue properties (negative SSBC term).

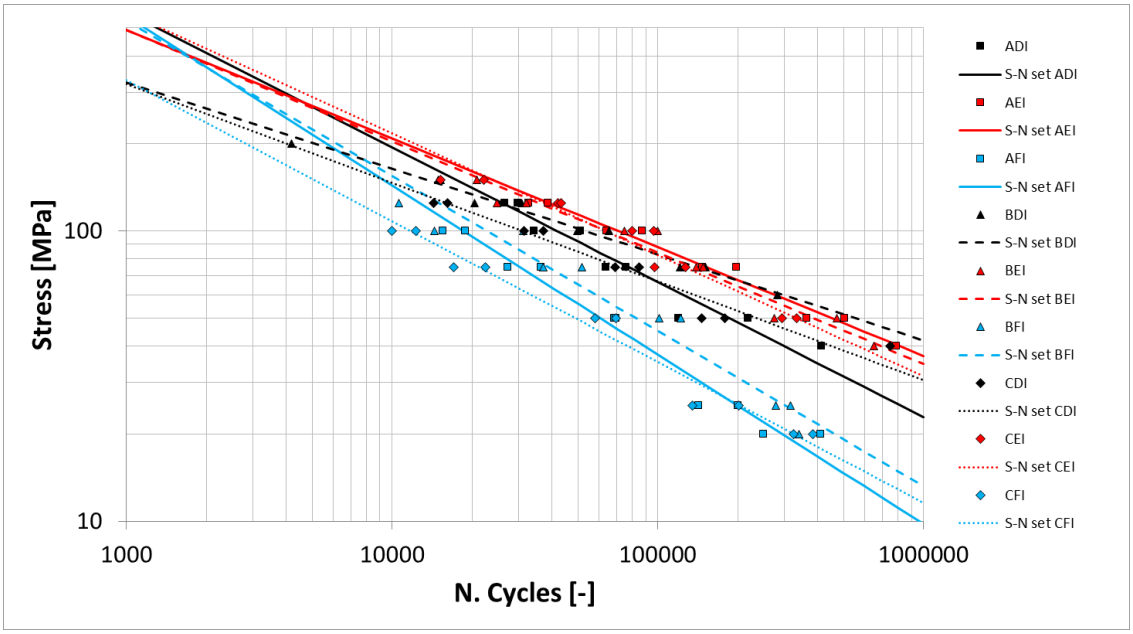

Figure 86: S-N curves for machined samples

*Table 35: ANOVA analysis for machined samples: **SSBR** refers to the **heat treatment**, **SSBC** refers to the **build orientation***

	SSQ	DoF	MSQ	Fcalc.	p-value	Significant?
SSBR	0.2043	2	0.1021	43.84	5.16E-13	YES
SSBC	0.0107	2	0.0053	2.29	1.09E-01	NO
SSI	0.0090	4	0.0022	0.96	4.33E-01	NO
Error	0.1608	69	0.0023			
Total	0.3847	77				

The last comparison was carried out between the samples that had undergone T6, which appear to ensure the best fatigue performance. The curves and the results of the ANOVA analysis are listed in Figure 87 and Table 36. Due to the aforementioned geometrical error, which can alter the results, the horizontally built series were not considered in this comparison. Therefore, slanted and vertically specimens only were considered. The surface finishing was considered as row factor: the positive SSBR value highlights a significant influence of the surface treatment on the fatigue response of the AlSi10Mg heat treated. At high cycles, the best fatigue performance was achieved for shot-peened and shot-peened and fine blasted samples. At low cycles, conversely, machining leads to higher fatigue life. The build orientation does not affect the results (SSBC). As is possible to observe in Figure 87, curves of same surface treatment are overlapped.

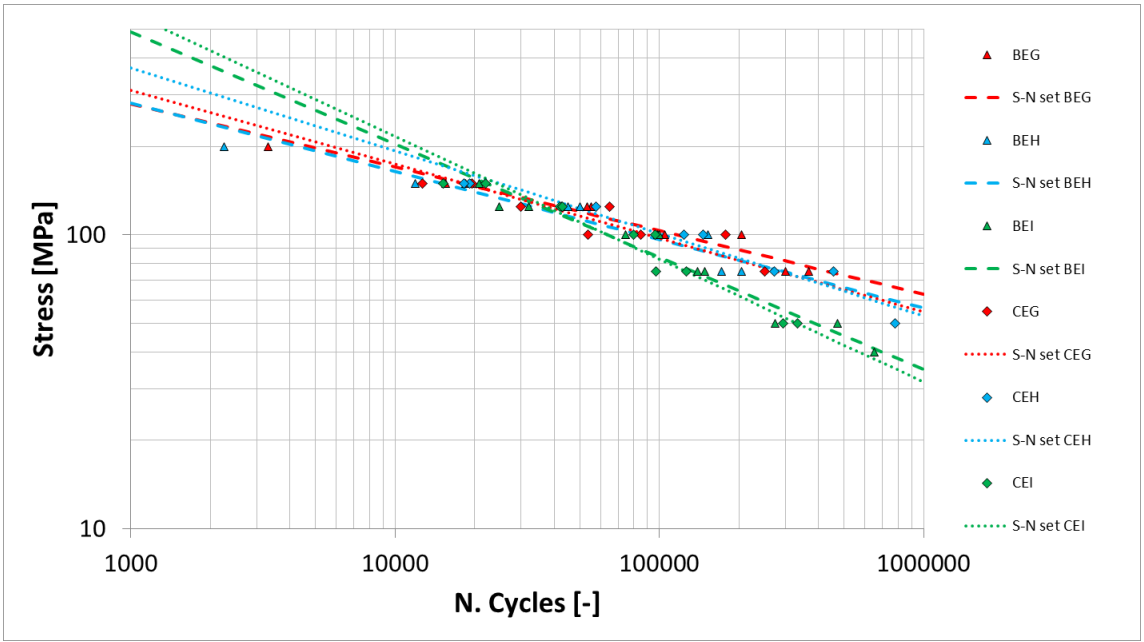

Figure 87: S-N curves for heat treated samples.

*Table 36: ANOVA analysis for T6 heat treated samples: **SSBR** refers to the **surface treatment**, **SSBC** refers to the **build orientation***

	SSQ	DoF	MSQ	Fcalc.	p-value	Significant?
SSBR	0.0189	2	0.0095	4.88	1.23E-02	YES
SSBC	0.0008	1	0.0008	0.42	5.22E-01	NO
SSI	0.0006	2	0.0003	0.15	8.65E-01	NO
Error	0.0833	43	0.0019			
Total	0.1035	48				

Finally, it is possible to summarize the results in the following points:

- all the considered factors affect the fatigue strength. However, the effect of each one is affected by the level of the other two (high interaction between the factors).
- The stress relief heat treatment always appears as a disadvantage. If applied, the obtained fatigue strength was always lower or, at most equal, to that in the as built state. Therefore, it is evident that its application does not seem to be suitable.
- The T6 heat treatment increases fatigue performance. Therefore, it is recommended to apply it to maximize fatigue performance. Furthermore, it homogenizes the performance: after apply T6, the fatigue strength becomes independent from the built orientation.
- Machining allows to reduce the largest surface defects. This leads to benefits in horizontal specimens, where the generated defects upon support removal negatively affect the fatigue performance, thus making related results unacceptable. In slanted and vertically oriented specimens, where these defects are not present, machining does not lead to the greater performance, with respect to the samples treated by shot-peening or shot-peening and fine blasting.

3.3.5 Density measurement for porosity evaluation

Density measurements were carried out by the immersion method. Density evaluation allows to obtain information about the internal porosity level. In fact, specimens with high porosity exhibit a lower density. In additively manufactured components, porosity does not only depend on the used process parameters, but are also affected by the application of post-process heat treatments. In fact, the heat treatment thermal cycles could alter the dimensions of the pores, causing a decrease in density. The density of all the samples were measured. Three measurements were carried out for each specimen. Results are resumed in Figure 88 in terms of set grand mean. No significant differences were found between series. For comparison purpose, the data sheet density was indicated by a red dotted line in the graph bars.

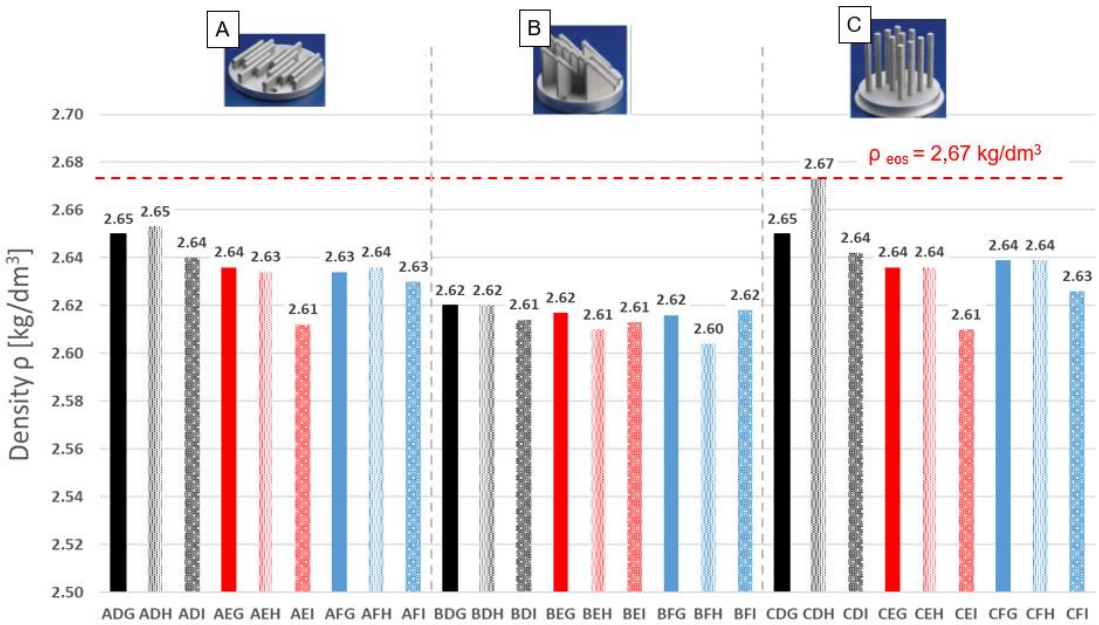

Figure 88: Density measurements for all the studied families

3.3.6 Fractographic analyses

Fractographic analyses were carried out to assess the fracture behavior. After the fatigue tests, all the fracture surfaces were checked by a stereoscopic microscope. A first result, shown in Figure 89, concerns the non-circularity of the horizontally manufactured specimens. As can be observed in the pictures, the actual specimen profile is far away from the theoretical circular one. The fracture surfaces are oriented with the crack initiation area in upward position. Moreover, in these series, the upper part of the image corresponds to the area, where supports were removed. An irregular geometry leads to a stress distribution with a trend that differs from the theoretical one and surface defects act as crack triggers. Also, if the geometry is significantly damaged, like in the ADG01 specimen, the gravity center of the sample shifts from the longitudinal axis, inducing vibrations during the fatigue tests. Consequently, results could be affected by errors, which lead to a worsening of the fatigue performance. Geometrical errors like those described above, were found in ADG, ADH, AEG and AEH series, which are those that exhibit fatigue performance being less than expected. Although AFG and AFH series are manufactured with the same orientation and surface finishing, a regular shape was found for them. This outcome indicates that the geometric errors are due to a careless removal of the supports, which occurred only for some specific sample sets. All the specimens involved in this experiment were manufactured by an external company, and we are not

able to control the production phases. Furthermore, they were delivered in different batches, which could mean that supports were removed by different operators. Even in slanted a regular shape was found, as is possible to see in Figure 90. Obviously, in machined samples, no geometrical errors were found for both horizontally and slanted orientations Figure 91.

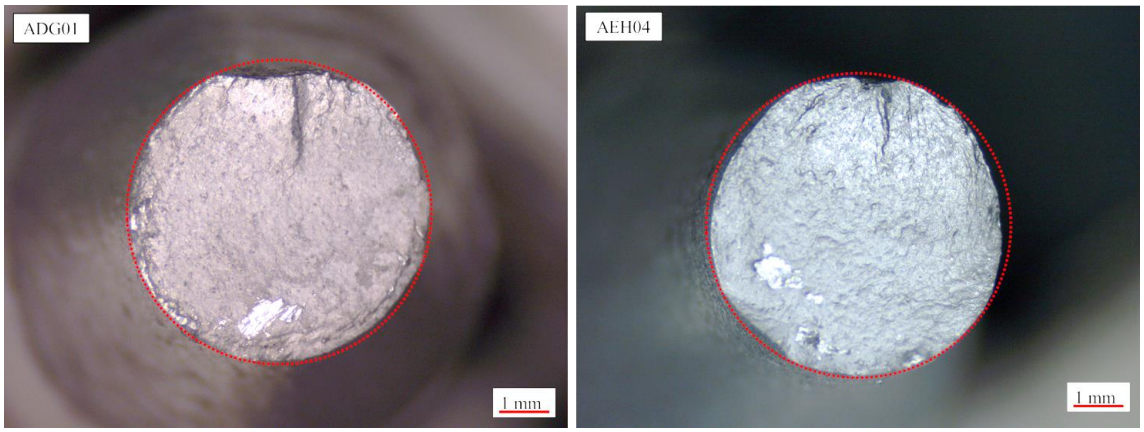

Figure 89: Stereoscopic images of fracture surfaces in horizontally built samples for shot-peened (ADG01) and shot-peened and fine blasted (AEH04) surface finishing.

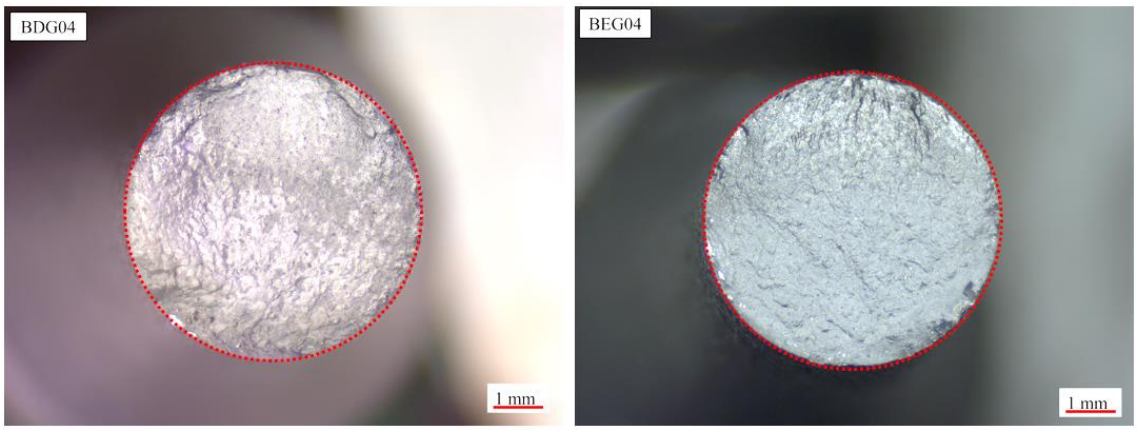

Figure 90: Stereoscopic images of fracture surfaces in slanted built and shot-peened samples

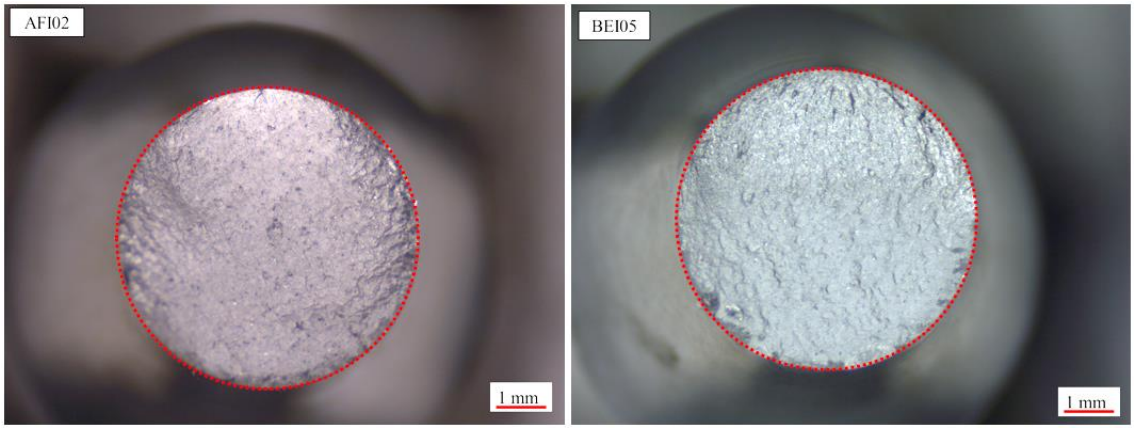

Figure 91: Stereoscopic images of machined specimens. Fracture surfaces of horizontally (AFI02) and slanted (BEI05) built samples.

The observation of the vertically built specimens made it possible to highlight some used scan parameters. Figure 92 shows a fracture surface of a vertically built and shot-peened sample in the as built condition.

The contour line, the angle between two successive layers and the hatch distance are clearly visible.

The hatch spacing was found to range from 150 to 180 µm. This value could alter the number and the dimensions of porosities and defects, affecting the fatigue life. In [3.12; 3.27], where the hatch spacing increased up to 220 µm, a lower fatigue strength was found. However, the measured value was found to be in a range that ensure a good fatigue behavior.

The contour was found to be equal to 250 µm, aligned with the literature survey. However, a study of Beevers et. All [3.11] shows a negative contribution of a 270 µm contour. In samples, where contour is not applied, a better fatigue performance was found, due to a more reduced surface roughness. Furthermore, numerous porosities, which can lead to fatigue crack nucleation, were found in the area between the contour and the internal net.

The amplitude of the angle between two layers was found to be equal to 68°, less than reported in [3.3; 3.28 - 3.29].

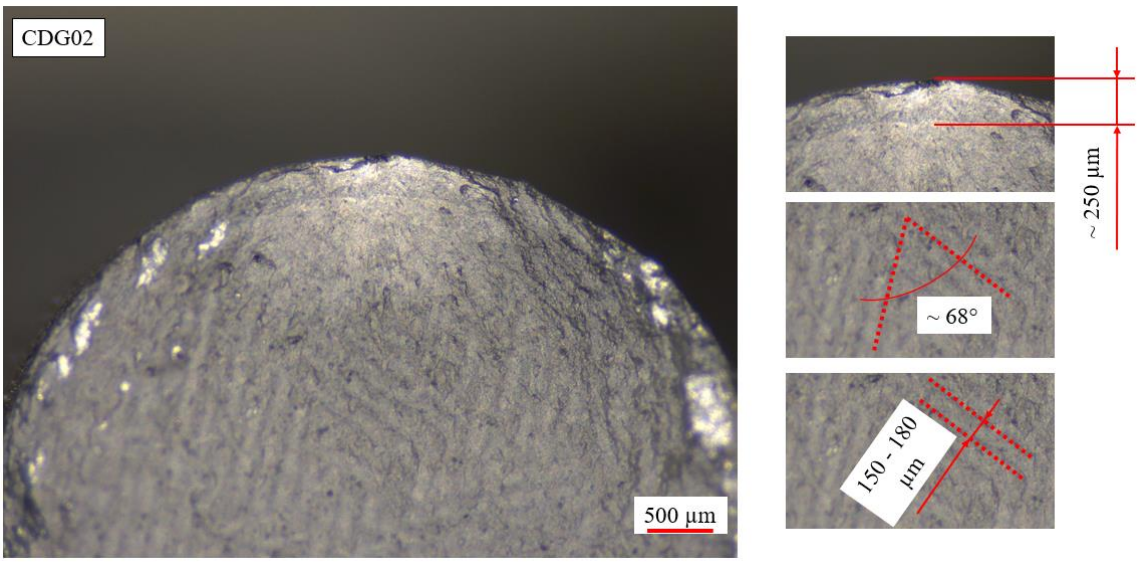

Figure 92: Stereoscopic images of vertically built specimen and details of the contour line, the overlapping angle and the hatch distance

By the stereoscope microscopy observations, it emerged that in the unmachined specimens fracture initiates from surface defects. For the horizontal series the initiating point is mostly located in the zones, where supports were present. Although there are no

supports in the gage of slanted series, the side of the specimens that was facing down has a worse roughness than that at the opposite side. Cracks mostly initiated on this side with the higher roughness, as expected. In machined samples, the initiating points were located in both surface defects and, especially, subsurface porosities, regardless of build orientation. Some examples of crack initiation source (CIS) observed by a SEM-FEM are shown from Figure 93 to Figure 95.

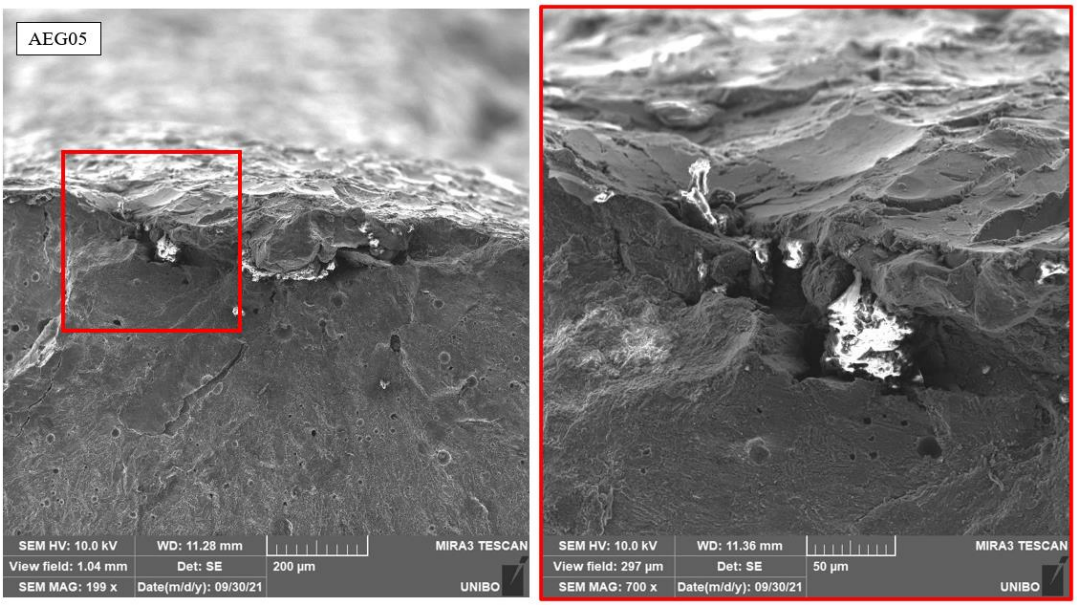

Figure 93: Crack initiation source due superficial and sub-superficial inclusions

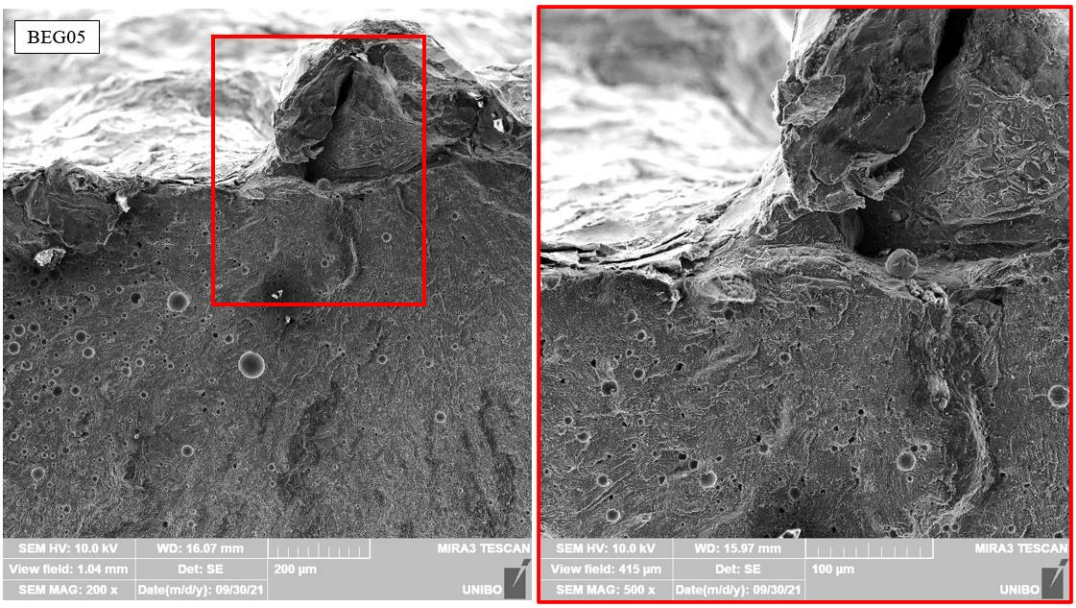

Figure 94: Crack initiating source from a superficial defect

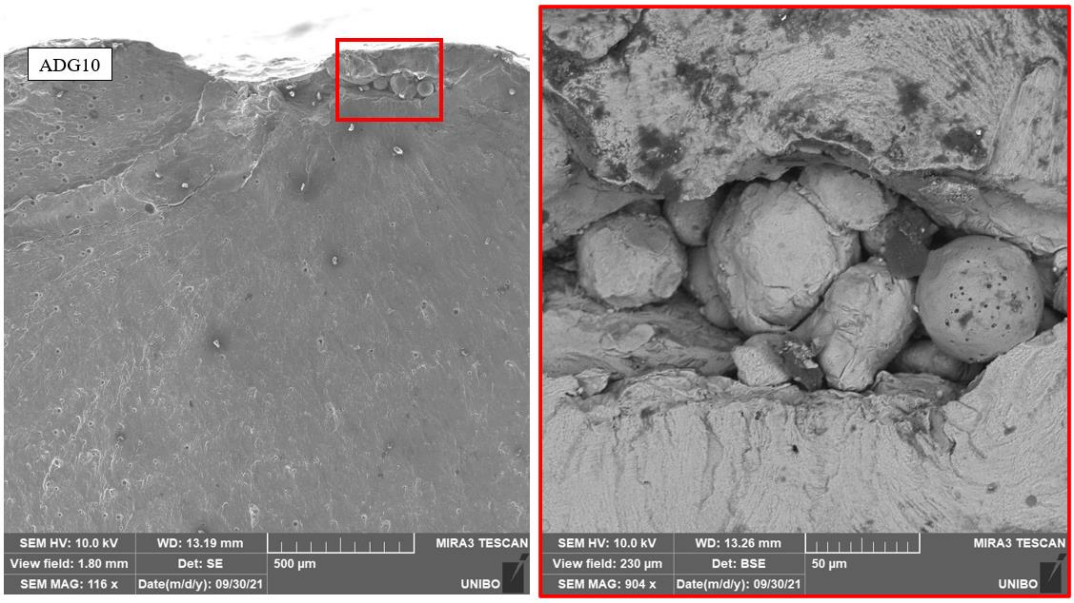

Figure 95: Crack initiation source from superficial imperfection and a detail un-melted powder.

Finally, high magnification SEM images were captured to investigate the fracture behavior (Figure 96). Specimens as built (xDx series) display a mixed (ductile and brittle) fracture behavior. The dimples structures, which appear on the overload fracture zone (OFZ) of T6 heat treated samples, indicate that the heat treatment increase the plasticity of the samples (ductile fractures). Dimples are not clearly visible in stress relieved specimens, indicating a mixed fracture behavior like in as built samples.

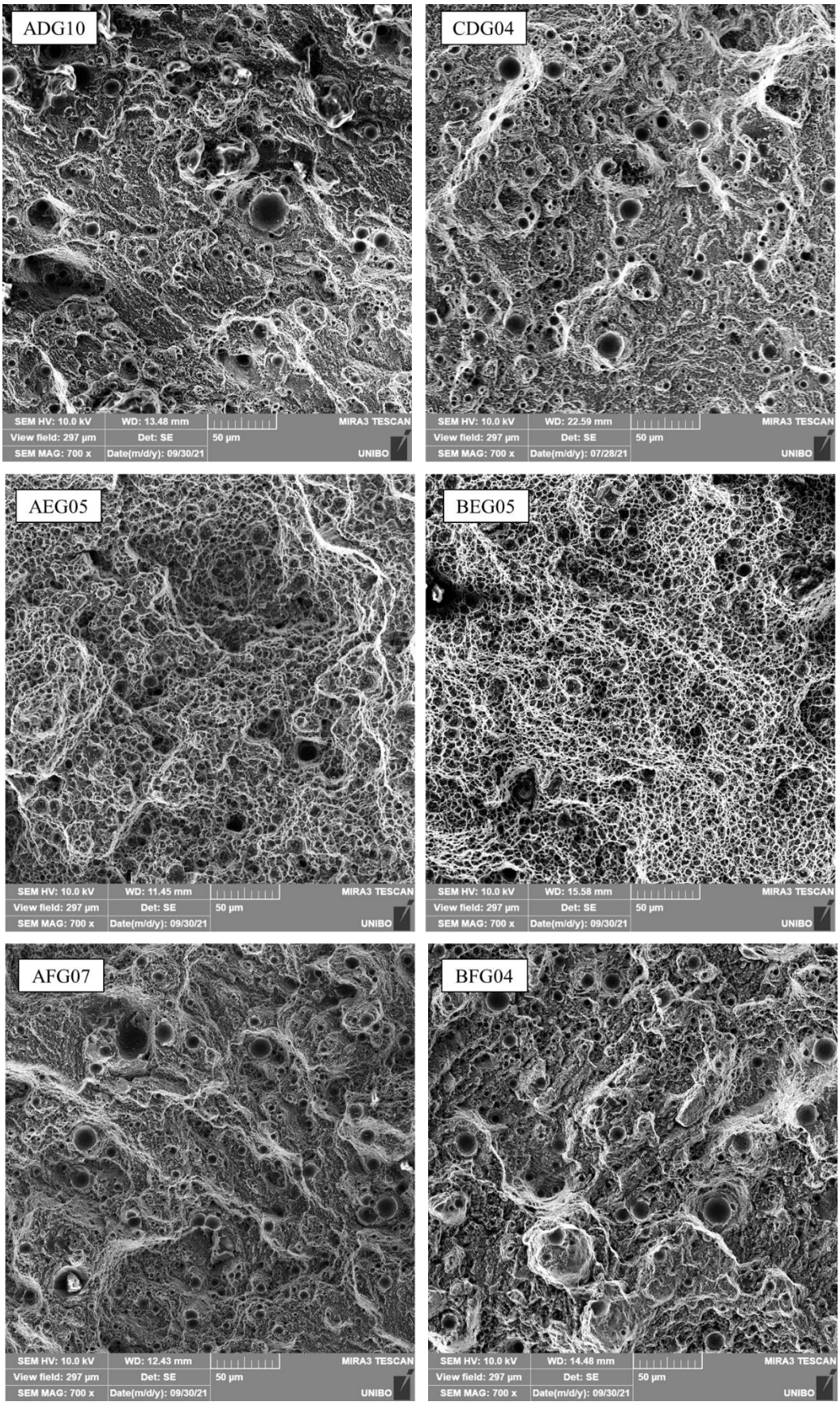

Figure 96: High magnification SEM images of the overload fracture zone (OFZ) for specimens as built (samples n° ADG10 and CDG04), T6 heat treated (samples n° AEG05 and BEG05) and stress relieved (samples n° AFG07 and BFG04).

3.3.7 Micrographic analyses

Micrographic analyses were performed to assess the microstructure induced by the considered heat treatment and to evaluate some used scanning strategies. The main steps to obtain the micrographies are provided below:

- Cutting of at least one section (of the sample gage) being parallel to the base plate and another one with perpendicular orientation: for this purpose, a cross cutting machine equipped with specific disks for aluminum alloys was used Figure 97. Samples were fixed in a clamp after a carefully checking the positioning. To obtain a section parallel to the base plate in slanted manufactured samples, the specimens have to be rotated with the higher roughness zone facing down and with the head that during the manufacturing process is next to the base plate facing up (Figure 98). During the cutting operation, the involved area was cooled by emulsified liquid.

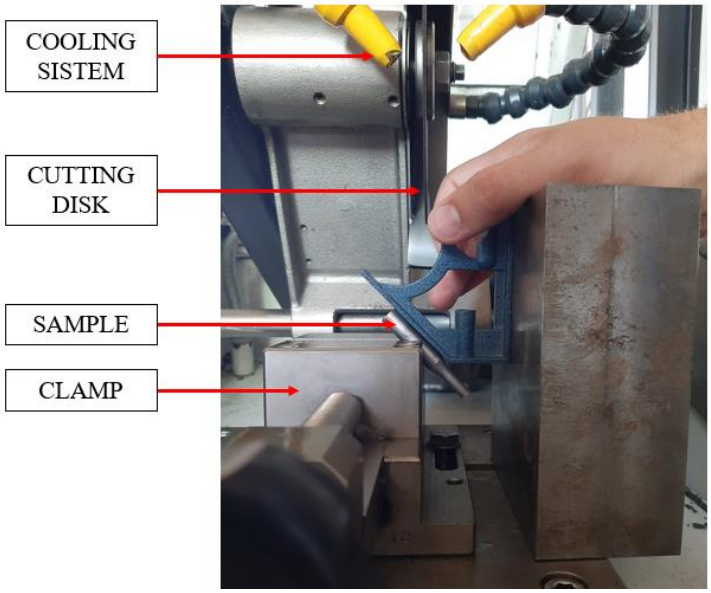

Figure 97: Positioning operation for cutting a section parallel to the base plate

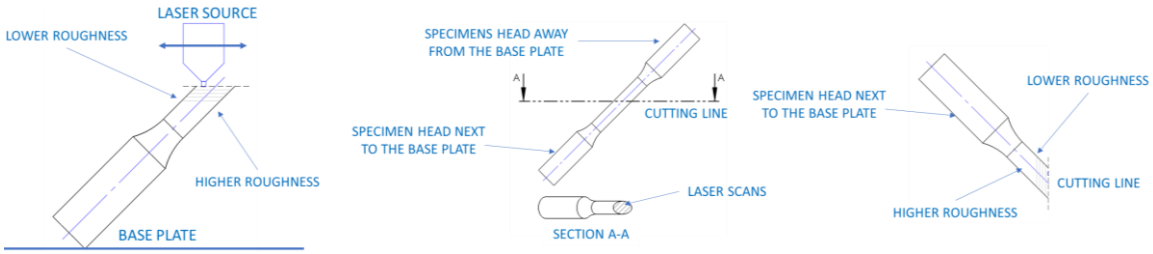

Figure 98: Positioning details in slanted manufactured specimens for a correct cutting operation

- Incorporation of the cut sections in a resin. If electrochemical tests are not needed, insulating resin was used. The incorporation facilitates cut sections handling subsequent observation.
- Polishing: a random orbital polisher was used for the operation. In this phase, the resin incorporated specimens are sanded with increasingly fine-grained papers (grain from P60 to P2500) and subsequently polished with cloth disks wetted by alumina powder dissolved in water (0.01 μm grain of alumina powder).
- The obtained surfaces were observed for the first time under an optical microscope, to evaluate the success of the polishing process. These images can be very useful for evaluating the porosity level of the section and the absence of scratches. In fact, if observed under an optical microscope, they appear uniform in color with black dots that correspond to the porosities. By using image processing software (ImageJ), it is possible to evaluate the percentage of black areas with respect to the areas of the base material, thus working out the porosity level of the section. By repeating this operation for multiple sections of the same specimen, a reliable estimate of the porosity of the entire sample can be obtained without using expensive and complex instrumentations.
- To highlight the microstructure, the surfaces were then chemically etched. The chemical reagent used is Keller's reagent. It was applied at room temperature for 27 seconds. Then, the specimens were washed by water and dried.

Figure 99 shows an example of micrographies captured by the optical microscope. Before the chemical etching, the surface appears uniform with black dots, as described above: this image can be used to evaluate the porosity level. After applying Keller's reagent, grains boundary oxidized highlighting the scanning strategy and the microstructure. As a first remark, scanning parameters could be carefully checked. Particularly, the hatch distance, the hatch angle and the contour were found to be the same for all the build orientations and aligned to those measured before and depicted in Figure 92.

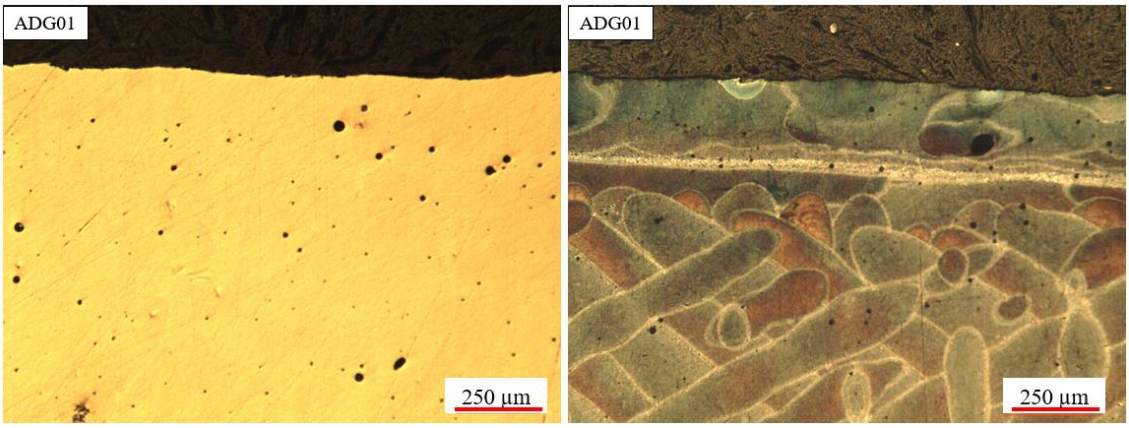

Figure 99: Optical microscope micrographies of a section parallel to the base plate of a horizontally as built sample before (on the left) and after (on the right) the application of the Keller chemical reagent

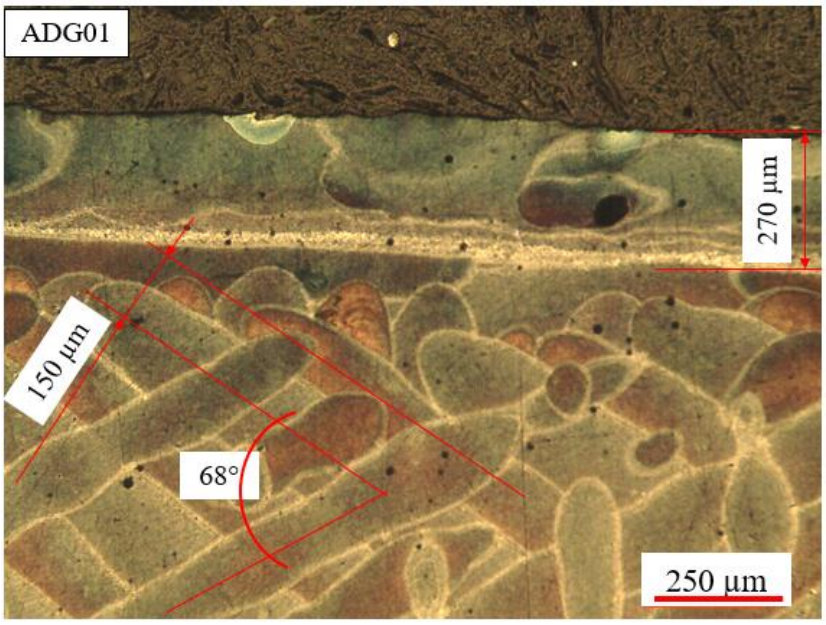

Figure 100: Optical microscope image of a section parallel to the base plate. A detail of some adopted scanning parameters

A cross section of a horizontally as built samples is shown in Figure 101.

As previously highlighted for fracture surfaces analysis, a section with remarkable circularity geometric errors can also be observed here. Figure 101a is captured by the stereoscopic microscope. Unlike the optical microscope, the used stereoscope has macro enlargements that allow to observe the entire sample section. The optical microscope was used to take pictures at higher magnification than those allowed by the stereoscope. Figure 101b shows the last manufactured layer, where melting pools, which are found to have 245 mm depth, are clearly visible. It was written above that failure in horizontally manufactured specimens always initiates in the zone, where supports were present. Causes appear very clear from the Figure 101c. A large number of porosities were found

in the areas affected by the supports. Geometric non-uniformities combined with high porosity cause stresses intensification that led to a premature fatigue failure. A final observation concerns the thermally altered zone in the supported area. In fact, the thermal flow is altered by the presence of the supports, that significantly affects the cooling rates. The structure appears similar to that obtained after the T6 heat treatment (as will be seen later).

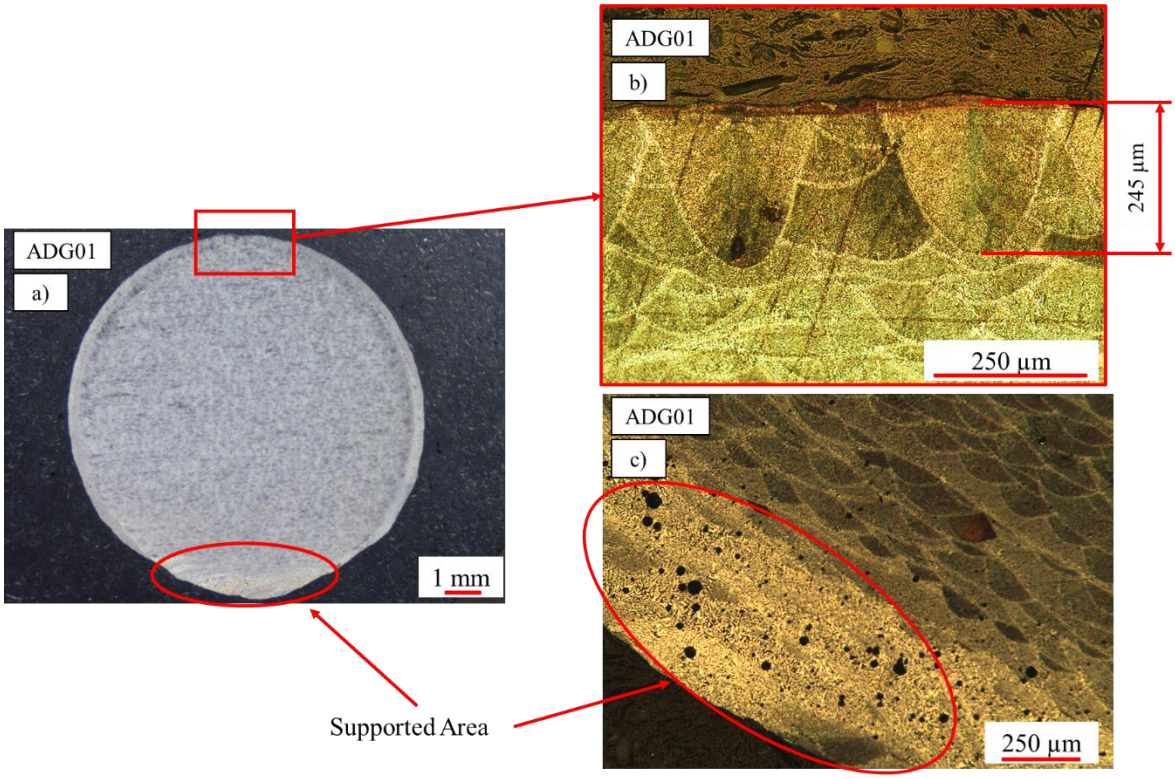

Figure 101: Cross section in a horizontally as built sample observed by a stereoscope (a). Details of the melting pools (b) and the supported area (c) captured by the optical microscope.

The effect of the heat treatment on the microstructure is visible in Figure 102 and Figure 103. From both the stereoscopic and optical microscope observations no differences between the as built condition and the stress relief condition were found. The scans can be distinctly seen in both cases, already based on the stereoscope acquisitions (Figure 102a and Figure 102e). Optical microscope micrographies show a smaller grain size within the scan, and larger in the overlap area between two adjacent passes (Figure 102b and Figure 102f). The high magnification SEM images indicate similar features cand be observed in the microstructure for both as built and stress relieved samples. The microstructure is made up of α-Al columnar grains with Silicon segregated at the boundaries (Figure 103a and Figure 103c). The α-Al and Si phases are distinguishable in the SEM images by gray and light gray colors, respectively. This microstructure is yielded by the fast cooling-rate

that the material experiences during processing, as reported in literature [3.17; 3.30 - 3.31]. The T6 heat treatment radically changes the microstructure. Even from stereoscopic images some differences appear: the section appears homogeneous and laser scans are not easily distinguishable (Figure 102c). A microstructure that keeps the same regardless of the build orientation was revealed by the optical microscope (Figure 102d).

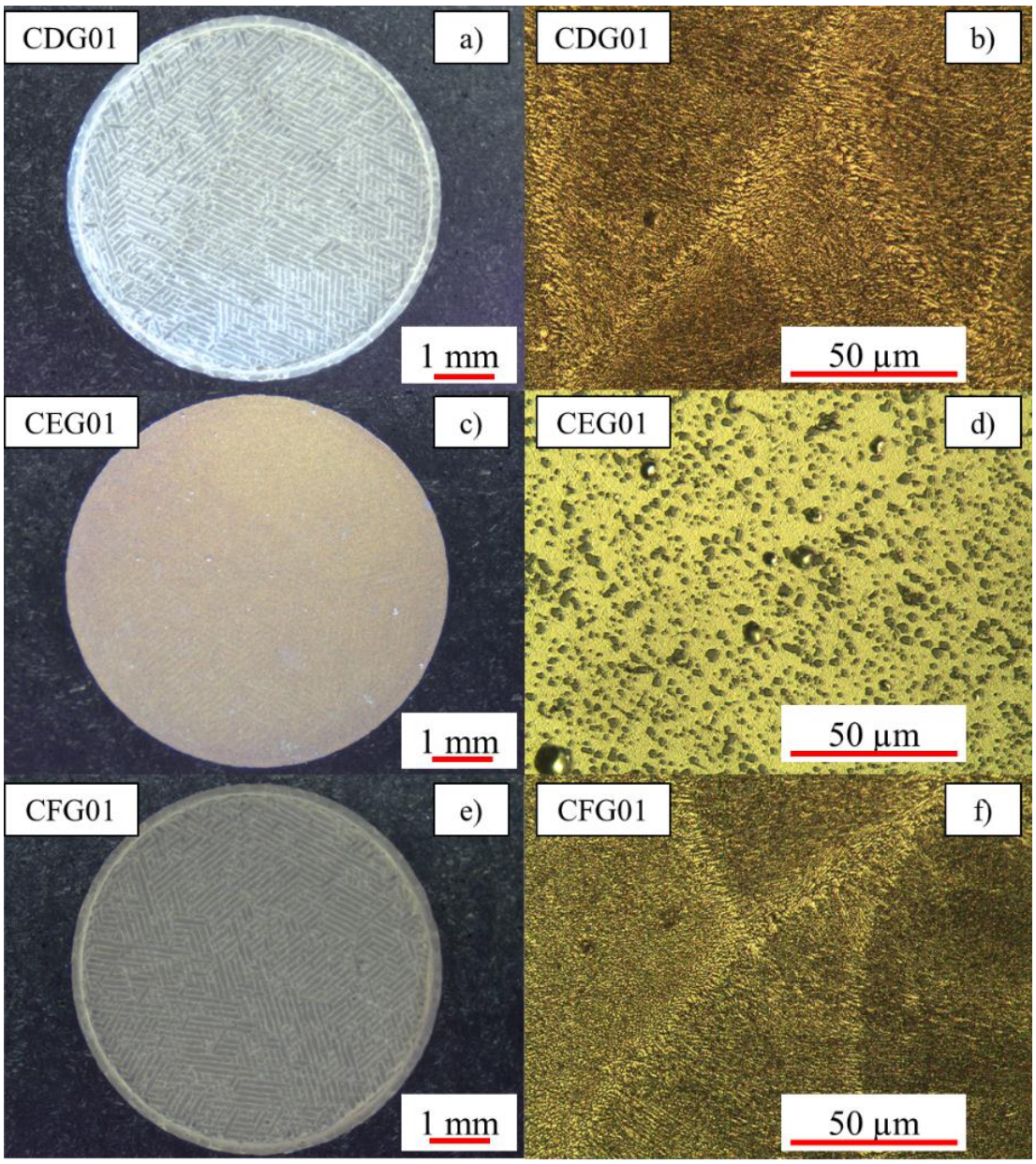

Figure 102: Stereoscopic images (a,c,e) and optical microscopic images (b,d,f) of chemical etched surfaces for samples as built (a,b), T6 heat-treated (c,d) and stress relieved (e,f).

High magnification SEM images (Figure 103b) highlight dendrite Si break into separate particles (light gray in the picture). After age hardening, Silicon particles exhibits a mean width of 2 µm.

The compound of Silicon particles and of Aluminum base was analyzed. Figure 104 shows the considered points and areas for the chemical analysis. For both the Silicon particles and Aluminum matrix two measurements were performed: AEG01.1 and AEG01.2 were taken at the center of the light gray particles, whereas AEG01.3 and AEG01.4 were taken in the base material. Further measurements of all the area in the picture was considered to check the mean chemical composition of the alloy (yellow square namely AEG01.5). The spectrums of the chemical compounds are reported in Figure 105, whereas the values are listed in Table 37.

The chemical analysis reveals light grey particles contain more than 93% of Silicon (points 1 and 2), whereas the base material mainly consists of Aluminum.

As regards the chemical composition of the considered area, a higher concentration of Silicon than that declared by the powder supplier was found (17% against the 9 - 11% expected, see Table 24).

Due to the discrepancies on the silicon value, further verifications were performed aimed at measuring the chemical composition in different parts of the specimen. In addition, samples from different families were also considered. Even in the latter cases, higher silicon concentrations than expected were found, each with very close values and an average of 15.9%.

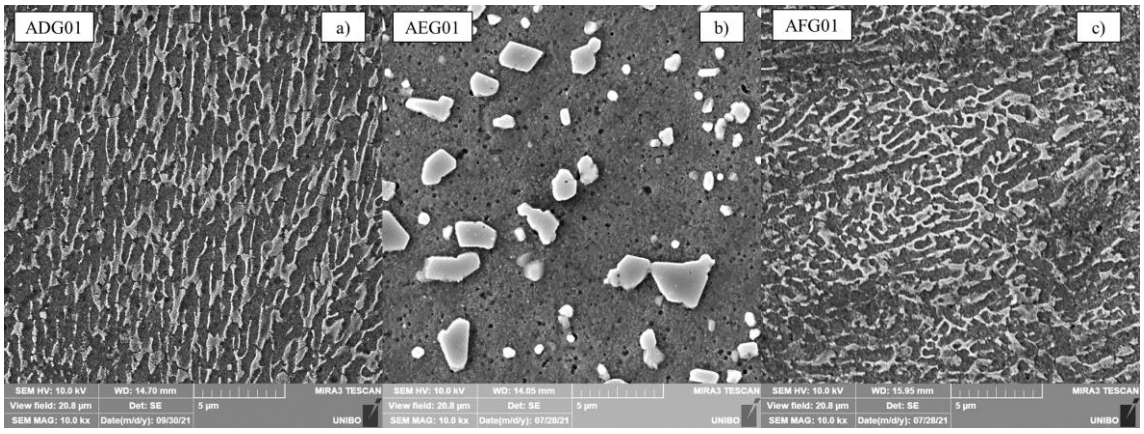

Figure 103: High magnification SEM images. Microstructure in as built samples (a), after T6 heat treatment (b), after stress relief (c).

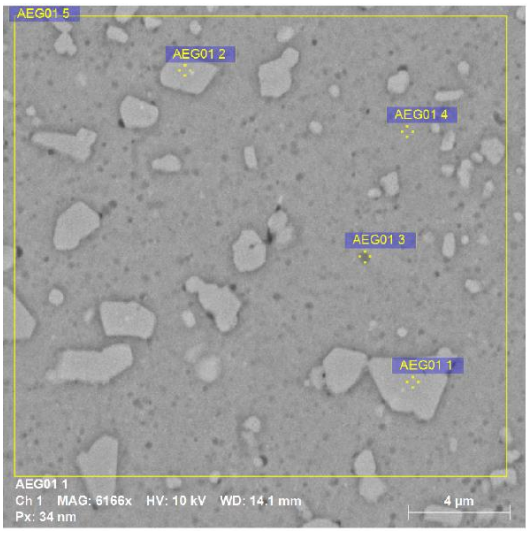

Figure 104: AlSi10Mg chemical compound analysis after age hardened. A detail of detected points and area.

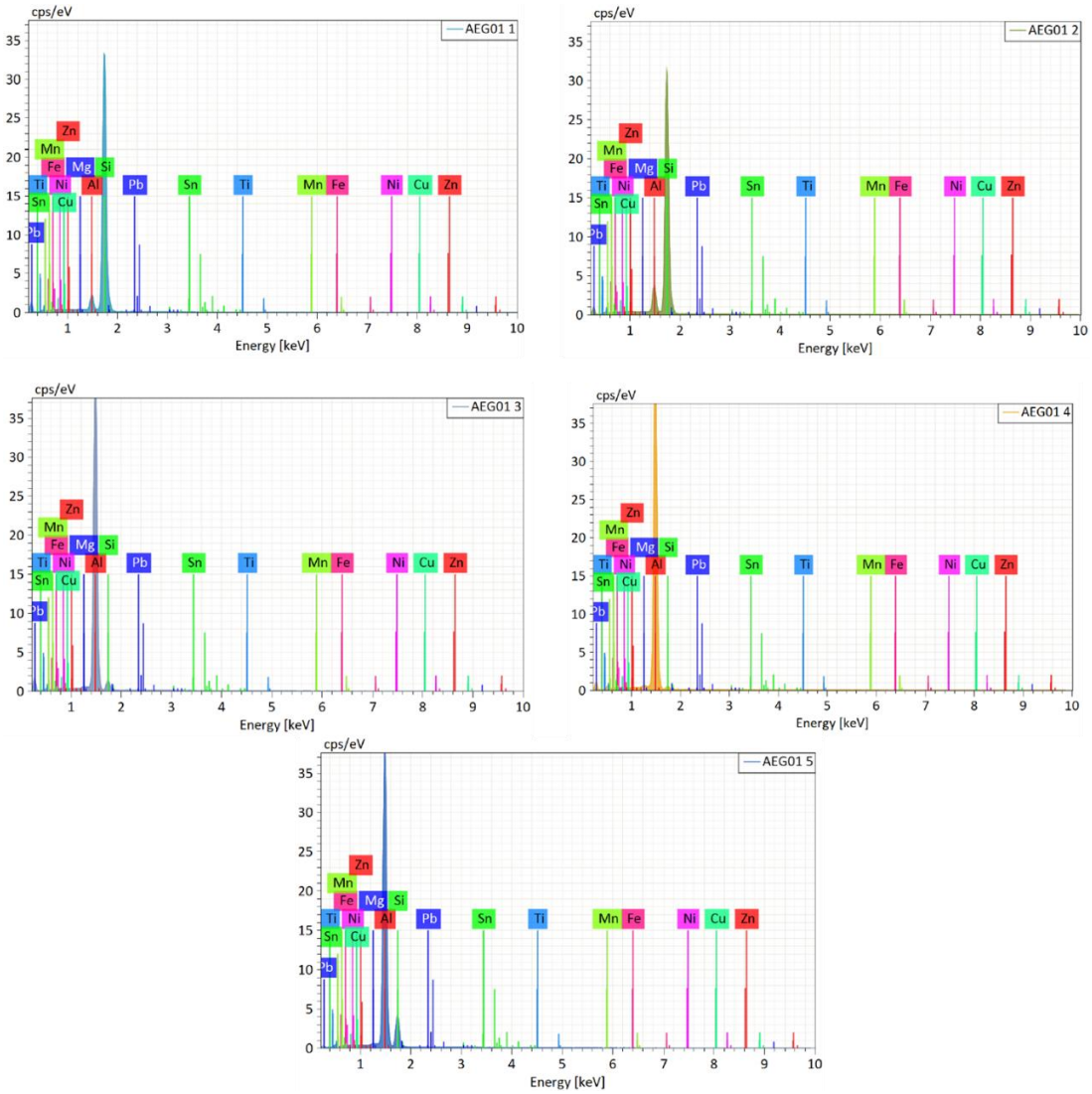

Figure 105: Spectrums of chemical compound for the considered points/area.

Table 37: Chemical compounds for the analyzed points/area

Spectrum	Mg	Al	Si	Ti	Mn	Fe	Ni	Cu	Zn	Sn	Pb
AEG01 1	0.07	2.94	96.46	0.00	0.38	0.01	0.00	0.04	0.00	0.10	0.00
AEG01 2	0.04	5.97	93.11	0.00	0.03	0.62	0.00	0.00	0.00	0.06	0.16
AEG01 3	0.08	92.50	6.68	0.16	0.37	0.20	0.01	0.00	0.00	0.00	0.00
AEG01 4	0.15	98.94	0.67	0.00	0.01	0.00	0.02	0.02	0.00	0.11	0.08
AEG01 5	0.80	80.10	17.24	0.11	0.00	0.08	0.43	0.64	0.55	0.00	0.05

3.3.8 Conclusions

In the light of the results emerged from the tests described above, several conclusions can be drawn.

As a first one, all the considered factors, namely the build orientation, the heat treatment and the surface treatment, do significantly affect the additively manufactured AlSi10Mg fatigue behavior.

However, the factors also interact each other. In fact, the effect of each one depends by the level of the other factors.

Regarding the heat treatments, it has been highlighted that the performed stress relief treatment does not lead to improvements of the fatigue life. Moreover, in some cases, it even leads to worse fatigue strength.

The T6 heat treatment has a remarkably positive effect on the fatigue life, which arises from an increase of ductility and a completely microstructure homogenization. In T6 heat treated samples, no differences in terms of fatigue strength were found for all the considered build orientation, meaning it was significantly beneficial regardless of the part build orientation. Therefore, it appears to be advisable to apply this treatment. However, conflictual results regarding this point have been found in the literature. In agreement with what the present outcomes, in an improvement of the fatigue strength, following the application of T6 heat treatment, was observed in [3.1]. On the other hand, according to [3.29; 3.31], generation and coarsening of separated Si particles, due to age hardening, may result in the decrease of mechanical and fatigue properties.

The occurrence that different results were obtained with the same heat treatment suggests that there are additional factors to be considered, as they may interact with the heat treatment. A clear and complete description of all the actually used process parameters is often missing in the literature. Therefore, it is often difficult to reliably compare the results based on the same input factors.

With regard to surface treatments, some recommendations can be drawn. Machining was found to be the least performing in terms of fatigue life at high number of cycles. The

best results were obtained for shot-peened families. In fact, residual compressive stresses, which are beneficial from the point of view of fatigue strength, are induced in the specimen outer layer after shot-peening. Conversely, following machining, the outer layers are removed, thus eliminating the beneficial effect of shot-peening.

On the other hand, machining allows removal of the defects located in these layers, mainly at the interface between contours and internal scans. In fact, the performance differences between the machined series were very small and appear to be mainly dependent on the carried-out heat treatment and independent of the build orientation. Furthermore, as it can be seen in Appendix, machined specimens led to less scattered fatigue data.

Although the possibility of obtaining shapes that are difficult or impossible to achieve by conventional machining, is one of the most advantages of additive process, some issues may arise for very complex geometries. When it is difficult to perform machining, it is advisable to keep a larger component dimensioning, especially for highly stressed components in the zone, where supports are applied. In fact, geometric errors and high porosities were found in unmachined samples, particularly in the area facing the base plate or where supports were detached. Stress concentrations are induced at this area leading to premature failure.

The highest fatigue limit was observed for slanted, T6 heat treated and shot peened samples (BEG series). However, in this case too, the fatigue strength was a little under expectations. The calculated fatigue limit is 62.8 MPa, whereas the supplier provides a limit of 110 MPa for machined and non-heat-treated specimens.

Static tensile tests also highlighted lower performance than that declared by the powder supplier: the achieved yield strength and elastic modulus were aligned with those expected, whereas the ultimate tensile strength was even 20% lower than the declared.

The analysis on the alloy compound showed a Silicon percentage outside the imposed limits (15% against a range of 9-11%). This reason could explain the observe performance differences.

3.4 The Stainless Steel CX

3.4.1 The experimental plan

The stainless steel CX is an innovative alloy for additive manufacturing processes. To date, no results about fatigue properties are available yet. As repeated several times in the previous paragraphs, process and post process parameters can alter the mechanical characteristics. Starting from the process parameters suggested by the powder supplier, and knowing that post manufactured treatment, like heat and surface treatments, could alter the fatigue response, a two-factor experimental plan was investigated. The first considered factor was the heat treatment: the response without and with heat treatment was assessed. The second considered factor concerned machining: the response of unmachined samples, to be regarded as the zero level, was compared to that of ground specimens.

In the supplier datasheet [3.22], the build orientation appears no to affect the mechanical properties. Therefore, in this thesis, the build orientation was not considered. All the specimens were vertically manufactured and produced during a single production process (one batch). EOSINT M290 machine equipped with Ytterbium fiber laser with 400W power, with working space 250 mm wide and 250 mm long was used. The production process used the EOS standard direct part set, recommended as default for industrial applications, with layer thickness of 30 μm and building volume rate of 3.2mm^3/s. Fresh powder was used for sample production, meaning that totally new (not recycled) powder was used upon fabrication.

The followed experimental design is summarized in Table 38: four sets were built: “NN” (not heat treated and not machined), “HN” (heat treated and not machined), “NM” (not heat treated and machined) and “HM” (heat treated and machined). Fifteen specimens were built for each combination, for a total of sixty samples. After the stacking process the samples of the “NN” type underwent shot peening that was performed by stainless steel shots with 0.7 mm diameter driven by air stream under 5 bar pressure. As for the aluminum, this treatment is usually carried out to close the surface porosities and to induce a beneficial compressive residual stress state aiming at balancing the stacking process-induced positive residual stresses. Set HN samples were treated by shot-peening as above and then underwent heat treatment according to the following procedure. This was split into two stages: solution annealing and aging, whose details are provided in the points below.

Solution annealing

- Heating up to 900°C with heating rate around 5.5-6°C/min.
- Parts kept at the controlled temperature of 900°C for 45 minutes.
- Rapid cooling in compressed air stream from 900°C to 150°C with 150°C/min cooling rate.
- A further cooling from 150°C to room temperature with cooling rate around 10°C/min.

Ageing phase

- Heating from room temperature to 530°C with heating rate around 5.5-6°C/min.
- Parts kept at the controlled temperature of 530°C for 3 hours.
- Cooling in a furnace to the room temperature.

It must be remarked it is consistent with that recommended by EOS in [3.22]. However, very few details are available in the scientific literature and in supplier datasheets regarding the practical procedure to conduct this treatment and specially to comply with the strict specifications related to cooling or heating rates. From this point of view, the conducted procedure was highly demanding, as it required a controlled argon flow (around 1.5 litres/minute) to assist heating as well as rapid cooling.

Samples of the "NM" type (Non-heat treated and Machined) were initially ground with 0.5 mm allowance. Afterwards, they underwent shot-peening according to the specifications above. In previous studies dealing with on Maraging Steel it was found that beneficial effects are given on the fatigue response by peening treatment, when it is performed after machining [3.5]. As highlighted in this Ref., powder suppliers usually recommend to run shot-peening before machining. However, proceeding this way, the treated layer is completely removed, thus making the peening treatment barely ineffective. Conversely, running shot-peening after grinding makes it possible to take advantage of the peening-induced compressive residual state. Since this positive effect is not strictly related to material properties, it is reasonable to think that it may also apply to the CX stainless steel.

Fatigue tests were run at 100 Hz. The samples were fatigued until failure or up to 10^7 cycles, to be regarded as runout. The tests were devoted to the determination of the S-N curves in the finite life domain and of the fatigue limits for infinite life.

Table 38: Experimental plan involved stainless steel CX samples.

		Factor 2: Surface condition	
		Shot peened	Machined and shot peened
Factor 1: heat treatment	No heat treated	Type NN	Type NM
	Heat treated	Type HN	Type HM

3.4.2 Preliminary checks

As for the aluminum samples (3.3.2), diameter and the roughness measurements were performed to check the compliance with design specifications. Six diameter measurement and eight roughness measurements were taken at the gage. The mean value and the standard deviation of the performed measurements are listed in Table 39. As the specimens were vertically manufactured, good diameter accuracy was ensured. The roughness in non-machined specimens was slightly higher than those in the supplier datasheet (about 5 µm), especially in the heat treated and non-machined set (HN). The roughness of machined samples was consistent with the performed process.

Table 39: Mean values of the gage diameters and the gage roughness for the four considered series

Gage diameter [mm]				Gage roughness [µm]		
	Mean Value	St. Dev.			Mean Value	St. Dev.
N N	5.943	0.016		N N	6.456	1.054
H N	5.998	0.014		H N	13.021	1.619
N M	6.041	0.004		N M	1.810	0.372
H M	6.027	0.005		H M	1.136	0.282

Rockwell Hardness (HRC) measurements were also carried out, running 3 measurements per sample. Only machined samples were involved in this analysis, in order to avoid hardness measurements being altered by surface asperities in unmachined samples. To not damage the gage, measurements were taken on 120° equally spaced points at sample heads. The results were worked out based on the recommendations in [3.32], in order to consider the actual convex surface curvature, thus properly correcting the experimental yields. Hardness measurements are 31.0 ± 1.5 HRC, when considering not heat-treated material (Set NM), and 47.0 ± 0.9 for Heat-treated material (Set HM). Confidence intervals take the worst scenario of twice the standard deviations into account.

3.4.3 Fatigue tests

Even for the maraging stainless steel CX, the S-N curves were determined complying with Standard ISO 12107. Confidence bands were determined corresponding to 10 and 90% probabilities of failure and 90% confidence level. According to Standard prescriptions, both the linear and the quadratic model were implemented and the General Linear Test was applied to assess whether the improvement yielded by the quadratic model was significant. However, it always proved to be negligible; therefore, the linear interpolation model was applied instead. The fatigue limits were worked out by abbreviated staircase (averagely, 7 nominal specimens) based on the Dixon method [3.33].

Given the more limited specimens number compared to the aluminum alloy experiment (60 CX instead of 270 AlSi10Mg specimens), all the fatigue test details are reported in Table 40. The table provide specimen identifier, the applied load and the observed life. When the test was stopped with un-failure outcome, "Run-out" achievement is highlighted instead. All the results were processed by the linear model being expressed by Eq. 3.19, which can be turned into Eq. 3.20. The calculated coefficients b_0 and b_1 are collected in Table 41. Figure 106 shows all the fatigue S-N curves in the finite life domain along with the related experimental points.

The plots in Figure 106 suggest that both machining and the heat treatment have a positive effect on the fatigue performance. The same ANOVA-based extended statistical method used for the aluminum experiment was applied here to properly compare the S-N curves. In particular, the two-factor design were addressed, in order to assess whether the visible differences among the curves are significant, if compared to the scattering of the experimental campaign. The outcome of the statistical assessment is reported Table 42 and can be commented with reference to the plots in Figure 106. The conclusion was that both heat treatment and machining significantly affect the fatigue life. Moreover, the two factors have a strong interaction. Glancing at the plots in Figure 106, it is possible to highlight the heat treatment effect. Except for lower cycle numbers (where the curve for Set NN crosses those for the HN and NM sets), the curves of the heat-treated specimens HN and HM are generally higher than those for non-heat-treated conditions, i.e., NN e NM. This outcome highlights the performed heat treatment remarkably enhances the fatigue strength regardless of surface conditions. At the same way, curves for sets with and without machining can be compared: NM and HM series generally exhibit higher strength than the unmachined sets NN and HN, apart for curve crossing under 10^5 cycles.

The S-N for the NN set drops down sharply due to the high roughness, which is not mitigated by the beneficial impact of heat treatment.

Table 40: Stress amplitude and cycles to failure for all the CX samples tested

Specimen ID	Stress Amplitude [MPa]	Cycles to failure [N]	Failure / Run-out	Specimen ID	Stress Amplitude [MPa]	Cycles to failure [N]	Failure / Run-out
NN01	250	232,776	Failure	NM01	290	-	Run-out
NN02	210	178,020	Failure	NM02	370	-	Run-out
NN03	150	482,491	Failure	NM03	490	1,188,897	Failure
NN04	130	-	Run-out	NM04	470	-	Run-out
NN05	140	401,602	Failure	NM05	530	410,073	Failure
NN06	130	437,264	Failure	NM06	570	94,880	Failure
NN07	120	-	Run-out	NM07	510	3,021,711	Failure
NN08	130	807,573	Failure	NM08	490	3,684,946	Failure
NN09	120	507,927	Failure	NM09	470	3,637,581	Failure
NN10	180	193,414	Failure	NM10	450	6,663,286	Failure
NN11	150	516,068	Failure	NM11	430	7,051,186	Failure
NN12	140	496,799	Failure	NM12	470	4,721,623	Failure
NN13	180	260,096	Failure	NM13	510	455,715	Failure
NN14	160	340,074	Failure	NM14	530	285,329	Failure
NN15	160	239,176	Failure	NM15	570	90,763	Failure
HN01	530	30,068	Failure	HM01	570	5,107,225	Failure
HN02	450	146,459	Failure	HM02	610	2,019,502	Failure
HN03	410	154,817	Failure	HM03	650	2,517,512	Failure
HN04	330	4,275,075	Failure	HM04	530	-	Run-out
HN05	290	815,554	Failure	HM05	550	9,172,727	Failure
HN06	270	-	Run-out	HM06	530	5,409,167	Failure
HN07	290	2,496,471	Failure	HM07	510	-	Run-out
HN08	270	733,711	Failure	HM08	530	7,915,220	Failure
HN09	270	-	Run-out	HM09	510	7,727,850	Failure
HN10	290	-	Run-out	HM10	490	-	Run-out
HN11	330	338,580	Failure	HM11	510	9,953,979	Failure
HN12	370	67,344	Failure	HM12	570	6,582,830	Failure
HN13	370	51,895	Failure	HM13	610	4,278,751	Failure
HN14	330	111,571	Failure	HM14	650	657,022	Failure
HN15	410	57,290	Failure	HM15	690	1,868,941	Failure

$$\boldsymbol{Log(N) = b_0 + b_1 \cdot Log(S)} \qquad \textit{Eq. 3.19}$$

$$S = 10^{\frac{b_0}{b_1}} \cdot N^{-\frac{1}{b_1}}$$ *Eq. 3.20*

Table 41: Coefficients of the determined S-N curves, according to the linear model of ISO 12107

Set #	b_0	b_1	$10^{b0/b1}$	$-1/b_1$
NN	9.441	1.768	218742	-0.566
HN	18.955	5.354	3470	-0.187
NM	52.247	17.114	1129	-0.058
HM	21.559	5.390	9996	-0.186

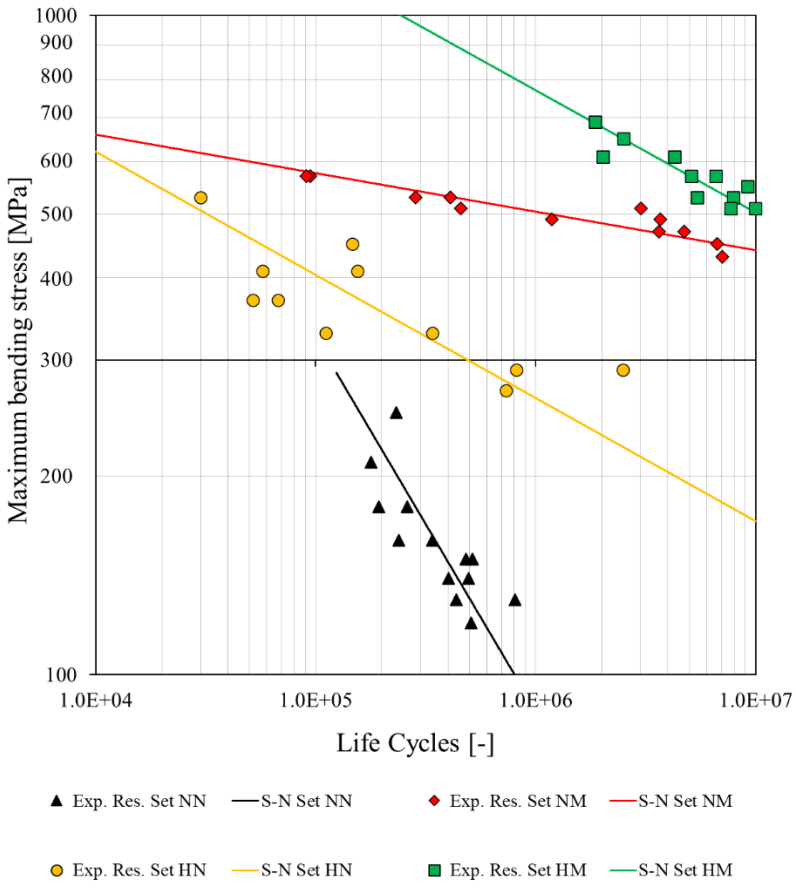

Figure 106: Stainless Steel CX S-N curves in the finite life domain for all the samples

The interaction effect may also be discussed, based on curves trends. This point may be addressed, comparing the slopes the curves, being related to the coefficient b_1 (Table 41) of curve equations in the logarithmic scale. Interaction generally arises from a different effect of one factor, depending on the current level of the other one. In the curves of the HN and HM series, the coefficient b_1 assumes approximately the same value and, in fact,

their slopes keep approximately the same. This means that for heat-treated series, the improvement yielded by surface grinding is the same both for low and for high life cycles regimes. On the other hand, the S-N curves for the NN and NM sets have considerably different slopes and their the b_1 coefficients are also highly different. This outcome indicates that, when heat treatment is not performed, machining leads to a noticeable fatigue enhancement under not high loads corresponding to high life cycles regime. Therefore, the effect of machining is different in untreated and treated parts. It can be easily observed that the effect of heat treatment also keeps different for unmachined and machined parts.

Table 42: Analysis of variance results for CX samples

	Sums of Squares	**Degrees of Freedom**	**Sums of Squares after scaling**	**Fisher's ratio**	**p-value**	**Significant?**
SSBR: Effect of Heat Treatment	0.0826	1	0.0826	30.85	$2.16 \cdot 10^{-6}$	YES
SSBC: Effect of Machining	0.2831	1	0.2831	105.65	$1.17 \cdot 10^{-12}$	YES
SSI: Interaction	0.0483	1	0.0483	18.03	$1.30 \cdot 10^{-4}$	YES
SSE: Error (data scattering)	0.1045	39	0.0027			
Total	0.5185	42				

The fatigue curves along with their confidence bands are singularly plotted in Figure 107. The Fatigue Limit (FL) nominal values are displayed in the bar graph in Figure 108, where the corresponded confidence intervals at the 90% confidence level are also appended to the bars.

The bar graph highlights and confirms the beneficial effects of both heat treatment and allowance for machining. Taking the samples type NN (not treated and not machined) as reference, heat treatment without machining leads to more than doubled FL (fatigue limit). On the other hand, grinding without heat treatment has the capability of remarkably incrementing the FL by a factor three. The combination of heat treatment and machining with subsequent shot-peening leads to a further improvement: the FL for set HM appears to be more than four times increased with respect to that for type NN. The HM series results the best studied combination. The reasons for this result can be justified based on several argumentations. It is known that a poor finish worsens the fatigue properties. The machining process drops down surface roughness, which is reduced from 6-13 μm to 1μm or less, thus making the surface smoother and reducing the number of potential crack

nucleation sites. Furthermore, the removal of the outermost layers erases the external contours that are usually the most affected by detrimental porosities and voids. On the other hand, heat treatment has the capability of relaxing the stacking process-induced tensile residual stresses that detrimentally affect the fatigue response and of making material structure more uniform. An interesting point for design purposes is the estimation of the ratio between the determined fatigue limits and the ultimate tensile strength (UTS) declared by the powder supplier in [3.22] with and without heat treatment. A 0.5 ratio between fatigue limit and ultimate tensile strength is commonly accepted for metallic wrought materials [3.34], but this generally does not apply to additively processed parts [3.24 - 3.25]. To properly tackle this question, two dashed lines have been appended to the bar graph in Figure 108, in order to indicate the levels corresponding to 50% of the UTS in the two conditions above.

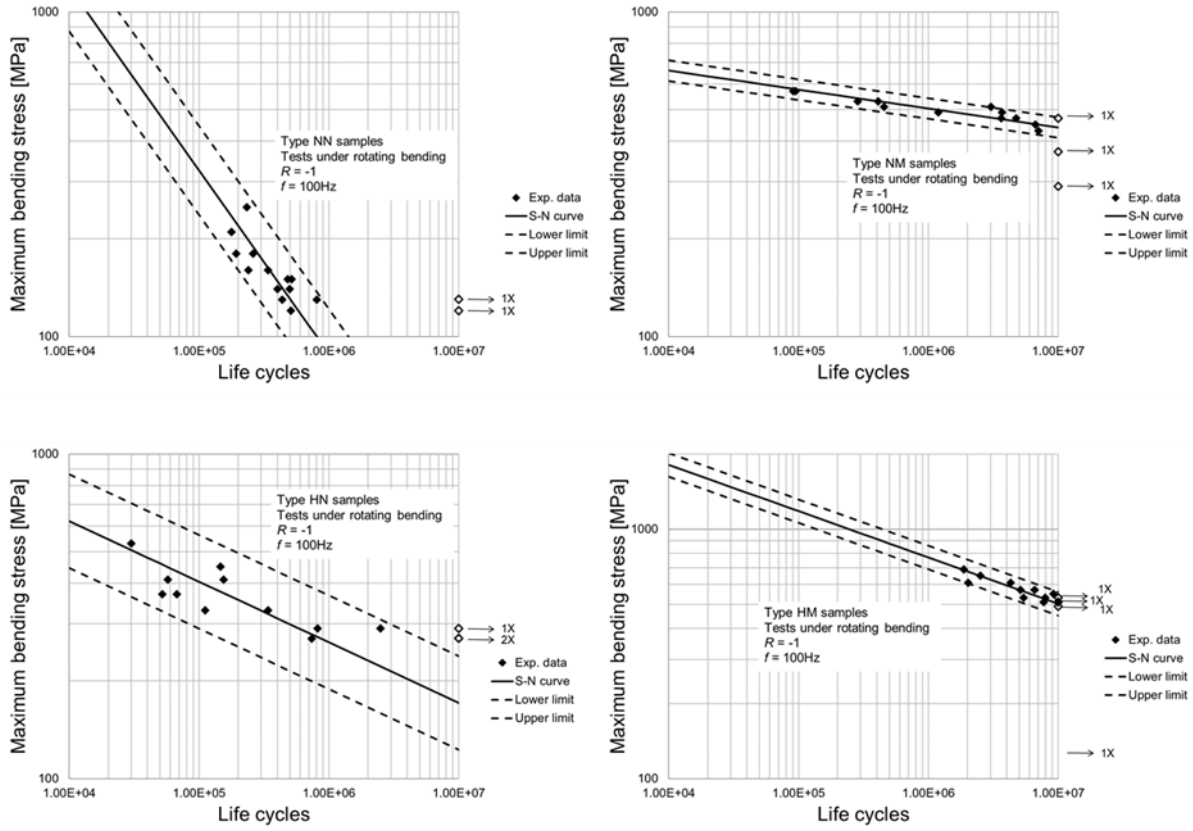

Figure 107: Stainless Steel CX S-N curves with upper and lower bounds, according to ISO 12107

It is worth mentioning that the ratio between the FL and the UTS is sharply incremented by machining, when considering untreated samples: from 0.11 to 0.41. This is also increased for heat treated samples from 0.16 to 0.29. This latter value is indeed lower than the previous one and also keeps much lower than 50% of UTS for treated material. An important outcome is the 0.29 fatigue limit versus UTS ratio for treated and machined

samples is very close to the corresponding values retrieved for Maraging steel MS1 and for Stainless Steel 15-5 PH1 [3.5 - 3.6; 3.24 - 3.25] and, therefore, may be assumed as a reference for design for this class of materials. A further remarkable outcome is that machining parts, even without heat treating them, can be regarded as a highly efficient combination. On one hand the ratio over UTS is the highest one and very close to 0.5, on the other hand the corresponding fatigue limit keeps very close to the highest one retrieved for the head treated and machined samples (450MPa against 510MPa).

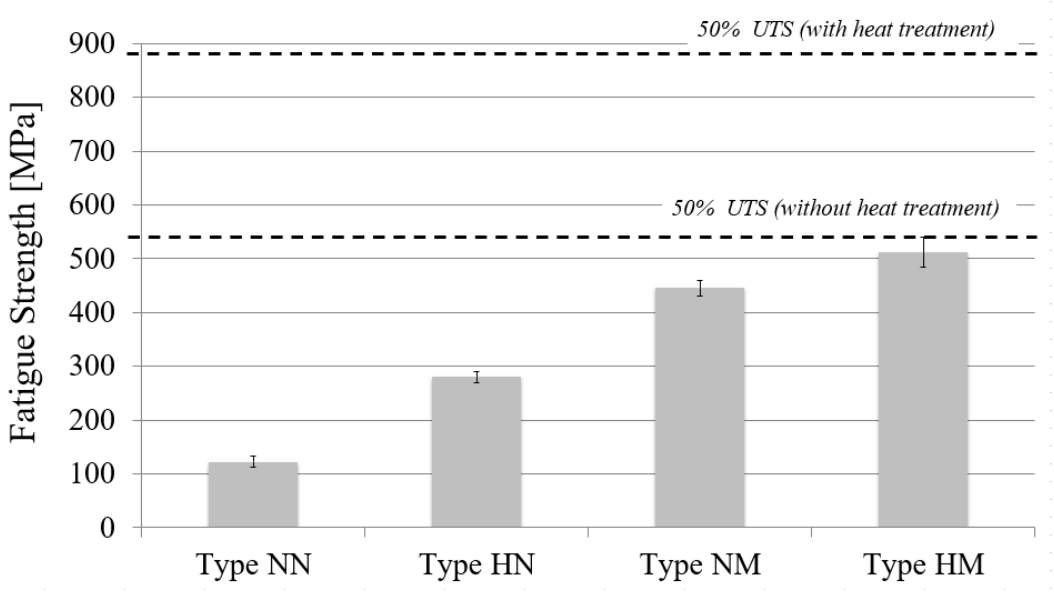

Figure 108: Stainless Steel CX Fatigue strength at 10 million cycles

3.4.4 Porosity evaluation

To estimate the porosity level, density analyses were performed by the immersion method. As in 3.3.5, three measurements for each sample were carried out. The mean values of each Set are shown in Table 43, in terms of average density and as a percentage with respect to the declared data by EOS [3.22] that is equal to 7.69 g/cm3.

Table 43: Stainless Steel CX density measurements

	Measured density [kg/m^3]	**Relative density (declared density by EOS [24]: 7,690 kg/m^3)**
Set NN	7,651	99.5%
Set HN	7,631	99.2%
Set NM	7,674	99.8%
Set HM	7,666	99.7%

Not remarkable differences were observed: the retrieved data were all aligned and greater than 99% the declared value by the powder supplier. A 0.5-1% average level of voids is usually commonly accepted and consistent with the specifications of most powder suppliers [3.22; 3.35]. However, it could be argued that relative density estimates are highly affected by the declared value by the supplier. In other words, the porosity level is estimated indirectly, based on this input. Therefore, in order to confirm, the previous result, a further analysis was carried out. Three specimens per type were cut along the longitudinal and transverse directions. The surfaces were then polished and observed by stereoscopic measurement. In these conditions, without any chemical etching, a large part of the area generally appears black. The presence of porosities is highlighted by a different light reflection that makes them appear bright. The images were then processed, turning them into grayscale and reversing the colors. A processed image with inverted colors is displayed in Figure 109a with reference to a longitudinal section (i.e., along the sample main axis of inertia, along the build orientation) of a machine sample. Another image is shown in Figure 109b with regard to an unmachined sample. In this case, a cross section (build surface) is displayed. Related details, with corresponding scales are provided in Figure 109c and Figure 109d respectively.

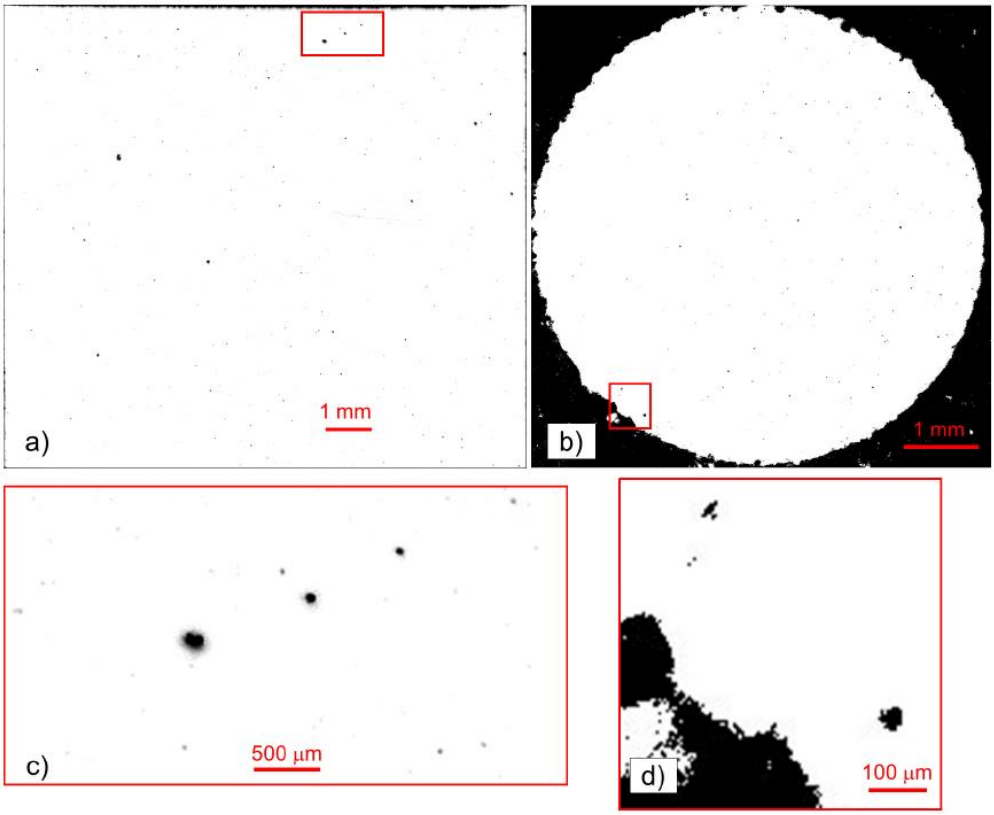

Figure 109: (a) Graphically processed polished longitudinal section of a machined sample; (b) graphically processed polished cross section of an unmachined sample; (c) a detail of (a); (d) a detail of (b) with visible sub-surface porosities

In these images, voids and porosities are highlighted by dark shadows in a white landscape: the amount of black may be easily determined by graphic processing with the aid of several freeware software. Therefore, the ratio between the black and the white pixels can be regarded as a reliable indicator of the porosity level in the investigated area. This outcome, if confirmed by similar analysis on the same component, may be extended to the entire part [3.36]. The retrieved data indicate the porosity level is consistent for all the sample sets: it is in particular 0.1% for NN, HN ad NM Sets, and a bit high, up to 0.3 % for the HM Set.

3.4.5 Fractographic analyses

Fracture surfaces were analyzed by the aforementioned Zeiss Stemi 305 stereoscopic microscope, the Nikon Optiphot-100 optical microscope and the Tescan Mira 3 SEM to individuate crack nucleation sites and to highlight any internal defects, oxides or porosities. Some fracture surfaces are shown in Figure 110. It was found that almost the totality of failure starts from surface defects with multiple nucleation points for not machined specimens (types NN and HN). As it is well known, a high surface roughness has the detrimental effect of triggering crack initiation and consequent propagation. Conversely, in most (over 90%) machined samples (NM and HM types), the failure grows up from internal porosities located at a distance from the edge up to 500 μm. This outcome is clearly due to the removal of surface defects and roughness crests, as also confirmed by the much better fatigue response versus unmachined specimens. In addition, part machining with 0.5 mm allowance has also the capability of removing contour lines. Thus, several sub-surface defects and voids, which are often present at the interface between laser scans and contour lines (as highlighted above and as it is also visible in the detail in Figure 109d), are also removed. A detail of the crack initiation sources is shown in Figure 111 for an unmachined sample and Figure 112 for a machined one. It can be observed that in unmachined sample surface irregularities acted as sharp notches. Conversely, when considering machined samples, sub-surface voids were usually the primary reason for crack initiation.

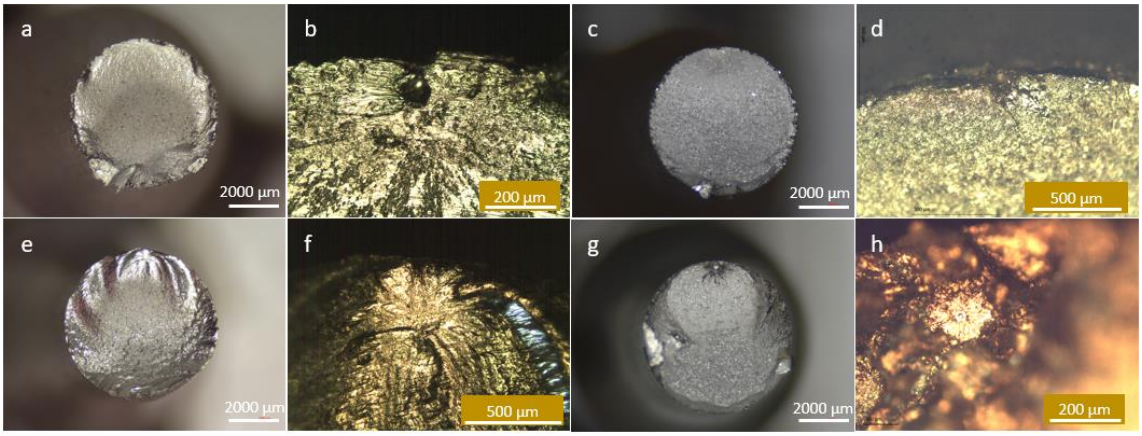

Figure 110: Fracture surfaces observed by stereoscope (a,c,e,f) and by optical microscope (b,d,f,h). Sample n°: NN08 (a,b); HN05 (c,d); NM05 (e,f); HM13 (g,h).

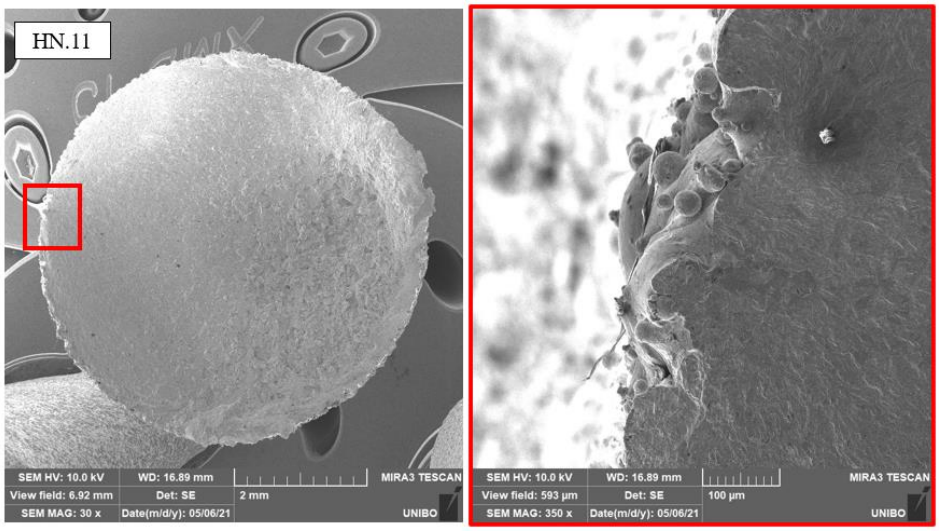

Figure 111: Crack initiation source in an unmachined sample. Superficial un-melted powder and sub-superficial pore.

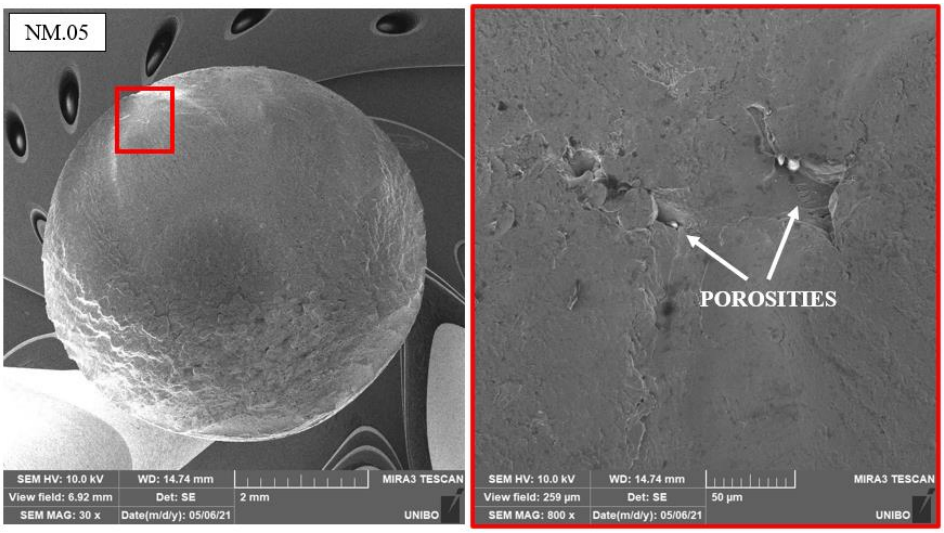

Figure 112: Crack initiation source in a machined sample. Sub-surface porosities.

Details of beach-marks are provided in Figure 113 for both not heat-treated and treated conditions. Not significant differences may be observed between the retrieved patterns that also keep the same spacing (300 nm). As for final fracture mode, not-heat-treated samples exhibited a ductile fracture as clearly highlighted by dimples in Figure 114 (sample NN.10) with reference to ultimate fracture. Heat-treatment had indeed the relevant role of significantly increasing the fatigue strength, but fracture turned to be brittle with trans-granular mode (cleavage). This is clearly visible in sample HN.03 in Figure 114, although some spots of ductile fracture (highlighted in the same picture) are still present. Material embrittlement is in agreement with hardness increase and toughness drop observed in [3.37].

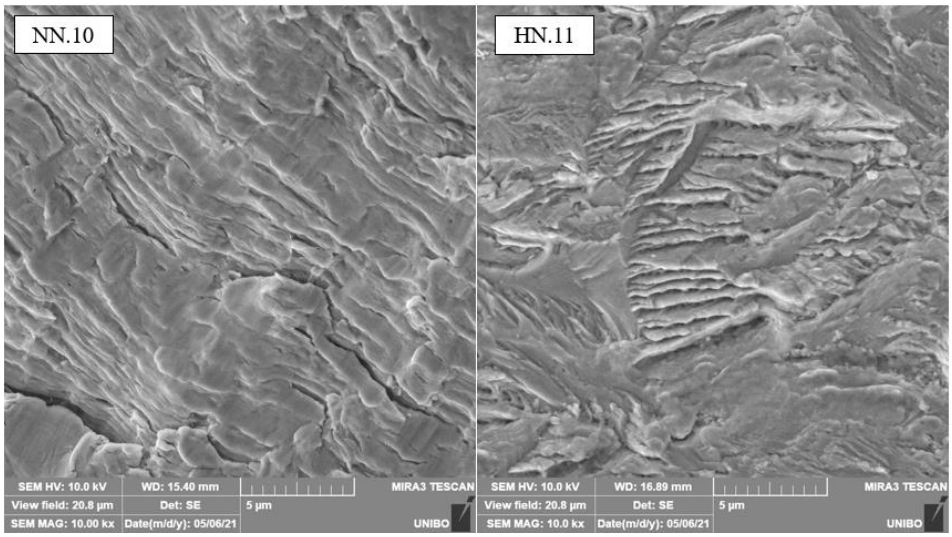

Figure 113: Benchmarks in not heat-treated (NN.10) and in heat treated (HN.11) conditions

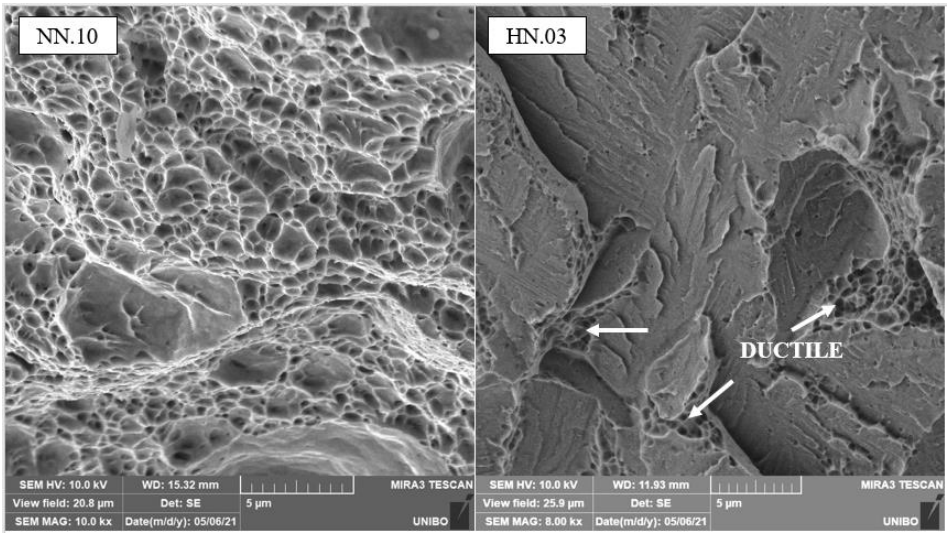

Figure 114: Ductile fracture in not heat-treated conditions (NN.10) and brittle trans-granular fracture in heat-treated conditions

3.4.6 Micrographic analyses

Micrographies were performed by the optical microscope and by the scanning electron microscope. These analyses were aimed at assessing the microstructure in the as-built condition and following heat-treatment, thus assessing heat-treatment strengthening effect. As in 3.3.7, a section parallel to the base plate and another one perpendicular were cut from three samples of each family.

Vilella's reagent with surface pre-heating was utilized as chemical etchant. The outcomes of micrographies by optical microscope are shown in Figure 115 and Figure 116. The first one refers to not heat-treated specimens (NN and NM Sets). The picture in Figure 115a was taken, following a cut along the sample longitudinal section (a plane containing the sample main axis of inertia). Therefore, the microstructure along the vertical stacking direction is here depicted. Conversely, the micrography in Figure 115b refers to a transverse cut along the cross section, which means the microstructure on the build surface is here investigated. Stacked layers are clearly visible in Figure 115a, whereas laser scans can be observed on the build surface in Figure 115b. The retrieved microstructure is completely different in the heat-treated specimens, where the typical structure of additively processed parts is no longer visible and the difference between stacked layers and laser scans also vanishes. A microscope observation is displayed in Figure 116, considering the same chemical etching. This image refers to a longitudinal plane along the build orientation, but exactly the same pattern was observed in the perpendicular plane.

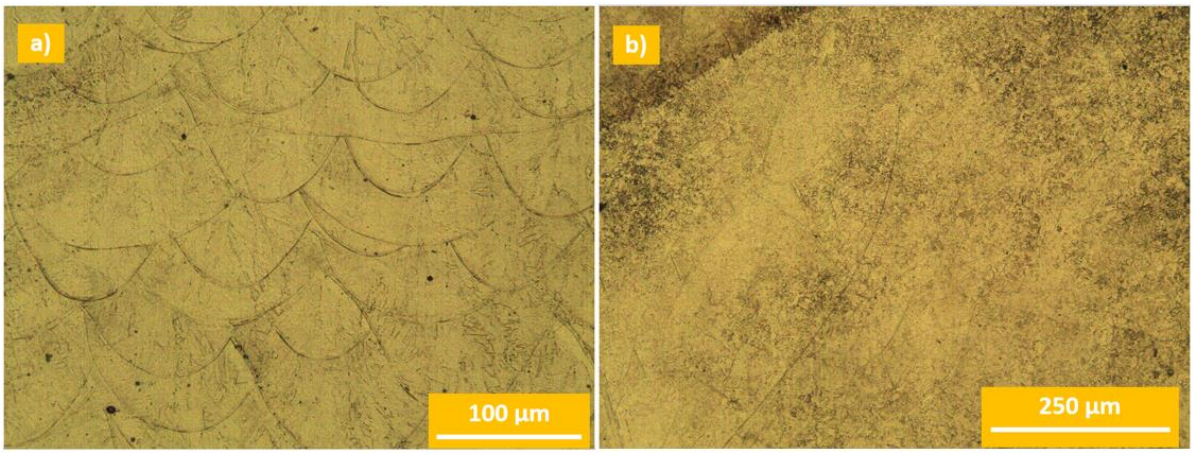

Figure 115: Micrographies surfaces. a) Sample NM09, longitudinal section. b) Sample NN01, cross section

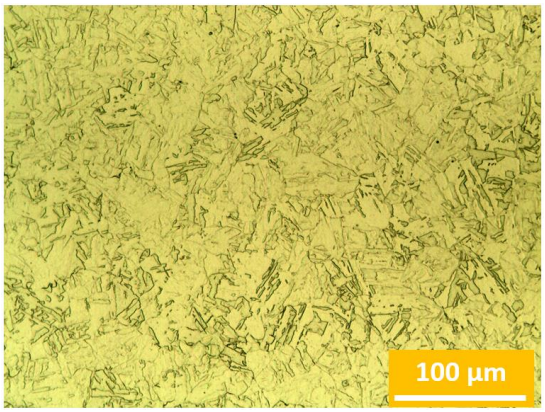

Figure 116: Micrography involving a heat-treated sample (from Set HM)

The microstructure in the as-built and heat-treated conditions were then investigated by SEM trials. In particular, the analysis involving not-heat-treated samples, has made it possible to get awareness of the solidification morphology, following the stacking process. The picture in Figure 117a, taken on the build surface, indicates the solidification process has led to a set of equiaxed and columnar cells.

The generation of these morphologies arises from the actual solidification rate and thermal gradient. For instance, a high cooling rate leads to the development of a fine equiaxed cellular structure. A similar structure was observed in other samples from not-heat-treated specimens, regardless of surface orientation with respect to build orientation. A detail of precipitates is displayed in Figure 117b. As previously highlighted, the structure of this maraging stainless steel consists of fine nanoprecipitates being uniformly distributed in a martensitic matrix. After the annealing and aging heat-treatments, the existing precipitates (mainly β-NiAl) tend to grow-up, whereas additional ones are induced to nucleate. This general growth of precipitates plays an important role for material strengthening [3.37]. The observed microstructure in heat-treated samples is shown in Figure 118a. It is worth mentioning that heat treatment leads to around 1 µm wide elongated grains. The annealing and aging treatments leads to precipitate growth from the range 20 nm to 70 nm to that between 50 nm and 130nm. Consistently with the observations in [3.37], this is the most relevant mechanism that leads to strength enhancement against fatigue. A detail of Figure 118a, along with precipitate compounds, is provided in Figure 118b and Figure 118c.

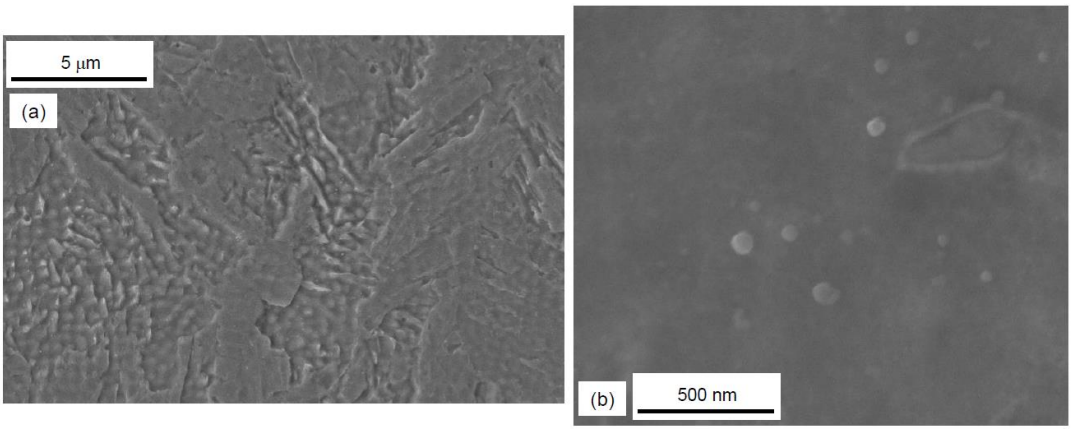

Figure 117: SEM observations in the not heat-treated state: a) equiaxed columnar cell structures, b) observed precipitates

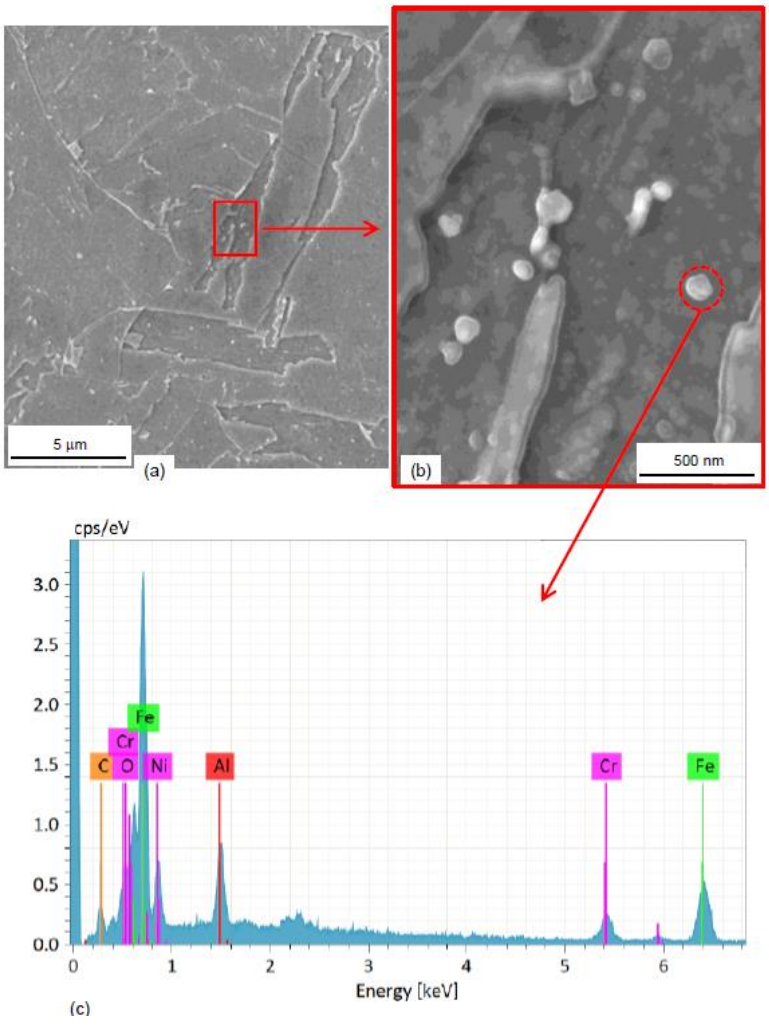

Figure 118: SEM observations after heat-treatment: a) elongated grains; b) detail of (a) with precipitates; c) precipitate compounds

3.4.7 Conclusions

The fatigue performance of additively manufactured maraging stainless steel CX were accurately evaluated, determining the effects of heat treatment and of machining. Both heat treatment and machining have a remarkably positive effect, even if performed singularly. The effect of the machining is particularly relevant even without heat treatment. It indicates this material is highly sensitive to surface irregularities triggering cracks: running machining leads to a 4-time incremented fatigue limit. An important point is when heat treatment and machining are applied together (in this order and with subsequent shot-peening), since they lead to a synergic beneficial effect: the fatigue strength is furtherly enhanced due to the interaction between the two factors. In this case, the ratio between the fatigue limit for infinite life and the ultimate tensile strength is 0.29. When specimens are machined but not heat-treated, the fatigue limit keeps very close to the highest one retrieved for the head treated and machined samples (450MPa against 510MPa). In not machined families, it was observed that fractures generally start from multiple nucleation sites on the surface.

Conversely, machining has the capability of removing the contour layers and smoothing the external surface, thus moving initiation sites to inner layers. Therefore, machining, even without heat treatment, seems to be a good trade off to remarkably enhance fatigue strength.

However, the effect of the heat treatment is not negligible. In this research, only vertically oriented samples were considered. Performing heat-treatment have a big impact at completely removing the stacked structure. It seems to be reasonable that applying heat treatment, possible strength differences due to the build orientation could be removed.

The microstructural properties were observed before and after the heat treatment. It was seen the precipitation size is incremented upon the two-stage heat treatment; in addition, new precipitates tend to nucleate at dislocation tangles and then to grow up. This mechanism leads to hardness and static and fatigue strength increment. On the other hand, final fracture observation indicated a ductile mode for untreated samples and a mainly brittle mode for the treated ones, although some ductile fracture spots are still present.

3.5 References

[3.1] Erhard Brandl, Ulrike Heckenberger, Vitus Holzinger, Damien Buchbinder. Additive manufactured AlSi10Mg samples using Selective Laser Melting (SLM): Microstructure, high cycle fatigue, and fracture behavior. Materials and Design 34 (2012) 159–169

[3.2] Leonhard Hitzler, Christoph Janousch, Jochen Schanz, Markus Merkel, Burkhard Heine, Florian Mack, Wayne Hall, Andreas Öchsner. Direction and location dependency of selective laser melted AlSi10Mg specimens. Journal of Materials Processing Technology 243 (2017) 48–61.

[3.3] Yang, T.; Liu, T.; Liao, W.; MacDonald, E.; Wei, H.; Chen, X.; Jiang, L. The influence of process parameters on vertical surface roughness of the AlSi10Mg parts fabricated by selective laser melting. J. Mater. Process. Technol. 266, (2019), 26–36

[3.4] Binnur Sagbas. Post-Processing Effects on Surface Properties of Direct Metal Laser Sintered AlSi10Mg Parts. Metals and Materials International (2020) 26:143–153. https://doi.org/10.1007/s12540-019-00375-3.

[3.5] Croccolo, D., De Agostinis, M., Fini, S., Olmi, G., Robusto, F., Kostić, S. Ć., Bogojević, N. Fatigue response of as-built DMLS maraging steel and effects of aging, machining, and peening treatments. Metals, 2018, 8(7) doi:10.3390/met8070505.

[3.6] Croccolo, D., De Agostinis, M., Fini, S., Olmi, G., Robusto, F., Ćirić-Kostić, S., Bogojević, N. Sensitivity of direct metal laser sintering maraging steel fatigue strength to build orientation and allowance for machining. Fatigue and Fracture of Engineering Materials and Structures, 2019, 42(1), 374-386. doi:10.1111/ffe.12917.

[3.7] EOS GmbH – Electro Optical Systems, Material Data Sheet: EOS AlSi10Mg. https://www.eos.info/03_system-related-assets/material-related-contents/metal-materials-and-examples/metal-material-datasheet/aluminium/material_datasheet_eos_aluminium-alsi10mg_en_web.pdf

[3.8] Maamoun, A.H.; Xue, Y.F.; Elbestawi, M.A.; Veldhuis, S.C. The effect of selective laser melting process parameters on the microstructure and mechanical properties of Al6061 and AlSi10Mg alloys. Materials (Basel). 12, (2018), 1–24.

[3.9] Kempen, K.; Thijs, L.; Van Humbeeck, J.; Kruth, J.-P. Mechanical Properties of AlSi10Mg Produced by Selective Laser Melting. In Proceedings of the Physics Procedia; (2012); Vol. 39, pp. 439–446.

[3.10] Rosenthal, I.; Stern, A.; Frage, N. Microstructure and Mechanical Properties of AlSi10Mg Parts Produced by the Laser Beam Additive Manufacturing (AM) Technology. Metallogr. Microstruct. Anal. 3, (2014), 448–453

[3.11] Beevers, E.; Brandão, A.D.; Gumpinger, J.; Gschweitl, M.; Seyfert, C.; Hofbauer, P.; Rohr, T.; Ghidini, T. Fatigue properties and material characteristics of additively manufactured AlSi10Mg – Effect of the contour parameter on the microstructure, density, residual stress, roughness and mechanical properties. Int. J. Fatigue 117, (2018), 148–162

[3.12] Tang, M.; Pistorius, P.C. Oxides, porosity and fatigue performance of AlSi10Mg parts produced by selective laser melting. Int. J. Fatigue 94, (2017), 192–201

[3.13] Alberto Boschetto, Luana Bottini, Daniela Pilone. Effect of laser remelting on surface roughness and microstructure of AlSi10Mg selective laser melting manufactured parts. The International Journal of Advanced Manufacturing Technology. https://doi.org/10.1007/s00170-021-06775-3.

[3.14] Lv, F.; Shen, L.; Liang, H.; Xie, D.; Wang, C.; Tian, Z. Mechanical properties of AlSi10Mg alloy fabricated by laser melting deposition and improvements via heat treatment. Optik (Stuttg). 179, (2019), 8–18.

[3.15] Girelli, L.; Tocci, M.; Gelfi, M.; Pola, A. Study of heat treatment parameters for additively manufactured AlSi10Mg in comparison with corresponding cast alloy. Mater. Sci. Eng. A 739, (2019), 317–32

[3.16] Girelli, L.; Tocci, M.; Montesano, L.; Gelfi, M.; Pola, A. Optimization of heat treatment parameters for additive manufacturing and gravity casting AlSi10Mg alloy. IOP Conf. Series: Materials Science and Engineering 264 (2017) 012016 doi:10.1088/1757-899X/264/1/012016.

[3.17] Ben Amir, Eyal Grinberg, Yuval Gale, Oren Sadot, Shmuel Samuha. Influences of platform heating and post-processing stress relief treatment on the mechanical properties and microstructure of selective-laser-melted AlSi10Mg alloys. Materials Science & Engineering A 822 (2021) 141612

[3.18] Hirata, T.; Kimura, T.; Nakamoto, T. Effects of hot isostatic pressing and internal porosity on the performance of selective laser melted AlSi10Mg alloys. Mater. Sci. Eng. A 772, (2020)

[3.19] EOS GmbH – Electro Optical Systems, Material Data Sheet: EOS Stainless Steel CX, München, 2017. www.eos.info

[3.20] H. Asgari, M. Mohammadi, Microstructure and mechanical properties of stainless steel CX manufactured by Direct Metal Laser Sintering. Materials Science & Engineering A 709 (2018) 82–89.

[3.21] Z. Guo, W. Sha, D. Vaumousse, Microstructural evolution in a PH13-8 stainless steel after ageing, Acta Mater. 51 (2003) 101–116, https://doi.org/10.1016/S1359-6454(02)00353-1

[3.22] EOS GmbH – Electro Optical Systems, Material Data Sheet: EOS stainless steel CX. https://www.eos.info/03_system-related-assets/material-related-contents/metal-materials-and-examples/metal-material-datasheet/stainlesssteel/material_datasheet_eos_stainlesssteel_cx_premium_en_web.pdf

[3.23] M. Sanjari, A. Hadadzadeh, H. Pirgazi, A. Shahriari, B.S. Amirkhiz, L.A.I. Kestens, M. Mohammadi, Selective laser melted stainless steel CX: Role of built orientation on microstructure and micro-mechanical properties. Materials Science & Engineering A 786 (2020) 139365.

[3.24] Croccolo, D., De Agostinis, M., Fini, S., Olmi, G., Bogojevic, N., & Ciric-Kostic, S. Effects of build orientation and thickness of allowance on the fatigue behaviour of 15–5 PH stainless steel manufactured by DMLS. Fatigue and Fracture of Engineering Materials and Structures, 2018, 41(4), 900-916. doi:10.1111/ffe.12737

[3.25] Croccolo D, De Agostinis M, Fini S, Olmi G, Vranic A, Ciric-Kostic S. Influence of the build orientation on the fatigue strength of EOS maraging steel produced by additive metal machine. Fatigue & Fracture of Engineering Materials & Structures, 2016, 39, p. 637-647.

[3.26] G. Olmi. Low cycle fatigue experiments on Turbogenerator steels and a new method for defining confidence bands. J Test Eval.n2012;40:4 Paper ID JTE104548.

[3.27] Ming Tang, Petrus Christiaan Pistorius. Fatigue life prediction for AlSi10Mg components produced by selective laser melting. International Journal of Fatigue 125 (2019) 479–490.

[3.28] Changchun Zhang, Haihong Zhu, Zhiheng Hu, Luo Zhang, Xiaoyan Zeng. A comparative study on single-laser and multi-laser selective laser melting AlSi10Mg: defects, microstructure and mechanical properties. Materials Science & Engineering A 746 (2019) 416–423

[3.29] Changchun Zhang, Haihong Zhu, Hailong Liao, Yong Cheng, Zhiheng Hu, Xiaoyan Zeng. Effect of heat treatments on fatigue property of selective laser melting AlSi10Mg. International Journal of Fatigue 116 (2018) 513–522.

[3.30] Shafaqat Siddique, Muhammad Imran, Eric Wycisk, Claus Emmelmann, Frank Walther,
Influence of process-induced microstructure and imperfections on mechanical properties of AlSi12 processed by selective laser melting, Journal of Materials Processing Technology, Volume 221, 2015, Pages 205-213, ISSN 0924-0136, https://doi.org/10.1016/j.jmatprotec.2015.02.023.
[3.31] Nesma T. Aboulkhair, Ian Maskery, Chris Tuck, Ian Ashcroft, Nicola M. Everitt. The microstructure and mechanical properties of selectively laser melted AlSi10Mg: The effect of a conventional T6-like heat treatment
[3.32] ASTM E18-16. Standard Test Methods for Rockwell Hardness of Metallic Materials. ASTM International, West Conshohocken, PA, United States.
[3.33] Dixon WJ, Massey F Jr. Introduction to Statistical Analysis. McGraw-Hill, New York, United States, 1983.
[3.34] Niemann G, Winter H, Hohn BR. Maschinenelemente. Germany: Springer-Verlag; 2005
[3.35] I. Maskery, N.T. Aboulkhair, M.R. Corfield, et al. Quantification and characterisation of porosity in selectively laser melted al-Si10-mg using X-ray computed tomography. Mater Charact. 2016; 111:193-204
[3.36] Branco R, Costa J.D.M, Berto F, Razavi SMJ, Ferreira JAM, Capela C, Santos L, Antunes F. Low-Cycle Fatigue Behaviour of AISI 18Ni300 Maraging Steel Produced by Selective Laser Melting. Metals. 2018; 8: 32.
[3.37] Chang C, Yan X, Bolot R, Gardan J, Gao S, Liu M, Liao H, Chemkhi M, Deng S. Influence of post-heat treatments on the mechanical properties of CX stainless steel fabricated by selective laser melting. J Mater Sci. 2020; 55: 8303–8316

APPENDIX: AlSi10Mg fatigue curves

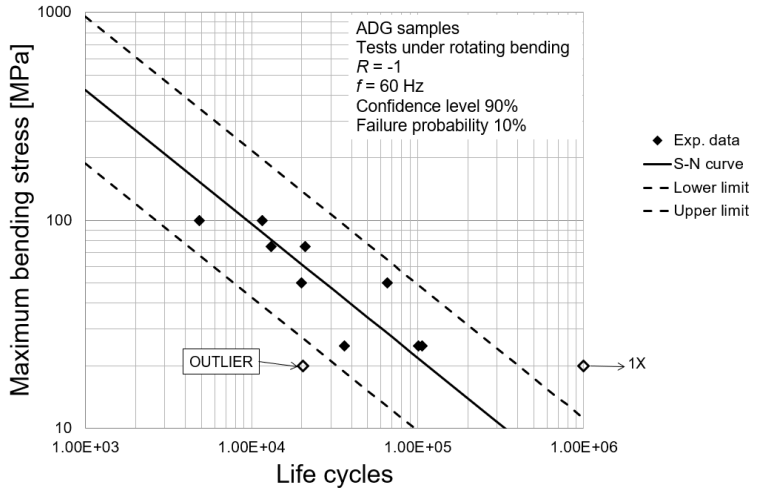

Figure 119: Alsi10Mg fatigue curve. Set ADG: horizontally built, no-heat treated, shot-peened

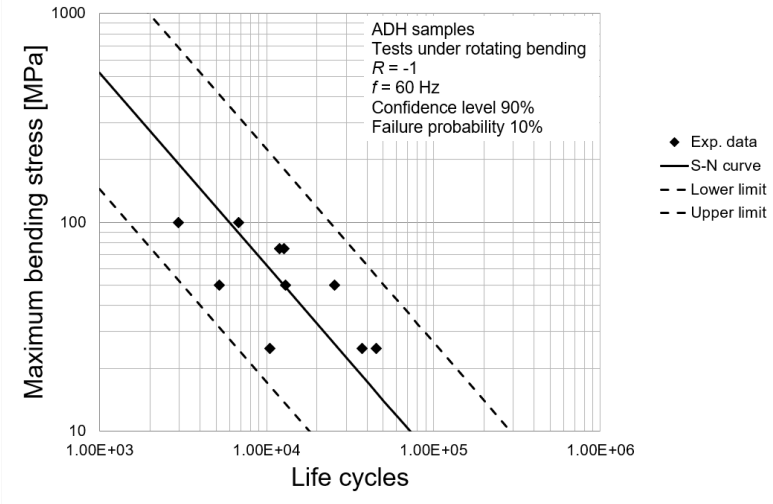

Figure 120: Alsi10Mg fatigue curve. Set ADH: horizontally built, no-heat treated, shot-peened and fine blasted

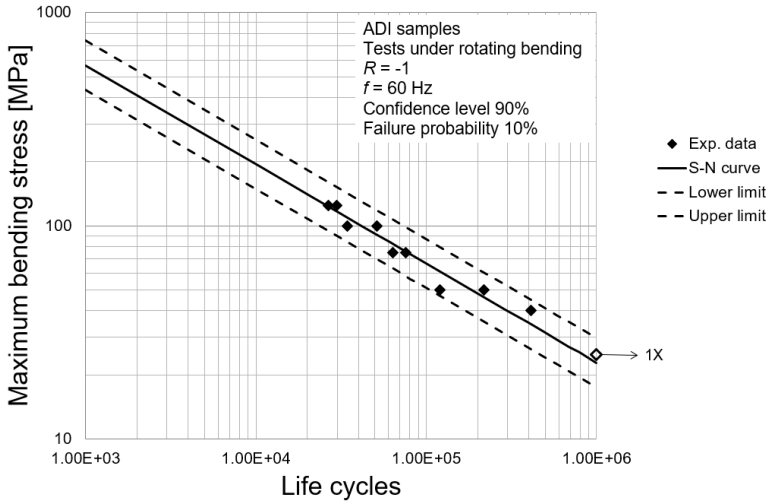

Figure 121: Alsi10Mg fatigue curve. Set ADI: horizontally built, no-heat treated, machined

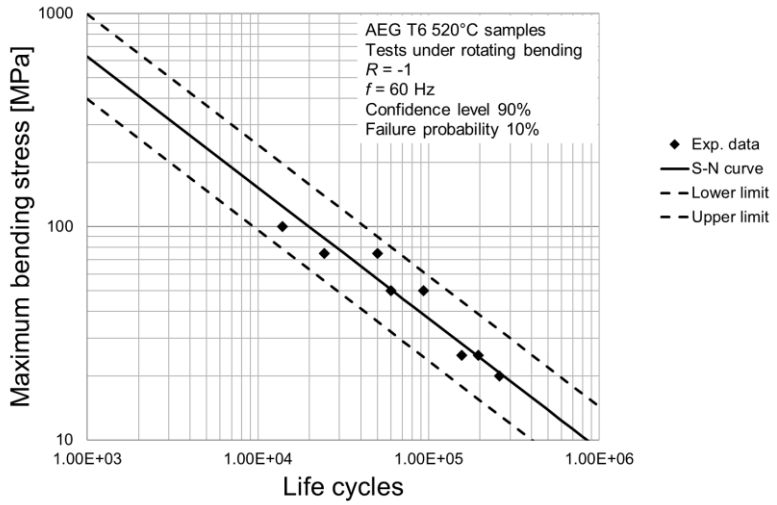

Figure 122: Alsi10Mg fatigue curve. Set AEG: horizontally built, T6 heat treated, shot-peened

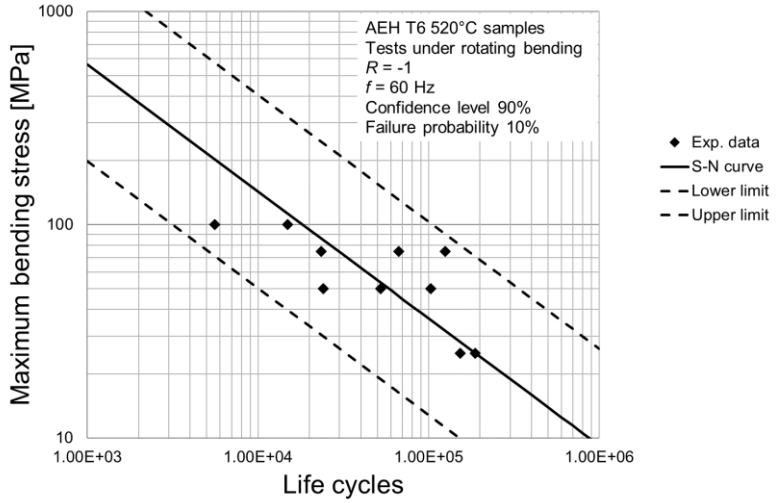

Figure 123: Alsi10Mg fatigue curve. Set AEH: horizontally built, T6 heat treated, shot-peened and fine blasted

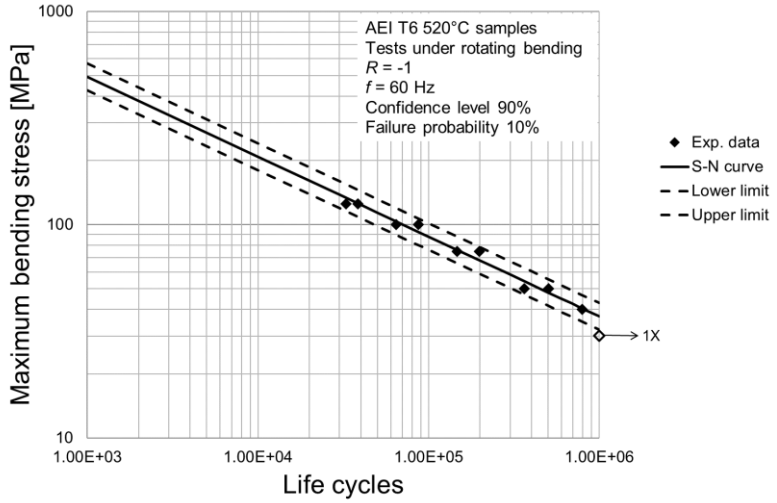

Figure 124: Alsi10Mg fatigue curve. Set AEI: horizontally built, T6 heat treated, machined

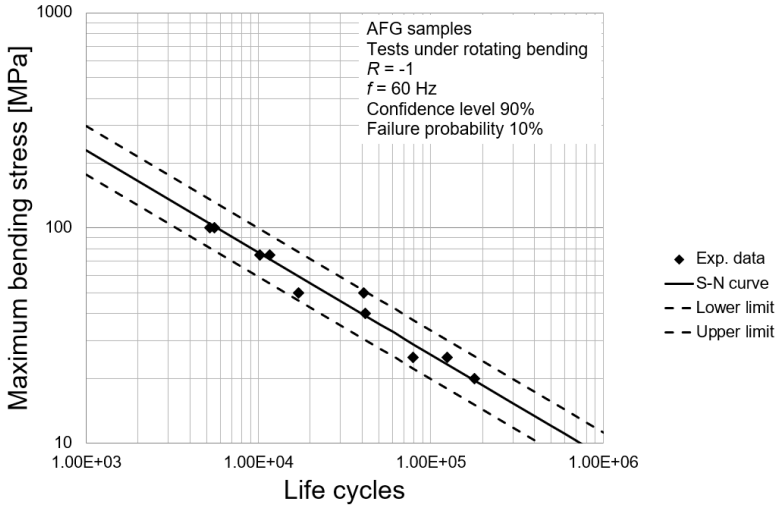

Figure 125: Alsi10Mg fatigue curve. Set AFG: horizontally built, stress relieved, shot-peened

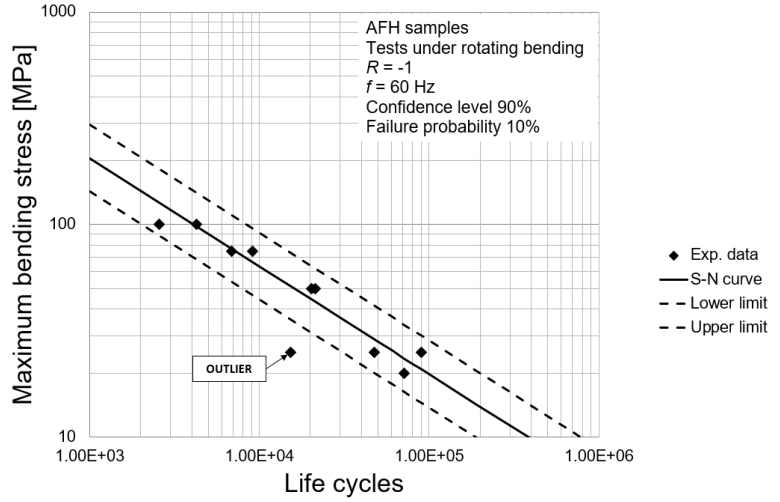

Figure 126: Alsi10Mg fatigue curve. Set AFH: horizontally built, stress relieved, shot-peened and fine blasted

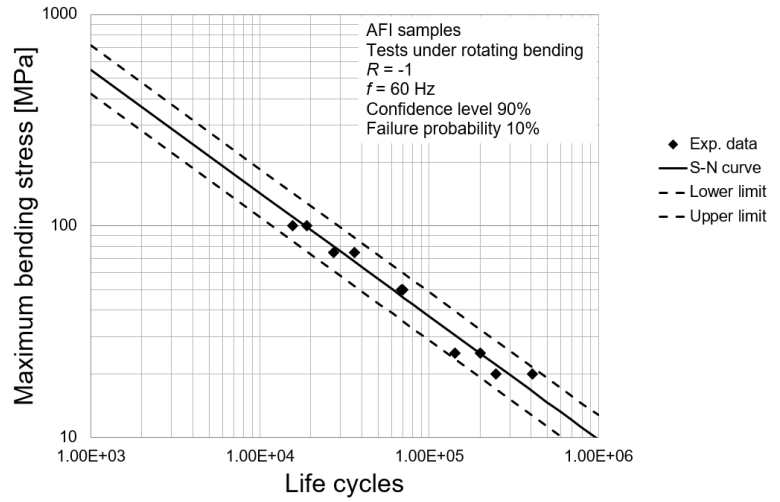

Figure 127: Alsi10Mg fatigue curve. Set AFI: horizontally built, stress relieved, machined

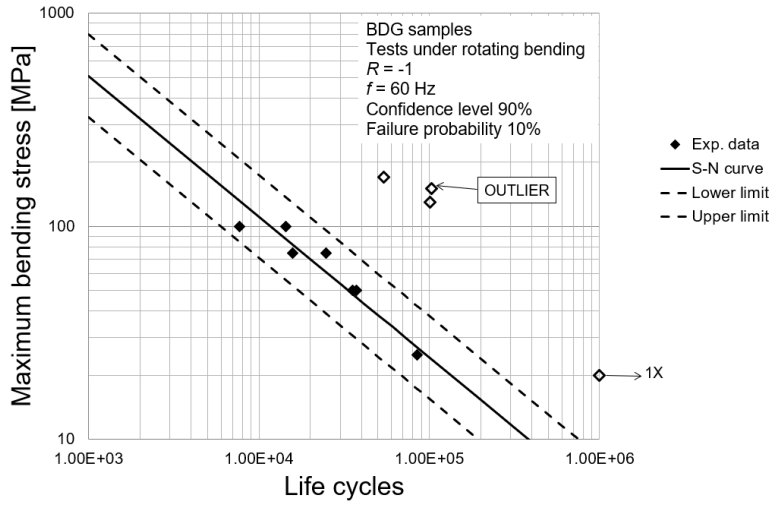

Figure 128: Alsi10Mg fatigue curve. Set BDG: slanted built, no-heat treated, shot-peened

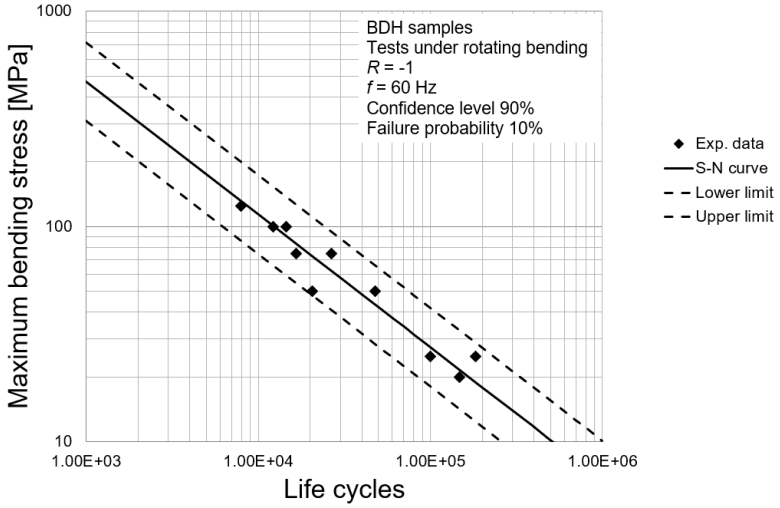

Figure 129: Alsi10Mg fatigue curve. Set BDH: slanted built, no-heat treated, shot-peened and fine blasted

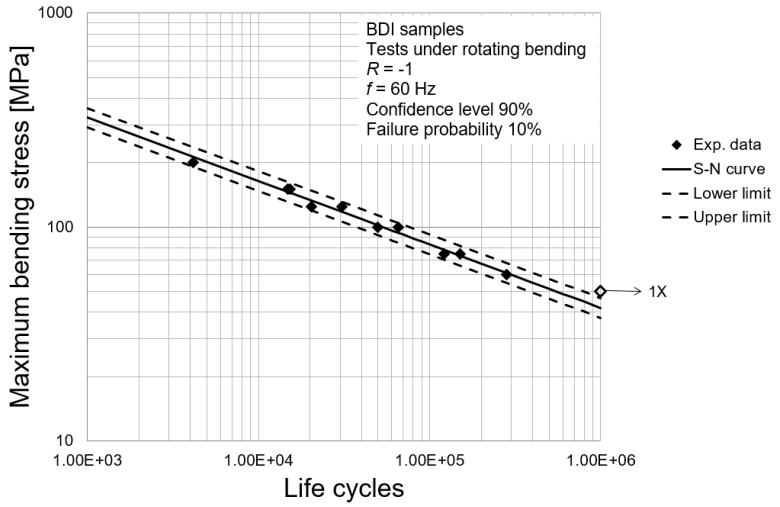

Figure 130: Alsi10Mg fatigue curve. Set BDI: slanted built, no-heat treated, machined

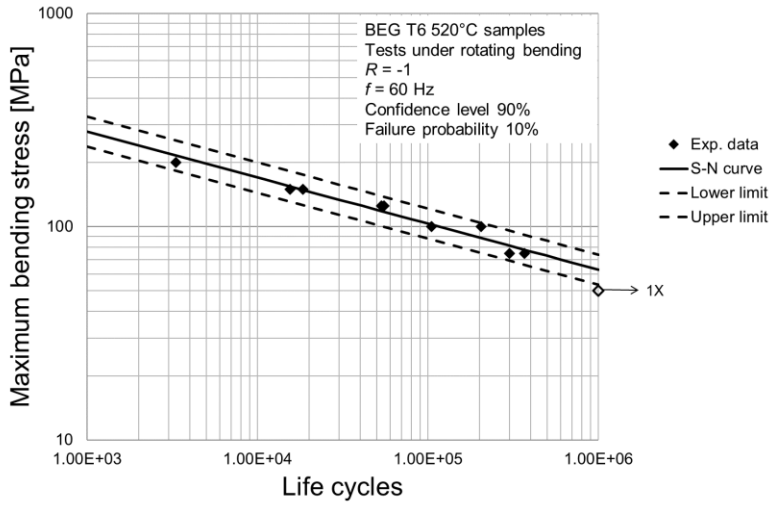

Figure 131: Alsi10Mg fatigue curve. Set BEG: slanted built, T6 heat treated, shot-peened

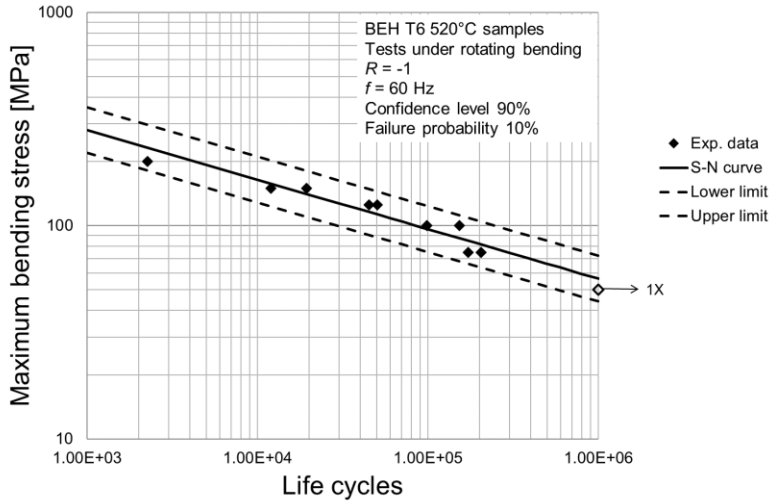

Figure 132: Alsi10Mg fatigue curve. Set BEH: slanted built, T6 heat treated, shot-peened and fine blasted

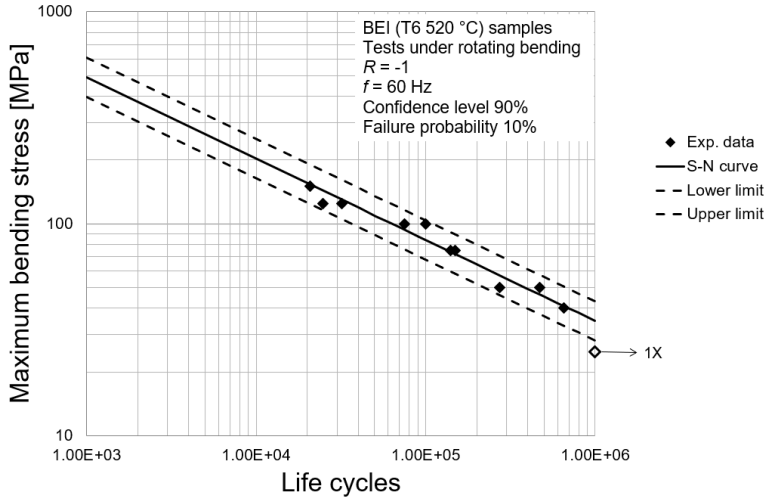

Figure 133: Alsi10Mg fatigue curve. Set BEI: slanted built, T6 heat treated, machined

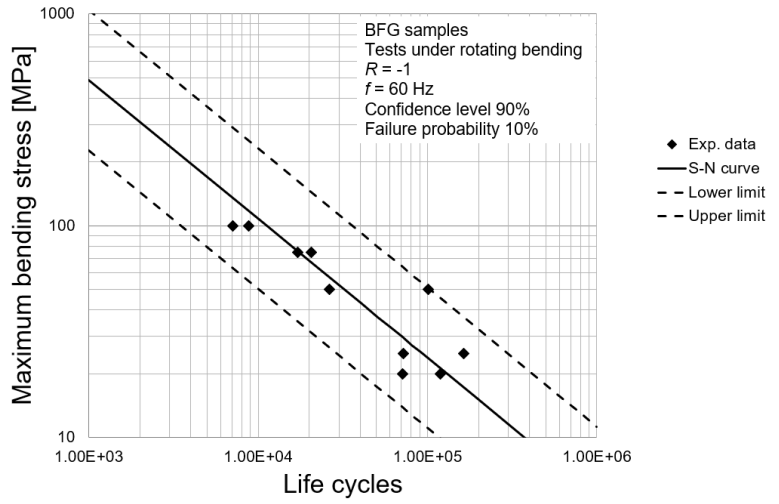

Figure 134 : Alsi10Mg fatigue curve. Set BFG: slanted built, stress relieved, shot-peened

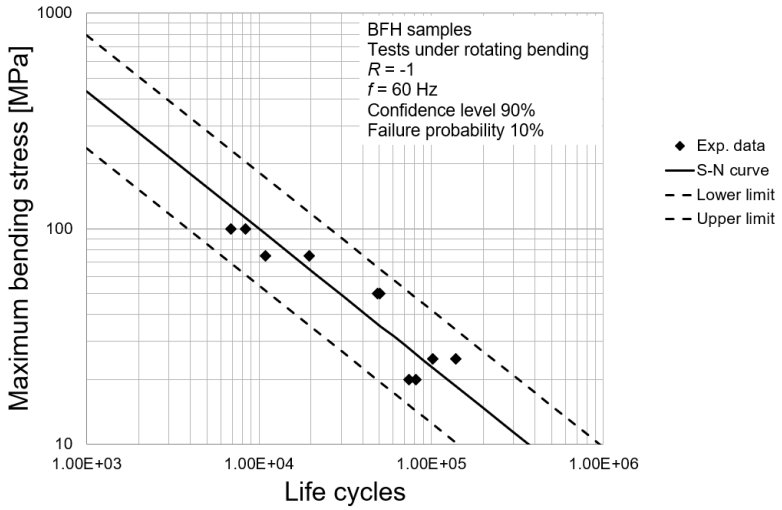

Figure 135: Alsi10Mg fatigue curve. Set BFH: slanted built, stress relieved, shot-peened and fine blasted

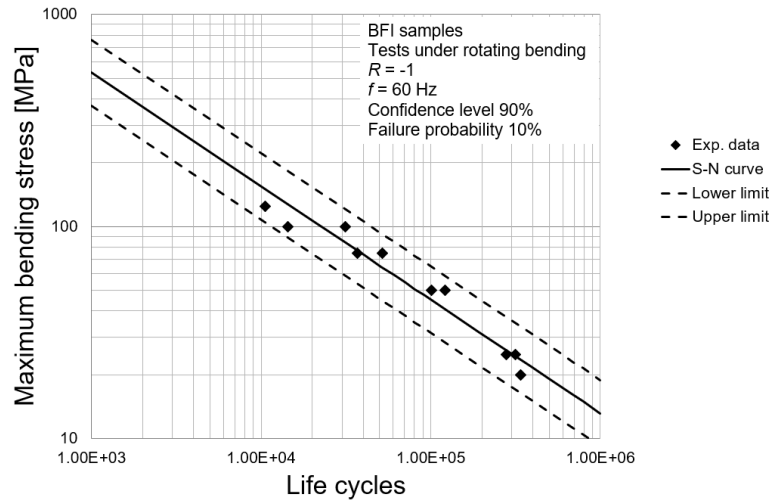

Figure 136: Alsi10Mg fatigue curve. Set BFI: slanted built, stress relieved, machined

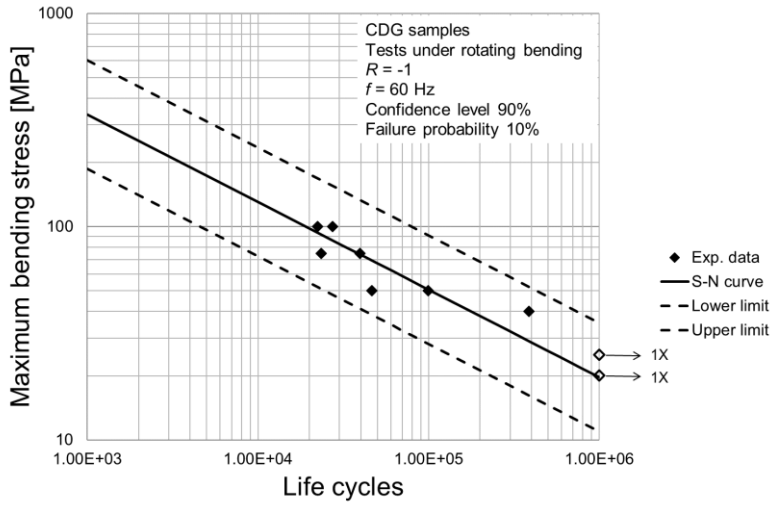

Figure 137: Alsi10Mg fatigue curve. Set CDG: vertically built, no-heat treated, shot-peened

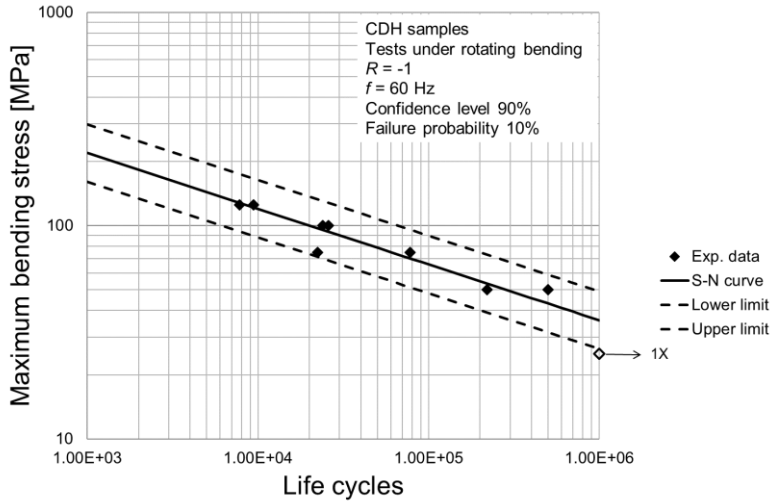

Figure 138: Alsi10Mg fatigue curve. Set CDH: vertically built, no-heat treated, shot-peened and fine blasted

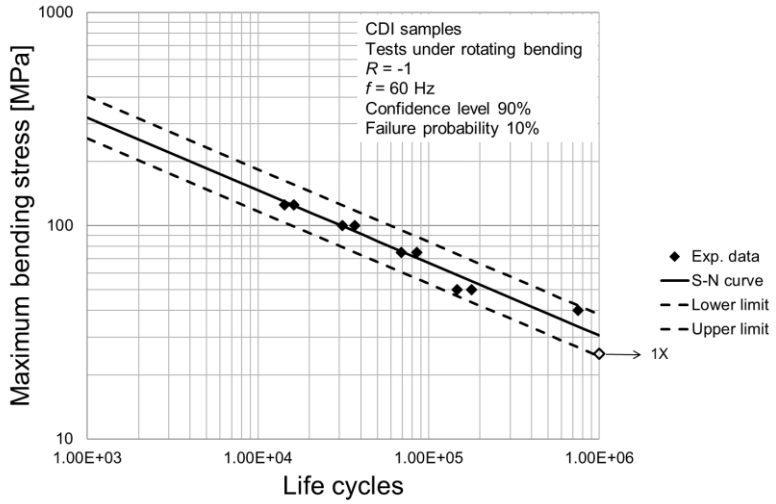

Figure 139: Alsi10Mg fatigue curve. Set CDI: vertically built, no-heat treated, machined

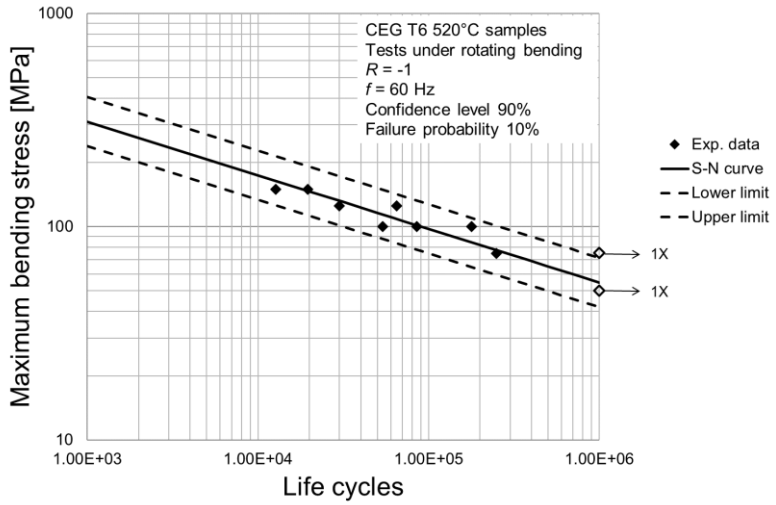

Figure 140: Alsi10Mg fatigue curve. Set CEG: vertically built, T6 heat treated, shot-peened

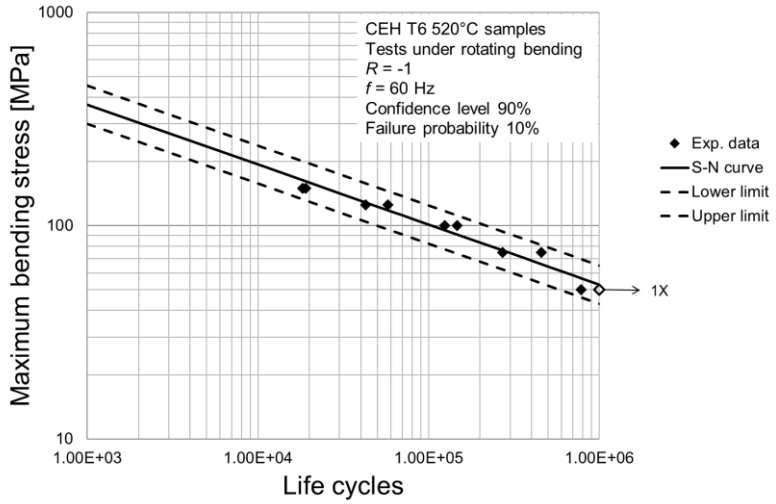

Figure 141: Alsi10Mg fatigue curve. Set CEH: vertically built, T6 heat treated, shot-peened and fine blasted

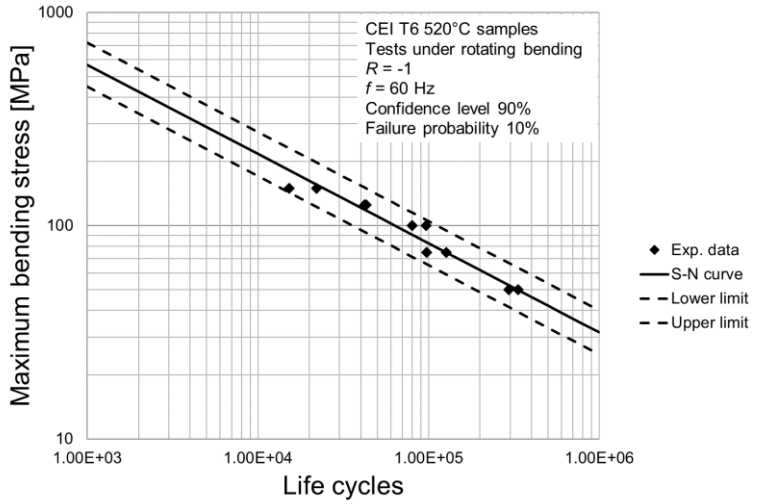

Figure 142: Alsi10Mg fatigue curve. Set CEI: vertically built, T6 heat treated, machined

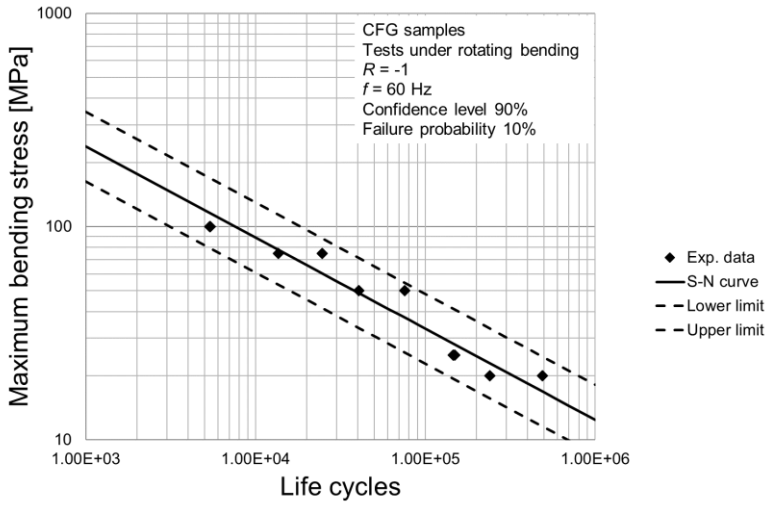

Figure 143: Alsi10Mg fatigue curve. Set CFG: vertically built, stress relieved, shot-peened

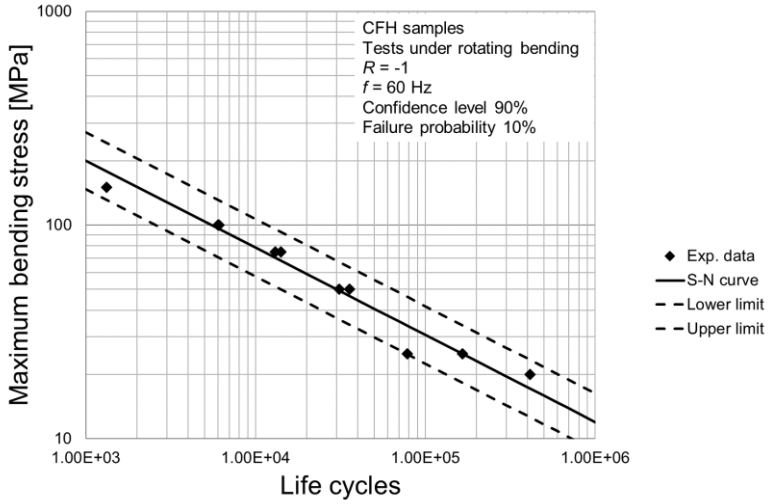

Figure 144: Alsi10Mg fatigue curve. Set CFH: vertically built, stress relieved, shot-peened and fine blasted

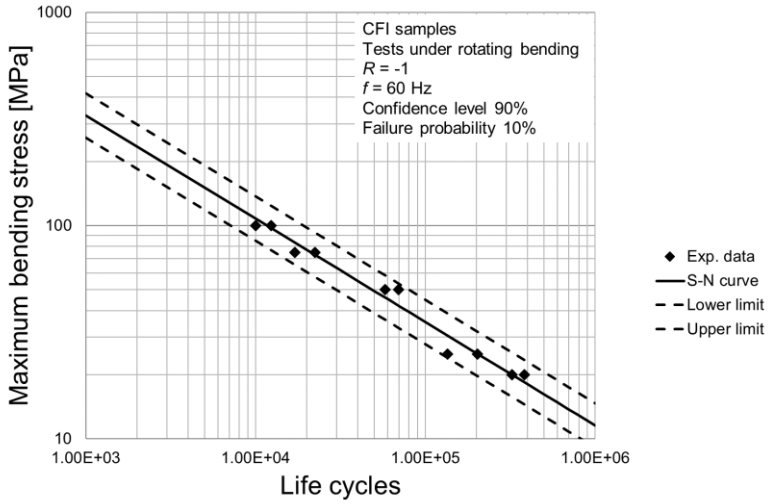

Figure 145: Alsi10Mg fatigue curve. Set CFI: vertically built, stress relieved, machined